# Photoelectrochemical conversion of protons and CO from functionalized silicon photocathodes

Dong Fu

UNIVERSITE MATIERE BRETAGNE MOLECULES LOIRE ET MATERIAUX

UNIVERSITÉ DE RENNES 1

# THESE DE DOCTORAT DE

L'UNIVERSITE DE RENNES 1
COMUE UNIVERSITE BRETAGNE LOIRE

ECOLE DOCTORALE N° 596
*Matière Molécules et Matériaux*
Spécialité : *Sciences des Matériaux*

Par

**Dong FU**

## Conversion photoélectrochimique des protons et $CO_2$ à partir de photocathodes en silicium fonctionnalisées

**Thèse présentée et soutenue à Rennes, le 07/11/2019**

**Unité de recherche : UMR CNRS 6226**

**Rapporteurs avant soutenance :**

**Valérie KELLER-SPITZER**
Directrice de Recherche CNRS – ICPEES
Université Strasbourg

**Ally AUKAULOO**
Professeur ICMMO
Université Paris-Sud Orsay

**Composition du Jury :**

**Valérie KELLER-SPITZER**
Directrice de Recherche CNRS – ICPEES
Université Strasbourg / Rapporteur

**Ally AUKAULOO**
Professeur ICMMO
Université Paris-Sud Orsay / Rapporteur

**Emmanuel CADOT**
Professeur Université - ILV
Université Paris-Saclay Versailles / Président

**Florence GENESTE**
Directrice de Recherche CNRS – ISCR
Université de Rennes 1 / Membre Invitée

**Bruno FABRE**
Directeur de Recherche CNRS – ISCR
Université de Rennes 1 / Co-directeur de thèse

**Gabriel LOGET**
Charge de Recherche CNRS – ISCR
Université de Rennes 1 / Co-directeur de thèse

*For my dear daughter (Elena), my mother and my wife*

## Acknowledgements

First, I would like to thank my supervisor, Professor Bruno Fabre for opportunity to do this thesis. Thank you for supporting me throughout the thesis, for your excellent advice, and to discuss about the work. I would also like to thank my second supervisor, Dr. Gabriel Loget, for teaching me how to fabricate electrodes in the lab, and for answering all my questions. Thanks to all of my collaborators on the ANR project “Chalco-POM-Based Electrocatalysts for high performance energy conversion – Chalco-Cat”.

Finally, I would especially like to thank my wonderful family, my parents and my wife, for supporting me during these three years. Thank you!

Dong FU, Rennes, November 2019

# Résumé

Ces travaux de thèse ont porté sur l'élaboration et la caractérisation de photocathodes à base de Si de type-*p* modifiées avec des électrocatalyseurs du type POM (Polyoxometalates) ou métalliques à base de bismuth (Bi) pour les réactions HER (Hydrogen Evolution Reaction) et CDRR ($CO_2$ reduction reaction) respectivement.

La production d'énergie basée sur la combustion de combustibles fossiles a provoqué une grave pollution de l'environnement et le réchauffement de la planète. Par conséquent, l'utilisation de sources d'énergie à haute densité massique telles que l'hydrogène, ainsi que la conversion des émissions de $CO_2$ en produits à haute valeur ajoutée sont deux domaines qui ont fait l'objet d'une attention considérable de la part des chercheurs désireux d'évoluer vers un environnement durable. Dans ce cadre, la conversion photoélectrochimique utilisant l'énergie solaire apparaît comme une méthode prometteuse. Pour cela, le silicium représente un candidat idéal pour la conversion de l'énergie solaire en raison de son abondance terrestre et de ses propriétés semi-conductrices particulières. Avec une petite bande interdite d'environ 1.1 eV et un bord de bande de conduction approprié, le silicium de type *p* est considéré comme un matériau prometteur pour la photocathode. Cependant, ses performances sont fortement affectées par sa faible stabilité et son activité catalytique. Des recherches sont donc en cours pour trouver des stratégies efficaces afin d'améliorer ses performances. Dans ce cadre, le contrôle de la morphologie de surface, la stratégie de modification de la surface ainsi que les jonctions à l'interface sont des paramètres essentiels qui font actuellement l'objet de recherches approfondies.

Dans la première application, les matériaux électrocatalytiques d'intérêt étudiés sont dérivés de clusters $\{Mo_3S_4\}$ comme complexes de coordination incorporés dans le réseau des polyoxométallates (POM). Les polyoxométallates (POMs) sont des entités polynucléaires résultant de la connexion de polyèdres $[MO_y]^{n-}$ où M est un centre métallique. Les POMs représentent des espèces intermédiaires entre l'ion métallate basique mononucléaire $[MO_4]^{n-}$ libre en solution et l'oxyde métallique $MO_x$ solide. L'entité $\{Mo_3S_4\}$ est utilisée dans la formation de complexes de coordination du fait de sa réactivité avec un grand nombre de métaux de transition. Ce composé dit pseudo-cuboïdal possède trois atomes de molybdène susceptibles de réagir avec des ligands aux propriétés très diverses (aquo, amino, hydrure, halogénure,…). Les systèmes comportant des métaux de transition et des entités soufrées sont très étudiés car ils possèdent d'excellentes propriétés catalytiques. Les assemblages POM-entité thiomolybdique comportant des métaux de transition et des entités soufrées sont très étudiés car ils possèdent d'excellentes propriétés catalytiques. Ils sont engagés dans des processus de transfert d'électrons et de protons et sont souvent impliqués dans les sites actifs de molécules biologiques.

La seconde application liée à l'énergie des semi-conducteurs en silicium de type *p* est la réaction d'électro-réduction du $CO_2$ (CDRR). Des photocathodes en silicium de type *p* modifiées avec différents co-catalyseurs ont été développées pour réduire le $CO_2$ en carburants organiques. L'incorporation de cocatalyseurs pourrait améliorer considérablement les performances des électrodes semi-conductrices pour la réduction de $CO_2$. Parmi les cocatalyseurs, le bismuth (Bi), un cocatalyseur de métal non toxique et peu coûteux, est capable de réduire le $CO_2$ en acide formique. Par conséquent, le développement de silicium de type *p* comportant des électrocatalyseurs à base de bismuth est prévu pour obtenir une sélectivité de réduction élevée, et réaliser une activité catalytique favorable pour la réduction photoélectrochimique du $CO_2$.

La thèse est divisée en quatre chapitres principaux, précédés d'une introduction générale et suivis d'une conclusion générale. L'un des objectifs de cette thèse est également axé sur une approche fondamentale consistant à proposer des corrélations structure-activité.

Dans le chapitre 1, la partie bibliographique est consacrée à l'état de l'art sur la production électrocatalytique d'hydrogène par réduction de $H^+$ et à la réduction du $CO_2$. Dans une première partie, la réaction HER est abordée d'un point de vue mécanistique avec une présentation des différentes catégories d'électrocatalyseurs efficaces pour surmonter certaines limitations relatives au surpotentiel et à la barrière cinétique apparaissant dans ces réactions. Un éclairage particulier est fait notamment sur l'utilisation de complexes moléculaires immobilisés sur des électrodes et sur l'importance de la modification des ligands possédant des fonctions d'accroche appropriées. Les POMs sont ensuite décrits et leurs utilisations comme électrocatalyseurs discutées. Dans une seconde partie, nous nous sommes intéressés aux concepts de base de la réaction de CDRR et aux co-catalyseurs spécifiques relatifs à cette réaction d'intérêt : des métaux, notamment le Bi, des oxydes métalliques, des chalcogénures, des complexes organo-métalliques et certaines catégories de POMs. Ce chapitre bibliographique se termine par unediscussion des phénomènes photoélectrocatalytiques se produisant à l'interface semi-conducteur/électrolyte, des divers semi-conducteurs d'intérêt pour la photo-dissociation de l'eau et pour la réduction photo-assistée du $CO_2$, et de l'utilisation de photocathodes à base de Si modifiées par des co-catalyseurs.

Le chapitre 2 (intitulé « Polyoxothiometalate-Derivatized Silicon Photocathodes for Sunlight-Driven Hydrogen Evolution Reaction ») est centré sur l'élaboration de photocathodes à base de Si, décorées avec des structures polyoxotungstates ($AsW_{12}O_{42}$) intégrant des entités à base de $\{Mo_3S_4\}$. Ces photocathodes modifiées sont ensuite évaluées vis-à-vis de la réaction HER en conditions acides, et les activités sont corrélées aux propriétés structurales et aux modifications chimiques. Cette approche vise à surmonter les limitations intrinsèques du silicium en termes de cinétique de transfert de charge

et tire profit de la capacité de fonctionnalisation des POMs. Dans ce cadre, nous avons tout à bord caractérisé les précurseurs moléculaires utilisés, puis le matériau $Mo_3S_4$-POM résultant, avant d'optimiser la teneur sur les électrodes de Si. Les structures $Mo_3S_4$-POM sont déposées par drop-casting sur les surfaces Si(100)-H. Cette étape est ensuite validée par suivi du photocourant cathodique pour la réaction HER sous irradiation solaire artificielle (AM 1.5G, 100 mW $cm^{-2}$), par voltampérométrie cyclique et par des caractérisations détaillées (XPS, AFM) avant et après réaction d'électrolyse. Les photocathodes modifiées présentant les meilleures activités [celles recouvertes de 7.2 x $10^{-5}$ mmol $cm^{-2}$ pour $Mo_3S_4$(acac-Bu) ou 7.2 x $10^{-6}$ mmol $cm^{-2}$ pour $Mo_3S_4$-POM] ont été étudiées sous irradiation. Nous avons ensuite enregistré les courbes chronoampérométriques correspondantes durant l'électrolyse pour les 2 types de photocathodes modifiées. Les réponses photoélectrochimiques ont mise en avant la stabilisation des électrodes modifiées en milieu acide après une courte période d'activation d'environ 5 minutes, qui pourrait être liée à un relargage du dépôt de l'électrode. Nous avons ensuite déterminé les « turnover frequencies » (TOFs) en fonction du potentiel appliqué. Des valeurs élevées (en considérant le nombre de sites actifs estimé par des mesures XPS et AFM) ont été calculées. De telles photocathodes modifiées présentaient des densités de photocourant cathodique supérieures à -26 mA $cm^{-2}$ ainsi qu'une excellente stabilité pour la réduction des protons en $H_2$ dans le milieu acide pendant plus de 45 h.

Le chapitre 3 (intitulé « X-ray absorption spectroscopy study of $Mo_3S_4$ based polyoxothiometalate electrocatalysts during HER ») est consacré à des mesures de spectroscopie d'absorption des rayons X (X-ray Absorption Spectroscopy XAS) sous conditions *operando* (réalisées au synchrotron SOLEIL sur la ligne ROCK) afin de suivre l'évolution de l'environnement des atomes de Mo des électocatalyseurs $Mo_3S_4$-POM déposés sur la photocathode de Si. Après avoir rappelé quelques principes de base et conditions expérimentales de la technique, nous avons décrit la préparation des échantillons reposant sur le dépôt des co-catalyseurs sur l'électrode de type *p*-Si hydrogénée. Des résultats préliminaires obtenus à partir de composés de référence à l'état solide ont permis d'établir les liens entre l'évolution du pré-seuil et du seuil de Mo dans le spectre XAS avec les changements de degré d'oxydation du Mo ou de la structure de coordination du Mo. Ensuite, nous avons enregistré les spectres XAS de la surface modifiée par l'électrocatalyseur $Mo_3S_4$-POM en milieu acide avant et au cours d'une réaction d'électrolyse. Les données obtenues sont en accord avec un changement de coordination des centres de Mo durant la réaction, suggérant la formation d'une première sphère de coordination (M-O) de géométrie octaédrique plutôt que d'espèces (Mo-S) de géométrie tétraédrique. Ces changements peuvent être expliqués par la substitution partielle, autour des centres Mo, des ligands sulfure $S^{2-}$ par des groupements oxo $O^{2-}$, ce qui corrobore certains résultats déjà mis en évidence dans le chapitre 2.

Le chapitre 4 (intitulé « Efficient reduction of $CO_2$ to formate at Bi-modified *p*-Si photocathode ») porte sur la modification de photocathodes de Si avec des cocatalyseurs à base de Bi et sur leurs performances catalytiques vis-à-vis de la réduction photo-assistée du $CO_2$.Au démarrage de cette étude, aucune étude n'avait été publiée sur l'intégration de catalyseurs à base de Bi sur Si pour la réduction photoélectrocatalytique du $CO_2$. L'objectif visé était la conversion du $CO_2$ préférentiellement en formate. Les photocathodes modifiées Bi ont été préparées par photoélectrodéposition du précurseur $Bi(NO_3)_3.5H_2O$ en milieu 1M $HNO_3$ sous illumination. Nous avons tout à bord optimisé la méthode de photoélectrodéposition en termes de durée, pour en conclure qu'une augmentation de la durée d'illumination n'était pas bénéfique au regard de l'activité des électrodes ainsi préparées. Les photocathodes obtenues ont, dans un premier temps, été évaluées vis-à-vis de la réaction d'HER ainsi que CDRR. Nous avons mis en évidence que la durée de déposition la plus courte (5s) conduit à la fois à un potentiel de seuil moins négatif et à des densités de photocourant cathodique plus élevées. Les caractérisations de ces photocathodes modifiées Bi ont ensuite été réalisées par MEB, EDX et XPS. Les caractérisations morphologiques montrent des structures dendritiques de plus en plus denses avec la durée de déposition. Ces surfaces apparaissent moins homogènes après réaction de CDRR d'une durée de 30 min, en adéquation avec l'hypothèse préalable de perte de Bi due à la réaction. Les analyses XPS confirment la présence de Bi sous forme $Bi^0$ et $Bi^{3+}$, ces dernières espèces étant attribuées à la présence de $Bi_2O_3$. Après électrolyse, nous avons constaté la modification de certains pics caractéristiques observés sur les spectres XPS de $C_{1s}$ et $O_{1s}$. Enfin, les produits de réaction ont été identifiés et quantifiés en phase gazeuse (CO, $H_2$) et liquide (formate dissout) après 30 minutes de réaction, en termes d'efficacité faradique, de sélectivité, de densité de photocourant et de vitesse de formation. Il a ainsi été observé que la formation de formate est la réaction majoritaire. Néanmoins, des réactions parasites telles que HER se produisent et des traces de CO ont été détectées. En résumé, de telles photocathodes modifiées à partir de Bi présentent des densités de photocourant cathodique d'environ -24 mA $cm^{-2}$ et un rendement faradique pour formate supérieur à 72%.

La conclusion générale résume les principaux points marquants de ce travail de thèse et quelques perspectives dans le domaine de l'activation photoélectrochimique de petites molécules ont été ensuite proposées.

# Table of contents

# List of Abbreviations

| Short Name | Full Name |
|---|---|
| BE | Binding energy |
| CB | Higher unoccupied energy level |
| CDRR | $CO_2$ Reduction Reaction |
| CNTs | Carbon nanotubes |
| DMF | Dimethylformamide |
| EXAFS | Extended X-ray absorption fine structure |
| FE | Faradaic efficiency |
| HER | Hydrogen evolution reaction |
| MOFs | Metal organic frameworks |
| NPs | Nanoparticles |
| OER | Oxygen evolution reaction |
| PECs | Photoelectrochemical cells |
| PEDOT | Poly(3,4-ethylenedioxythiophene) |
| POM | Polyoxometalates |
| *p*-Si | *p*-type Silicon |
| rms | root-mean-square |
| SC | Semiconductor |
| Si–H | Hydride-terminated Si |
| SiNWs–H | Hydride-terminated Si nanowires |
| TOF | Turnover frequency |
| VB | Lower occupied energy level |
| XAFS | X-ray absorption fine structure |
| XANES | X-ray absorption near edge structure analysis |
| XAS | X-ray absorption spectroscopy |
| XRD | X-ray diffraction |

# Introduction

Energy production based on burning fossil fuels has caused serious environmental pollution and global warming. Therefore, the use of promising energy carriers such as hydrogen as well as the conversion of $CO_2$ emission into value-added products are two fields which have recently attracted tremendous research attention in order to evolve towards a sustainable environment.[1,2] Photoelectrochemical conversion is a promising method to take benefit of solar energy which has huge advantages towards other energy sources such as: inexhaustible supply, universality, high capacity and environmental friendliness.[3] Until now, silicon is the most widely used semiconductor for solar energy conversion because of its earth abundance. With a small bandgap of ca. 1.1 eV and an appropriate conduction band edge, *p*-type silicon is also considered as a promising photocathode material. However, its performance is strongly affected by its low stability and catalytic activity,[4] and research is currently pursued on finding effective strategies to improve its performance. In this regard, the cocatalyst loading, surface morphology control, surface modification strategy and surface phase junctions, are essential parameters that are currently intensively investigated.[3]

Polyoxometalates (POM) represent one class of compounds largely explored in inorganic chemistry, highlighted by the large number of complexes recently discovered.[5] POMs can include in their molecular framework many elements in a wide range of structures with various electronic configurations and bonding patterns which can impart an unmatched and tunable range of physical and chemical properties.[6] In the course of the Chalco-Cat project (funded by ANR), we investigated a challenging electrocatalytic process of great societal interest, namely the Hydrogen Evolution Reaction (HER) by using *p*-type silicon semiconducting photocathodes. Investigations have been carried out using a convergent and global approach with the same class of electrocatalytic materials deriving from the $\{Mo_3S_4\}$ cluster as coordination complexes or incorporated within a polyoxometalate framework.

Another energy-related application of *p*-type silicon semiconductor is $CO_2$ reduction reaction (CDRR), which was reported in the early 1980s.[7] Since then, *p*-Si photocathodes modified with different molecular cocatalysts have been demonstrated to reduce $CO_2$ into organic fuels. Incorporation of cocatalysts could greatly improve the performance of semiconducting electrodes for $CO_2$ reduction, because the cocatalysts can function as trapping sites for the electrons, and further promote the charge separation and alter the selectivity of the products.[8] Among the investigated cocatalysts, in recent years, bismuth (Bi) as a nontoxic and inexpensive metal cocatalyst, has a great potential for reduction of $CO_2$ to formic acid.[9,10] Therefore, the development of *p*-type silicon incorporating Bi-based electrocatalysts is expected to yield high selectivity, and improved catalytic activity for photoelectrochemical reduction of $CO_2$. This study constitutes another axis of interest of this thesis.

The first chapter of this thesis discusses the electrochemical fundamentals of HER and CDRR, summarizes different types of studied electrocatalytic systems, introduces the photoelectrocatalysis at *p*-type silicon photocathode surfaces and reports different examples of co-catalyst-modified *p*-Si photocathodes that can efficiently enhance HER or CDRR.

Chapter two discusses the HER catalytic performance of $\{Mo_3S_4\}$-based clusters as coordination complexes or incorporated within a polyoxometalate framework. We present *p*-type silicon photocathodes decorated with $\{Mo_3S_4\}$-based assemblies incorporating the polyoxotungstate $\{AsW_{12}O_{42}\}$ matrix and we demonstrate their efficiency for sunlight-driven HER under acid pH conditions. Structural and chemical changes at these surfaces are investigated during the catalytic reaction process.

In the third chapter, we attempt to determine the catalytic reaction mechanism used in the second chapter by using *in operando* X-ray absorption spectroscopy (XAS) and photoelectrocatalytic investigations. The basic theory of XAS technique is introduced and our experimental conditions are described. We then discuss the XAS spectra and electrochemical results recorded simultaneously. We give a particular focus on Mo K-edge X-ray absorption near edge structure analysis (XANES), which provides preliminary elements of the hydrogen evolution catalytic mechanism occurring on our modified *p*-type silicon photocathodes in acidic conditions.

Chapter four focuses on the conversion of $CO_2$ to added-value products through a photoelectrochemical approach. We modify silicon photocathodes with a Bi cocatalyst by electrodeposition and its effective $CO_2$ reduction performance as well as reduction product selectivity are presented. Furthermore, characterization of the Bi-modified silicon photocathodes is presented both before and after electrolysis under irradiation. Overall, these investigations might potentially contribute to future research on photoelectrocatalytic $CO_2$ reduction.

Finally, in the conclusions and perspectives section, we summarize and discuss the main results presented in this thesis, and also provide some possible perspectives to continue this contribution.

## References


[1] Jain, I. P. Hydrogen the fuel for 21st century. *International Journal of Hydrogen Energy*. **2009**, *34*(17), 7368-7378.

[2] Zhang, W., Hu, Y., Ma, L., Zhu, G., Wang, Y., Xue, X., Chen, R., Yang, S., Jin, Z. Progress and perspective of electrocatalytic $CO_2$ reduction for renewable carbonaceous fuels and chemicals. *Advanced Science*. **2018**, *5*(1), 1700275.

[3] Gong, J., Li, C., Wasielewski, M. R. Advances in solar energy conversion. *Chemical Society Reviews*. **2019**, *48*(7), 1862-1864.

[4] Huang, Q., Ye, Z., Xiao, X. Recent progress in photocathodes for hydrogen evolution. *Journal of Materials Chemistry A*. **2015**, *3*(31), 15824-15837.

[5] López, X., Carbó, J. J., Bo, C., Poblet, J. M. Structure, properties and reactivity of polyoxometalates: a theoretical perspective. *Chemical Society Reviews*. **2012**, *41*(22), 7537-7571.

[6] Wang, S. S., Yang, G. Y. Recent advances in polyoxometalate-catalyzed reactions. *Chemical Reviews*. **2015**, *115*(11), 4893-4962.

[7] Taniguchi, I., Aurian-Blajeni, B., JO'M, B. The reduction of carbon dioxide at illuminated *p*-type semiconductor electrodes in nonaqueous media. *Electrochimica Acta*. **1984**, *29*(7), 923-932.

[8] White, J. L., Baruch, M. F., Pander III, J. E., Hu, Y., Fortmeyer, I. C., Park, J. E., Zhang, T., Liao, K., Gu, J., Yan, Y., Shaw, T. W., Abelev, E., Bocarsly, A. Light-driven heterogeneous reduction of carbon dioxide: photocatalysts and photoelectrodes. *Chemical Reviews*. **2015**, *115*(23), 12888-12935.

[9] Ding, P., Hu, Y., Deng, J., Chen, J., Zha, C., Yang, H., ... Zhao, X. Controlled chemical etching leads to efficient silicon–bismuth interface for photoelectrochemical $CO_2$ reduction to formate. *Materials Today Chemistry*. **2019**, *11*, 80-85.

[10] Guo, S. X., Zhang, Y., Zhang, X., Easton, C. D., MacFarlane, D. R., Zhang, J. Phosphomolybdic acid-assisted growth of ultrathin bismuth nanosheets for enhanced electrocatalytic reduction of $CO_2$ to formate. *ChemSusChem*. **2019**, *12*(5), 1091-1100.

# Chapter 1. Bibliographic Overview

## 1.1 Background

Energy is an essential and strategical component for sustainability and security. The problems of increasing energy demand, depletion of fossil fuels and the urge to maintain a clean environment, require an important transformation of the energy grids. The clean production of fuels and energy from sunlight represents an exciting challenge for the future, which now seems plausible thanks to the recent developments in energy conversion technologies, catalysts, and materials.[1] In this context, a currently explored alternative to the use of fossil fuels is the use of photoelectrochemical cells (PECs), which can harvest solar energy to create high-energy products that could be used as renewable fuels.

The term "solar fuel" indicates a product that has been produced directly or indirectly from the utilization of a renewable source of energy (e.g. sunlight) and having a negative carbon impact. [2,3,4,5] Using solar energy as the vector for a sustainable energy scenario derives from the three following concepts: clean, cheap and abundant. Over the last past years, the development of high-scale solar fuel systems has been an area of increasing research activity.[1] It has been estimated that, by 2050, solar energy could be the largest source of electricity ahead of fossil fuels, wind, hydro and nuclear. [6,7] Solar energy can be transduced to chemical energy, typically by reducing protons ($H^+$) to hydrogen ($H_2$), or carbon dioxide ($CO_2$) to organic compounds ($C_xO_y$).

On the one hand, solar $H_2$ derived from water electrolysis through a PEC can be employed as an energy carrier and converted into electricity using fuel cell technology without carbon emission, thus an ecological energy infrastructure only based on sunlight, water and electricity can be conceived. Compared to gasoline, if $H_2$ has a lower volumetric density (8 vs 32 MJ $L^{-1}$), it has a higher gravimetric density (120 vs 44 MJ $kg^{-1}$) resulting in a high energy per mass unit. If $H_2$ itself is to be used as a fuel, the development and utilization of advanced storage methods will be required. The US Department of Energy's Fuel Cell Technologies program has already routinely demonstrated hydrogen fuel cell vehicles capable of driving 250 miles on a single 4 kg tank of $H_2$, which is twice as efficient as today's gasoline vehicles.[8]

On the other hand, in order to reduce the $CO_2$ emissions produced from fossil-fuel-based power plants, $CO_2$ can be captured and further processed to produce fuels that can readily integrate into the current production infrastructures. The two main methods for $CO_2$ conversion based on solar energy include (1) catalytic conversion using solar-derived $H_2$, and (2) direct $CO_2$ reduction using $H_2O$ and solar energy. In such a scenario, involving a "solar refinery", as shown in **Figure 1-1**, solar energy can also be utilized in the form of heat, promoting thermochemical reactions and as a photon source for photochemical reactions. This upgrading of $CO_2$ can be accomplished by using sunlight as a renewable energy source to drive catalytic reactions.

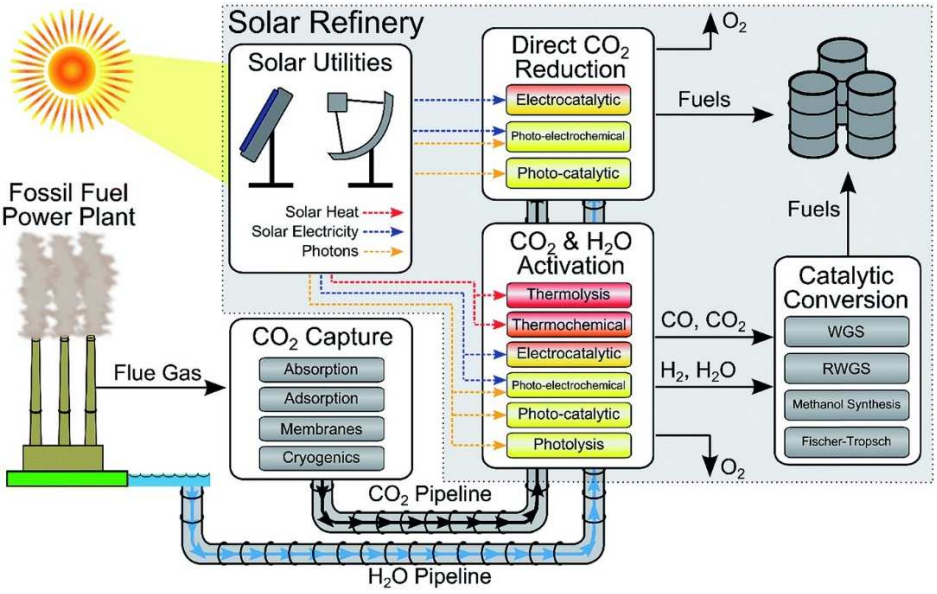


**Figure 1-1**: Schematic for solar fuels production. The approximate temperature requirements for the solar-driven conversion processes are color-coded (red: high temperature, yellow: ambient temperature, WGS: water-gas shift reaction, RWGS: reverse water-gas shift reaction).[9]

In this frame, the aim of this thesis was to explore two different photoelectrochemical systems for solar fuel production. The first system concerns the production of solar $H_2$ by photoelectrochemical $H^+$ reduction on polyoxothiometalate-derivatized silicon (Si) photocathodes and the second system deals with the photo-assisted $CO_2$ reduction reaction (CDRR) with Bi-based modified Si photocathodes. This thesis will provide a deeper understanding of co-catalyst-modified Si photocathodes for effective HER and CDRR.

## 1.2 Electrocatalytic hydrogen evolution reaction (HER)

### 1.2.1 HER fundamentals

$H_2$ has been referred to as an ideal energy carrier for the future because of its high energy density and environmentally friendly production possibilities.[10,11] Currently, about 44.5 million tons of $H_2$ is produced worldwide from various sources. 96 % of $H_2$ is produced by steam methane reforming and coal gasification and only 4 % of total $H_2$ is produced by water electrolysis. Most of the $H_2$ is used for industrial applications, e.g., oil reforming and ammonia production for fertilizer.[12,13] Among these $H_2$ production methods, water electrolysis (that has more than 200 years history) is the only one that can induce zero carbon emission, which is the key to solve the current ecological problems that humanity

faces. Therefore, $H_2$ production through electrocatalytic water splitting is considered as a promising alternative clean and sustainable fuel to finite fossil fuels. [14,15,16]

1.2.1.1 Historical developments of water electrolysis

Dating back to 1783, Antoine Lavoisier recognized and named hydrogen, he successfully proved that water was composed of two elements namely hydrogen and oxygen. In 1789, Jan Rudolph Deiman and Adriaan Paets van Troostwijk employed an electrostatic machine to produce electricity which was discharged on gold electrodes in a Leyden jar filled with water.[17] Alessandro Volta invented the voltaic pile in 1800, and, a few weeks later, William Nicholson and Anthony Carlisle discovered electrolysis, it was the first time that water was decomposed into $H_2$ and $O_2$ using an electric current, and the potential applications were gradually recognized.[18] In 1833, Faraday summarized the quantitative aspects of the electrolysis experiments into Faraday's Law, which pushed forward the development of electrochemistry, and the concept of water electrolysis was scientifically defined and acknowledged.[19] In 1869, water electrolysis became a cheap method for the production of $H_2$ when Zénobe Gramme invented the Gramme machine. Four years later, Jules Verne in his famous book "The Mysterious Island" indicated that water can be the basis for fuel and the four important sources of hydrogen produced commercially are natural gas, oil, coal, and electrolysis of water.[20] A large number of different electrolyzer designs were developed in the 1920s and 1930s and during the same period, several large 100 MW size plants were built worldwide.[21] However, during the period of the Second World War, developments largely ceased due to the massive availability of hydrocarbon-based energy and hydroelectricity in the ammonia fertilizers industry. It is not until the oil crisis in the 1970s that $H_2$ energy derived from water electrolysis received renewed interest as a promising method to solve the energy crisis and sustainable supply problems.[22]

The advantages of water electrolysis were traditionally decried because the electricity generally utilized in this process originates from fossil fuels. Now that solar energy and wind power have made tremendous progress, water electrolysis is well-established as a promising strategy to store the energy produced by these renewable sources. Once the renewable resources meet the supply-demand, the stored $H_2$ can be applied for electricity conversion into fuel cells. This overall concept of $H_2$ renewable energy system for distributed power generation is displayed in **Figure 1-2**.

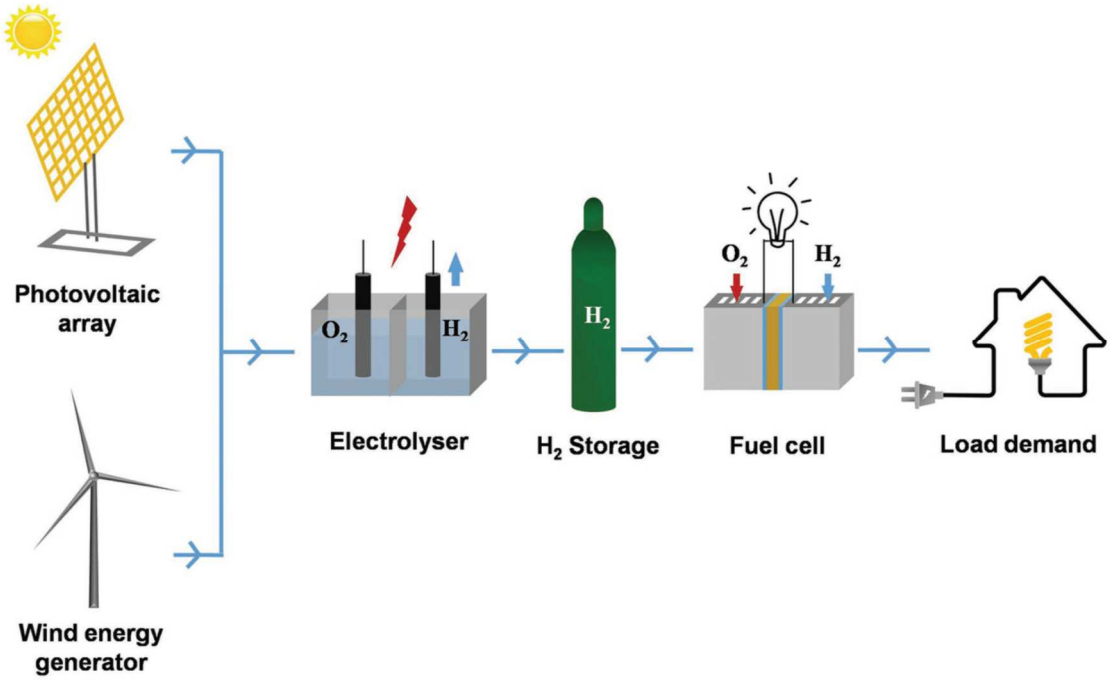


**Figure 1-2**: Overall concept of an $H_2$ renewable energy system for distributed power generation.[23]

1.2.1.2 Mechanistic aspects of HER

Water electrolysis requires a thermodynamic potential of 1.23 V at 25 °C to produce $H_2$ at the cathode and $O_2$ at the anode, as shown below.

$$Total\ reaction \quad H_2O \rightarrow H_2 + 1/2\ O_2 \qquad (1)$$

In acidic solution, the two half-reactions are:

$$Cathode \quad 2H^+ + 2e^- \rightarrow H_2 \qquad (2)$$

$$Anode \quad H_2O \rightarrow 2H^+ + 1/2O_2 + 2e^- \qquad (3)$$

HER is a multi-step process taking place on the surface of an electrode.[24] In acid solution, the first step of HER is the Volmer or discharge reaction (4), in this step, an electron transfer to the electrode is coupled to proton adsorption on an empty active site of the electrode to yield an absorbed hydrogen atom ($H_{ads}$), the proton source being an hydronium cation ($H_3O^+$).

$$H^+ + e^- \rightarrow H_{ads} \qquad (4)$$

Subsequently, $H_2$ formation may occur via two different reaction pathways. In one possibility, the transfer of a second electron to the absorbed hydrogen atom is coupled to the transfer of another proton from the solution to evolve $H_2$, which is the so-called Heyrovsky or *ion + atom* reaction (5). In

another possibility, which was confirmed for platinum (Pt), two $H_{ads}$ combine on the surface of the electrode to give $H_2$, in the so-called Tafel or *atom + atom* reaction (6).

$$H_{ads} + H_3O^+ + e^- \rightarrow H_2 + H_2O \qquad (5)$$

$$H_{ads} + H_{ads} \rightarrow H_2 \qquad (6)$$

This is shown in **Figure 1-3**, where Volmer (discharge) reaction is displayed by blue arrows, and the two following possible mechanisms are represented by purple and red arrows (Volmer-Heyrovsky and Volmer-Tafel, respectively).

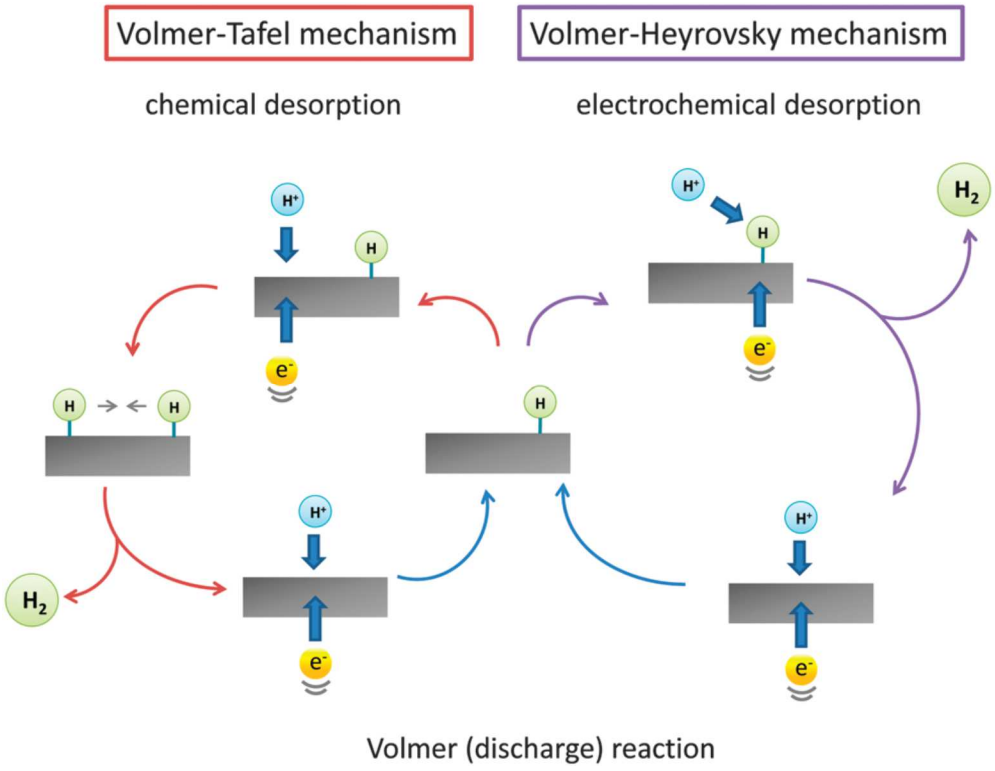


**Figure 1-3**: The HER mechanisms on the surface of an electrode in acidic solutions.[25]

Based on thermodynamics, the application of only 1.23 V of external potential would be sufficient to induce water splitting in an electrochemical cell. However, in practice, water electrolysis is much less efficient and an external potential well above the thermodynamic minimum value of 1.23 V is required. This overpotential is essential to drive the electron transfer processes at significant rates and to overcome the kinetic barriers imposed by the high activation energies in order to form the reaction intermediates on the electrode surface. Electrocatalysts are materials that can lower the overpotential for triggering HER.

Sabatier's principle provides a qualitative rational concept for comparing the differences in catalytic activity among HER catalysts. It sets Pt as the state-of-the-art HER electrocatalyst because of the suitable interaction between the catalyst and the substrate, as the Pt surface has the right affinity for the key reaction intermediate to adsorb while also being weak enough for product release. In this concept, the binding energy of $H_{\mathrm{ads}}$ is the sole and crucial descriptor for identifying HER electrocatalysts[24] and states that a good HER catalyst should have the ideal trade-off between binding and releasing of the hydrogen atoms.

A plot of catalytic activity versus binding energy results in a curve well-known as "volcano plot", which is shown in **Figure 1-4**. This plot was constructed by Trasatti who collected experimental data for HER in acid solutions. He used the energy of hydride formation instead of hydrogen adsorption because the experimental or theoretical data were not available at this time.[26] The reaction rate is expressed in terms of exchange current density, which is proportional to the reaction rate at the equilibrium potential. Since then, several versions have been presented in order to understand catalytic reaction with the aid of a single descriptor, typically the energy of adsorption of a single intermediate. [27,28] In recent years, the discovery of new HER electrocatalytic materials is a growing field of research. They could help to enhance HER activity and stability, despite most of them showed lower specific activity than Pt in acidic solution. These HER catalysts will be discussed in the next section.

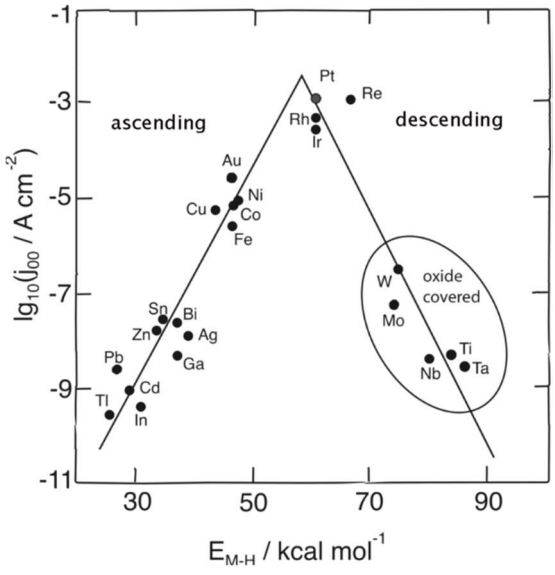


**Figure 1-4**: Trasatti's volcano plot for the hydrogen evolution reaction in acid solutions. $j_{00}$ denotes the exchange current density, and $E_{M-H}$ the energy of hydride formation.[29]

### 1.2.2 Electrocatalysts for HER

Based on the HER reaction mechanism, acidic electrolytes are preferred to increase the concentration of protons in the electrolyte, therefore, development of efficient and stable HER catalysts in acidic conditions is very important for commercial applications.

1.2.2.1 Pt, Ni, Mo, and other metal-based catalysts

- Platinum

Pt sits very near the top of the hydrogen volcano curve, with an almost thermo-neutral $\Delta G_H$, and is considered as the best-performing catalyst for HER, requiring negligible overpotentials to achieve high reaction rates in acidic solutions. Unfortunately, Pt is expensive and scarce, limiting its widespread technological use. To overcome the challenges associated with the cost of $H_2$ production from electrolysis, significant efforts are being made to markedly decrease the Pt loading and increase the Pt utilization efficiency.

One approach to promoting Pt activity towards HER is to reduce the size of supported Pt and to use nanoparticles (NPs), clusters, or even single atoms. For instance, Pt-based electrocatalysts are usually manufactured in the form of NPs deposited on large-surface-area supporting substrates, such as reduced graphene oxide.[30] HER in acidic media at low overpotential can be also achieved by the decoration of platinum NPs on conductive polymers such as poly (3,4-ethylenedioxythiophene, PEDOT).[31] Moreover, single platinum atom catalysts are investigated for the HER, where exhibiting significantly enhanced catalytic activity (up to 37 times) and high stability in comparison with the state-of-the-art commercial platinum/carbon catalysts.[32]

Another strategy is to increase the HER activity by alloying Pt with another (mainly transition) metals or by depositing it onto a specific electrode surface. For example, owing to the synergistic effect between Pt and Cu, the PtCu alloy shell nanocrystal with the Pd substrate shows superior HER catalytic activity and stability in comparison with commercial platinum/carbon catalysts.[33] Another study suggested a class of trimetallic PtFeCo alloy nanostructures with controllable compositions, the surface structure enabling further enhancement of the HER activity by increasing the number of active sites and reducing the contact resistance.[34]

- Nickel

As the scarcity and high cost of Pt could limit its widespread use, currently, the researchers have been consistently inspired to utilize the Ni-based electrocatalysts for HER as an alternative to Pt due to its

similar chemical properties, same group number in the periodic table, and inexpensive abundant quantity of Ni.[35]

Due to its instability in acid media, Ni metal cannot be employed alone but the incorporation of nanostructured Ni derivatives into state-of-the-art electrode materials can effectively increase the electrochemically active surface area of binary or ternary alloy materials and enhance their HER catalytic activity. Especially, Ni/Pt alloys-based catalysts and Ni/Mo alloys-based catalysts have a considerable role in reducing the overpotential and enhancing the catalytic activity by tuning the native electronic structure of the catalytic surface. A synergistic effect confers a more positive charge to the Mo atoms and a more negative charge to the Ni atoms, which, in turn, decreases the Gibbs free energy for hydrogen bonding on the surface of molybdenum carbide and facilitate its desorption. Furthermore, Ni-based metal organic frameworks (MOFs) have emerged as a promising class of materials attracting more attention for HER. Overall, high efficiency HER by using Ni in different forms and in combination with metals or nonmetals has been a hot research topic.[35]

- Molybdenum

In 2005, Hinnemann *et al*. demonstrated theoretically that $MoS_2$ could be considered as a promising HER electrocatalyst. They showed by computation that the free energy of atomic hydrogen bonding to the $MoS_2$ edge was close to that of Pt, raising the interest on $MoS_2$ as a highly active HER electrocatalyst. This was the first time that the $MoS_2$ edge structure was considered as the actual active site.[36] Further studies to identify the active sites of $MoS_2$ have been reported by Jaramillo *et al* who prepared different sizes of $MoS_2$ NPs with a predominance of sulfide Mo-edges. Electrocatalytic activity measurements showed that the catalytic performance of $MoS_2$ nanoparticles is related to the edge state length, rather than the area coverage, directly establishing the relationship between $MoS_2$'s edges and the catalytic active sites.[37]

- Other metals

Some other transition metals have been considered as noble metal-free HER electrocatalysts, mainly including iron (Fe), cobalt (Co), tungsten (W) and copper (Cu). Several typical transition metals based-electrocatalysts have been reported for efficient HER electrocatalysis.

Fe is the most abundant transition metal in the Earth's crust ($5.63 \times 10^4$ mg $kg^{-1}$) and is present in the active site of [Fe-Fe] hydrogenase, which catalyzes the formation of $H_2$ close to the thermodynamic potential. Its catalytic activity is higher than that of Pt and is the best-known catalyst for HER.[38]

As another example, cobalt sulfides are currently emerging for HER. For instance, Jin's group synthesized metallic $CoS_2$ materials with three different morphologies – film, microwires and nanowires. They systematically studied their structures, activities, and stabilities, then concluded that

the morphology played a crucial role in the overall catalytic efficiency. They suggested that $CoS_2$ micro- and nano- structuring could promote the release of evolved gas bubbles from the electrode surface, and thereby the increase of its operational stability.[39]

Tungsten carbide, one of the most important metal carbides, was first found to have Pt-like catalytic properties. While tungsten carbide was demonstrated to be an excellent substrate to support noble metal catalysts (e.g., Pt), the development of pristine tungsten carbide as a high-performance catalyst is more appealing due to the avoidance of noble metals.[40]

Copper phosphide was demonstrated to be HER-active by Sun's group. They prepared self-supported $Cu_3P$ nanowire arrays on commercial porous copper foams. This material showed a high catalytic performance in acidic solution, and it could achieve a current density of 10 mA $cm^{-2}$ at a low overpotential (143 mV).[41]

1.2.2.2 Molecular complexes HER catalysts

A few molecular based-metal complexes have been reported as potential candidates for HER. Especially, most reports focused on molecular catalysts adsorbed on the surface of an electrode rather than homogeneous molecular catalytic systems. The immobilization of molecular catalysts onto surfaces provides a variety of advantages over homogeneous systems. First, immobilization of molecular catalysts can provide asymmetry as a feature inherent to interfaces and impart a greater degree of control over the local environment by spatially confining system components. Second, such localization can help to avoid unwanted side reactions, improving selectivity and making a system more robust.[42] This strategy could be sometimes realized by a simple physisorption method, however, in the large majority of cases, it requires chemical modification of the ligand structure with an appropriate anchoring unit. The choice of the anchor depends on the surface chemistry of the substrate and the type of targeted application process.[43]

The development of molecular metal complexes consisting of abundant and cheap metals (e.g., Fe,[44] Co,[45] Ni[46]) holds the promises for HER. However, for the majority of these metal complexes, the electrocatalytic activity towards the reduction of $H^+$ has been reported in organic solvents and only rarely in an aqueous medium. Furthermore, these molecular catalysts often suffer from degradative processes in solution. Hence, the design and preparation of new molecular catalysts capable to perform the $H_2$ production in aqueous phase might provide important insights.

1.2.2.3 POMs as HER catalysts

Polyoxometalates (POMs) are composed of cations and polymetallic species with structural diversity, in which the oxo-metal polyhedral of $MO_x$ (x = 5, 6) are the basic construction units. M generally represents early transition metals in their high oxidation state, e.g., W, Mo, V, Nb, Ta, and so on, which can be partly substituted by other metals, including Al, Ti, Cr, Mn, Fe, Co, Ni, Cu, Zn, *etc*. Some polyanions are centered by heteroatoms that significantly affect their properties. In addition, they are often recognized as electron reservoirs due to their strong capacity to accept and release electrons. More importantly, their structure and constituting elements can be tuned artificially to obtain special properties.[47] The application of POMs to catalysis is stimulated by their fascinating properties, including tunable acidity and redox properties, inherent resistance to oxidative decomposition, high thermal stability, and impressive sensitivity to light and electricity.

There are various POMs structures which can be identified by X-ray diffraction (XRD), several of them formed solely from transition metals (iso- POM, **Figure 1-5** [a]), while others containing a central heteroatom (hetero- POM, **Figure 1-5** [b-d]).

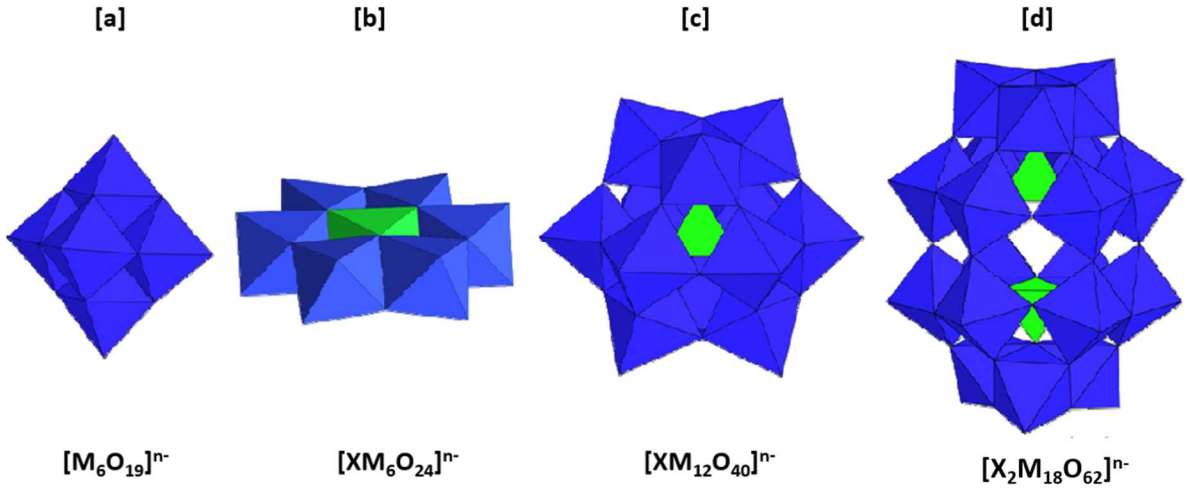


**Figure 1-5**: Polyhedral representation of [a] Linqvist, [b] Anderson, [c] Keggin, [d] Wells-Dawson polyoxoanions. The blue octahedrons conform to the metal oxide core.[48]

Keggin structure $[XM_{12}O_{40}]^{n-}$ is composed of one heteroatom surrounded by four oxygen atoms to form a tetrahedron. The heteroatom is located centrally and caged by 4 triads $\{(M^{VI}O)_3(\mu\text{-}O)_3\}^{6+}$ units linked to one another by the neighboring oxygen atoms. There are a total of 24 bridging oxygen atoms that link the 12 addenda atoms. The metal centers in the 12 octahedral units are arranged on a sphere almost equidistant from each other. Several structural isomers exist by rotating these triads around their central axes, which are noted as α, β, γ, and δ according to the number of triads rotated by 60°.

Different lacunar POMs can be obtained from the initial Keggin structure $[\alpha\text{-}XM_{12}O_{40}]^{n-}$. **Figure 1-6** shows one monolacunar POM by removing a $\{M^{VI}O\}^{4+}$ fragment as well as two trilacunar POMs named $[\alpha_a\text{-}XM_9O_{34}]^{n'-}$ and $[\alpha_b\text{-}XM_9O_{34}]^{n''-}$ by removing either three $\{M^{VI}O\}^{4+}$ fragments which are adjacent to three different triads or one triad. All of these structures have coordinating unsaturated oxygen atoms capable of interacting with various cations. The nature of cations in POMs, as transition metals, cationic complexes, and organic cations, *etc*. also greatly impacts the properties of the POM compounds including acidic, electronic, crystallographic properties and solubility.

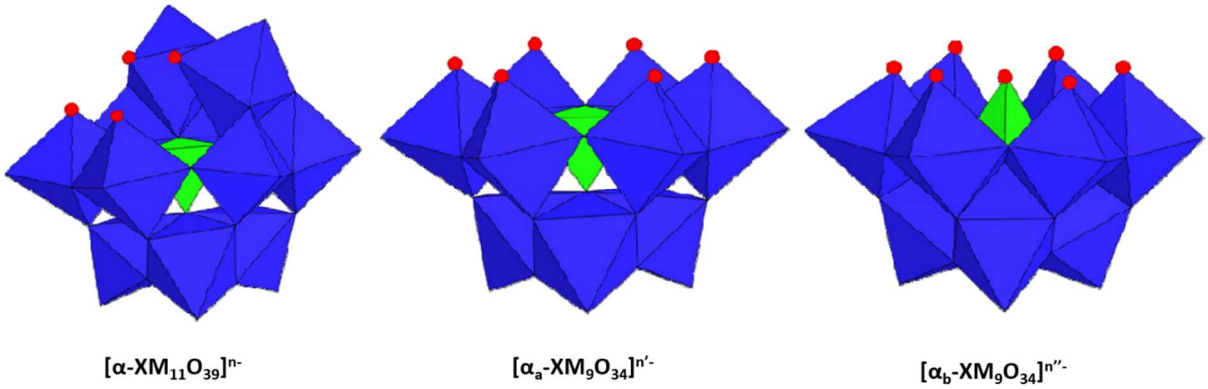


**Figure 1-6**: Structures of monolacunar POM $[\alpha\text{-}XM_{11}O_{39}]^{n-}$ and two trilacunar POMs $[\alpha_a\text{-}XM_9O_{34}]^{n'-}$, $[\alpha_b\text{-}XM_9O_{34}]^{n''-}$ in polyhedral representations.[48]

POMs are a well-known class of discrete, anionic early transition-oxide clusters widely used as electrocatalysts for various challenging reactions including the HER. The first work on HER electrocatalytic activity by POMs was reported in 1985 by Keita and Nadjo.[49] In 2007, their team developed electrode surfaces modified with $[H_7P_8W_{48}O_{184}]^{33-}$, $[Co_6(H_2O)_{30}(Co_9Cl_2(OH)_3(H_2O)_9(\beta\text{-}SiW_8O_{31})_3)]^{5-}$ and $[(Co_3(B\text{-}\beta\text{-}SiW_9O_{33}(OH))(B\text{-}\beta\text{-}SiW_8O_{29}OH)_2)_2]^{22-}$ for HER.[50] These very effective POM-based electrocatalysts were deposited on glassy carbon (GC) electrodes or confined in polyvinylpyridine films on the electrode, which promoted a micro-environment effect. The HER activation of these electrodes was attributed to the proton and electron reservoir-like properties of the polyanions.[50] In the same year, the use of a composite based on the classical 12-tungstophosphate $[PW_{12}O_{40}]^{3-}$ Keggin ion in combination with carbon nanotubes (CNTs) was reported for HER by Xu and co-workers.[51] More recently, Cronin and co-workers reported that the Mo-derivative $[PMo_{12}O_{40}]^{3-}$ electrocatalyst can be used for successful water splitting,[52] they also reported on a highly efficient HER electrocatalyst based on $[SiW_{12}O_{40}]^{4-}$ associated with Pt.[53] Overall, Keggin-type structures are the most studied POMs in catalysis due to their unique stability.

Most POMs are good candidates as HER electrocatalysts in homogenous liquid phase thanks to their electron and proton reservoir behaviors. However, their use as very effective HER heterogeneous electrocatalysts in water is restricted by several drawbacks including their high solubility, low surface area and the high overpotentials required to afford significant current densities. As we mentioned in section 1.2.2.2, there are various advantages for the HER heterogeneous electrocatalysis over homogenous systems including the use of an ultra-small amount of catalyst and the proximity of the catalyst and the electron source. Based on these considerations, we expected in this thesis the improvement of HER activity by a heterogeneous POMs-based electrocatalytic system.

## 1.3 Electrocatalytic $CO_2$ reduction reaction (CDRR)

$CO_2$ is an extremely disturbing greenhouse gas that has been released excessively through fossil fuels burning over the last decades. In order to minimize climate change, it is important that the release of $CO_2$ into the environment ceases in the near future. Converting $CO_2$ into fuels or commodity chemicals is recognized as a worthwhile ecological approach in order to decrease $CO_2$ emissions. $CO_2$ can be converted through diverse routes, including biochemical, electrochemical, photochemical, radiochemical, and thermochemical reactions.[54] Among these methods, CDRR technologies are appealing because they operate with high reaction rates and good efficiencies under ambient conditions, they can be easily coupled with carbon-free electricity sources (e.g., wind, solar, hydroelectricity, *etc*.), and the reaction rate can be easily controlled by tuning the external bias. Furthermore, a great advantage of the CDRR is that several voltage-dependent products are accessible, including formic acid, carbon monoxide, *etc*.[55]

### 1.3.1 Fundamentals of CDRR

$CO_2$ is one of the most stable molecules due to the strong C=O double bond that has an energy of 750 kJ $mol^{-1}$, much larger than that of C–C (336 kJ $mol^{-1}$), C–O (327 kJ $mol^{-1}$), or C–H (441 kJ $mol^{-1}$). Therefore, significant energy input is required to break the C=O bond, essential for $CO_2$ reduction. CDRR can take place through several pathways involving multiple electron transfers in both aqueous and non-aqueous phases on suitable electrocatalysts. The major reduction products are carbon monoxide (CO), formic acid (HCOOH), methanol ($CH_3OH$), methane ($CH_4$), among others. Based on a thermodynamic study, a variety of CDRR half-reactions and their corresponding potentials (versus the standard hydrogen electrode, SHE) leading to different products in aqueous solution (pH = 7) are listed in **Table 1-1**.[56]

| Reduction potentials of $CO_2$ | $E°$ [V] vs SHE at pH 7 |
|---|---|
| $CO_2 + e^- \rightarrow CO_2^-$ | - 1.90 |
| $CO_2 + 2H^+ + 2e^- \rightarrow HCOOH$ | -0.61 |
| $CO_2 + 2H^+ + 2e^- \rightarrow CO + H_2O$ | -0.52 |
| $CO_2 + 4H^+ + 4e^- \rightarrow HCHO + H_2O$ | -0.51 |
| $CO_2 + 6H^+ + 6e^- \rightarrow CH_3OH + H_2O$ | -0.38 |
| $CO_2 + 8H^+ + 8e^- \rightarrow CH_4 + 2H_2O$ | -0.24 |
| $2CO_2 + 12H^+ + 12e^- \rightarrow C_2H_4 + 4H_2O$ | -0.34 |
| $2H^+ + 2e^- \rightarrow H_2$ | -0.42 |

**Table 1-1**: Standard electrochemical potentials for $CO_2$ reduction.

Some of the above reactions (e.g., reduction to $CH_3OH$, $C_2H_4$ or $CH_4$) are thermodynamically more favorable than two-electron HER ($E^0$ = -0.41 V vs SHE at pH 7) according to the relationship $\Delta G = - \alpha F E^0$, where α is the number of electrons transferred during the redox reaction and $F$ is the Faraday constant. However, the actual electrode potentials required to drive the reactions are much more negative than the equilibrium ones. This is because after chemical absorption of molecular $CO_2$ on the working electrode, a key intermediate $CO_2^{\bullet -}$ anion radical has to be formed by one-electron transfer to a $CO_2$ molecule. This first step reaction does not initiate until -1.90 V vs SHE in order to reorganize the originally linear molecule into a bent anion radical (**Figure 1-7**).

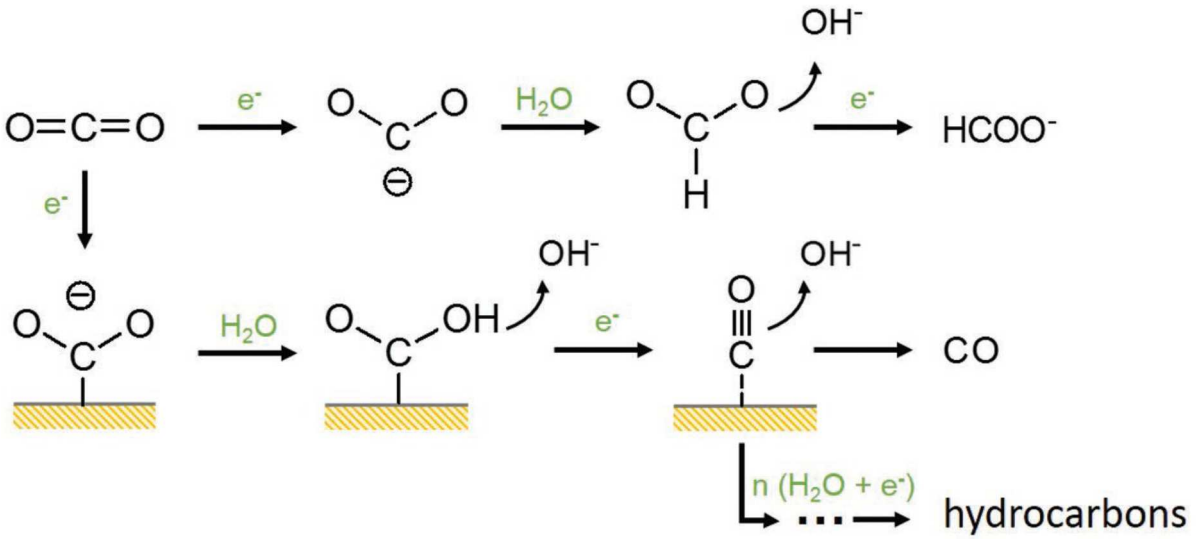


**Figure 1-7**: Possible reaction pathways for CDRR on metal electrodes in aqueous solutions.[57]

The generation of the $CO_2^{\bullet-}$ intermediate has been regarded as a rate-determining step for CDRR in most cases. Once $CO_2^{\bullet-}$ is formed, it may be subsequently protonated onto its oxygen atom, resulting in the formation of $^{\bullet}$COOH. Then, the $^{\bullet}$COOH intermediate is reduced to CO and subsequently released from the working electrode surface. Alternatively, $CO_2^{\bullet-}$ protonated on its carbon atom to form $HCOO^{\bullet}$ intermediate instead of $^{\bullet}$COOH at high overpotentials, which is further reduced to formate ($HCOO^-$). Consequently, most CDRR reactions yield CO or formate as the primary reduction products. The further reduction of CO into hydrocarbons occurs only on very few electrocatalysts (e.g., Cu).

In the present work, the attention will be paid on the heterogeneous CDRR, which occurs at the electrode-electrolyte interface. Three steps are mainly considered when modeling these heterogeneous catalytic processes:[54]

(1) Chemical adsorption of $CO_2$ on the surface of a catalyst (cathode).
(2) Electron transfer and/or proton migration to break C–O bonds and/or form C–H bonds.
(3) Rearrangement of product species followed by desorption from the electrode surface and diffusion into the electrolyte.

Furthermore, there are several important parameters for evaluating catalytic performance including the following: (1) Overpotential ($\boldsymbol{\eta}$, the difference between the thermodynamic and actual electrode reduction potentials); (2) Current density ($j$, the ratio of the magnitude of current to the geometric surface area $A$ of the working electrode). (3) Faradaic efficiency ($E_{Faradaic} = \alpha nF / Q$, where $\alpha$ is the number of electrons transferred, $n$ is the number of moles of the target product, $F$ is the Faraday constant and $Q$ is the consumed electrical charge).

### 1.3.2 Electrocatalysts for CDRR

The electrocatalyst employed for CDRR and the applied potential have a great influence on the final reduction products. The cost-effective electrochemical reduction process of $CO_2$ requires good electrocatalysts that are stable, selective and efficient. These electrocatalysts can be generally categorized into metals, inorganic metal-based compounds, and metal-organic complexes.

#### 1.3.2.1 Metal catalysts

Metal electrocatalysts for CDRR can be mainly divided into four groups based on the different reaction routes and main products (CO, $HCOO^-$, hydrocarbons, and $H_2$) as described by Hori[58] and illustrated in **Figure 1-8**.

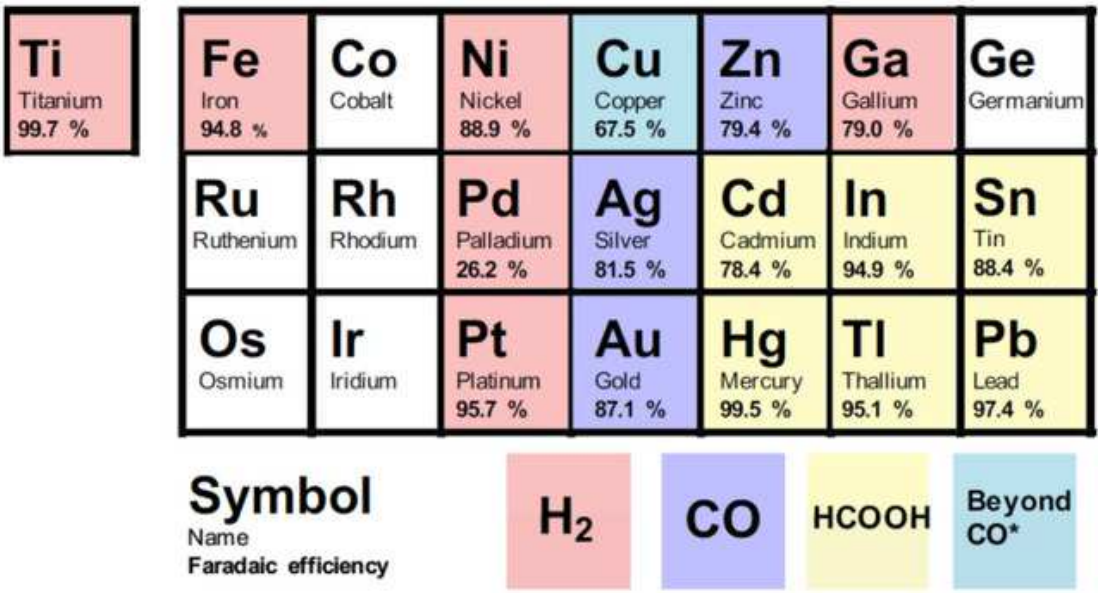


**Figure 1-8**: Major product classification of metal catalysts for CDRR, shown in a cropped periodic table and classified by their major reaction product and Faradaic efficiency.[59]

(1) The reduction of $CO_2$ to formic acid: Sn and Pb have been particularly studied, and they are classified in this group. They mainly generate $HCOO^-$ or formic acid in aqueous solution owing to their weak bonding with $CO_2^{\bullet-}$ intermediates, which can be easily desorbed from the surface of Sn and Pb.[60] In recent years, different parameters of Sn and Pb electrodes have been studied, such as electrocatalysts size, surface modification, and reaction conditions. For example, Castillo *et al.* have shown that Sn NPs were helpful to overcome the mass transfer limitation of $CO_2$ onto the electrode surface and reached an enhanced Faradaic efficiency for $HCOO^-$ generation.[61] For the aspect of surface modification, it was reported that rationally-designed

$SnO_x$-derived Sn electrodes could electroreduce $CO_2$ into formic acid with superior Faradaic efficiency at relatively low overpotentials.[62] Wu *et al.* investigated the effects of electrolyte for the electrochemical reduction of $CO_2$ on Sn electrodes, they found that $SO_4^{2-}$ and $Na^+$ favor higher Faradaic and energy efficiencies, while $HCO_3^-$ and $K^+$ enable a higher rate of formate production.[63]

(2) The second class of metals, which comprises Au, Ag, and Zn, has aroused intense attention for the specific selectivity for CO generation. They can bind the $CO_2^{\bullet-}$ intermediate, catalyze the cleavage of C–O bond in $CO_2$, and allow resulting CO to easily desorb from the electrode as the major reduction product. The reaction activity and selectivity of Au NPs strongly depend on the particle size. In the case of relatively small Au NPs, the increasing amount of low-coordination and active edge sites could contribute to the stabilization of $^{\bullet}$COOH intermediates and the production of CO rather than the competitive HER process.[64] Bulk Ag metal, as well as Ag nanostructures, present also outstanding selectivity for CO generation. For example, through surface modification, such as electrochemical deposition, [65] the derived Ag electrocatalysts can exhibit higher specific surface area and stronger adsorption of $^{\bullet}$COOH and $^{\bullet}COO^-$ intermediates, thus leading to higher activity and suppression of HER. Modified Ag nanocatalysts can perform CO generation with a Faradaic yield as high as 90% at relatively low overpotentials.

(3) Cu is the only metal of the third group as this is the only one that can reduce $CO_2$ beyond CO or formic acid. In addition to the two-electron reduction products, methane, ethane, ethylene, methanol, and ethanol were all reported as possible reduction products, which depends on the Cu catalyst pre-treatment. However, poor selectivity and degradation are two challenges that need to be tackled for practical applications. Different strategies have been exploited to promote the electrocatalytic performance of Cu. The morphology of Cu catalysts[66] and the Cu particle size[67] have a profound influence on the catalytic activity and product selectivity. Furthermore, surface roughening of the Cu surface is effective to improve CDRR performance owing to the enlarged surface area and the generation of a significant number of active surface sites. These active sites such as edges, steps, and defects are suggested to have lower energy barriers for the formation of key $CO_2$ reduction intermediates.[68]

(4) The other metals such as Pd, Fe, Ni and Ti have low HER overpotentials with strong CO adsorption, they can reduce $CO_2$ to CO or HCOOH but their Faradaic efficiency is generally much lower than the metals of the first or second group due to the competing HER.

1.3.2.2 Bi as electrocatalyst for CDRR

Bismuth (Bi) is a promising metal catalyst presenting interesting features of low toxicity, cost-effectiveness, and excellent stability. In addition, the HER overpotential on Bi is comparatively high which makes it a good candidate to be used for CDRR. It has been reported that the main reaction product of Bi in aqueous electrolytes is formic acid.

Similar to other electrocatalysts, the CDRR activity on Bi is also dependent on its morphology. Previous studies have demonstrated that dendritic Bi prepared by electrodeposition in combination with halide ions, show very high current density and formate selectivity for $CO_2$ reduction.[69] Lv *et al.* applied electrodeposition to synthesize a nano-sized Bi-based catalyst on a Cu foil, achieving the selectivity for formate production of 91.3 %.[70] In **Table 1-2** we compared the catalytic performance of Bi-based electrocatalysts recently reported in the literature for the reduction of $CO_2$ to formate.

| Electrocatalyst | Overpotential | Faradaic Efficiency | Current density or Mass activity | Year | Ref |
|---|---|---|---|---|---|
| Bi / BiOCl | 0.66 V | ~ 92 % | 3.7 mA $mg^{-1}$ | 2014 | [71] |
| Bi nanodendrites | 0.95 V | 96.4 % | 15.2 mA $cm^{-2}$ | 2016 | [69] |
| Microstructured Bi | 0.95 V | 63 % | 13.6 mA $cm^{-2}$ | 2017 | [72] |
| | 0.80 V | 90 % | 3.8 mA $cm^{-2}$ | | |
| Bi plate | 0.89 V | 15.2 % | 1.9 mA $cm^{-2}$ | 2017 | [70] |
| Nanosized Bi / Cu foil | 0.99 V | 94.0 % | 4.6 mA $cm^{-2}$ | 2017 | [70] |
| Nano-Bi obtained via reduction | 0.93 V | 98.4 % | 9.7 mA $cm^{-2}$ | 2017 | [73] |
| Nanosized Bi | 0.89 V | 84 % | 9.1 mA $cm^{-2}$ | 2017 | [74] |
| Bi nanoflakes | 0.21 V | 79.5 % | No report | 2017 | [75] |
| Nano-flowered Bi | 0.83 V | 99.2 % | 7.5 mA $cm^{-2}$ | 2018 | [76] |
| Bi nanoparticles | 0.83 V | 94.7 % | 3.3 mA $cm^{-2}$ | 2018 | [77] |
| Ultrathin Bi nanosheets | 0.68 V | 95 % | 16 mA $cm^{-2}$ | 2018 | [78] |

**Table 1-2:** Comparison of the catalytic performance of Bi-based electrocatalysts reported in the literature for the reduction of $CO_2$ to formate.

Considering the above reports, Bi-based materials are highly promising catalysts for the reduction of $CO_2$ to formate. However, the influence of the morphology or the structure of the catalysts on their properties remains unclear. Therefore further research on these materials may provide a feasible pathway explaining for the noteworthy yield of HCOOH production and further enhance performance through design and optimization of Bi-based electrocatalysts and electrolytes.

1.3.2.3 Metal compounds

Inorganic metal compounds like metal oxides and metal chalcogenides have been popularly employed as electrocatalysts for $CO_2$ reduction.

Metal oxides-based electrocatalysts have gradually got attention due to their decent efficiency and selectivity for $CO_2$ electroreduction. $PbO_2$ cathode exhibited a Faradaic efficiency of 60 % for HCOOH generation in $KHCO_3$ aqueous solution.[79] Some other earth-abundant and low-toxicity metals, such as Ni and Co, were also investigated. NiO showed a Faradaic efficiency up to 35.2 % for syngas (CO and $H_2$) products.[80] Ultrathin $Co_3O_4$ layers were also employed as an effective electrocatalyst, showing an optimum Faradaic efficiency of 64.3 %for $HCOO^-$ production after 20 h reaction.[81] These results indicated that the introduction of oxidation states in some metal catalysts can improve CDRR performance. However, the lack of stability of these materials is a critical issue that merits to be solved in the future.

Several metal chalcogenides were also reported to be active catalysts for CDRR. The reaction intermediates can bind to different active sites on the surface of metal chalcogenides, and the different edge sites can perform different roles for the various products. In 2014, bulk $MoS_2$ as a highly efficient electrocatalyst for selectively reducing $CO_2$ to CO was first demonstrated by Salehi-Khojin *et al.*, in a mixture of 96 mol % water and 4 mol % ionic liquid. An impressive cathodic current density of 65 mA $cm^{-2}$ and a $CO_2$-to-CO Faradaic efficiency of 98% were achieved at $\eta$ = 0.65 V which is much better than Au and Ag NPs.[82] $WSe_2$ was considered as another promising candidate for CO production with a current density 60 times higher than that of Ag NPs due to its low work function and high d-electron density on the W-terminated edge sites, which can facilitate rapid electron transfer during $CO_2$ reduction, resulting in more stable $^{\bullet}$COOH and $^{\bullet}$CO intermediates, and an easier formation of CO at low overpotentials.[83]

Furthermore, metal carbides [84] and other carbon-based materials, such as carbon fibers [85] or nanoporous carbon[86], were reported to achieve CO, $CH_4$, $HCOO^-$ formation with high selectivity and low overpotential due to preferable $CO_2$ adsorption and their capability to bind CDRR active intermediates.

1.3.2.4 Metal-organic complexes

Electrocatalysts based on metal-organic complexes have attracted significant attention for decades due to their remarkable selectivity. Despite some disadvantages, such as complicated synthetic routes, low reduction activity, and toxic effects, some of them are still considered as promising molecular electrocatalysts for CDRR.

Metal-macrocyclic complexes, composed of a transition metal central atom and an organic macrocyclic ligand, such as porphyrin, cyclam or others, have been tested thoroughly for CDRR.[87] As early reported, $CO_2$ can be effectively converted into CO using Fe-porphyrin molecules and a derived Fe-porphyrin complex could achieve a stable electrocatalytic performance over 4 h for CO generation with a Faradaic yield above 90 %.[88] Artero *et al.* reported a composite electrode prepared by the electrodeposition of $[Cu(cyclam)](ClO_4)_2$ complex that can reduce $CO_2$ into HCOOH with a Faradaic efficiency of 90 % in dimethylformamide (DMF)/$H_2O$ mixture (97:3, v/v).[89] As another example, bipyridine complexes with transition metal atoms, such as Ru[90] and Mn,[91] were also considered as promising molecular electrocatalysts for reducing $CO_2$ to CO or HCOOH. These intriguing molecular catalysts can tune the product selectivity and enhance catalytic activity. Some other complexes with different components, such as phosphine[92], polyaniline[93], *etc*. have also been investigated as molecular CDRR electrocatalysts (**Figure 1-9**).

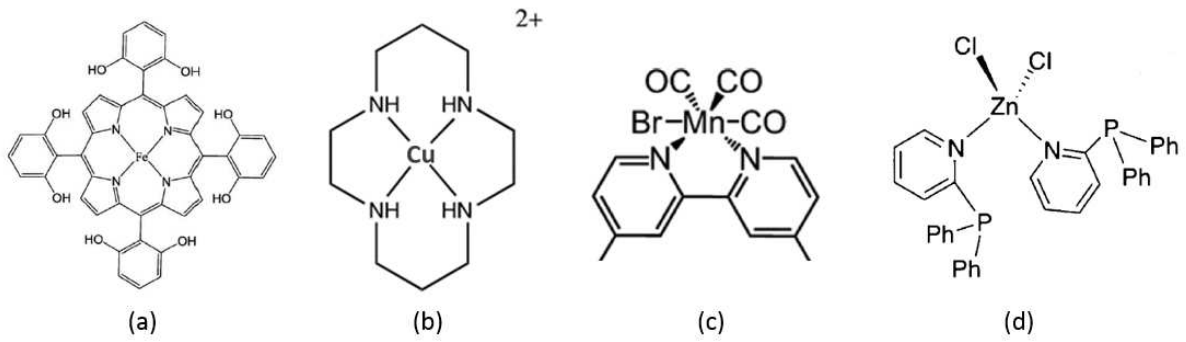


**Figure 1-9:** Examples of metal-organic electrocatalysts for CDRR, (a) Fe-porphyrin complex[88], (b) Cu-cyclam[89], (c) Mn-bipyridine complex[91] and (d) Zn-phosphine complex[92].

1.3.2.5 POMs as electrocatalysts for CDRR

Transition-metal-substituted POMs can be used to capture and transform $CO_2$ into valuable fuels by CDRR. These macromolecules are considered as competitive $CO_2$ electrocatalysts because of several reasons that are now listed: (1) multivacant species in POMs act as all-inorganic ligands towards extra

transition-metal cations, especially abundant first-row transition-metal cations, which could fix $CO_2$; (2) owing to the high oxidation states of metal in peripheral metal-oxygen polyhedral of $MO_x$, POMs anions undergo several rapid one- and two-electron reversible reductions, and further display reversible redox processes that are sensitive to the presence of protons; (3) POMs can promote the formation of H-bond networks in the vicinity of the $CO_2$ coordination center to favor proton-coupled electron transfer, which can occur when the proton source is close to the catalytic center.[94]

In early studies, POMs were demonstrated to electroreduce $CO_2$ without co-catalysts. Proust *et al.* reported that the POM catalyst $[(n\text{-}C_8H_{17})_4N]_6[SiW_{11}O_{39}Co(OH_2)]$ promotes the electrocatalytic reduction of $CO_2$ to CO in a $CH_2Cl_2$ electrolyte, in the presence of protons and water and that the formation of CO is concomitant with the production of formaldehyde.[94] However, the low product yield limits its extensive application. More recently, several Keggin-type POMs were used to synthesize structural metal composites, which have demonstrated high catalytic activities and selectivities for $CO_2$ electroreduction to CO or HCOOH with high Faradaic efficiencies. For instance, Zhang *et al.* synthesized an Ag–$[PMo_{12}O_{40}]^{3-}$ (PMo) nanocomposite with the presence of $[PW_{12}O_{40}]^{3-}$ exhibiting highly attractive properties for $CO_2$ reduction to CO in water-containing DMF with high Faradaic efficiencies for CO formation (90 ± 5 %) over a wide potential range.[95] The same group also reported porous ultrathin Bi–PMo nanosheets catalyzing $CO_2$ to formate reduction in 0.5 M $NaHCO_3$ solution with a Faradaic efficiency of 93 ± 2 % at -0.86 V vs RHE with a formate partial current density as high as 30 mA $cm^{-2}$.[96]

## 1.4 Photoelectrocatalysis at semiconducting surfaces

### 1.4.1 Photoelectrocatalysis

Photoelectrocatalysis is a powerful method derived from the combination of heterogeneous photocatalysis and electrochemical techniques that can be described as a multidisciplinary field involving surface science, electrochemistry, solid-state physics, and optics.[97] In 1972, the use of semiconducting $TiO_2$ on photoelectrocatalytic water splitting, as reported by Fujishima and Honda, had a huge impact on this field. Indeed, they demonstrated that the photoelectrolysis of water applying an anodic bias to the illuminated $TiO_2$ was possible, which opened a large area of research.[98] Since then, photoelectrocatalysis has been successfully explored to promote the oxidation of organic molecules,[99] the reduction of inorganic ions,[100] $CO_2$ reduction,[101] and water splitting reaction. [102,103]

The basic concept of photoelectrocatalysis is that when a semiconductor (SC) surface irradiated by light [$h\nu \geq$ band gap energy ($E$g)], the generation of electron/hole pairs ($e^-/h^+$) is induced by the promotion of an electron from the valence band (lower occupied energy level, VB) to the conduction band (higher unoccupied energy level, CB). In the frame of this thesis, we will consider a *p*-type SC,

where the minority charge carriers are electrons. If the transfer of electrons through the SC/electrolyte interface is possible, photoelectrochemical reactions can be driven on a SC photoelectrode surface with improved efficiency (**Figure 1-10, A**).

In contrast, if the photoelectrons transfer toward the redox active species is inefficient, charge carriers will tend to recombine or get trapped in the surface states of the SC, which are typically induced by grain boundaries or by the termination of the crystal lattice.[104] Electron-hole recombination processes occurring at the ps to ns timescales (~ $10^{-9}$ s), which are several orders of magnitude faster than interfacial charge carrier transfer processes (~ $10^{-3}$ – $10^{-8}$ s) can thus competitively occur.[105,106]

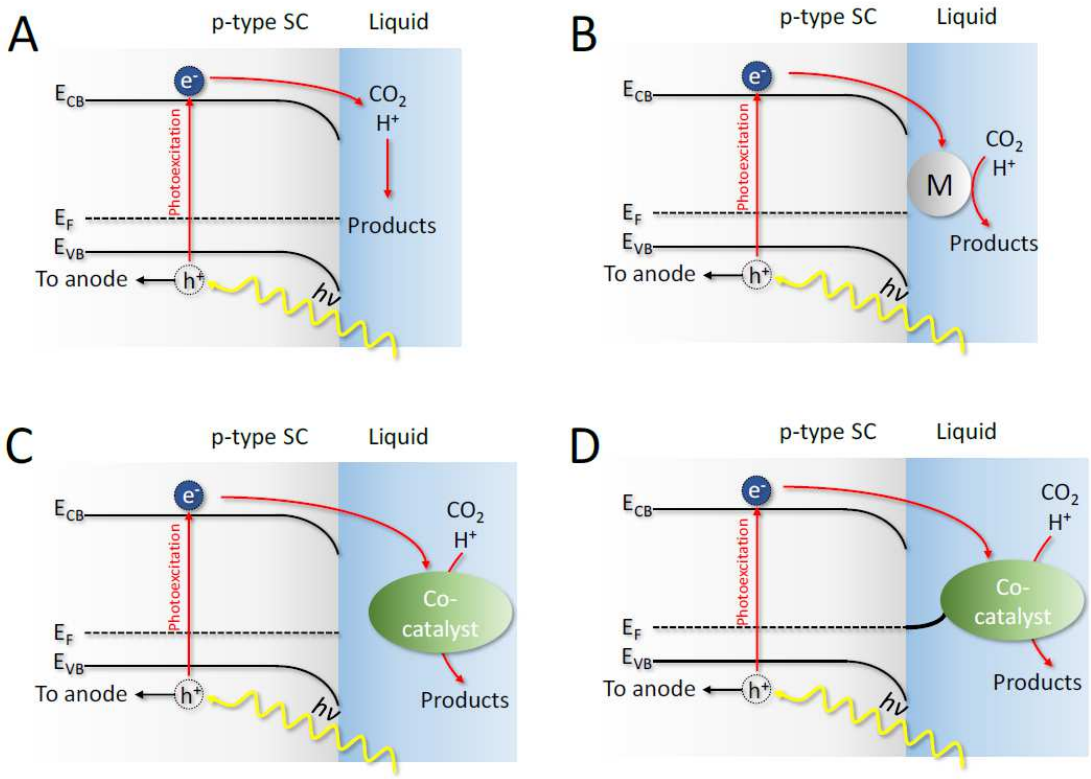


**Figure 1-10**: Schematic diagrams of four different schemes for light-assisted $CO_2$ / $H^+$ reduction on a *p*-type SC photocathode: (A) heterogeneous catalysis on a SC electrode, (B) heterogeneous catalysis on a metal-decorated SC electrode, (C) homogeneous catalysis through a SC/co-catalyst junction, and (D) heterogeneous catalysis on a co-catalyst-decorated SC electrode.[107]

The combination of a SC with a co-catalyst is a promising approach for enhancing the solar-to-chemical conversion efficiency through improving the charge carrier transfer properties (**Figure 1-10 B, C, and D**). In these cases, the SC only acts as a light absorber. After charge separation, the photogenerated charge carriers are transferred to the co-catalyst, on which all redox processes occur. Co-catalysts can

be, for example, (1) metal or metal oxide species; (2) inorganic complexes; or (3) organic molecules, *etc*. Co-catalysts can be intimately linked to the SC surface, then catalysis occurs on the surface of the catalyst (heterogeneous catalysis) or co-catalysts can be dissolved in the solution, thus catalysis occurs in the liquid phase (homogeneous catalysis) (**Figure 1-10, C** and **D**). More importantly, when metal co-catalysts are used, their Fermi level must lie below the $E_{CB}$ of the SC and above the redox potential of the desired reaction to shuttle electrons efficiently.[108]

### 1.4.2 Semiconductors for photoelectrocatalysis

1.4.2.1 Semiconductor photoelectrodes for water splitting

The SC materials should satisfy several fundamental conditions to be ideal for photoelectrochemical water splitting. For example, they should have proper CB and VB edge positions for water reduction or oxidation, respectively. Efficient light absorption of a large portion of the solar spectrum requires an appropriate band gap and absorption coefficient. Moreover, photoelectrodes should have good charge transport characteristics and durability in different operation conditions, such as acidic or basic electrolytes.

The CB/VB edge positions must straddle the water oxidation/reduction potentials since they determine the maximum redox potentials of photogenerated $e^-/h^+$ in a SC.[109] SCs having a lower VB energy (below the water oxidation potential) are beneficial as photoanodes for water oxidation and SCs having a higher CB energy (higher than the water reduction potential) are beneficial as photocathodes for water reduction. These SC photoelectrode materials can be generally divided into several classes: Group IV SCs (Si, Ge), Group III-V SCs (GaAs, GaP, InP, $GaInP_2$), metal oxides SCs ($TiO_2$, $Cu_2O$, $Fe_2O_3$) and metal chalcogenides semiconductors ($MoS_2$, ZnSe, CdS), *etc*. **Figure 1-11** shows the band gap and band edge positions of the various SC materials with respect to a reversible hydrogen electrode (RHE). Among these SCs, Si, GaAs, GaP, and $GaInP_2$, have appropriate potentials for water reduction, and $WO_3$ and $BiVO_4$ have proper potentials for water oxidation.

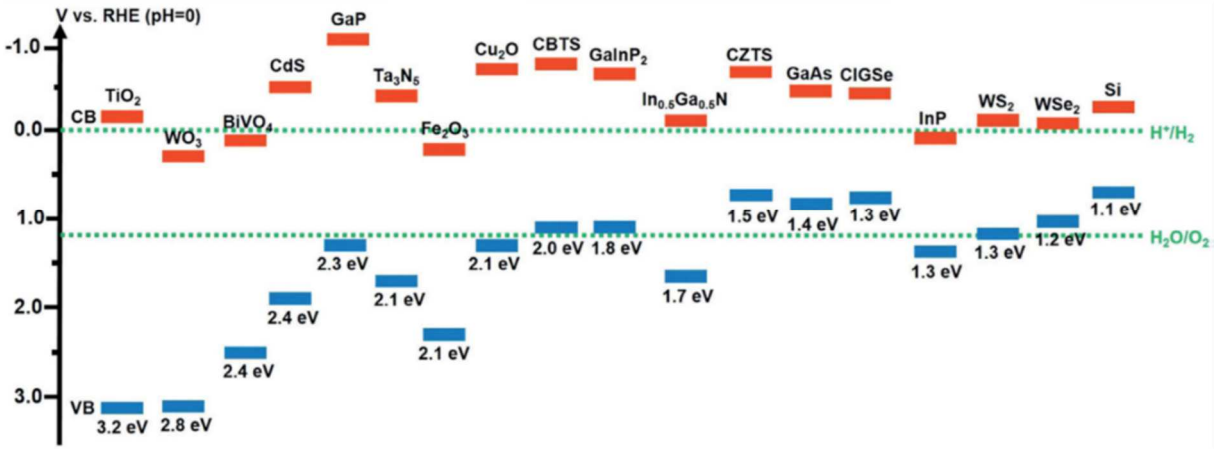


**Figure 1-11**: Band gaps and band edge positions of various SCs with respect to the redox potentials of water splitting (pH = 0) (CBTS: $Cu_2BaSnS_4$; CZTS: $Cu_2ZnSnS_2$; CIGSe: $Cu(InGa)Se_2$).[110]

1.4.2.2 Semiconductor photoelectrodes for CDRR

As mentioned in **Table 1-1**, single-electron $CO_2$ reduction requires a highly negative potential of -1.9 eV, which makes the one-electron reduction process very difficult on conducting electrodes. The CDRR can thus be enhanced by employing SC *p*-type materials to lower the required electrical energy. Similar to HER photocatalysts, an ideal SC for CDRR requires a CB energy higher than that of the $CO_2$/reduced product couple. Upon absorbing radiation from the light source, photogenerated electrons in the CB of photocatalyst can thus form products such as HCOOH, CO, and $CH_4$, by reducing $CO_2$. The relation between the energy levels of the photocatalyst and the redox species determines the type of reaction that takes place. In the ideal case, simultaneously, the photogenerated holes in the VB of the photocatalyst should have an energy low enough to oxidize $H_2O$. **Figure 1-12** displays the band edge positions of some typical SC photocatalysts for $CO_2$ reduction.

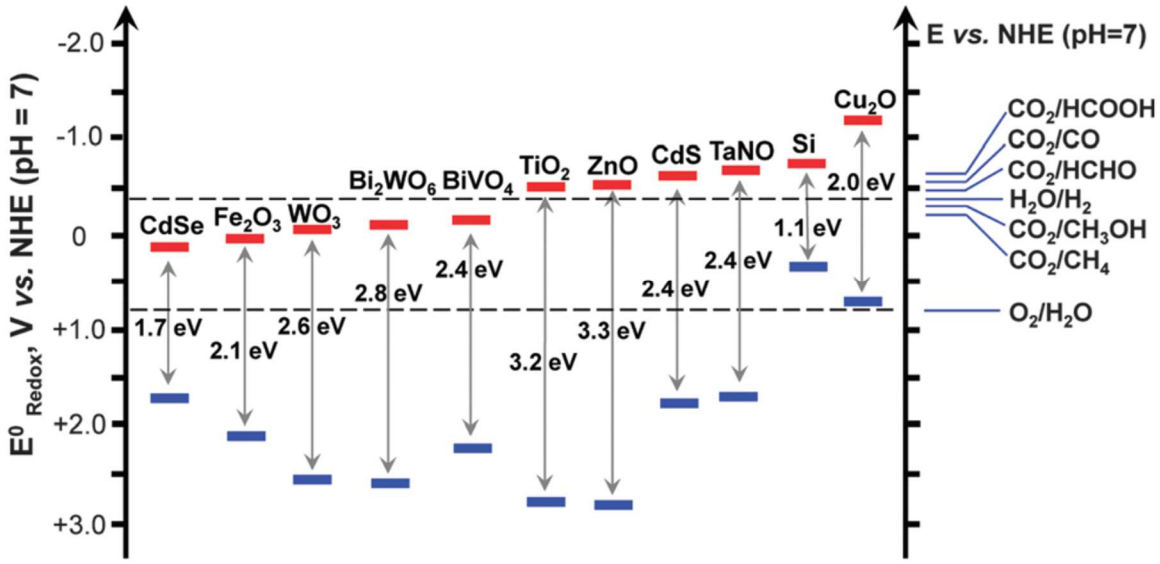


**Figure 1-12**: Band edge positions of some typical SC photocatalysts relative to the energy levels of the redox couples involved in the reduction of $CO_2$.[106]

### 1.4.3 Single-crystal silicon as a photocathode

Si is the second abundant element on the earth. Single-crystal Si is one of the most important crystal materials, widely used in the electronic and photovoltaic industries. Intrinsic Si can be doped with elements (e.g., B, Al, P, As, *etc*.) in different valence states to form *n*-type or *p*-type SCs, which can be used as photoanodes or photocathodes. *p*-type Si (*p*-Si) photocathodes meet most of the requirements for practical HER[111] and CDRR[112] applications.

#### 1.4.3.1 Optical properties of single-crystal silicon photocathode

A SC absorbs shorter wavelengths than its band gap. As the bandgap of Si is as small as ~ 1.12 eV, Si can thus absorb wavelengths shorter than approximately 1127 nm according to $\lambda = 1240 / E_g$, which is relatively well matched to the solar spectrum. This property renders Si a promising material for photoelectrodes in a photoelectrochemical system because a large number of photons can be absorbed and converted to photocurrent compared to other wider band gap SCs (e.g., GaAs, *E*g = 1.4 eV and single-layer $MoS_2$, *E*g = 1.8 eV). As shown in **Figure 1-13**, the portion of the solar spectrum that can be absorbed by the SCs mentioned above were calculated by integrating the solar irradiation spectrum below the wavelength corresponding to the bandgap. Consequently, Si can absorb 80 %, GaAs 62 %, and $MoS_2$ 50 % of the full solar spectrum, which clearly indicates Si as a promising absorber for our applications.

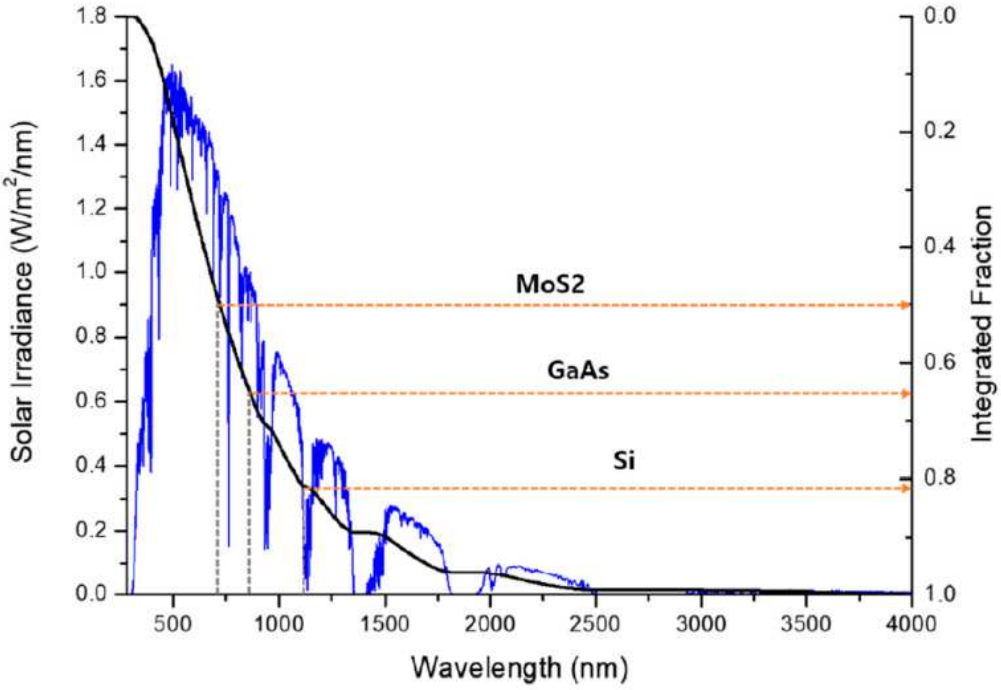


**Figure 1-13**: Solar irradiance spectrum of air mass (AM) 1.5G for a 37° tilted surface. The ratio of absorbed solar light irradiance is integrated and shown on the right-side y-axis of the graph (the blue line represents the irradiance unit of wavelength under 1 sun, and the black line represents the accumulated solar irradiance starting wavelength of 280 nm).[113]

SCs are also distinguished according to the nature of the optical transition between the CB and VB. Indeed, there are two fundamental types of semiconductors: direct and indirect. In a direct SC, the momentum of electrons in the CB is the same as the momentum of holes in the VB, thus free photogenerated carriers can be directly created upon excitation by a photon (energy $h\nu > E_g$). In an indirect SC, the momentum of electrons in the CB is different from the momentum of holes in the VB, thus, a phonon (collected vibration state of the crystal with energy $h\omega$) is needed in conjunction with a photon to make the energetic transition from the VB to the CB (**Figure 1-14**). As a consequence, the absorption coefficient of indirect SCs is much smaller than that of direct SCs, a difference that can be two orders of magnitude. Si is an indirect SC and its bandgap is related to absorption coefficient $\alpha$, as shown below:

$$\alpha = \frac{A(h\nu - Eg)^m}{h\nu}$$

where *A* is a constant determined by the SC, *hv* is the light energy obtained from Planck's constant ($h$ = 6.63 × $10^{-34}$ J s) and *v* is the frequency determined by the speed of light (3 × $10^{-8}$ m $s^{-1}$) over the

wavelength ($\lambda$ in nm) by the Planck-Einstein relation. For direct SCs, $m$ = 1/2, whereas for indirect SCs (e.g., Si), $m$ = 2.

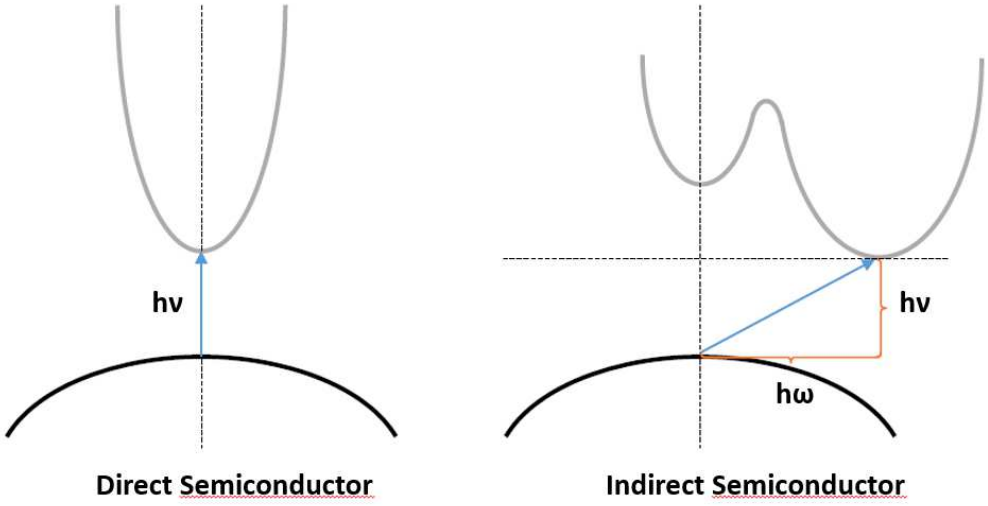


**Figure 1-14**: Direct and indirect optical transitions in a SC. The indirect transition requires the assistance of a phonon with the energy $h\omega$.

1.4.3.2 Thermodynamics and kinetics of single-crystal silicon photocathode

Monocrystalline Si is suitable for HER since the $E_{CB}$ is well above the water reduction level. Its band gap of 1.1 eV can theoretically provide a maximum photovoltage ($V_{ph}$) of 0.8 V from a junction p-Si/$SiO_x$/$MoS_2$.[114] The $V_{ph}$ can be defined as the difference between the quasi-Fermi levels of the electrons ($E_{F,n}$) and holes ($E_{F,p}$) at the SC/electrolyte interface during illumination. It is often interpreted as the thermodynamic driving force of the photoelectrode (**Figure 1-15**). A photocathode must possess a large internal $V_{ph}$ to decrease the electrical potential required for HER or CDRR. Unfortunately, $V_{ph}$ can be difficult to determine because the energetics at the SC/electrolyte interface are frequently influenced by nonideal factors such as defects and surface states.[115]

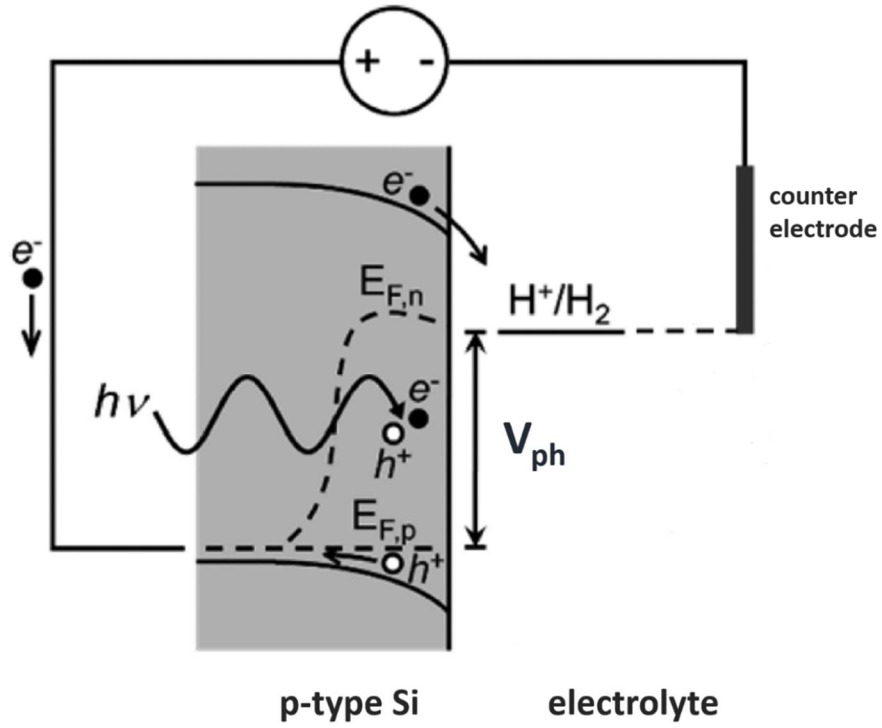


**Figure 1-15**: Schematic showing the band positions, quasi-Fermi levels for electrons ($E_{F,n}$), holes ($E_{F,p}$), and obtainable photovoltage ($V_{ph}$) for a *p*-type Si photocathode in relation to the $H^+/H_2$ electrochemical potential. Adapted from ref [116].

In addition to having a large internal $V_{ph}$, a positive flatband potential ($E_{fb}$) is necessary for a *p*-type SC to ensure a proper band bending. $E_{fb}$ is an important parameter to determine the energy levels of the SC bands. Such a parameter can be calculated using the commonly used Mott-Schottky relationship:

$$\frac{1}{C_{sc}^2} = \left(\frac{2}{qN\varepsilon\varepsilon_0}\right)\left(E - E_{fb} - \frac{kT}{q}\right)$$

Where $C_{sc}$ is the capacitance of the space charge region, $q$ is the electron charge, $N$ is the dopant density, $\varepsilon$ is the dielectric constant of SC (11.9 for Si), $\varepsilon_0$ is the permittivity in vacuum, $E$ is the applied potential, and $kT/q$ is the temperature dependent term, equals to 0.0257 V at 298 K. The $E_{fb}$ value measured for *p*-Si-based photocathodes was, for instance 0.47 V vs. Ag/AgCl in contact with 0.1 M $FeSO_4$ + 0.1 M $H_2SO_4$ solution in the dark and -0.20 V vs. Ag/AgCl under illumination.[117]

For the kinetic aspects, the charge-transfer kinetics on a bare Si interface without catalysts depends on the change of the surface charge density,[118] which is influenced by processes such as charge storage at the surface, charge transfer to the solution, and charge recombination. Both the charge-transfer and the recombination rates depend on the illumination intensity and the applied bias.[119, 120] In

addition, the $SiO_x$ layer gradually formed from the anodic decomposition of Si can significantly block the current. Moreover, when Si photocathodes are used in acid media under high-density illumination and cathodic bias, surface recombination rate and resistivity of Si can also increase, the latter being caused by acceptor atoms being neutralized by the incorporated H atoms. [121,122]

In general, Si is a strong absorber, and *p*-type Si attracted a lot of research interest as a photocathode. However, in spite of its abundance, nontoxicity, and low cost, there are so many challenges of utilizing bare *p*-Si for solar-fuel production from water splitting and $CO_2$ reduction, such as:

(1) Low photovoltage, which is intrinsically limited by the recombination processes and the band gap of Si;[123]

(2) Slow charge-transfer kinetics on bare Si surface in contact with an aqueous solution, which in turn results in large overpotentials for producing useful current values;

(3) Fast charge carrier recombination rate, originating from the concentration of surface states.[124]

### 1.4.4 Strategies for increasing the efficiency of *p*-type silicon photocathodes

To overcome the intrinsic disadvantages of *p*-Si for solar-fuel production and improve efficiency, surface alteration techniques are necessary. They can be divided into several types, the two principal approaches being the surface texturing and the co-catalyst coating.

Surface texturing techniques can be preferentially introduced to the crystalline Si photocathode to effectively enhance light absorption by inducing internal reflection, suppressing the incident angle effect and minimizing the polarization sensibility.[125] In addition, surface textures (e.g., micro- or nanostructures) can also provide enlarged junction areas and more efficient collection of photogenerated minority carriers, which decouple light absorption and charge separation directions for an improved charge collection efficiency.[126]

Another strategy to improve both photocathode efficiency and stability is the coating of a heterogeneous co-catalyst on the Si surface. These co-catalyst coatings, which can modify the interfacial energetics of photocathodes should ideally meet the following conditions: (1) the coating should be pinhole and defect-free to minimize the self-passivation or corrosive reactions; (2) the coating should offer minimum light reflection and adsorption to maximize the light absorption by Si; (3) the co-catalyst film should be capable of driving photoinduced charges efficiently to the electrolyte with a minimal resistivity. In case of monocrystalline Si, the nature of the Si/electrolyte interface is

particularly critical, because the formation of a native oxide ($SiO_x$) layer on the Si surface by spontaneous oxidation of Si occurs at room temperature. Removing this native oxide using HF solution prior to the coating process, as it will be used in this thesis, leads to the formation of hydride-terminated Si (Si–H), which is known as one of the surfaces with the lowest recombination velocity.[127] Then, the immobilization of a co-catalyst on the freshly prepared *p*-type Si–H surface can further achieve an improvement of HER or CDRR performance. Co-catalysts deposited on *p*-Si photocathodes and their beneficial effects for the photoelectrocatalysis will be presented in the following sections.

### 1.4.5 Co-catalysts for photoelectrocatalysis

In photoelectrocatalysis, the nature of the loaded co-catalyst and their interaction with the SC interface are important. The co-catalyst can provide trapping sites for the photogenerated charges and promote charge separation, thus enhancing the quantum efficiency. Most importantly, suitably loaded co-catalysts on SCs can significantly increase the photoelectrocatalytic activities and stabilities.[128] Thus, the discovery of new co-catalysts for solar-fuel production reactions is a prominent and growing field of research.

For example, in the frame of solar water splitting reactions, co-catalysts for HER and oxygen evolution reaction (OER) having numerous different elemental compositions have been reported. Jaramillo *et al.* presented 18 electrocatalysts for HER and 26 electrocatalysts for OER in aqueous acidic or alkaline solution (**Figure 1-16**), evaluated and compared their activity, their short-term (2 hours) stability and electrochemically active surface area in order to promote the development of new catalytic systems. Among HER catalysts, several could operate at 10 mA $cm^{-2}$ with overpotentials < 0.1 V in acidic and/or alkaline solutions. Among OER catalysts in acidic solution, no non-noble metal-based materials showed promising activity and stability, whereas, in alkaline solution, many OER catalysts performed efficiently with comparable or better specific catalytic activity compared to Ir and Ru catalysts. This is in contrast with most HER catalysts that showed lower specific activity than Pt in both acidic and alkaline solutions.

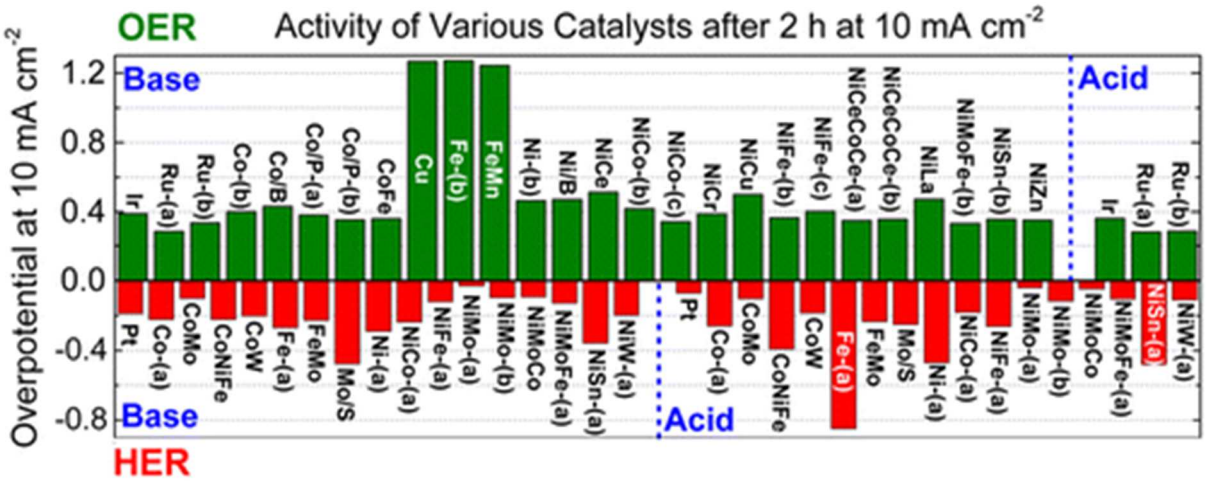


**Figure 1-16:** Comparisons of electrocatalysts activity in short-term (2 hours) stability for HER or OER in acidic or alkaline solution.[129]

### 1.4.6 Co-catalysts on *p*-Si photocathode for HER

For the photoelectrochemical HER, highly conductive and active catalysts can be used directly on the SC surface to form a heterojunction photoelectrode. These catalysts act as a dual-functional layer to form the heterojunction with SC and sustain fast reaction kinetics. Si has proven a popular choice as a photoactive substrate for depositing HER electrocatalysts because of its stability under low pH conditions. An early key result in this area was established by Chorkendorff *et al.*, who deposited catalytic $Mo_3S_4$ clusters onto a pillar-structured *p*-Si substrate. This design provided a large surface area for HER catalyst while optimizing photocurrent collection efficiency. The pillared Si-$MoS_x$ arrays exhibited higher current densities (-10 mA $cm^{-2}$ at 0 V vs RHE) compared with planar Si substrates decorated with the same electrocatalyst.[130] Additional examples of the use of *p*-type Si as the photoactive substrate for HER are given in **Table 1-3**:

| Co-catalyst Material | Onset potential / $V_{RHE}$ [a] | $E$ / $V_{RHE}$ at $j$ = - 10 mA $cm^{-2}$ | Stability / h | Electrolyte | Ref |
|---|---|---|---|---|---|
| Pt (1.5 nm) | 0.27 | 0.17 | No report | $H_2SO_4$ (pH ~ 2) | 131 |
| Ti (30 nm) / Pt (20 nm) | 0.50 | - 0.13 | No report | 0.5M $H_2SO_4$ | 132 |
| $SrTiO_3$ (4 nm) / Ti (30 nm) / Pt (20 nm) | 0.45 | 0.25 | 35 | 0.5M $H_2SO_4$ | 133 |
| $WC_2$ (4.9 nm) / Pt | 0.48 | 0.28 | 1 | 0.5M $H_2SO_4$ | 134 |
| Ti (5 nm) / NiFe (1.1 µm) | 0.15 | - 0.05 | 24 | 1M KOH | 135 |
| $TiO_2$ (1.1 µm) / $NiP_3$ | 0.40 | - | 24 | Acetic acid (pH = 4.5) | 136 |
| Cobalt dithiolene polymer | 0.20 | - 0.20 | 0.33 | $H_2SO_4$ (pH = 1.3) | 137 |
| NiMo (85 % : 15 % ) | 0.14 | 0.04 | No report | Aqueous solution (pH = 4.5) | 138 |
| $NiCoSe_x$ | 0.22 | 0.15 | 2 | 0.5M $H_2SO_4$ | 139 |
| $CoSe_2$ (300 nm) | 0.21 | - 0.04 | 0.33 | 0.5M $H_2SO_4$ | 140 |
| $CoS_2$ | 0.25 | - | 9 | 0.5M $H_2SO_4$ | 141 |

[a] Determined for a photocurrent density of 1 mA $cm^{-2}$.

**Table 1-3**: Examples of co-catalyst modified *p*-Si photocathodes for photoelectrocatalytic HER. Experimental results were measured under simulated 1 Sun illumination (AM 1.5G, 100 mW $cm^{-2}$).

### 1.4.7 Co-catalysts on *p*-Si photocathode for CDRR

Many research works for photoelectrocatalytic systems for CDRR have been performed on *p*-Si photoelectrodes. In early studies, Aurian-Blajeni *et al.* investigated the effect of polyaniline coatings on Si. The polyaniline-coated *p*-Si had a much lower overpotential than bare *p*-Si, with onset potential close to -1.0 V vs SCE under illumination from a Xe lamp. This system produced predominantly formic acid and some formaldehyde, with combined Faradaic efficiencies of 20 – 30 %, though the efficiency dropped as more charge was passed.[142] *p*-Si photocathodes modified with either Cu, Au, or Ag particles have been shown to produce CO, $CH_4$, and $C_2H_4$ in aqueous media.[143,144] It was reported that the fine control of the particles surface structure was very important in order to decrease surface carrier recombination and to control the barrier height and energy-level matching between the SC and

solution.[143] Additionally, it was determined that the theoretical optimum yield would occur with particles of 5 nm in size, though particles of 20 – 200 nm in size were experimentally employed.[144]

In later studies, graphene has been used as a heterogeneous co-catalyst for selective conversion of $CO_2$ to CO (95 % Faradaic efficiency) using *p*-Si nanowire photocathodes.[145] Furthermore, Song *et al.* reported Si photocathodes coated with a nanoporous Au thin film that produced CO with 96 % Faradaic efficiency.[146] More recently, Li *et al.* reported that the controlled chemical etching of *p*-Si wafer by $Ag^+$ ions yields effective SC/co-catalyst interface for photoelectrochemical CDRR, producing photocathodes exhibiting a large photocurrent density (~ 10 mA $cm^{-2}$ under 0.5 sun), a great $CO_2$-to-CO Faradaic efficiency (90 % at - 0.5 V vs RHE), and an impressive operational stability for 8 h.[147] Besides these heterogeneous co-catalyst examples, there are also some intriguing reports for homogeneous CDRR on which molecular catalysts are combined with *p*-Si to produce 2-electron reduction products, such as CO.[148,149] Re-based co-catalyst [Re(*t*$Bu_2$–bpy)$(CO)_3$Cl] exhibited a catalytic effect on irradiated *p*-Si SC electrode, with a positive 500 mV shift of the catalytic peak. [148] Therefore, the light input can make the use of Si-based photocathode a potential energy saving pathway for CDRR. Fabre *et al.* also developed *p*-type Si–H nanowires (SiNWs–H), to be used as photocathodes to accomplish CDRR using Mn carbonyl complexes. The choice of SiNWs–H over the planar Si-H was driven by the fact that they could produce higher photocurrents with less negative overpotentials in MeCN:$H_2O$ solutions. In this system, the efficient CO production was achieved without concomitant $H_2$ generation, providing potential promise for hybrid molecular SiNWs–H modified photocathodes.[149]

## Summary

This bibliographic chapter introduced the electrochemical fundamentals of HER and CDRR and summarized different types of electrocatalytic systems that can be employed to perform these technologically and economically important reactions. In addition, the photoelectrocatalysis at the *p*-Si surface was discussed from an optical and a thermodynamic point-of-view. Finally, different examples of co-catalyst-modified *p*-Si photocathodes that can efficiently enhance HER or CDRR performance were presented. All these elements provide the essential background of the present thesis.

**References**

[1] Passalacqua, R.; Centi, G.; Perathoner, S. Solar production of fuels from water and $CO_2$: Perspectives and opportunities for a sustainable use of renewable energy. *Oil & Gas Science and Technology–Revue d' IFP Energies nouvelles*. **2015**, *70* (5), 799-815.

[2] Centi, G.; and Siglinda P. Perspectives and state of the art in producing solar fuels and chemicals from $CO_2$. *Green Carbon Dioxide: Advances in $CO_2$ Utilization.* **2014**, 1-24.

[3] Protti, S.; Albini, A.; Serpone, N. Photocatalytic generation of solar fuels from the reduction of $H_2O$ and $CO_2$: a look at the patent literature. *Physical Chemistry Chemical Physics*. **2014**, *16*(37), 19790-19827.

[4] Thomas, J. M. Reflections on the topic of solar fuels. *Energy & Environmental Science*. **2014**, *7*(1), 19-20.

[5] Centi, G.; Perathoner, S. Towards solar fuels from water and $CO_2$. *ChemSusChem: Chemistry & Sustainability Energy & Materials*. **2010**, *3*(2), 195-208.

[6] Cédric, P. Technology Roadmap: Solar Photovoltaic Energy. *International Energy Agency*. **2014**.

[7] Cédric, P. Technology Roadmap: Solar Thermal Electricity. *International Energy Agency*. **2014**.

[8] Multi-Year Research, Development and Demonstration Plan Executive Summary, Fuel Cell Tehnologies Office, US Department Of Energy, **2012**.

[9] Herron, J. A.; Kim, J.; Upadhye, A. A.; Huber, G. W.; Maravelias, C. T. A General Framework for the Assessment of Solar Fuel Technologies. *Energy & Environmental Science*. **2015**, *8*(1), 126–157.

[10] Wang, J.; Xu, F.; Jin, H.; Chen, Y.; Wang, Y. Non-Noble Metal-based Carbon Composites in Hydrogen Evolution Reaction: Fundamentals to Applications. *Advanced Materials*. **2017**, *29*(14), 1605838.

[11] Schlapbach, L. Technology: Hydrogen-fuelled vehicles. *Nature*. **2009**, *460*(7257), 809.

[12] Bates, M. K.; Jia, Q.; Ramaswamy, N.; Allen, R. J.; Mukerjee, S. Composite Ni/NiO-$Cr_2O_3$ catalyst for alkaline hydrogen evolution reaction. *The Journal of Physical Chemistry C.* **2015**, *119*(10), 5467-5477.

[13] Santos, D. M.; Sequeira, C. A.; Figueiredo, J. L. Hydrogen production by alkaline water electrolysis. *Química Nova*. **2013**, *36*(8), 1176-1193.

[14] Fellet, M.; Tiede, D. M. Search for water-splitting catalysts for global usage. *MRS Bulletin*. **2017**, *42*(3), 190-194.

[15] Li, Q.; Mahmood, N.; Zhu, J.; Hou, Y.; Sun, S. Graphene and its composites with nanoparticles for electrochemical energy applications. *Nano Today*. **2014**, *9*(5), 668-683.

[16] Mahmood, N.; Zhang, C.; Yin, H.; Hou, Y. Graphene-based nanocomposites for energy storage and conversion in lithium batteries, supercapacitors and fuel cells. *Journal of Materials Chemistry A*. **2014**, *2*(1), 15-32.

[17] De Levie, R. The electrolysis of water. *Journal of Electroanalytical Chemistry*. **1999**, *476*(1), 92-93.

[18] Kreuter, W.; Hofmann, H. Electrolysis: the important energy transformer in a world of sustainable energy. *International Journal of Hydrogen Energy*. **1998**, *23*(8), 661-666.

[19] Rieger, P. H. *Electrochemistry*. Prentice-Hall, New Jersey, USA **1987**.

[20] Carmo, M.; Fritz, D. L.; Mergel, J.; Stolten, D. A comprehensive review on PEM water electrolysis. *International Journal of Hydrogen Energy*. **2013**, *38*(12), 4901-4934.

[21] LeRoy, R. L. Industrial water electrolysis: present and future. *International Journal of Hydrogen Energy*. **1983**, *8*(6), 401-417.

[22] Smyrl, W. H.; Conway, B. E.; Yeager, E.; White, R. E. Electrochemical Materials Science. *Comprehensive Treatise of Electrochemistry*, Plenum Press, New York, London, **1981**.

[23] Badwal, S. P.; Giddey, S. S.; Munnings, C.; Bhatt, A. I.; Hollenkamp, A. F. Emerging electrochemical energy conversion and storage technologies. *Frontiers in Chemistry*. **2014**, *2*, 79.

[24] Murthy, A. P.; Madhavan, J.; Murugan, K. Recent advances in hydrogen evolution reaction catalysts on carbon/carbon-based supports in acid media. *Journal of Power Sources*. **2018**, *398*, 9-26.

[25] Morales-Guio, C. G.; Stern, L. A.; Hu, X. Nanostructured hydrotreating catalysts for electrochemical hydrogen evolution. *Chemical Society Reviews*. **2014**, *43*(18), 6555-6569.

[26] Trasatti, S. Work function, electronegativity, and electrochemical behaviour of metals: III. Electrolytic hydrogen evolution in acid solutions. *Journal of Electroanalytical Chemistry and Interfacial Electrochemistry*. **1972**, *39*(1), 163-184.

[27] Nørskov, J. K.; Bligaard, T.; Logadottir, A.; Kitchin, J. R.; Chen, J. G.; Pandelov, S.; Stimming, U. Trends in the exchange current for hydrogen evolution. *Journal of the Electrochemical Society*. **2005**, *152*(3), J23-J26.

[28] Skúlason, E.; Tripkovic, V.; Björketun, M. E.; Gudmundsdottir, S.; Karlberg, G.; Rossmeisl, J.; ... Nørskov, J. K. Modeling the electrochemical hydrogen oxidation and evolution reactions on the basis of density functional theory calculations. *The Journal of Physical Chemistry C*. **2010**, *114*(42), 18182-18197.

[29] Quaino, P.; Juarez, F.; Santos, E.; Schmickler, W. Volcano plots in hydrogen electrocatalysis–uses and abuses. *Beilstein Journal of Nanotechnology*. **2014**, *5*(1), 846-854.

[30] Kalasapurayil, A. K.; Ramasamy, M. Electrochemical Deposition of Platinum Nanoparticles on Reduced Graphene Oxide for Hydrogen Evolution from Acid Water. *ChemistrySelect*. **2016**, *1*(21), 6673-6680.

[31] Abdolmaleki, A.; Mohamadi, Z.; Ensafi, A. A.; Atashbar, N. Z.; Rezaei, B. Efficient and stable HER electrocatalyst using Pt-nanoparticles @ poly(3, 4- ethylene dioxythiophene) modified sulfonated graphene nanocomposite. *International Journal of Hydrogen Energy*. **2018**, *43*(17), 8323-8332.

[32] Cheng, N.; Stambula, S.; Wang, D.; Banis, M. N.; Liu, J.; Riese, A.; ... Botton, G. A. Platinum single- atom and cluster catalysis of the hydrogen evolution reaction. *Nature Communications*. **2016**, *7*, 13638.

[33] Bao, M; Amiinu, I. S; Peng, T.; Li, W.; Liu, S.; Wang, Z.; Pu, Z.; He, D.; Xiong, Y.; Mu, S. Surface Evolution of PtCu Alloy Shell over Pd Nanocrystals Leads to Superior Hydrogen Evolution and Oxygen Reduction Reactions. *ACS Energy Lett*. **2018**, *3* (4), pp 940–945.

[34] Du, N.; Wang, C.; Wang, X.; Lin, Y.; Jiang, J.; Xiong, Y. Trimetallic TriStar nanostructures: tuning electronic and surface structures for enhanced electrocatalytic hydrogen evolution. *Advanced Materials*. **2016**, *28*(10), 2077-2084.

[35] Vij, V.; Sultan, S.; Harzandi, A. M.; Meena, A.; Tiwari, J. N.; Lee, W. G.; ... Kim, K. S. Nickel-based electrocatalysts for energy-related applications: oxygen reduction, oxygen evolution, and hydrogen evolution reactions. *ACS Catalysis*. **2017**, *7*(10), 7196-7225.

[36] Hinnemann, B.; Moses, P. G.; Bonde, J.; Jørgensen, K. P.; Nielsen, J. H.; Horch, S.; ... Nørskov, J. K. Biomimetic hydrogen evolution: $MoS_2$ nanoparticles as catalyst for hydrogen evolution. *Journal of the American Chemical Society*. **2005**, *127*(15), 5308-5309.

[37] Jaramillo, T. F.; Jørgensen, K. P.; Bonde, J.; Nielsen, J. H.; Horch, S.; Chorkendorff, I. Identification of active edge sites for electrochemical $H_2$ evolution from $MoS_2$ nanocatalysts. *Science*, **2007**, *317*(5834), 100-102.

[38] Kaur-Ghumaan, S.; Stein, M. [NiFe] hydrogenases: how close do structural and functional mimics approach the active site?. *Dalton Transactions*. **2014**, *43*(25), 9392-9405.

[39] Faber, M. S.; Dziedzic, R.; Lukowski, M. A.; Kaiser, N. S.; Ding, Q.; Jin, S. High-performance electrocatalysis using metallic cobalt pyrite ($CoS_2$) micro-and nanostructures. *Journal of the American Chemical Society*. **2014**, *136*(28), 10053-10061.

[40] Wirth, S.; Harnisch, F.; Weinmann, M.; Schröder, U. Comparative study of IVB–VIB transition metal compound electrocatalysts for the hydrogen evolution reaction. *Applied Catalysis B: Environmental*. **2012**, *126*, 225-230.

[41] Tian, J.; Liu, Q.; Cheng, N.; Asiri, A. M.; Sun, X. Self‐Supported $Cu_3P$ Nanowire Arrays as an Integrated High-Performance Three-Dimensional Cathode for Generating Hydrogen from Water. *Angewandte Chemie International Edition*. **2014**, *53*(36), 9577-9581.

[42] Dalle, K. E.; Warnan, J.; Leung, J. J.; Reuillard, B.; Karmel, I. S.; Reisner, E. Electro-and Solar-Driven Fuel Synthesis with First Row Transition Metal Complexes. *Chemical Reviews*. **2019**, *119* (4), 2752–2875.

[43] Bullock, R. M.; Das, A. K.; Appel, A. M. Surface immobilization of molecular electrocatalysts for energy conversion. *Chemistry – A European Journal*. **2017**, *23*(32), 7626-7641.

[44] Cavell, A. C.; Hartley, C. L.; Liu, D.; Tribble, C. S.; McNamara, W. R. Sulfinato iron (III) complex for electrocatalytic proton reduction. *Inorganic Chemistry*. **2015**, *54*(7), 3325-3330.

[45] Lassalle-Kaiser, B.; Zitolo, A.; Fonda, E.; Robert, M.; Anxolabéhère-Mallart, E. In Situ Observation of the Formation and Structure of Hydrogen-Evolving Amorphous Cobalt Electrocatalysts. *ACS Energy Letters*. **2017**, *2*(11), 2545-2551.

[46] Aimoto, Y.; Koshiba, K.; Yamauchi, K.; Sakai, K. A family of molecular nickel hydrogen evolution catalysts providing tunable overpotentials using ligand-centered proton-coupled electron transfer paths. *Chemical Communications*. **2018**, *54*(91), 12820-12823.

[47] Wang, S. S.; Yang, G. Y. Recent advances in polyoxometalate-catalyzed reactions. *Chemical Reviews*. **2015**, *115*(11), 4893-4962.

[48] Pope, M. T.; Müller, A. Polyoxometalate chemistry: an old field with new dimensions in several disciplines. *Angewandte Chemie International Edition in English*. **1991**, *30*(1), 34-48.

[49] Keita, B.; Nadjo, L. Activation of electrode surfaces: Application to the electrocatalysis of the hydrogen evolution reaction. *Journal of Electroanalytical Chemistry and Interfacial Electrochemistry*. **1985**, *191*(2), 441-448.

[50] Keita, B.; Kortz, U.; Holzle, L. R. B.; Brown, S.; Nadjo, L. Efficient hydrogen-evolving cathodes based on proton and electron reservoir behaviors of the phosphotungstate $[H_7P_8W_{48}O_{184}]^{33-}$ and the Co(II)-containing silicotungstates $[Co_6(H_2O)_{30}\{Co_9Cl_2(OH)_3(H_2O)_9(\beta\text{-}SiW_8O_{31})_3\}]^{5-}$ and $[\{Co_3(B\text{-}\beta\text{-}SiW_9O_{33}(OH))(B\text{-}\beta\text{-}SiW_8O_{29}OH)_2\}_2]_{22}$. *Langmuir*. **2007**, *23*(19), 9531-9534.

[51] Xu, W.; Liu, C.; Xing, W.; Lu, T. A novel hybrid based on carbon nanotubes and heteropolyanions as effective catalyst for hydrogen evolution. *Electrochemistry Communications*. **2007**, *9*(1), 180-184.

[52] Symes, M. D.; Cronin, L. Decoupling hydrogen and oxygen evolution during electrolytic water splitting using an electron-coupled-proton buffer. *Nature Chemistry*. **2013**, *5*(5), 403.

[53] Rausch, B.; Symes, M. D.; Chisholm, G.; Cronin, L. Decoupled catalytic hydrogen evolution from a molecular metal oxide redox mediator in water splitting. *Science*. **2014**, *345*(6202), 1326-1330.

[54] Sun, Z.; Ma, T.; Tao, H.; Fan, Q.; Han, B. Fundamentals and challenges of electrochemical $CO_2$ reduction using two-dimensional materials. *Chem*. **2017**, *3*(4), 560-587.

[55] Amos, P.; Louis, H.; Adesina Adegoke, K.; Eno, E. A.; Udochukwu, A. O.; Odey Magub, T. Understanding the Mechanism of Electrochemical Reduction of $CO_2$ Using Cu/Cu-Based Electrodes: A Review. *Asian Journal of Nanosciences and Materials*. **2018**, 183-224.

[56] Bard, A. *Standard potentials in aqueous solution*. Routledge. **2017**.

[57] Hori, Y.; Wakebe, H.; Tsukamoto, T.; Koga, O. Electrocatalytic process of CO selectivity in electrochemical reduction of $CO_2$ at metal electrodes in aqueous media. *Electrochimica Acta*. **1994**, *39*(11-12), 1833-1839.

[58] Hori, Y.; Murata, A.; Takahashi, R. Formation of hydrocarbons in the electrochemical reduction of carbon dioxide at a copper electrode in aqueous solution. *Journal of the Chemical Society, Faraday Transactions 1: Physical Chemistry in Condensed Phases.* **1989**, *85*(8), 2309-2326.

[59] Bagger, A.; Ju, W.; Varela, A. S.; Strasser, P.; Rossmeisl, J. Electrochemical $CO_2$ reduction: a classification problem. *ChemPhysChem*. **2017**, *18*(22), 3266-3273.

[60] Li, H.; Oloman, C. Development of a continuous reactor for the electro-reduction of carbon dioxide to formate – Part 1: Process variables. *Journal of Applied Electrochemistry*. **2006**, *36*(10), 1105.

[61] Del Castillo, A.; Alvarez-Guerra, M.; Solla-Gullón, J.; Sáez, A.; Montiel, V.; Irabien, A. Electrocatalytic reduction of $CO_2$ to formate using particulate Sn electrodes: Effect of metal loading and particle size. *Applied Energy*. **2015**, *157*, 165-173.

[62] Cui, C.; Han, J.; Zhu, X.; Liu, X.; Wang, H.; Mei, D.; Ge, Q. Promotional effect of surface hydroxyls on electrochemical reduction of $CO_2$ over $SnO_x$/Sn electrode. *Journal of Catalysis*. **2016**, *343*, 257-265.

[63] Wu, J.; Risalvato, F. G.; Ke, F. S.; Pellechia, P. J.; Zhou, X. D. Electrochemical reduction of carbon dioxide I. Effects of the electrolyte on the selectivity and activity with Sn electrode. *Journal of the Electrochemical Society*. **2012**, *159*(7), F353-F359.

[64] Mistry, H.; Reske, R.; Zeng, Z.; Zhao, Z. J.; Greeley, J.; Strasser, P.; Cuenya, B. R. Exceptional size-dependent activity enhancement in the electroreduction of $CO_2$ over Au nanoparticles. *Journal of the American Chemical Society*. **2014**, *136*(47), 16473-16476.

[65] Sun, K.; Wu, L.; Qin, W.; Zhou, J.; Hu, Y.; Jiang, Z.; ... Wang, Z. Enhanced electrochemical reduction of $CO_2$ to CO on Ag electrocatalysts with increased unoccupied density of states. *Journal of Materials Chemistry A*. **2016**, *4*(32), 12616-12623.

[66] Hori, Y.; Takahashi, I.; Koga, O.; Hoshi, N. Electrochemical reduction of carbon dioxide at various series of copper single crystal electrodes. *Journal of Molecular Catalysis A: Chemical*. **2003**, *199*(1-2), 39-47.

[67] Reske, R.; Mistry, H.; Behafarid, F.; Roldan Cuenya, B.; Strasser, P. Particle size effects in the catalytic electroreduction of $CO_2$ on Cu nanoparticles. *Journal of the American Chemical Society*. **2014**, *136*(19), 6978-6986.

[68] Tang, W.; Peterson, A. A.; Varela, A. S.; Jovanov, Z. P.; Bech, L.; Durand, W. J.; ... Chorkendorff, I. The importance of surface morphology in controlling the selectivity of polycrystalline copper for $CO_2$ electroreduction. *Physical Chemistry Chemical Physics*. **2012**, *14*(1), 76-81.

[69] Zhong, H.; Qiu, Y.; Zhang, T.; Li, X.; Zhang, H.; Chen, X. Bismuth nanodendrites as a high performance electrocatalyst for selective conversion of $CO_2$ to formate. *Journal of Materials Chemistry A*. **2016**, *4*(36), 13746-13753.

[70] Lv, W.; Zhou, J.; Bei, J.; Zhang, R.; Wang, L.; Xu, Q.; Wang, W. Electrodeposition of nano-sized bismuth on copper foil as electrocatalyst for reduction of $CO_2$ to formate. *Applied Surface Science*. **2017**, *393*, 191-196.

[71] Zhang, H.; Ma, Y.; Quan, F.; Huang, J.; Jia, F.; Zhang, L. Selective electro-reduction of $CO_2$ to formate on nanostructured Bi from reduction of BiOCl nanosheets. *Electrochemistry Communications*. **2014**, *46*, 63-66.

[72] Zhang, X.; Lei, T.; Liu, Y.; Qiao, J. Enhancing $CO_2$ electrolysis to formate on facilely synthesized Bi catalysts at low overpotential. *Applied Catalysis B: Environmental*. **2017**, *218*, 46-50.

[73] Qiu, Y.; Du, J.; Dong, W.; Dai, C.; Tao, C. Selective conversion of $CO_2$ to formate on a size tunable nano-Bi electrocatalyst. *Journal of $CO_2$ Utilization*. **2017**, *20*, 328-335.

[74] Bei, J.; Zhang, R.; Chen, Z.; Lv, W.; Wang, W. Efficient reduction of $CO_2$ to formate Using in situ prepared nano-sized Bi electrocatalyst. *Int. J. Electrochem. Sci*. **2017**, *12*, 2365-2375.

[75] Kim, S.; Dong, W. J.; Gim, S.; Sohn, W.; Park, J. Y.; Yoo, C. J.; ... Lee, J. L. Shape-controlled bismuth nanoflakes as highly selective catalysts for electrochemical carbon dioxide reduction to formate. *Nano Energy*. **2017**, *39*, 44-52.

[76] Qiu, Y.; Du, J.; Dai, C.; Dong, W.; Tao, C. Bismuth Nano-Flowers as a Highly Selective Catalyst for Electrochemical Reduction of $CO_2$ to Formate. *Journal of The Electrochemical Society*. **2018**, *165*(10), H594-H600.

[77] Zhang, X.; Hou, X.; Zhang, Q.; Cai, Y.; Liu, Y.; Qiao, J. Polyethylene glycol induced reconstructing Bi nanoparticle size for stabilized $CO_2$ electroreduction to formate. *Journal of Catalysis*. **2018**, *365*, 63-70.

[78] Han, N.; Wang, Y.; Yang, H.; Deng, J.; Wu, J.; Li, Y.; Li, Y. Ultrathin bismuth nanosheets from in situ topotactic transformation for selective electrocatalytic $CO_2$ reduction to formate. *Nature Communications*. **2018**, *9*(1), 1320.

[79] Yadav, V. S. K.; Purkait, M. K. Synthesis of $Pb_2O$ electrocatalyst and its application in the electrochemical reduction of $CO_2$ to HCOOH in various electrolytes. *RSC Advances*. **2015**, *5*(50), 40414-40421.

[80] Bashir, S. M.; Hossain, S. S.; ur Rahman, S.; Ahmed, S.; Hossain, M. M. NiO/MWCNT catalysts for electrochemical reduction of $CO_2$. *Electrocatalysis*. **2015**, *6*(6), 544-553.

[81] Gao, S.; Jiao, X.; Sun, Z.; Zhang, W.; Sun, Y.; Wang, C.; ... Liang, L. Ultrathin $Co_3O_4$ layers realizing optimized $CO_2$ electroreduction to formate. *Angewandte Chemie International Edition*. **2016**, *55*(2), 698-702.

[82] Asadi, M.; Kumar, B.; Behranginia, A.; Rosen, B. A.; Baskin, A.; Repnin, N.; ... Klie, R. F. Robust carbon dioxide reduction on molybdenum disulphide edges. *Nature Communications*. **2014**, *5*, 4470.

[83] Asadi, M.; Kim, K.; Liu, C.; Addepalli, A. V.; Abbasi, P.; Yasaei, P.; ... Zapol, P. Nanostructured transition metal dichalcogenide electrocatalysts for $CO_2$ reduction in ionic liquid. *Science*. **2016**, *353*(6298), 467-470.

[84] Kim, S. K.; Zhang, Y. J.; Bergstrom, H.; Michalsky, R.; Peterson, A. Understanding the low-overpotential production of $CH_4$ from $CO_2$ on $Mo_2C$ Catalysts. *ACS Catalysis*. **2016**, *6*(3), 2003-2013.

[85] Kumar, B.; Asadi, M.; Pisasale, D.; Sinha-Ray, S.; Rosen, B. A.; Haasch, R.; ... Salehi-Khojin, A. Renewable and metal-free carbon nanofibre catalysts for carbon dioxide reduction. *Nature Communications*. **2013**, *4*, 2819.

[86] Li, W.; Seredych, M.; Rodríguez‐Castellón, E.; Bandosz, T. J. Metal-free Nanoporous Carbon as a Catalyst for Electrochemical Reduction of $CO_2$ to CO and $CH_4$. *ChemSusChem*. **2016**, *9*(6), 606-616.

[87] Zhang, W., Hu, Y., Ma, L., Zhu, G., Wang, Y., Xue, X., ... Jin, Z. Progress and perspective of electrocatalytic $CO_2$ reduction for renewable carbonaceous fuels and chemicals. *Advanced Science*. **2018**, *5*(1), 1700275.

[88] Costentin, C.; Drouet, S.; Robert, M.; Savéant, J. M. A local proton source enhances $CO_2$ electroreduction to CO by a molecular Fe catalyst. *Science*. **2012**, *338*(6103), 90-94.

[89] Huan, T. N.; Andreiadis, E. S.; Heidkamp, J.; Simon, P.; Derat, E.; Cobo, S.; ... Artero, V. From molecular copper complexes to composite electrocatalytic materials for selective reduction of $CO_2$ to formic acid. *Journal of Materials Chemistry A*. **2015**, *3*(7), 3901-3907.

[90] Machan, C. W.; Sampson, M. D.; Kubiak, C. P. A molecular ruthenium electrocatalyst for the reduction of carbon dioxide to CO and formate. *Journal of the American Chemical Society*. **2015**, *137*(26), 8564-8571.

[91] Reuillard, B.; Ly, K. H.; Rosser, T. E.; Kuehnel, M. F.; Zebger, I.; Reisner, E. Tuning product selectivity for aqueous $CO_2$ reduction with a Mn (bipyridine)-pyrene catalyst immobilized on a carbon nanotube electrode. *Journal of the American Chemical Society*. **2017**, *139*(41), 14425-14435.

[92] Donovan, E. S.; Barry, B. M.; Larsen, C. A.; Wirtz, M. N.; Geiger, W. E.; Kemp, R. A. Facilitated carbon dioxide reduction using a Zn (II) complex. *Chemical Communications*. **2016**, *52*(8), 1685-1688.

[93] Zhao, C.; Yin, Z.; Wang, J. Efficient Electrochemical Conversion of $CO_2$ to HCOOH Using Pd-polyaniline/CNT Nanohybrids Prepared in Situ. *ChemElectroChem*. **2015**, *2*(12), 1974-1982.

[94] Girardi, M.; Blanchard, S.; Griveau, S.; Simon, P.; Fontecave, M.; Bedioui, F.; Proust, A. Electro-assisted reduction of $CO_2$ to CO and formaldehyde by $(TOA)_6[\alpha\text{-}SiW_{11}O_{39}Co(OH_2)]$ polyoxometalate. *European Journal of Inorganic Chemistry*. **2015**, (22), 3642-3648.

[95] Guo, S. X.; Li, F.; Chen, L.; MacFarlane, D. R.; Zhang, J. Polyoxometalate-Promoted Electrocatalytic $CO_2$ Reduction at Nanostructured Silver in Dimethylformamide. *ACS Applied Materials & Interfaces*. **2018**, *10*(15), 12690-12697.

[96] Guo, S. X.; Zhang, Y.; Zhang, X.; Easton, C. D.; MacFarlane, D. R.; Zhang, J. Phosphomolybdic Acid-Assisted Growth of Ultrathin Bismuth Nanosheets for Enhanced Electrocatalytic Reduction of $CO_2$ to Formate. *ChemSusChem*. **2019**, *12*(5), 1091-1100.

[97] Bard, A. J. Photoelectrochemistry. *Science*. **1980**, *207*(4427), 139-144.

[98] Fujishima, A.; Honda, K. Electrochemical photolysis of water at a semiconductor electrode. *Nature*. **1972**, *238*(5358), 37.

[99] Brugnera, M. F.; Rajeshwar, K.; Cardoso, J. C.; Zanoni, M. V. B. Bisphenol A removal from wastewater using self-organized $TiO_2$ nanotubular array electrodes. *Chemosphere*. **2010**, *78*(5), 569-575.

[100] Paschoal, F. M. M.; Nuñez, L.; de Vasconcelos Lanza, M. R.; Zanoni, M. V. B. Nitrate removal on a $Cu/Cu_2O$ photocathode under UV irradiation and bias potential. *Journal of Advanced Oxidation Technologies*. **2013**, *16*(1), 63-70.

[101] Chang, X.; Wang, T.; Yang, P.; Zhang, G.; Gong, J. The Development of Cocatalysts for Photoelectrochemical $CO_2$ Reduction. *Advanced Materials*. **2018**, 1804710.

[102] Gao, Y.; Zhang, S.; Bu, X.; Tian, Y. Surface defect engineering via acid treatment improving photoelectrocatalysis of $\beta\text{-}In_2S_3$ nanoplates for water splitting. *Catalysis Today*. **2019**, *327*, 271-278.

[103] Faraji, M.; Yousefi, M.; Yousefzadeh, S.; Zirak, M.; Naseri, N.; Jeon, T. H.; ... Moshfegh, A. Z. Two-dimensional materials in semiconductor photoelectrocatalytic systems for water splitting. *Energy & Environmental Science*. **2019**, *12*(1), 59-95.

[104] White, J. L.; Baruch, M. F.; Pander III, J. E.; Hu, Y.; Fortmeyer, I. C.; Park, J. E.; ... Shaw, T. W. Light-driven heterogeneous reduction of carbon dioxide: photocatalysts and photoelectrodes. *Chemical Reviews*. **2015**, *115*(23), 12888-12935.

[105] Wang, W. N.; Soulis, J.; Yang, Y. J.; Biswas, P. Comparison of $CO_2$ photoreduction systems: a review. *Aerosol Air Qual. Res*. **2014**, *14*(2), 533-549.

[106] Xie, S.; Zhang, Q.; Liu, G.; Wang, Y. Photocatalytic and photoelectrocatalytic reduction of $CO_2$ using heterogeneous catalysts with controlled nanostructures. *Chemical Communications*. **2016**, *52*(1), 35-59.

[107] Kumar, B.; Llorente, M.; Froehlich, J.; Dang, T.; Sathrum, A.; Kubiak, C. P. Photochemical and photoelectrochemical reduction of $CO_2$. *Annual Review of Physical Chemistry*. **2012**, *63*, 541-569.

[108] Tu, W.; Zhou, Y.; Zou, Z. Photocatalytic conversion of $CO_2$ into renewable hydrocarbon fuels: state-of-the-art accomplishment, challenges, and prospects. *Advanced Materials*. **2014**, *26*(27), 4607-4626.

[109] Van de Krol, R. Principles of photoelectrochemical cells. *In Photoelectrochemical hydrogen production*. Springer, Boston, MA. **2012**, p. 13-67.

[110] Chu, S.; Li, W.; Yan, Y.; Hamann, T.; Shih, I.; Wang, D.; Mi, Z. Roadmap on solar water splitting: current status and future prospects. *Nano Futures*. **2017**, *1*(2), 022001.

[111] Peter, L. M.; Upul Wijayantha, K. G. Photoelectrochemical water splitting at semiconductor electrodes: fundamental problems and new perspectives. *ChemPhysChem*. **2014**, *15*(10), 1983-1995.

[112] Kalamaras, E.; Maroto-Valer; M. M.; Shao, M.; Xuan, J.; Wang, H. Solar carbon fuel via photoelectrochemistry. *Catalysis Today*. **2018**, *317*, 56-75.

[113] Joe, J.; Yang, H.; Bae, C.; Shin, H. Metal Chalcogenides on Silicon Photocathodes for Efficient Water Splitting: A Mini Overview. *Catalysts*. **2019**, *9*(2), 149.

[114] Joe, J., Bae, C., Kim, E., Ho, T. A., Yang, H., Park, J. H., Shin, H. Mixed-Phase (2H and 1T) $MoS_2$ Catalyst for a Highly Efficient and Stable Si Photocathode. *Catalysts*. **2018**, *8*(12), 580.

[115] Thorne, J. E.; Li, S.; Du, C.; Qin, G.; Wang, D. Energetics at the surface of photoelectrodes and its influence on the photoelectrochemical properties. *The Journal of Physical Chemistry Letters*. **2015**, *6*(20), 4083-4088.

[116] Berglund, S. P., Abdi, F. F., Bogdanoff, P., Chemseddine, A., Friedrich, D., van de Krol, R. Comprehensive evaluation of $CuBi_2O_4$ as a photocathode material for photoelectrochemical water splitting. *Chemistry of Materials*. **2016**, *28*(12), 4231-4242.

[117] Harraz, F. A.; Sakka, T.; Ogata, Y. H. A comparative electrochemical study of iron deposition onto n- and p-type porous silicon prepared from lightly doped substrates. *Electrochimica Acta*. **2005**, *50*(27), 5340-5348.

[118] Babenko, S. D.; Balakai, A. A.; Lavrushko, A. G.; Moskvin, Y. L.; Shamaev, S. N. Kinetic analysis of photoelectrochemical hydrogen evolution over p-type silicon in acidic aqueous solutions of electrolytes. *Russian Chemical Bulletin*. **2000**, *49*(10), 1707-1711.

[119] Babenko, S. D.; Balakai, A. A.; Lavrushko, A. G.; Ponomarev, E. A.; Simbirtseva, G. V. Kinetics of the photoelectrochemical evolution of hydrogen at p-type Si. *Journal of Electroanalytical Chemistry*. **1995**, *382*(1-2), 175-177.

[120] Schlichthörl, G.; Ponomarev, E. A.; Peter, L. M. An Investigation of Hydrogen Evolution at p-Si by Intensity Modulated Photocurrent Spectroscopy and Photomodulated Microwave Reflectivity. *Journal of the Electrochemical Society*. **1995**, *142*(9), 3062-3067.

[121] De Mierry, P.; Etcheberry, A.; Rizk, R.; Etchegoin, P.; Aucouturier, M. Defects Induced in p-Type Silicon by Photocathodic Charging of Hydrogen. *Journal of The Electrochemical Society*. **1994**, *141*(6), 1539-1546.

[122] Hwang, Y. J.; Boukai, A.; Yang, P. High density n-Si/n-$TiO_2$ core/shell nanowire arrays with enhanced photoactivity. *Nano Letters*. **2008**, *9*(1), 410-415.

[123] Lewis, N. S. A Quantitative Investigation of the Open - Circuit Photovoltage at the Semiconductor/Liquid Interface. *Journal of The Electrochemical Society*. **1984**, *131*(11), 2496-2503.

[124] Schlichthörl, G.; Ponomarev, E. A.; Peter, L. M. An Investigation of Hydrogen Evolution at p-Si by Intensity Modulated Photocurrent Spectroscopy and Photomodulated Microwave Reflectivity. *Journal of the Electrochemical Society*. **1995**, *142*(9), 3062-3067.

[125] Sun, K.; Kargar, A.; Park, N.; Madsen, K. N.; Naughton, P. W.; Bright, T.; ... Wang, D. Compound semiconductor nanowire solar cells. *IEEE Journal of Selected Topics in Quantum Electronics*. **2011**, *17*(4), 1033-1049.

[126] Boettcher, S. W.; Spurgeon, J. M.; Putnam, M. C.; Warren, E. L.; Turner-Evans, D. B.; Kelzenberg, M. D.; ... Lewis, N. S. Energy-conversion properties of vapor-liquid-solid-grown silicon wire-array photocathodes. *Science*. **2010**, *327*(5962), 185-187.

[127] Higashi, G. S.; Chabal, Y. J.; Trucks, G. W.; Raghavachari, K. Ideal hydrogen termination of the Si (111) surface. *Applied Physics Letters*. **1990**, *56*(7), 656-658.

[128] Yang, J.; Wang, D.; Han, H.; Li, C. Roles of cocatalysts in photocatalysis and photoelectrocatalysis. *Accounts of Chemical Research*. **2013**, *46*(8), 1900-1909.

[129] McCrory, C. C.; Jung, S.; Ferrer, I. M.; Chatman, S. M.; Peters, J. C.; Jaramillo, T. F. Benchmarking hydrogen evolving reaction and oxygen evolving reaction electrocatalysts for solar water splitting devices. *Journal of the American Chemical Society*. **2015**, *137*(13), 4347-4357.

[130] Hou, Y.; Abrams, B. L.; Vesborg, P. C.; Björketun, M. E.; Herbst, K.; Bech, L.; ... Rossmeisl, J. Bioinspired molecular co-catalysts bonded to a silicon photocathode for solar hydrogen evolution. *Nature Materials*. **2011**, *10*(6), 434.

[131] Boettcher, S. W.; Warren, E. L.; Putnam, M. C.; Santori, E. A.; Turner-Evans, D.; Kelzenberg, M. D.; ... Lewis, N. S. Photoelectrochemical hydrogen evolution using Si microwire arrays. *Journal of the American Chemical Society*. **2011**, *133*(5), 1216-1219.

[132] Esposito, D. V.; Levin, I.; Moffat, T. P.; Talin, A. A. $H_2$ evolution at Si-based metal-insulator-semiconductor photoelectrodes enhanced by inversion channel charge collection and H spillover. *Nature Materials*. **2013**, *12*(6), 562.

[133] Ji, L.; McDaniel, M. D.; Wang, S.; Posadas, A. B.; Li, X.; Huang, H.; ... Edward, T. Y. A silicon-based photocathode for water reduction with an epitaxial $SrTiO_3$ protection layer and a nanostructured catalyst. *Nature Nanotechnology*. **2015**, *10*(1), 84.

[134] Berglund, S. P.; He, H.; Chemelewski, W. D.; Celio, H.; Dolocan, A.; Mullins, C. B. p-Si/$W_2C$ and p-Si/$W_2C$/Pt photocathodes for the hydrogen evolution reaction. *Journal of the American Chemical Society*. **2014**, *136*(4), 1535-1544.

[135] Zhao, J.; Cai, L.; Li, H.; Shi, X.; Zheng, X. Stabilizing silicon photocathodes by solution-deposited Ni–Fe layered double hydroxide for efficient hydrogen evolution in alkaline media. *ACS Energy Letters*. **2017**, *2*(9), 1939-1946.

[136] Leung, J. J.; Warnan, J.; Nam, D. H.; Zhang, J. Z.; Willkomm, J.; Reisner, E. Photoelectrocatalytic $H_2$ evolution in water with molecular catalysts immobilised on p-Si via a stabilising mesoporous $TiO_2$ interlayer. *Chemical Science*. **2017**, *8*(7), 5172-5180.

[137] Downes, C. A.; Marinescu, S. C. Efficient electrochemical and photoelectrochemical $H_2$ production from water by a cobalt dithiolene one-dimensional metal-organic surface. *Journal of the American Chemical Society*. **2015**, *137*(43), 13740-13743.

[138] McKone, J. R.; Warren, E. L.; Bierman, M. J.; Boettcher, S. W.; Brunschwig, B. S.; Lewis, N. S.; Gray, H. B. Evaluation of Pt, Ni, and Ni–Mo electrocatalysts for hydrogen evolution on crystalline Si electrodes. *Energy & Environmental Science*. **2011**, *4*(9), 3573-3583.

[139] Zhang, H.; Ding, Q.; He, D.; Liu, H.; Liu, W.; Li, Z.; ... Jin, S. A p-Si/NiCoSe$_x$ core/shell nanopillar array photocathode for enhanced photoelectrochemical hydrogen production. *Energy & Environmental Science*. **2016**, *9*(10), 3113-3119.

[140] Basu, M.; Zhang, Z. W.; Chen, C. J.; Chen, P. T.; Yang, K. C.; Ma, C. G.; ... Liu, R. S. Heterostructure of Si and $CoSe_2$: A Promising Photocathode Based on a Non‐noble Metal Catalyst for Photoelectrochemical Hydrogen Evolution. *Angewandte Chemie International Edition*. **2015**, *54*(21), 6211-6216.

[141] Chen, C. J.; Chen, P. T.; Basu, M.; Yang, K. C.; Lu, Y. R.; Dong, C. L.; ... Liu, R. S. An integrated cobalt disulfide ($CoS_2$) co-catalyst passivation layer on silicon microwires for photoelectrochemical hydrogen evolution. *Journal of Materials Chemistry A*. **2015**, *3*(46), 23466-23476.

[142] Aurian-Blajeni, B.; Taniguchi, I.; JO'M, B. Photoelectrochemical reduction of carbon dioxide using polyaniline-coated silicon. *Journal of Electroanalytical Chemistry and Interfacial Electrochemistry*. **1983**, *149*(1-2), 291-293.

[143] Hinogami, R.; Nakamura, Y.; Yae, S.; Nakato, Y. Modification of semiconductor surface with ultrafine metal particles for efficient photoelectrochemical reduction of carbon dioxide. *Applied Surface Science*. **1997**, *121*, 301-304.

[144] Hinogami, R.; Nakamura, Y.; Yae, S.; Nakato, Y. An approach to ideal semiconductor electrodes for efficient photoelectrochemical reduction of carbon dioxide by modification with small metal particles. *The Journal of Physical Chemistry B*. **1998**, *102*(6), 974-980.

[145] Yang, K. D.; Ha, Y.; Sim, U.; An, J.; Lee, C. W.; Jin, K.; ... Lee, H. E. Graphene quantum sheet catalyzed silicon photocathode for selective $CO_2$ conversion to CO. *Advanced Functional Materials*. **2016**, *26*(2), 233-242.

[146] Song, J. T.; Ryoo, H.; Cho, M.; Kim, J.; Kim, J. G.; Chung, S. Y.; Oh, J. $CO_2$ Reduction: Nanoporous Au Thin Films on Si Photoelectrodes for Selective and Efficient Photoelectrochemical $CO_2$ Reduction (Adv. Energy Mater. 3/2017). *Advanced Energy Materials*. **2017**, *7*(3), 1601103.

[147] Hu, Y.; Chen, F.; Ding, P.; Yang, H.; Chen, J.; Zha, C.; Li, Y. Designing effective Si/Ag interface via controlled chemical etching for photoelectrochemical $CO_2$ reduction. *Journal of Materials Chemistry A*. **2018**, *6*(44), 21906-21912.

[148] Kumar, B.; Smieja, J. M.; Kubiak, C. P. Photoreduction of $CO_2$ on p-type Silicon Using Re(bipy-But)$(CO)_3$Cl: Photovoltages Exceeding 600 mV for the Selective Reduction of $CO_2$ to CO. *The Journal of Physical Chemistry C*. **2010**, *114*(33), 14220-14223.

[149] Torralba-Peñalver, E.; Luo, Y.; Compain, J. D.; Chardon-Noblat, S.; Fabre, B. Selective Catalytic Electroreduction of $CO_2$ at Silicon Nanowires (SiNWs) Photocathodes Using Non-Noble Metal-Based Manganese Carbonyl Bipyridyl Molecular Catalysts in Solution and Grafted onto SiNWs. *ACS Catalysis*. **2015**, *5*(10), 6138-6147.

# Chapter 2. Polyoxothiometalate-Derivatized Silicon Photocathodes for Sunlight-Driven Hydrogen Evolution Reaction

## 2.1 Introduction

The solar production of hydrogen from the photoelectrochemical reduction of protons has been essentially motivated by the actual growing need for sustainable sources of high-density energies. [1,2,3] In this thematic area of solar fuels, silicon, with an energy gap of 1.12 eV,[4] is a very promising material to be used as a photocathode for the hydrogen evolution reaction (HER) because of its abundance, nontoxicity, and its tunable electronic properties.[5,6] This material fails however to promote efficient multielectron transfers due to slow charge transfer kinetics.[6,7] Consequently, deposition of pure metals (the archetypal example is platinum),[6,8,9,10] metal oxides,[11,12] or sulfides[13,14,15,16,17,18,19,20,21,22] onto silicon has been demonstrated to be an effective way to overcome intrinsic limitations of this semiconducting photocathode material for HER.[23]

In that context, silicon derivatized with molybdenum sulfide-based complexes, such as molybdenum disulfide and derivatives ($MoS_x$) [15,16,18,19,20,21,22] or bioinspired cuboidal molecular clusters incorporating the $[Mo_3S_4]^{4+}$ core,[13,14] have been explored as cheap and abundant alternatives to Pt and the resulting photocathodes were found to exhibit high catalytic efficiency for sunlight-driven HER in acid electrolytes. Interestingly, $\{Mo_3S_4\}$-based clusters offer rich coordination chemistry able to tune structural, redox and chemical reactivity, thus giving the access to a wide range of combinations and properties.[24,25,26,27] For instance, over the past decade, the development of synthetic strategies to access hybrid polyoxothiometalates including the $\{Mo_3S_4\}$ core within polyoxometalates framework (POMs) has been engaged.[28,29] The novelty of these systems lies on the combination at the molecular level of an identified active unit *i.e*. the $\{Mo_3S_4\}$ core with POM subunit behaving as electron reservoirs, *i.e*. the POM framework. Due to their high nuclearity, POMs can undergo multi-electron processes making them ideal candidates for engineering complex multi-step redox systems (from HER to $CO_2$ reduction). [30,31] Moreover, as POMs are highly functionalizable, and generally robust enough to retain their structural integrity during the redox process, we anticipate that such systems coupled to silicon should provide effective and robust photocathodes for sunlight-driven HER. Furthermore, these photocathodes should exhibit enhanced long-term stability compared with that observed for electrodes integrating uncoupled $\{Mo_3S_4\}$ coordination complexes. Indeed, it has been reported that the latter ones were susceptible to be degraded in the presence of traces of $O_2$ in the electrolytic solution.[13]

Herein, silicon photocathodes decorated with $\{Mo_3S_4\}$-based assemblies incorporating polyoxotungstate $\{AsW_{12}O_{42}\}$ matrix are demonstrated to be effective for sunlight-driven HER under acid pH conditions. Such photocathodes showed a superior catalytic activity and a better robustness compared with photocathodes modified with $\{Mo_3S_4\}$ clusters bearing an organic ligand such as butyl-acetylacetonate ligand (noted acac-Bu, hereafter). Moreover, we here investigate the structural and

chemical changes at these surfaces that occur during cathodic polarization and that were found to considerably improve the catalytic activity of the photocathodes as well as their stability.

## 2.2 Results and Discussion

### 2.2.1 Characterization of the molecular precursors

2.2.1.1 Molecular structure of $[Mo_3S_4(acac\text{-}Bu)_3(H_2O)_3]Cl\bullet H_2O$

Summary of crystallographic data are given in **Table 2-1**. The single-crystal X-ray diffraction analysis of $Mo_3S_4(acac\text{-}Bu)$ revealed the discrete core $\{Mo_3S_4\}$ coordinated to three butyl-acetylacetonate ligands (acac-Bu) (**Figure 2-1**). The coordination of the acac-Bu ligands takes place at the six equivalent equatorial sites of the Mo centers while three aquo ligands were found to be attached to the Mo centers at the axial sites. Geometrical parameters (bond lengths and angles) within the coordination complex were found usual as those previously reported for analogue $\{Mo_3S_4\}$-containing complexes.[32] Nevertheless, the acac-Bu derivative of the triangular cluster $\{Mo_3S_4\}$ exhibits a striking structural feature corresponding to the relative disposition of the three butyl alkyl chains which run in parallel along the $C_3$ axis of the cluster (**Figure 2-1b**). Such structural characteristics allow distinguishing clearly hydrophilic polar region, corresponding to the $\{Mo_3S_4(H_2O)_3\}$ part while the three butyl alkyl chains, arranged as pillars, delimit the hydrophobic domain. Then, amphiphilic behavior could be expected from such a cationic assembly which could be easily tuned depending on the length of the alkyl chains. Such studies are still ongoing progress.

| Compound | **3a** | *V*, Å$^3$ | 5997(2) |
|---|---|---|---|
| Formula | $Mo_3S_4C_{27}H_{54}O_{10,5}Cl$ | *Z* | 6 |
| *FW*, g.mol$^{-1}$ | 998,21 | $\rho_{calc}$, g.cm$^{-3}$ | 1,658 |
| *T*, K | 200(2) | $\mu$(Mo Kα), mm$^{-1}$ | 1,25 |
| crystal size (mm) | 0.30x0.18x0.10 | $\lambda$(Mo Kα), Å | 0.71073 |
| crystal system | hexagonal | $\theta$ range, deg | 1,1-30,0 |
| space group | *P6$_3$/m* | data collected | 234587 |
| *a*, Å | 20,702(2) | unique data | 6014 |
| *b*, Å | 20,702(2) | unique data $I > 2\sigma(I)$ | 5395 |
| *c*, Å | 16,158 (2) | no. Parameters | 227 |
| α, deg | 60 | $R(F)^a$ | 0,052 |
| $\beta$, deg | 120 | $R_w(F^2)^b$ | 1,164 |
| $\gamma$, deg | 90 | GOF | 1,20 |

**Table 2-1:** Summary of the crystallographic data for $[Mo_3S_4(acac\text{-}Bu)_3(H_2O)_3]Cl\bullet H_2O$

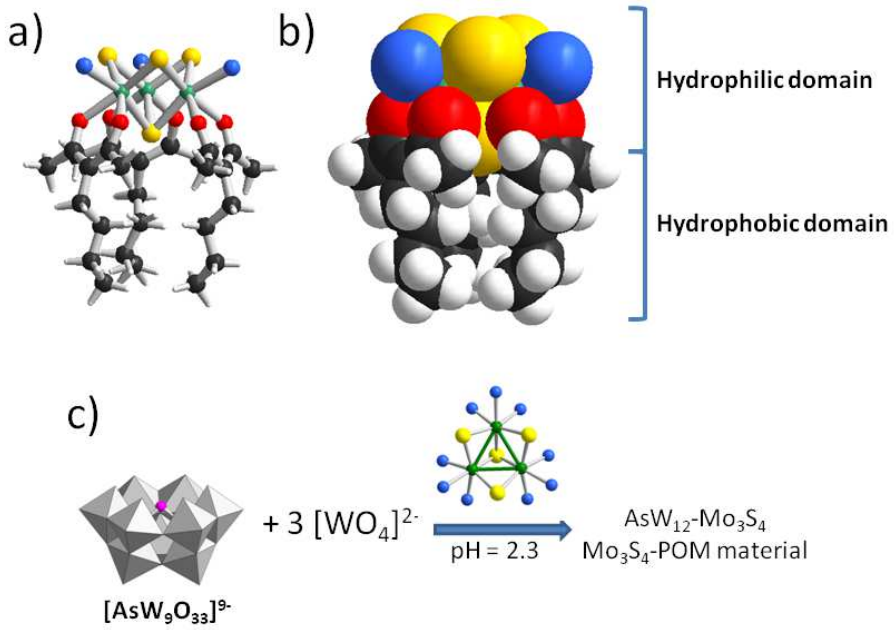


**Figure 2-1:** Ball and stick (a) and space-filling (b) structural representations of the $\{Mo_3S_4(H_2O)_3(acac\text{-}Bu)_3\}^+$ cationic unit (color code: green sphere = Mo; yellow sphere = S; red sphere = O; blue sphere = aquo ligand; black sphere = C and white sphere = H) showing the hydrophobic part clearly separated from the hydrophilic domain. c) Scheme of synthesis applied for the preparation of the $Mo_3S_4$-POM material resulting from the acidic condensation of tungstate (pH = 2.3) on the trivacant precursor $[AsW_9O_{33}]^{9-}$ in the presence of the $[Mo_3S_4(H_2O)_9]^{4+}$ aqua cluster.

### 2.2.1.2 $Mo_3S_4$-POM materials

The cationic cluster $\{Mo_3S_4\}^{4+}$ exhibits a high propensity to be incorporated as triangular unit within polyoxometalate framework. This is an elegant way to associate covalently the catalytic $\{Mo_3S_4\}$ component to an electron reservoir unit. $\{Mo_3S_4\}$-POM material was obtained as mixed rubidium-sodium salt from condensation processes of three equivalents of $WO_4^{2-}$ tungstate ions on the trivacant precursor $[AsW_9O_{33}]^{9-}$ anion in the presence of $[Mo_3S_4(H_2O)_9]^{4+}$ at pH 2.3 (**Figure 2-1c**). The resulting solid retains the elemental composition $Rb_3NaHAsW_{12}Mo_3S_4(H_2O)_3O_{42}\bullet 14H_2O$, consistent with the molecular unit $[AsW_{12}Mo_3S_4(H_2O)_3O_{42}]^{5-}$. The solid, as well the resulting aqueous solution exhibit the dark-brown color, featuring the coordination of the $\{Mo_3S_4\}$ core to the oxo group of the POM.[29] Thus, UV-vis spectrum (**Figure 2-2**) showed the characteristic weak absorption at 600 nm ($\varepsilon$ = 520 $cm^{-1}$ $mol^{-1}$ L) attributed to *d-d* transitions of the $Mo^{IV}$ centers. Furthermore, IR spectrum of $Mo_3S_4$-POM contains the main absorption related to the polyoxotungstate framework. The vibration band at 950 $cm^{-1}$ is attributed to the $\nu_{as}$(W=O) mode, while those observed at 850 and 798 $cm^{-1}$ are assigned to bridging $\nu_{as}$(W-O-W) modes.[33,34] Analysis of the IR spectrum of the $Mo_3S_4$-POM appears rather consistent with

saturated metal-oxo framework with regard to wavenumber range of the $\nu_{as}$(W-O-W) modes. Vacant polyoxometalates give rise to IR vibrations below 800 $cm^{-1}$. Such a result is consistent with the acidic conditions applied for the synthesis procedure (pH = 2.3) which preclude formation of any lacunary species. At last, $Mo_3S_4$-POM compound has been characterized by $^{183}W$ NMR spectroscopy. The $^{183}W$ NMR spectrum (**Figure 2-2**) shows a complex pattern consisting of more than twenty $^{183}W$ resonances in the -100/-200 ppm chemical shift range differing in their linewidth and relative intensity.[35] This result evidences that $Mo_3S_4$-POM solid contains a mixture of molecular species which could be isomers or which could differ slightly by their $W/Mo_3S_4$ ratio. Nevertheless, the observed resonances exhibit chemical shifts fully consistent with $W^{VI}$ centers in octahedral oxo environments. The cationic exchange process from alkali to tetra-*n*-hexylammonium salts alters neither the POM composition nor the IR spectrum (**Figure 2-2**).

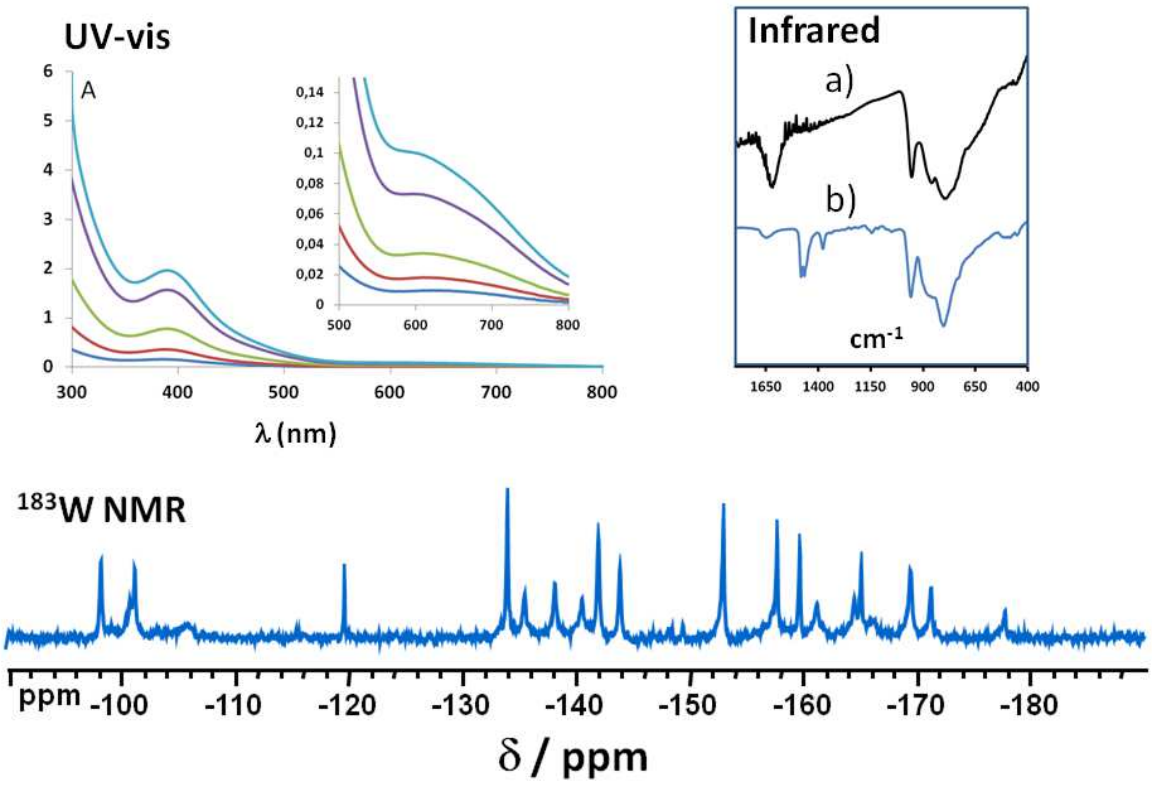


**Figure 2-2:** Spectroscopic characterization of the $Mo_3S_4$-POM material: UV-vis spectra of the $Rb_3NaHAsW_{12}Mo_3S_4(H_2O)_3O_{42}$ compound in aqueous solution carried out in $1\times10^{-4}$ - $2\times10^{-3}$ mol $L^{-1}$ concentration range. FTIR spectra of a) $Rb_3NaHAsW_{12}Mo_3S_4(H_2O)_3O_{42}$ and b) $(THA)_6AsW_{12}Mo_3S_4(H_2O)_3O_{42}$ (THA = tetra-*n*-hexylammonium). $^{183}W$ NMR spectrum of $Mo_3S_4$-POM as Li salt in saturated $D_2O$ solution.

### 2.2.2 Optimization of the catalyst-modified photocathodes for sunlight-driven HER

Before investigating the photoelectrocatalytic properties of the best photocathodes, a preliminary electrochemical study has been carried out in order to determine the optimal cluster loading leading to maximum catalytic activity. Toward this goal, three cluster loadings [namely, $7.2 \times 10^{-6}$, $3.6 \times 10^{-5}$ and $7.2 \times 10^{-5}$ mmol $cm^{-2}$ of $Mo_3S_4$(acac-Bu) or $Mo_3S_4(AsW_{12})$] have been tested for the deposition by drop-casting of the catalyst films onto Si(100)-H. The photoelectrochemical response of the freshly modified surfaces was then examined as a function of the nature and the amount of the deposited catalyst. As expected, no appreciable reduction current was measured in the dark for all electrodes. As shown in **Figure 2-3**, the first cyclic voltammetry scans of $Mo_3S_4$(acac-Bu)- and $Mo_3S_4(AsW_{12})$-modified Si(100) photocathodes in 1.0 M $H_2SO_4$ (pH 0.3) and under simulated sunlight (AM 1.5G, 100 mW $cm^{-2}$) revealed a broad and irreversible cathodic pre-peak within the range -0.3/-0.1 V vs RHE, followed by the higher HER photocurrent. It must be pointed out that this cathodic pre-peak was absent in the following scans and stable sigmoidal photocurrent curves showing the catalytic HER wave were usually obtained after two scans for all tested catalysts and concentrations (**Figure 2-4**). The disappearance of such a cathodic pre-peak has been previously observed by Jaramillo et al.[36] and Tran et al.[37] for $[Mo_3S_4]^{4+}$ and $[Mo_3S_{13}]^{2-}$ cluster-modified surfaces, respectively. It is consistent with either the irreversible conversion of the deposited film into a new material which is the active form of the catalyst or the cathodic desorption of the cluster into the electrolytic solution, as also proposed by Kristensen et al.[38] In this work, AFM and XPS measurements provide strong experimental evidence that these two events occurred concomitantly upon the electrochemical reduction of the modified photocathodes (*vide infra*). In the first event, we can thus hypothesize that the reduction of Mo(IV) to Mo(III) is accompanied by the replacement of $S^{2-}$ sulfido ligands in the cluster by oxo $O^{2-}$ groups leading to the formation of mixed O/S mixed valence core $\{Mo(IV)_{3-x}Mo(III)_xO_{4-n}S_n\}^{(4-x)+}$, as evidenced by post-electrochemistry XPS analysis (*vide infra*) and electrochemical measurements of the complexes in solution at a conventional glassy carbon electrode (**Figure 2-5**). For the latter, the observed Mo(IV)/Mo(III) reduction potential was very close to that previously reported for analogous $[Mo_3S_4]^{4+}$-based clusters.[39] At pH 7.3, this cathodic pre-peak was either much less intense for the $Mo_3S_4$(acac-Bu)-modified electrode or no longer observed for the immobilized catalyst $Mo_3S_4(AsW_{12})$ (**Figure 2-6**).

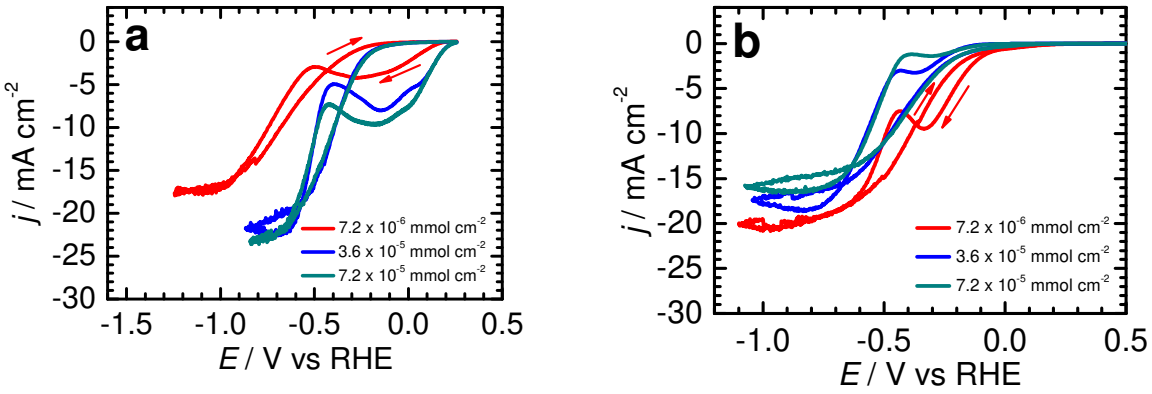


**Figure 2-3:** Light-Assisted HER at pH 0.3. First cyclic voltammetry scans at 20 mV $s^{-1}$ of $Mo_3S_4$(acac-Bu) (a) and $Mo_3S_4(AsW_{12})$ (b) modified Si(100) photocathodes (AM 1.5G, 100 mW $cm^{-2}$) in 1.0 mol $L^{-1}$ $H_2SO_4$, for different initial cluster loadings.

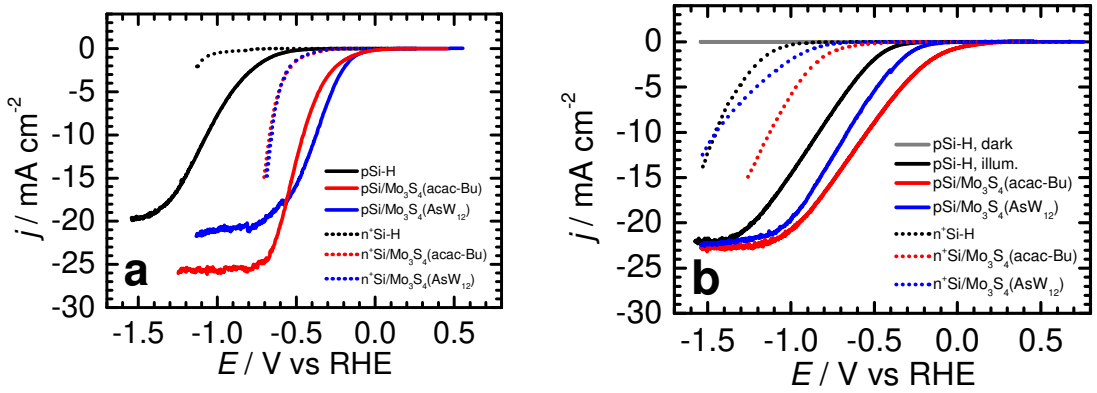


**Figure 2-4:** Photoelectrochemical HER at pH 0.3 (a) and 7.3 (b). *iR*-uncorrected LSVs at 20 mV $s^{-1}$ of optimized catalyst-modified *p*-type Si(100) photocathodes under simulated sunlight (AM 1.5G, 100 mW $cm^{-2}$) in 1.0 mol $L^{-1}$ $H_2SO_4$ (a) and 0.1 mol $L^{-1}$ KCl + 0.5 mol $L^{-1}$ $KHCO_3$ (b). For comparison, LSVs of modified $n^+$-type Si(100) surfaces in the dark are also shown. The initial cluster loading was 7.2 × $10^{-5}$ mmol $cm^{-2}$ for $Mo_3S_4$(acac-Bu) and 7.2 × $10^{-6}$ mmol $cm^{-2}$ for $Mo_3S_4(AsW_{12})$.

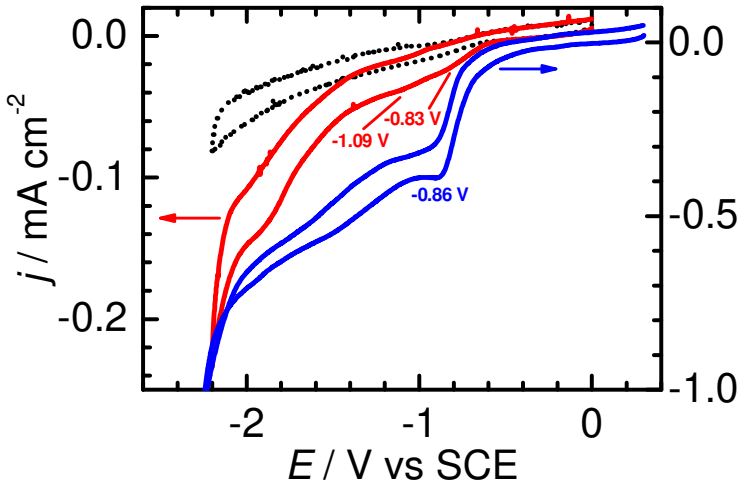


**Figure 2-5:** Cyclic voltammograms at 20 mV $s^{-1}$ of $[Mo_3S_4(acac\text{-}Bu)_3(H_2O)_3]Cl$, n $H_2O$ at 0.2 mM (red trace) and $[(n\text{-}C_6H_{13})_4N]_5[(Mo_3S_4)(AsW_{12}O_{42})]$ at 0.5 mM (blue trace) onto glassy carbon electrode in $CH_3CN$ + 0.1 mol $L^{-1}$ $Bu_4NClO_4$. The dotted black trace corresponds to the response of the glassy carbon electrode in the absence of the cluster.

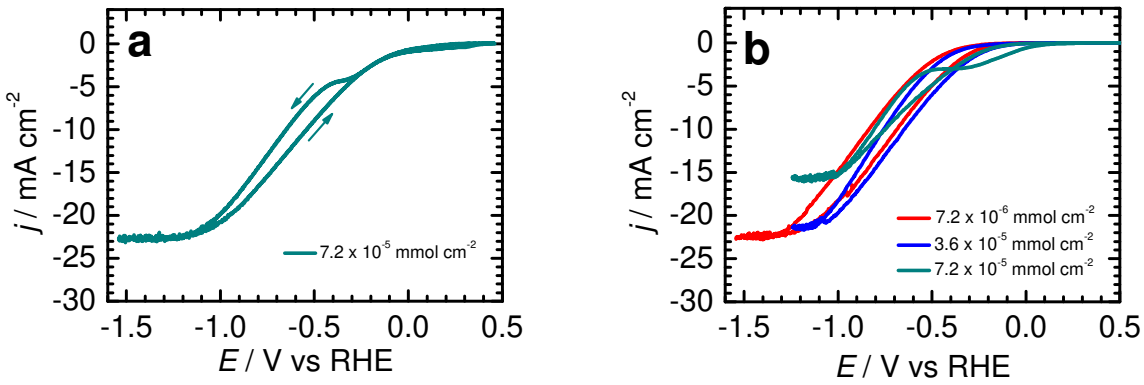


**Figure 2-6:** Light-Assisted HER at pH 7.3. First cyclic voltammetry scans at 20 mV $s^{-1}$ of $Mo_3S_4$(acac-Bu) (a) and $Mo_3S_4(AsW_{12})$ (b) modified Si(100) photocathodes (AM 1.5G, 100 mW $cm^{-2}$) in 0.1 mol $L^{-1}$ KCl + 0.5 mol $L^{-1}$ $KHCO_3$, for different initial cluster loadings.

Considering the stabilized catalytic response of the photocathodes, it can be emphasized that surfaces prepared from $Mo_3S_4$(acac-Bu) and $Mo_3S_4(AsW_{12})$ loadings of $7.2 \times 10^{-5}$ and $7.2 \times 10^{-6}$ mmol $cm^{-2}$, respectively, provided the highest photocurrent densities combined to lowest onset potentials (**Figure 2-4**). At pH 0.3, the $Mo_3S_4(AsW_{12})$ cluster was found to be catalytically superior to $Mo_3S_4$(acac-Bu) at low overpotentials (above -0.5 V vs RHE) as the resulting photocathode showed a higher onset potential (-0.02 V vs RHE against -0.04 V) and a lower overvoltage at 10 mA $cm^{-2}$ (0.37 V against 0.45 V, corresponding to 0.18 V against 0.36 V when the cell resistance was compensated) (**Figure 2-7**). For potentials more negative than -0.5 V vs RHE, the $Mo_3S_4$(acac-Bu)-modified photocathode yielded higher photocurrent densities probably owing to a higher amount of deposited catalyst. Compared with Si(100)-H illuminated under similar conditions, the decrease in the overpotential for HER measured at 10 mA $cm^{-2}$ was approximately 700-740 mV and 560-620 mV (whether Ohmic drop was corrected or not) for the $Mo_3S_4(AsW_{12})$- and $Mo_3S_4$(acac-Bu)-modified photocathodes, respectively.

Focusing on the potential necessary to reach a current density of 10 mA $cm^{-2}$ as an electrode activity metric, the *iR*-corrected value determined for the photocathode modified with $Mo_3S_4(AsW_{12})$ is well in line with 180-200 mV values reported for highly active $(Mo_3S_{13})^{2-}$. [40, 41, 42] $MoS_2$ nanomaterials deposited on planar substrates (e.g. FTO and glassy carbon) exhibited a lower activity for HER as these catalysts achieved 10 mA $cm^{-2}$ at ~200-250 mV overpotentials.[40] Not surprisingly, $MoS_2$ deposited on high surface area electrodes (graphene oxide, carbon fiber paper and carbon nanotubes) demonstrated excellent activity characterized by an only 110-150 mV overpotential.[40, 43, 44, 45, 46]

Moreover, from the difference between the onset potentials of the non-photoactive modified $n^+$-type Si (**Figures 2-4** and **2-8**) and illuminated *p*-type Si electrodes, it can be deduced that the semiconductor produces a photovoltage of 0.30 V when the deposited catalyst is $Mo_3S_4(AsW_{12})$ and 0.27 V when the catalyst is $Mo_3S_4$(acac-Bu). Both values are however smaller than that determined for Si(100)-H (i.e. 0.37 V), as a result of enhanced recombination of photogenerated charge carriers.

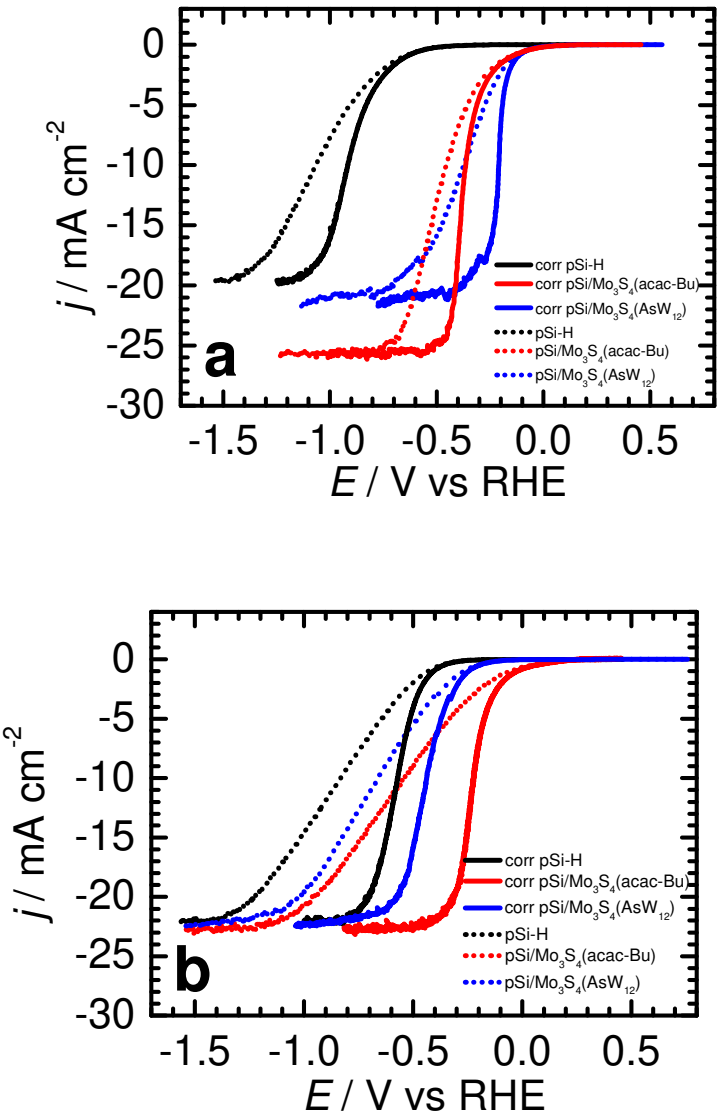


**Figure 2-7:** Effect of the *iR* compensation on the LSVs at 20 mV $s^{-1}$ of unmodified and catalyst-modified *p*-type Si(100) photocathodes under simulated sunlight (AM 1.5G, 100 mW $cm^{-2}$) in 1.0 mol $L^{-1}$ $H_2SO_4$ (a) and 0.1 mol $L^{-1}$ KCl + 0.5 mol $L^{-1}$ $KHCO_3$ (b). *iR*-uncorrected (dashed traces) and corrected (solid traces) LSVs. The initial cluster loading was $7.2 \times 10^{-5}$ mmol $cm^{-2}$ for $Mo_3S_4$(acac-Bu) and $7.2 \times 10^{-6}$ mmol $cm^{-2}$ for $Mo_3S_4(AsW_{12})$.

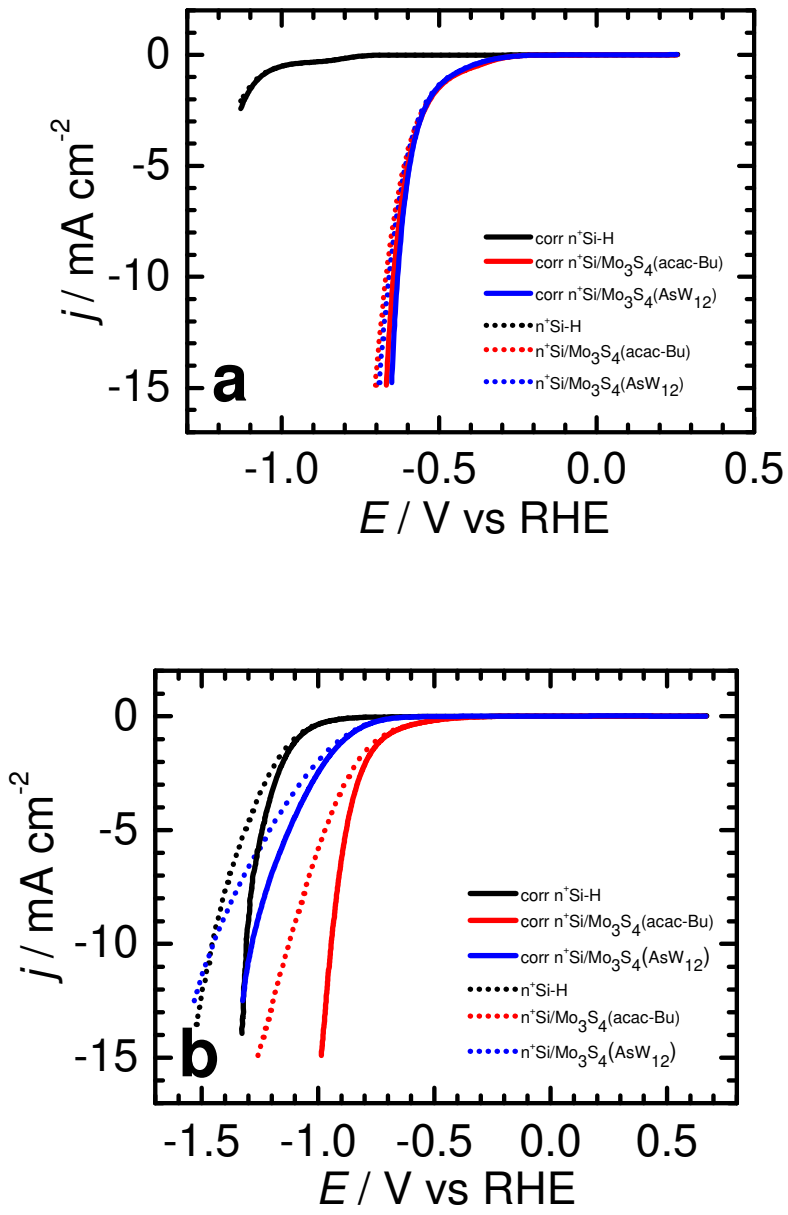


**Figure 2-8:** Effect of the *iR* compensation on the LSVs at 20 mV $s^{-1}$ of unmodified and catalyst-modified $n^+$-type Si(100) photocathodes in the dark in 1.0 mol $L^{-1}$ $H_2SO_4$ (a) and 0.1 mol $L^{-1}$ KCl + 0.5 mol $L^{-1}$ $KHCO_3$ (b). *iR*-uncorrected (dashed traces) and corrected (solid traces) LSVs. The initial cluster loading was 7.2 × $10^{-5}$ mmol $cm^{-2}$ for $Mo_3S_4$(acac-Bu) and 7.2 × $10^{-6}$ mmol $cm^{-2}$ for $Mo_3S_4(AsW_{12})$.

At pH 7.3, the catalytic performance of the $Mo_3S_4(AsW_{12})$-modified photocathode was found to be lower than that of $Mo_3S_4$(acac-Bu)-modified photocathode irrespective of the examined potential range, as supported by a lower onset potential (-0.18 V against +0.11 V) and a higher overpotential at 10 mA $cm^{-2}$ (0.66 V against 0.54 V, corresponding to 0.44 V against 0.22 V when the cell resistance was compensated) (**Table 2-2**). Moreover, the difference between the onset potentials of the non-photoactive modified $n^+$-type Si and illuminated *p*-type Si electrodes yielded clearly abnormally high photovoltage values, exceeding 0.60 V for both types of photocathodes. More reasonable values ranging from 0.22 to 0.45 V were determined when $n^+$-type Si electrodes were replaced by more conventional glassy carbon ones (**Figure 2-9**). Such results could be partly explained by differences in the catalyst-support interactions and/or surface energetics[47] of $n^+$ and *p*-doped Si at neutral pH.

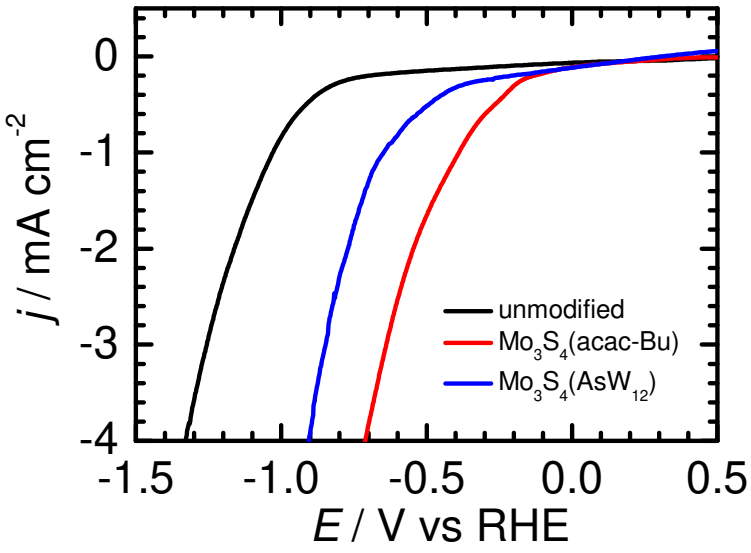


**Figure 2-9:** *iR*-uncorrected LSVs at 20 mV $s^{-1}$ of unmodified and catalyst-modified glassy carbon electrodes in 0.1 mol $L^{-1}$ KCl + 0.5 mol $L^{-1}$ $KHCO_3$ (pH 7.3). The initial cluster loading was $7.2 \times 10^{-5}$ mmol $cm^{-2}$ for $Mo_3S_4$(acac-Bu) and $7.2 \times 10^{-6}$ mmol $cm^{-2}$ for $Mo_3S_4(AsW_{12})$.

| Cathode | Onset potential / $V_{RHE}$ [b] | $E$ ($E_{corr}$) / $V_{RHE}$ at -10 mA $cm^{-2}$ [c] | $\Delta E_{ons}$/ V [d] | $j_L$ / mA $cm^{-2}$ [e] |
|---|---|---|---|---|
| **pH 0.3** | | | | |
| ***p*Si-H** | -0.52 | -1.07 (-0.92) | 0.37 | -19.9 |
| ***p*Si/$Mo_3S_4$(acac-Bu)** | -0.04 | -0.45 (-0.36) | 0.27 | -25.8 |
| ***p*Si/$Mo_3S_4$($AsW_{12}$)** | -0.02 | -0.37 (-0.18) | 0.30 | -21.5 |
| ***n*$^+$Si-H** [f] | -0.89 | < -1.30 | | |
| ***n*$^+$Si/$Mo_3S_4$(acac-Bu)** [f] | -0.31 | -0.65 (-0.64) | | |
| ***n*$^+$Si/$Mo_3S_4$($AsW_{12}$)** [f] | -0.32 | -0.68 (-0.63) | | |
| **pH 7.3** | | | | |
| ***p*Si-H** | -0.32 | -0.84 (-0.57) | 0.66 (0.45) | -22.0 |
| ***p*Si/$Mo_3S_4$(acac-Bu)** | +0.11 | -0.54 (-0.22) | 0.71 (0.30) | -22.7 |
| ***p*Si/$Mo_3S_4$($AsW_{12}$)** | -0.18 | -0.66 (-0.44) | 0.64 (0.22) | -22.3 |
| ***n*$^+$Si-H** [f] | -0.98 | -1.46 (-1.31) | | |
| ***n*$^+$Si/$Mo_3S_4$(acac-Bu)** [f] | -0.60 | -1.25 (-0.94) | | |
| ***n*$^+$Si/$Mo_3S_4$($AsW_{12}$)** [f] | -0.82 | -1.45 (-1.28) | | |

**TABLE 2-2:** Performances of the bare and catalyst-modified Si(100) electrodes for simulated sunlight-assisted HER at pH 0.3 and 7.3.[a]

[a] Determined from stable photocurrent-potential curves. [b] Determined for a current density of 0.25 mA $cm^{-2}$. [c] Between parentheses, *iR*-corrected potential values. [d] Difference between onset potentials of illuminated *p*-type and dark $n^+$-type electrodes. Between parentheses (pH 7.3), values obtained when dark $n^+$-type electrodes were replaced by glassy carbon ones. [e] Plateau current density corresponding to the light-limited catalytic current. [f] In the dark.

### 2.2.3 Electrochemistry-induced structural changes

The chemical composition and the morphology of the as-deposited and electrochemically reduced cluster films were examined by means of X-ray photoelectron spectroscopy (XPS) and atomic force microscopy (AFM). First, XPS measurements have been performed on the two types of optimized photocathodes to gain insights about the composition and molecular structure of the as-deposited films and about the nature of the catalytically active species. With the main carbon C 1s peak set at 285.0 eV, the characteristics peaks related to the cluster core are observed.

The freshly prepared $Mo_3S_4$(acac-Bu)-modified surface shows the main Mo $3d_{5/2}$ and Mo $3d_{3/2}$ lines at 230.3 and 233.4 eV, respectively, which are consistent with a molybdenum in the formal 4+ state (**Figures 2-10** and **2-11**). [48] Additionally, two minor components of Mo 3d are observed at 231.9 and 235.1 eV, which can be ascribed to Mo(+4) atoms in a different local environment, as previously reported by Jaramillo et al.[36] The presence of sulfur is evidenced by the S 2s signal at 226.6 eV. The S 2p region shows a main peak at 162.6 eV corresponding to unresolved contributions of $2p_{1/2}$ and $2p_{3/2}$ doublet of $S^{2-}$ ligands. A second minor peak at 164.1 eV is also observed which suggests the concomitant presence of $S_2^{2-}$ groups. Such observations are in perfect line with previous reports of molybdenum sulfide materials, which incorporate sulfur atoms in different oxidation states. [49,50] The experimental ratio between the areas under the Mo and S peaks is estimated at 0.75, as theoretically expected. Moreover, the C 1s spectrum shows a main component at 285.0 eV and a shoulder at 286.8 eV which are attributed to C-C and C=O bonds of the (acac-Bu) ligand, respectively. The corresponding C-C/C-O peak area ratio of 3.8 was also fully consistent with the expected atomic composition of the acac-Bu ligand (i.e. 7/2).

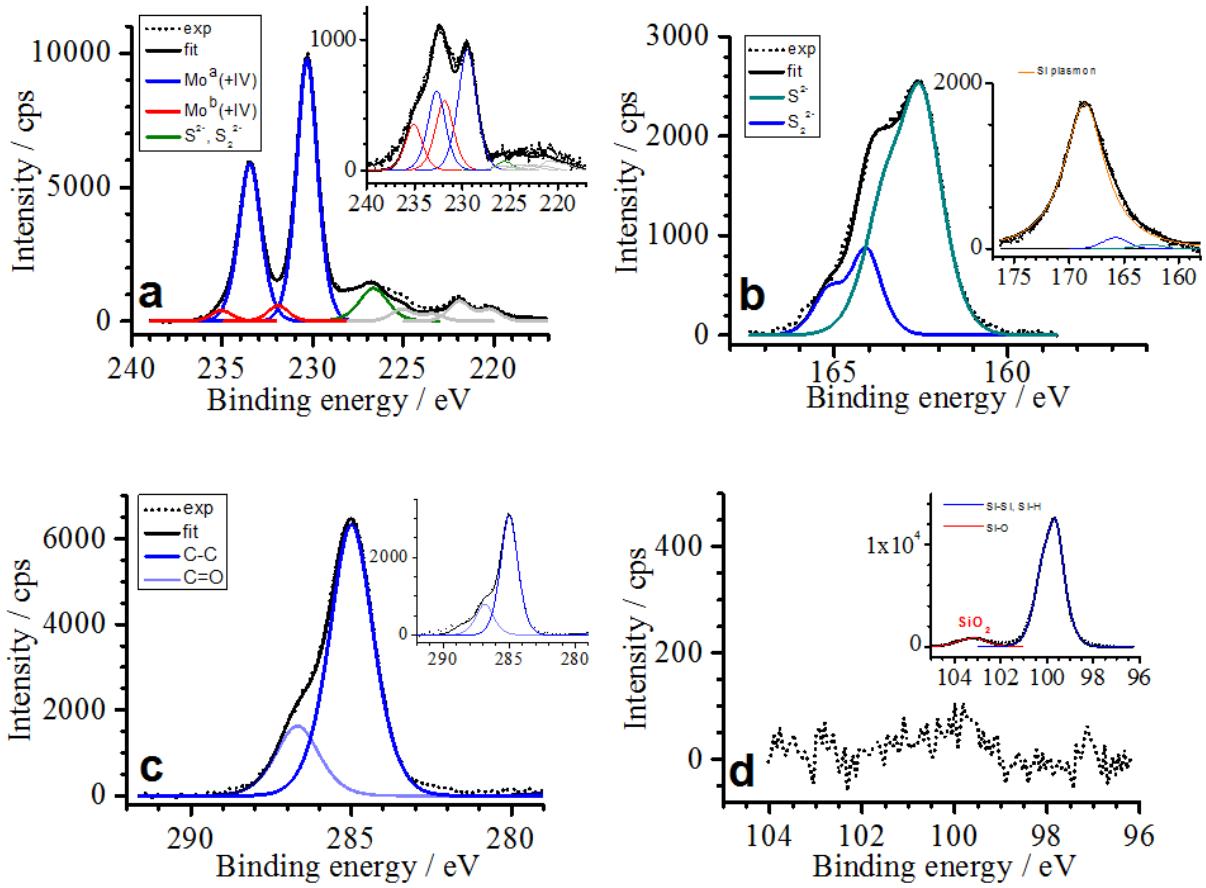


**Figure 2-10:** Mo 3d and S 2s (a), S 2p (b), C 1s (c) and Si 2p (d) high-resolution XPS spectra of the freshly prepared $Mo_3S_4$(acac-Bu)-modified surface before and after cathodic electrolysis at -0.84 V vs RHE for 2 h under simulated sunlight (insets). The peaks observed below 225 eV (highlighted in gray) are attributed to satellite peaks of the used XPS source. Experimental data and fitting envelopes are represented by black dotted and continuous lines, respectively. The colored lines are fitted curves using Gaussian-Lorentzian mixed peaks corresponding to different components. The initial cluster loading was $7.2 \times 10^{-5}$ mmol $cm^{-2}$.

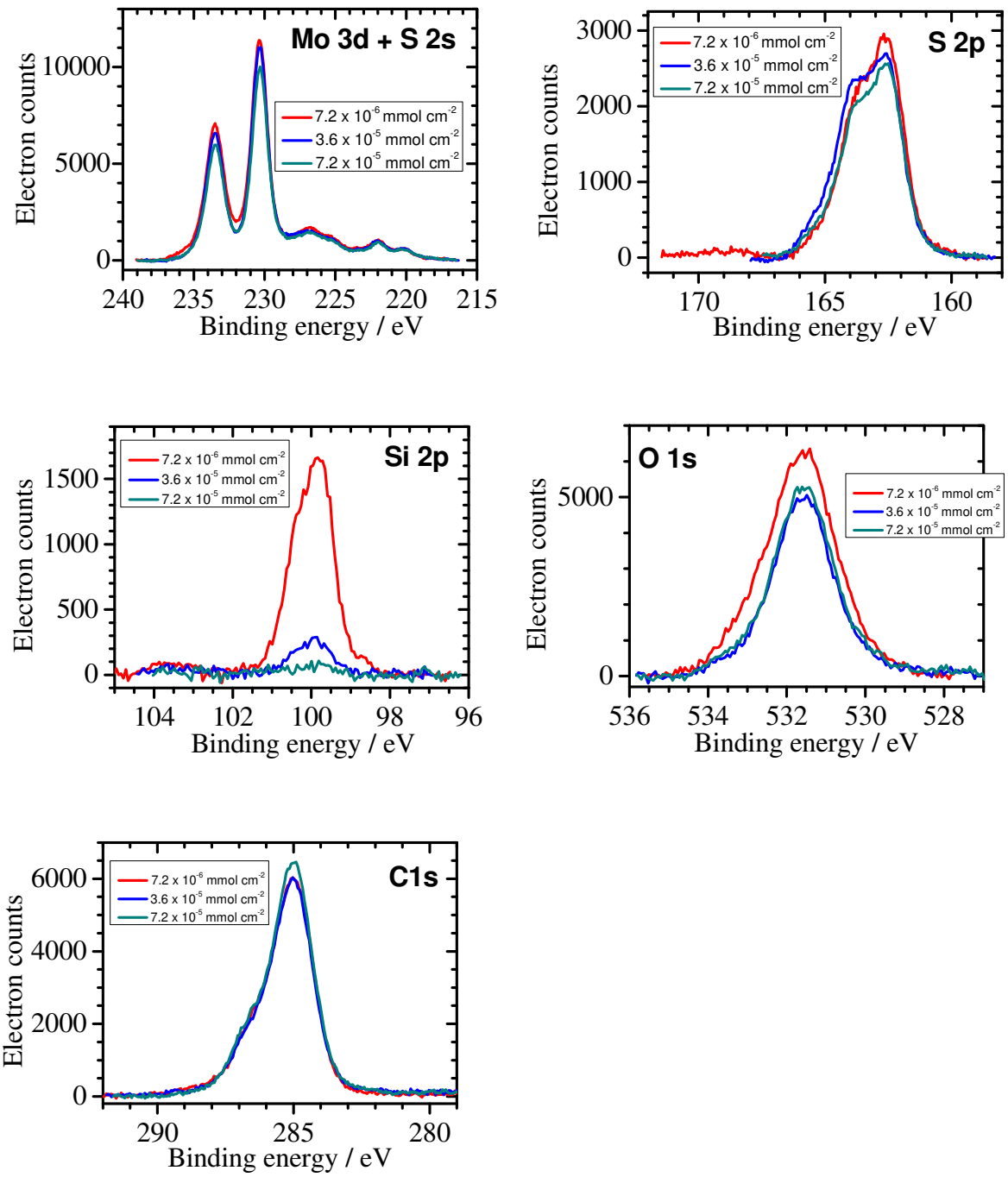


**Figure 2-11:** Experimental high-resolution XPS spectra showing the different characteristic atoms for the freshly prepared $Mo_3S_4$(acac-Bu)-modified Si(100) photocathodes, as a function of the initial cluster loading.

Now, for the freshly prepared $Mo_3S_4(AsW_{12})$-modified surface, the two Mo $3d_{5/2}$ peaks attributed to locally different Mo(4+) atoms are observed at 229.5 and 231.6 eV (**Figures 2-12** and **2-13**). Furthermore, the presence of $S^{2-}$ and $S_2^{2-}$ groups is also evidenced by the S 2s and S 2p signals at 226.6

and 161.9 eV, respectively. The ratio between the peak areas of the total Mo and S signals is 0.74, as theoretically expected. The W 4f and W 4d lines observed at 35.1 (W $4f_{7/2}$), 37.2 (W $4f_{5/2}$), 247.3 (W $4d_{5/2}$) and 259.9 (W $4d_{3/2}$) eV are consistent with W-O/W=O species involving tungsten in the formal 6+ state. [51, 52, 53] The experimental ratio Mo $3d_{5/2}$/W $4d_{3/2}$ is estimated at 0.23, in close agreement with the theoretical ratio (i.e. 0.25).

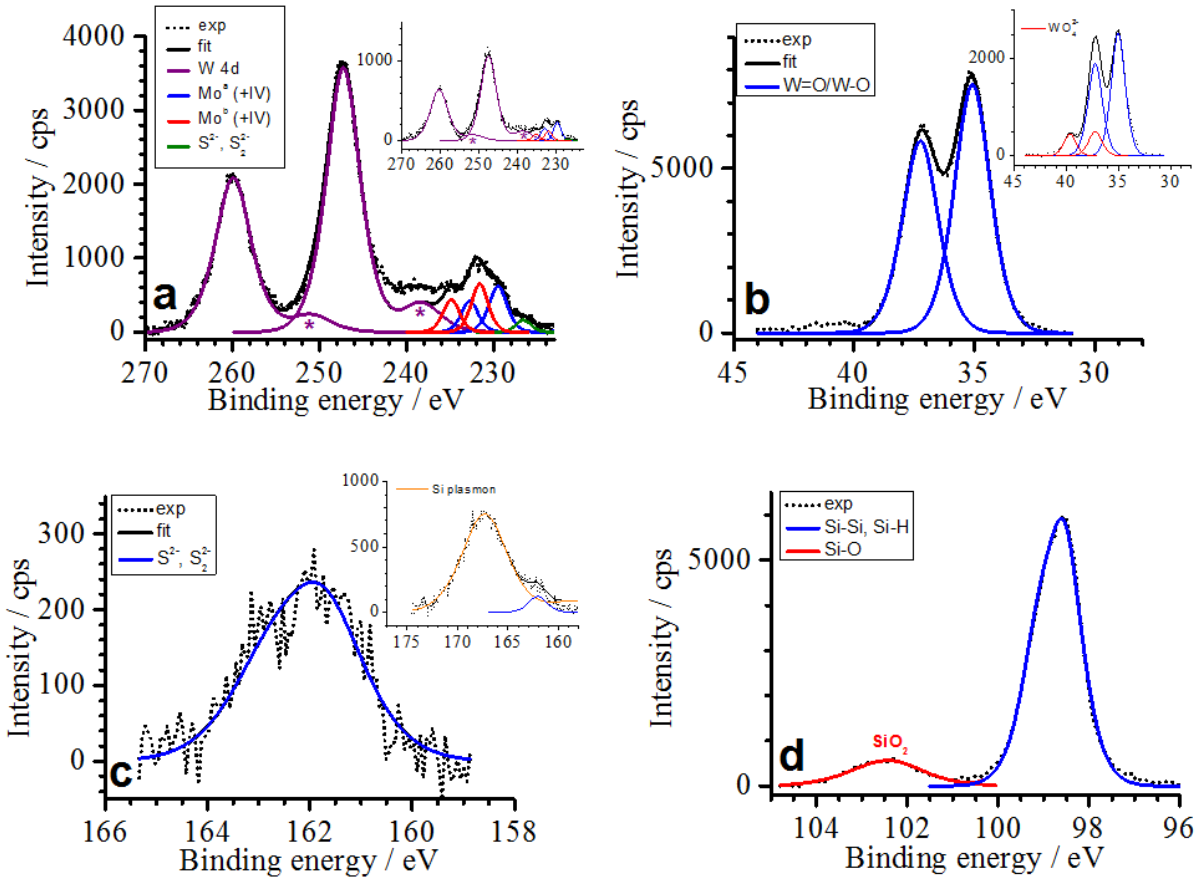


**Figure 2-12:** W 4d, Mo 3d and S 2s (a), W 4f (b) and S 2p (c) high-resolution XPS spectra of the freshly prepared $Mo_3S_4(AsW_{12})$-modified surface before and after cathodic electrolysis at -0.84 V vs RHE for 2 h under simulated sunlight (insets). Post-electrolysis Si 2p spectrum (d). The peaks observed at 238.3 and 251.1 eV (indicated by asterisks) are attributed to satellite peaks of the used XPS source. Experimental data and fitting envelopes are represented by black dotted and continuous lines, respectively. The colored lines are fitted curves using Gaussian-Lorentzian mixed peaks corresponding to different components. The initial cluster loading was $7.2 \times 10^{-6}$ mmol cm$^{-2}$.

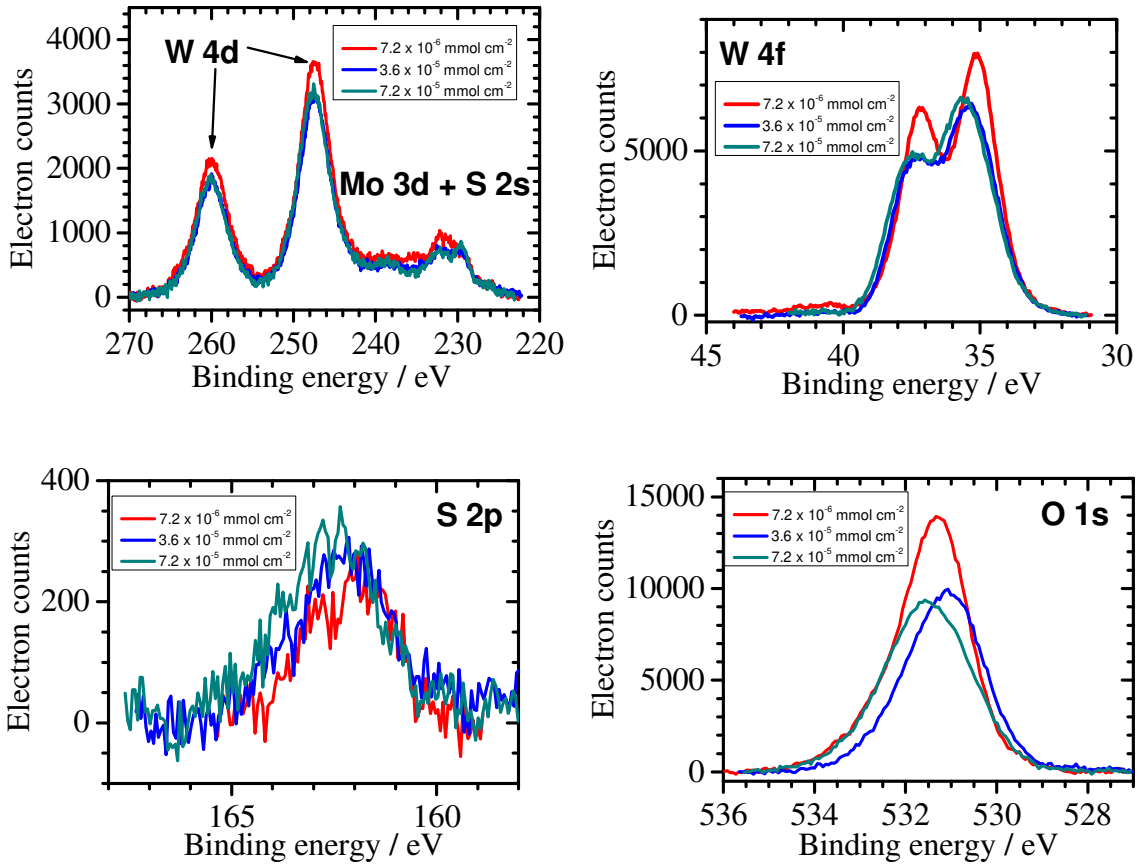


**Figure 2-13:** Experimental high-resolution XPS spectra showing the different characteristic atoms for the freshly prepared $Mo_3S_4(AsW_{12})$-modified Si(100) photocathodes, as a function of the initial cluster loading.

After cathodic electrolysis for 2 h with the deposited clusters, both the intensity and the position of the characteristic XPS signals were strongly modified. For both photocathodes, a large amount of the deposited material has been released into the electrolyte solution during the electrochemical test (about 90 and 70% for $Mo_3S_4$(acac-Bu)- and $Mo_3S_4(AsW_{12})$-modified surfaces, respectively), as confirmed by the dramatic decrease in the intensity of Mo 3d, W 4d, W 4f and S 2p XPS signals concomitantly with the appearance of both Si plasmon loss peak and Si 2p signal (insets in **Figures 2-10** and **2-12**). Such observations are in line with those reported for other $\{Mo_3S_4\}$-based cluster-modified surfaces.[13, 38] As a matter of fact, the $H_2$ bubbling at the surface of the photocathode provokes mechanical desorption of a large upper part of the immobilized layer which does not participate to the catalytic process. Moreover, the main Mo $3d_{5/2}$ and Mo $3d_{3/2}$ lines of the electrochemically reduced $Mo_3S_4$(acac-Bu)-modified surface were shifted to 229.4 and 232.6 eV which would be consistent with partial substitution of $S^{2-}$ sulfido ligands by $O^{2-}$ oxo groups in the metallic cluster. Such an assumption

is supported by XPS spectra of $[Mo_3O_{4-n}S_n]^{4+}$, [54] or refers to the presence of Mo(+III) in the cluster structure. [55] The Mo 3d component having the highest energy (assigned to Mo(+IV) atoms in a different local environment) was not affected by the electrolytic treatment, both in intensity and position. This leads to the hypothesis that this component could be the signature of the surface-confined, stable and catalytically active clusters. For the cathodically reduced $Mo_3S_4(AsW_{12})$-modified surface, the Mo 3d lines of the two components were only 0.3 eV-shifted towards more positive binding energies. Such a result would be rather consistent with a weaker lability of $S^{2-}$ ligands in the cluster incorporating the POM. Additionally, the W 4f spectrum shows an additional component at higher binding energies (37.2 and 39.6 eV for the $4f_{7/2}$ and $4f_{5/2}$ levels, respectively) that can be assigned to the formation of some tungstate species.[56] Finally, the Si 2p spectrum shows the presence of a substantial amount of Si oxides at about 102-103 eV for both cathodically reduced photocathodes. However, it could not be ruled that the oxidation of Si surface was either caused by the cathodic electrolysis or already present after the catalyst deposition since the Si 2p signal for the freshly prepared photocathodes was totally attenuated due to the thick catalyst layer.

From XPS data and using the treatment reported by Cicero et al.,[57] if one considers the Si(100) surface atom density of $6.8 \times 10^{14}$ atoms $cm^{-2}$,[58] the surface coverages of catalyst remaining after cathodic electrolysis can be estimated at $(8.0 \pm 0.5) \times 10^{13}$ $cm^{-2}$ and $(2.0 \pm 0.6) \times 10^{13}$ $cm^{-2}$ for the $Mo_3S_4$(acac-Bu)- and $Mo_3S_4(AsW_{12})$-modified photocathodes, respectively.

Electrochemistry-induced changes derived from XPS were also corroborated by the AFM analysis of the optimized photocathodes. After the catalyst deposition, both surfaces showed a rough and compact granular structure characterized by the presence of a few hundreds of nm-large agglomerates (**Figure 2-14**). The root-mean-square (rms) roughness was measured at ca. 6.0 ± 0.5 nm and 26.0 ± 2 nm for the $Mo_3S_4$(acac-Bu)- and $Mo_3S_4(AsW_{12})$-modified surfaces, respectively. After cathodic electrolysis, a much less dense array was observed with the presence of a few tens of nm-large catalyst aggregates and the surface of underlying Si became now visible. The rms roughness values were therefore considerably decreased and lower than 1.0 nm for both surfaces. The processing of AFM images yielded cluster surface density values of $(4.7 \pm 0.8) \times 10^{13}$ $cm^{-2}$ and $(6.4 \pm 0.8) \times 10^{12}$ $cm^{-2}$ for the $Mo_3S_4$(acac-Bu)- and $Mo_3S_4(AsW_{12})$-modified surfaces, respectively, considering the theoretical projected specific area of one cluster (**Figures 2-15** and **2-16**). Different reasons can be involved to explain such discrepancies between the cluster densities extracted from XPS and AFM data, especially for the $Mo_3S_4(AsW_{12})$-modified surface. AFM is believed to be a less reliable technique than XPS to estimate such a parameter essentially due to large uncertainties arising from (*i*) the calculation method based on the microscale analysis of the surface, (*ii*) the used processing method that is based on the

detection of a size threshold to determine the surface area covered by the cluster and (*iii*) differences between the experimental and theoretical specific areas occupied by the cluster.

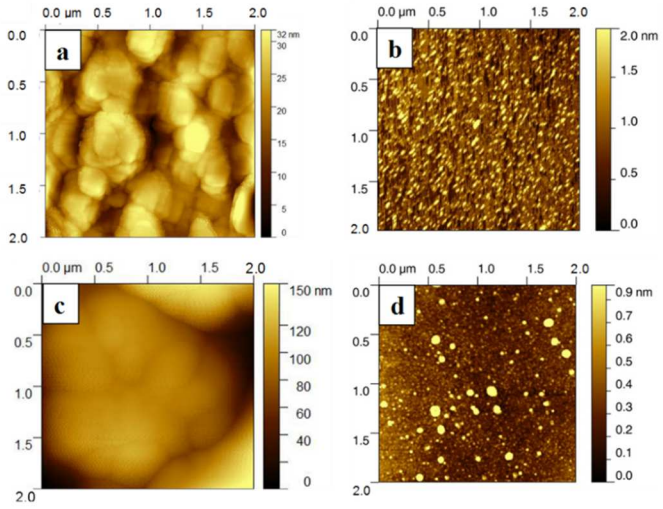


**Figure 2-14:** AFM images of $Mo_3S_4$(acac-Bu)- (a, b) and $Mo_3S_4(AsW_{12})$- (c, d) modified Si(100) surfaces before (a, c) and after cathodic electrolysis at -0.84 V vs RHE for 2 h under simulated sunlight (b, d). The initial cluster loading of optimized surfaces was $7.2 \times 10^{-5}$ mmol $cm^{-2}$ for $Mo_3S_4$(acac-Bu) and $7.2 \times 10^{-6}$ mmol $cm^{-2}$ for $Mo_3S_4(AsW_{12})$. Scan size: $2 \times 2$ $\mu m^2$.

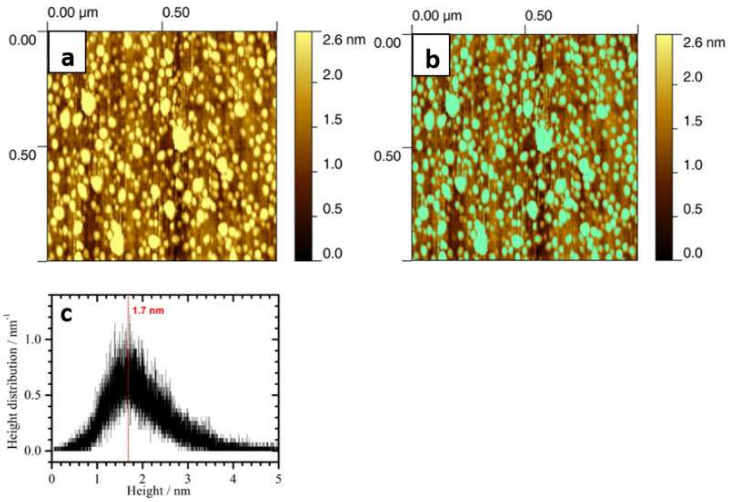


**Figure 2-15:** AFM image of the $Mo_3S_4$(acac-Bu)-modified Si(100) surface after cathodic electrolysis under simulated sunlight (a) and processed by the Gwyddion 2-34 software to determine the surface area covered by the cluster (b). (c) Corresponding mean height distribution. The initial cluster loading was $7.2 \times 10^{-5}$ mmol $cm^{-2}$. *The % surface area covered by $(Mo_3S_4)$(acac-Bu) can be estimated at 30 ± 5% (averaged on several images). If one considers that the theoretical projected specific area of one $(Mo_3S_4)$(acac-Bu) cluster is ca. $6.4 \times 10^{-15}$ $cm^2$ (diameter ~9 Å), the cluster density can thus be estimated at $(4.7 \pm 0.8) \times 10^{13}$ $cm^{-2}$. From XPS data, a value of $(8.0 \pm 0.5) \times 10^{13}$ $cm^{-2}$ was calculated.*

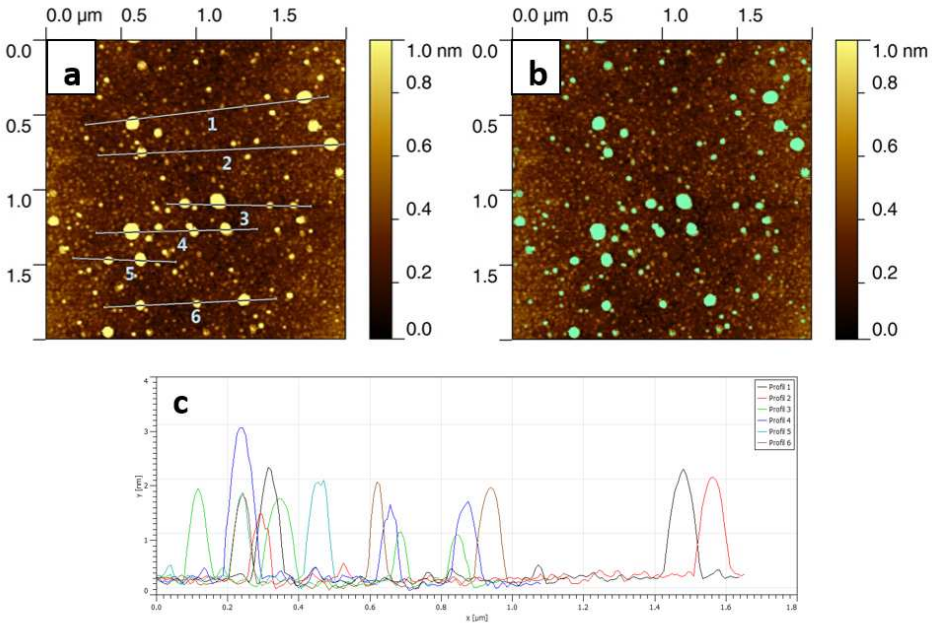


**Figure 2-16:** AFM image of the $Mo_3S_4(AsW_{12})$-modified Si(100) surface after cathodic electrolysis under simulated sunlight (a) and processed by the Gwyddion 2-34 software to determine the surface area covered by the cluster (b). The structure under the blue-colored spots corresponds to the rough structure of the underlying Si(100) surface (the mean rms roughness measured in different areas is about 0.7 Å which is close to 0.5 Å reported for Si(100)-H)[59]. (c) Cross-section profiles taken in different areas of the image, showing 1 to 2 nm-high features. The initial cluster loading was $7.2 \times 10^{-6}$ mmol $cm^{-2}$. *The % surface area covered by $(Mo_3S_4)(AsW_{12})$ can be estimated at 7 ± 1% (averaged on several images). If one considers that the theoretical projected specific area of one $(Mo_3S_4)(AsW_{12})$ cluster is ca. $1.1 \times 10^{-14}$ $cm^2$ (mean diameter ~ 12 Å), the cluster density can thus be estimated at $(6.4 \pm 0.8) \times 10^{12}$ $cm^{-2}$. From XPS data, a value of $(2.0 \pm 0.6) \times 10^{13}$ $cm^{-2}$ was calculated.*

### 2.2.4 Faradaic efficiency and turnover frequency (TOF) of the photocathodes for solar-driven HER

The cluster-supported photoelectrodes exhibiting the best electrocatalytic efficiencies [namely, those prepared from a cluster loading of $7.2 \times 10^{-5}$ mmol $cm^{-2}$ for $Mo_3S_4$(acac-Bu) or $7.2 \times 10^{-6}$ mmol $cm^{-2}$ for $Mo_3S_4(AsW_{12})$] were tested for more than 1 h in both electrolytic media under simulated sunlight. As shown in **Figure 2-17**, the photocurrent densities measured during the controlled-potential electrolysis tests were in quite good agreement with those derived from LSVs. Moreover, a careful examination of all chronoamperometric curves shows a short initial period (about 5 min) for which the cathodic current increases before stabilizing. This beneficial effect results probably from the loss of large amount of deposited clusters, as supported by the post-electrolysis XPS and AFM data (*vide supra*), leading to both a better light collection and higher conductivity at the solid-liquid interface.

At pH 0.3, the photocurrent densities measured for both photoelectrodes remained relatively stable during the electrolysis time (**Figure 2-17**). The amount of evolved $H_2$ was determined from the gas volume by measuring the amount of the electrolytic solution displaced in a sealed and graduated upside-down burette (Hoffman cell).[60] $H_2$ was quantitatively produced (Faradaic efficiency of 98 ± 2%) with a rate of 0.48 ± 0.02 mmol $cm^{-2}$ $h^{-1}$ irrespective of the nature of the tested cluster. At pH 7.3, both photocathodes were less stable but the production rate of $H_2$ was almost unchanged. Noticeably, the Faradaic efficiency for the photocathode incorporating $Mo_3S_4(AsW_{12})$ was higher than that with $Mo_3S_4$(acac-Bu), 99 ± 1% against 91 ± 1%.

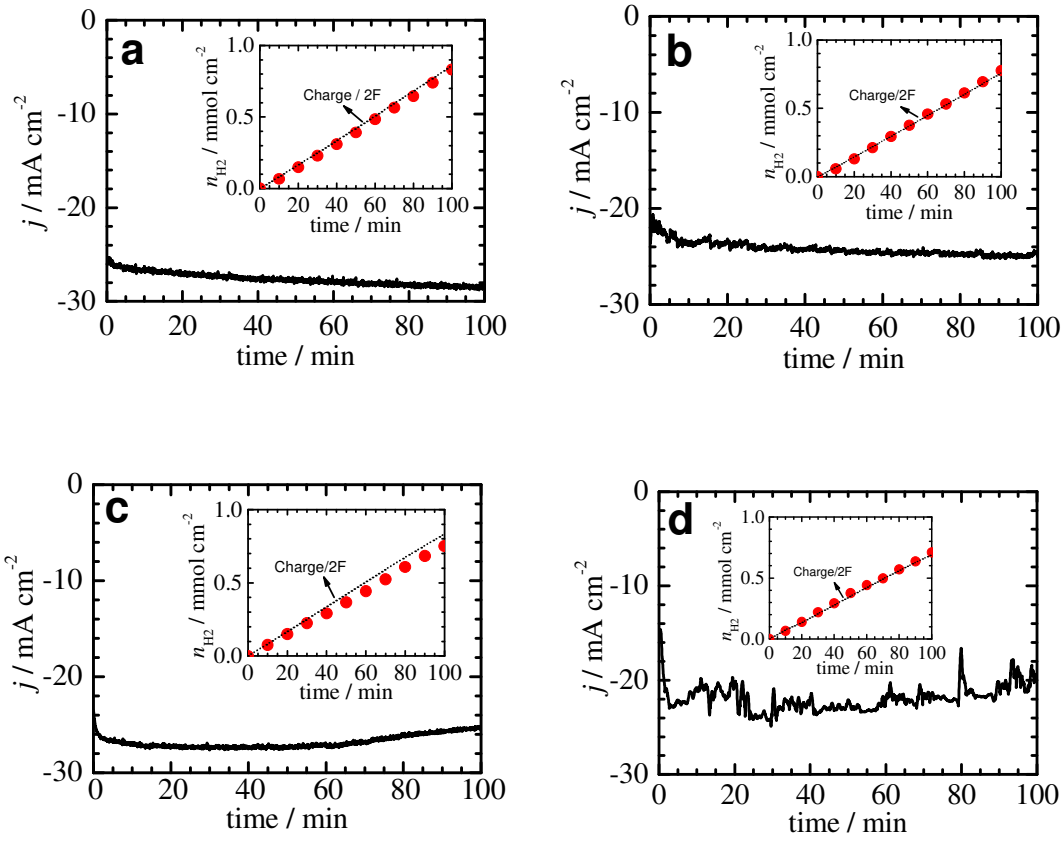


**Figure 2-17:** Photocurrent density–time curves under continuous illumination obtained during the controlled-potential electrolysis at -0.84 V vs RHE in a pH 0.3 solution (a, b) or -1.04 V vs RHE in a pH 7.3 solution (c, d) using optimized $Mo_3S_4$(acac-Bu) (a, c) or $Mo_3S_4(AsW_{12})$ (b, d) -modified photocathodes. (Insets) Amount of $H_2$ evolved at the photocathode as a function of the electrolysis time. The mole number of produced gas was calculated from the gas volume trapped in a Hoffman cell. The dotted black lines correspond to the theoretical fit assuming a 100% Faradaic efficiency. The current fluctuations are caused by the removal of $H_2$ bubbles from the photocathode surface. The surface areas of the photoelectrodes are 0.30 (a), 0.50 (b), 0.49 (c) and 0.51 (d) $cm^2$.

To quantify the catalytic efficiency of a system, the turnover frequency (TOF) as a function of the electrode potential has been determined. [40, 61] For an HER catalyst, the TOF corresponds to the ratio of the number of $H_2$ moles produced per second to the number of moles of catalytically active sites (see the experimental section for more details). It is therefore essential that the contribution of the electrode surface in the catalytic process is eliminated. Consequently, in this work, this quantity was determined from *iR*-corrected LSV curves of the optimized $Mo_3S_4$(acac-Bu)- and $Mo_3S_4(AsW_{12})$-modified photocathodes (**Figure 2-7**) within a potential window corresponding to the foot of the catalytic wave, [62] i.e. -0.2 to 0.0 V vs RHE (for both clusters at pH 0.3), -0.1 to 0.1 V vs RHE (for the $Mo_3S_4$(acac-Bu) cluster at pH 7.3) or -0.3 to -0.1 V vs RHE (for the $Mo_3S_4(AsW_{12})$ cluster at pH 7.3). It is noteworthy that limitations by the mass transport can be considered as negligible owing to the high concentration of the electrolyte. Moreover, another critical issue is the determination of the exact number of the active sites present at the electrode surface since it is quite obvious that an underestimation of this quantity will yield an overestimation of the TOF. In this work and according to previous reports on thiomolybdate-based HER electrocatalysts, [13, 36] the number of active sites should correspond to the cluster density remaining after the cathodically-induced desorption step and estimated from two different methods, namely XPS and AFM. Thereby, this is supported by the stability of both the photocurrents measured at pH 0.3 during preparative-scale electrolysis for a few tens of hours and by the LSV response after electrolysis, as shown in the next section. Nevertheless, for comparison, TOF values calculated using the initial loading of the deposited cluster are also considered. At pH 0.3, the variation of TOF with the electrode potential confirms the higher catalytic activity of the cluster $Mo_3S_4(AsW_{12})$ compared to $Mo_3S_4$(acac-Bu) (**Figure 2-18**). From the post-electrochemistry cluster density, TOF values in the range 20-80 $s^{-1}$ and 6-14 $s^{-1}$ were estimated at 0 V vs RHE for the $Mo_3S_4(AsW_{12})$ and $Mo_3S_4$(acac-Bu) clusters, respectively. Respective values of ca. 850-3300 $s^{-1}$ and 50-120 $s^{-1}$ were reached at -0.2 V vs RHE. At pH 7.3, the trend was inversed with $Mo_3S_4$(acac-Bu) being more active than $Mo_3S_4(AsW_{12})$ (**Figure 2-18b**). TOF values fall in the 60-250 $s^{-1}$ range for $Mo_3S_4(AsW_{12})$ at an overpotential of 0.2 V, while $Mo_3S_4$(acac-Bu) yielded 30-60 $s^{-1}$ TOF values at 0 V vs RHE.

Such exceptional values have never been reported for thiomolybdate-based HER electrocatalysts [41, 63] so far and exhibit ca. 2-3 orders of magnitude higher than those reported for the most active molybdenum sulfides, such as $MoS_2$ nanoparticles supported on Au(111). [41, 64] Much smaller TOF values [for instance, ca. 6 $s^{-1}$ and 0.1 $s^{-1}$ for $Mo_3S_4(AsW_{12})$ and $Mo_3S_4$(acac-Bu), respectively, at -0.2 V vs RHE and pH 0.3] competing with that of the best molybdenum sulfide-based HER catalysts [41] are calculated if the number of active cluster sites is assumed to be equal to the initial loading of the deposited cluster (**Figure 2-18**). As a matter of fact, a mean TOF between these two extreme limits should be rather representative of the real catalytic activity of the immobilized co-catalysts. Importantly, a special care

must be taken to the comparison of our TOF values estimated at a certain overpotential with those determined for other molybdenum sulfide- or thiomolybdate-based HER electrocatalysts since all reported TOF values up to date concern catalysts supported on surfaces other than semiconductors. Additionally, a few studies devoted to other molecular HER electrocatalysts attached to *p*-type semiconductors have reported an order-of-magnitude lower TOFs. For instance, metalloporphyrin covalently bound to *p*-type GaP yielded a TOF of ca. 4 $s^{-1}$ at 0 V vs RHE and pH 7 under identical illumination conditions. [65] In another example, a cobalt molecular complex bound to a $TiO_2$-protected $GaInP_2$ photocathode produced $H_2$ with a TOF of 3.4 $s^{-1}$ at 0 V vs RHE but under basic conditions (pH 13).[66] Besides the possible underestimation of the density of catalytically active sites, the high TOF values reported in this work may also be due to a significant contribution of the Si surface in the catalytic process even though special care has been taken to measure accurately the TOF of the alone immobilized catalyst (restricted potential range in which the current densities are expected to be controlled by the HER kinetics and use of high concentration of electrolyte).

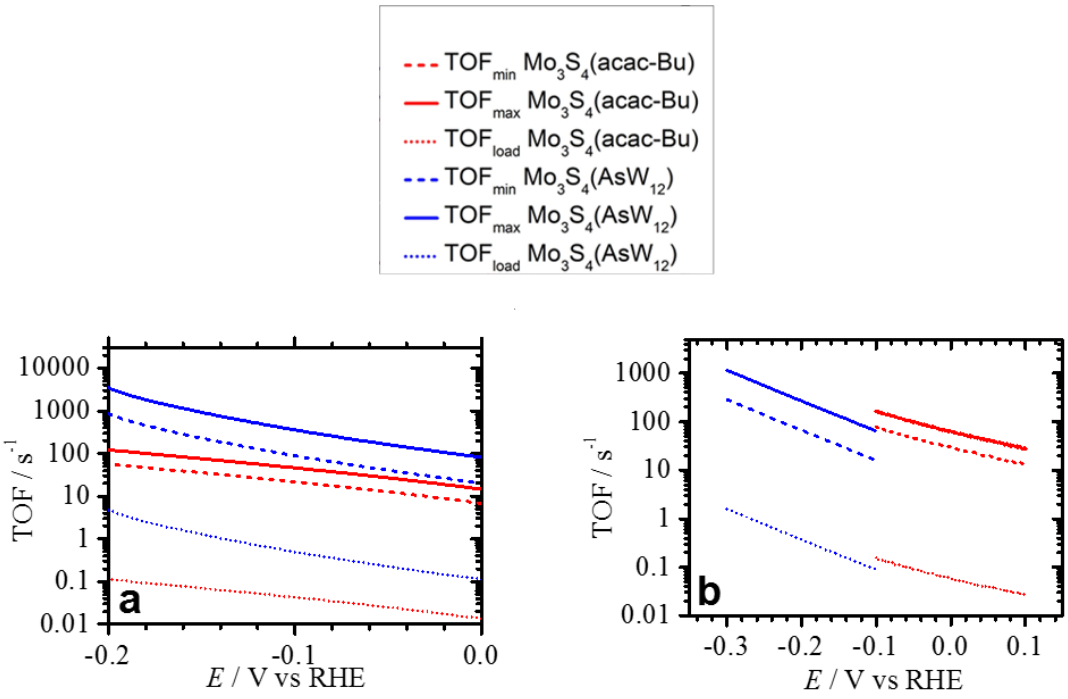


**Figure 2-18:** TOF of the $Mo_3S_4$(acac-Bu) (red lines) and $Mo_3S_4(AsW_{12})$ (blue lines) clusters deposited on *p*-type Si(100) surfaces for simulated sunlight-driven HER at pH 0.3 (a) and pH 7.3 (b). The minimum ($TOF_{min}$, dashed lines) and maximum ($TOF_{max}$, solid lines) TOF numbers were determined from upper and lower limits of the post-electrolysis cluster densities, respectively, estimated from XPS and AFM data. $TOF_{load}$ (dotted lines) was calculated from the initial loading of the deposited cluster.

### 2.2.5 Long-term stability of the catalyst-modified photocathodes

The stability criterion is another crucial requirement for modified photocathodes, mainly driven by the robustness of the interface. To assess the long-term stability of our photocathodes, controlled-potential electrolyses were carried out in both aqueous solutions over testing periods exceeding ca. 30 h. At pH 0.3, the $Mo_3S_4(AsW_{12})$-modified photocathode was found to be the most robust since no noticeable decrease in the photocurrent was observed after 40 h. In contrast, a 18% decrease in the cathodic photocurrent was measured for the $Mo_3S_4$(acac-Bu)-modified photocathode (**Figure 2-19**). Such a trend features the high stability of $Mo_3S_4(AsW_{12})$ POM material functioning under acidic conditions. The similarity between the LSVs before and after electrolysis supports the excellent stability of the $Mo_3S_4(AsW_{12})$-modified photocathode. At pH 7.3, in line with short-term stability tests detailed in the previous section, both photocathodes were found to be much less stable during the potentiostatic electrolysis with a comparable decrease in the photocurrent after 30 h, namely 38% against 45%. We believe that the lower stability and lower activity observed at pH 7.3 for both modified photocathodes can be ascribed to some decomposition reactions of the immobilized catalysts and/or a different Si chemical interface. In the case of the $Mo_3S_4$(acac-Bu) catalyst, the first process may originate from the substitution of the organic ligand by some anions from the electrolyte whereas a hydrolytic decomposition leading to the transformation (such as partial decondensation) of the {$Mo_3S_4$-POM} hybrid material is possible in the case of the second catalyst. [31,67] The second process associated to the electrode may lead to the gradual degradation of the Si/catalyst interface or could enhance catalyst desorption.[68]

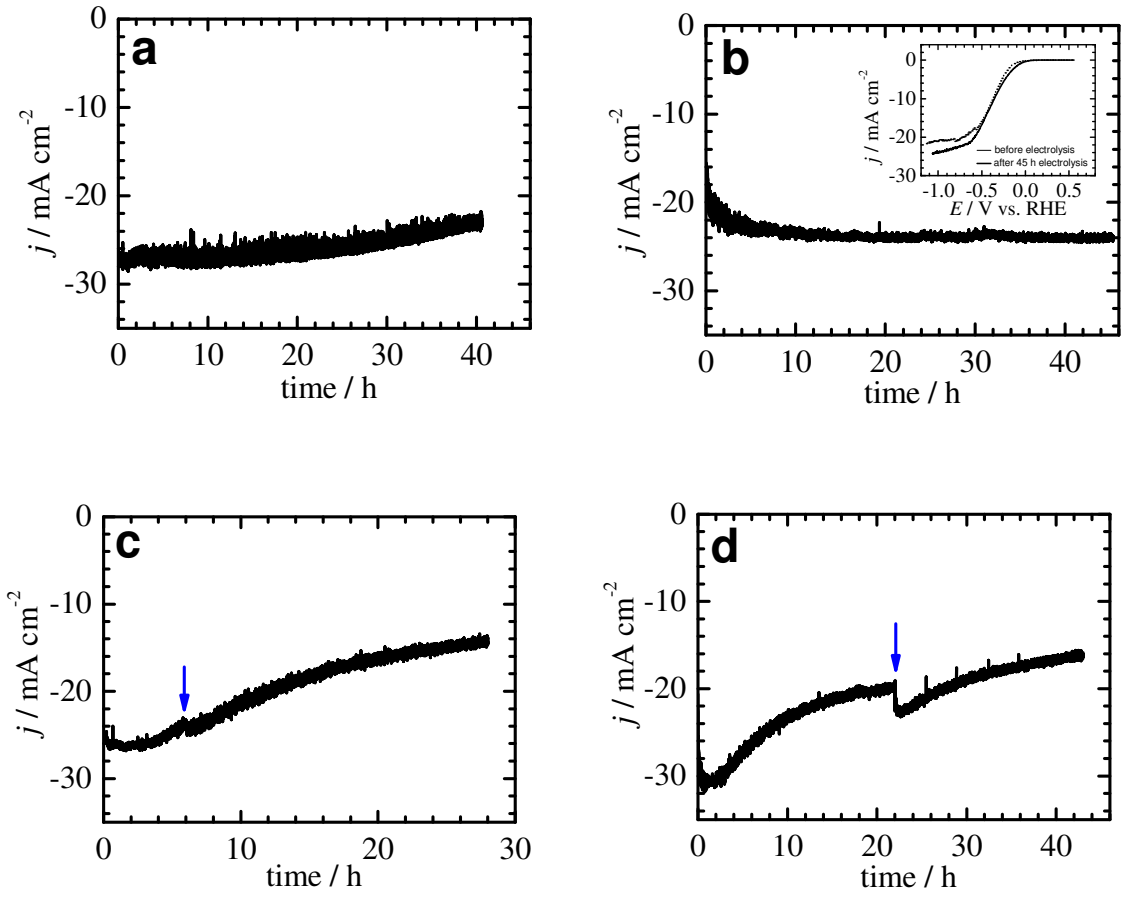


**Figure 2-19:** Long-term stability of the optimized $Mo_3S_4$(acac-Bu) (a, c) and $Mo_3S_4(AsW_{12})$ (b, d) -modified photocathodes for simulated sunlight-driven HER during the controlled-potential electrolysis at -0.84 V vs RHE in a pH 0.3 solution (a, b) or -1.04 V vs RHE in a pH 7.3 solution (c, d). (Inset) *iR*-uncorrected LSVs at 20 mV $s^{-1}$ (pH 0.3) of the $Mo_3S_4(AsW_{12})$-modified photocathode before and after electrolysis. The blue arrows indicate the removal of the $H_2$ bubbles from the surface.

## 2.3 Experimental

### 2.3.1 Reagents

Acetone (MOS electronic grade, Erbatron from Carlo Erba), anhydrous ethanol (RSE electronic grade, Erbatron from Carlo Erba) and 3-butylpentane-2,4-dione (Sigma-Aldrich) were used without further purification. The cationic cluster $\{Mo_3S_4\}^{4+}$ was prepared through previously reported procedure [69] and available in the solid state as $(NH_4)_2Mo_3S_4(H_2O)_9Cl_6 \bullet 3H_2O$. The chemicals used for the cleaning and etching of Si wafer pieces (30% $H_2O_2$, 96-97% $H_2SO_4$ and 50% HF solutions) were of VLSI ($H_2O_2$, from Sigma-Aldrich) and MOS ($H_2SO_4$ from O-BASF and HF from Sigma-Aldrich) semiconductor grade.

### 2.3.2 Syntheses of the compounds

**$[Mo_3S_4(acac\text{-}Bu)_3(H_2O)_3]Cl \bullet H_2O$.** $(NH_4)_2Mo_3S_4(H_2O)_9Cl_6 \bullet 3H_2O$ (1.0 g; 1.13 mmol) was dissolved in methanol (30 mL). 3-butylpentane-2,4-dione (noted acac-Bu) (0.695 g; 4.45 mmol) and 2.2 mL of 1 mol $L^{-1}$ KOH aqueous solution were mixed in 5 mL of methanol and then slowly added to the greenish $\{Mo_3S_4\}$-containing solution. The resulting dark-green solution was allowed to stand for crystallization. Two days after, well-shaped parallelepipedic crystals suitable for X-Ray diffraction analysis were collected. Yield: 0.66 g (60 % *vs* Mo). $^1$H NMR (300 MHz, MeOD): δ(ppm) = 8.89 (t, 3 H), 1.29 (2x2 H), 2.11 ppm (6 H), 2.29 (2 H). Anal. Calcd. for $Mo_3S_4C_{29}H_{55}O_{10}Cl$: Mo, 0.28; S, 0.12; C, 0.33; H, 0.054; Cl, 0.03; Found: Mo, 0.27; S, 0.11; C, 0.36; H, 0.058; Cl, 0.03.

**$Rb_3NaHAsW_{12}Mo_3S_4(H_2O)_3O_{42} \bullet 14\ H_2O$.** Sodium tungstate dihydrate $Na_2WO_4 \bullet 2\ H_2O$ (1.11 g; 3.36 mmol) and $Na_9AsW_9O_{33} \bullet 12\ H_2O$ (3.0 g; 1.12 mmol) were suspended in 30 mL of water and acidified by 3.5 mL of aqueous solution of 2 mol $L^{-1}$ hydrochloric acid until pH down to about pH = 5. Resulting solution was then heated at 50°C while 10 mL of aqueous solution containing $(NH_4)_2Mo_3S_4(H_2O)_9Cl_6 \bullet 3H_2O$ (1.0 g; 1.13 mmol) was slowly added drop by drop under gentle stirring. A cloudy brownish precipitate was formed and disappeared slowly after 30 min at 50 °C. The pH of the solution was 2.3. After solution cooled down room temperature, rubidium chloride (1.5 g; 12 mmol) was poured to the solution provoking the formation of a dark-brown solid. After 30 min under slow stirring, the solid was then collected through filtration using glass frit filter, washed with ethanol and dried using diethyl ether. Analysis of the resulting solid (2.8 g) was consistent with $Rb_3NaHAsW_{12}Mo_3S_4(H_2O)_3O_{42} \bullet 14\ H_2O$ leading to a yield of about 65%. Anal. Calcd. for $Rb_3NaH_{35}AsW_{12}Mo_3S_4O_{59}$: Rb, 6.5 ; Na, 0.6 ; As, 1.9 ; W, 55.7 ; Mo, 7.3 ; S, 3.2. Found: Rb, 6.6 ; Na, 0.55 ; As, 1.8 ; W, 55.7 ; Mo, 7.2 ; S, 3.3. TGA : weight loss of 8% between RT and 200°C corresponding to 17.5 water molecules distributed as fourteen crystallization water molecules and three aquo ligands attached to the $\{Mo_3S_4\}$ core and ½ constitutional water. IR ($cm^{-1}$): 950(s); 847(m); 780(vs); 656(w); 445(w).

**$[(n\text{-}C_6H_{13})_4N]_5AsW_{12}Mo_3S_4(H_2O)_3O_{42}$.** The cationic exchange has been carried out through liquid-liquid extraction of the POM as alkali salt from aqueous solution to toluene organic phase containing tetra-*n*-hexylammonium bromide. The 50 mL aqueous solution contained 2.55 mmol $L^{-1}$ in $Rb_3NaHAsW_{12}Mo_3S_4(H_2O)_3O_{42} \bullet 14\ H_2O$ while the organic phase corresponded to tetrahexylammonium bromide (0.40 g; 0.92 mmol) dissolved in 40 mL of toluene. Both solutions were contacted vigorously for 30 min and then decanted within a separatory funnel. The brownish organic phase was collected. The solvent was removed through rotary evaporator until obtaining dark-brown oily residue which was

thoroughly washed with ethanol and diethylether. Yield: 340 mg (46 %). Anal. Calcd: C, 27.7: H, 5.0; N, 0.9; Found: C, 28.3; H, 5.1; N, 1.1; EDX atomic ratios. Calc(found): W/Mo = 4(3.9); W/S = 3(2.8). TGA: weight loss of 35% between RT and 500°C in agreement with the combustion of five tetra-*n*-hexylammonium units. IR ($cm^{-1}$): 957(s); 850(m); 797(vs); 729(sh).

### 2.3.3 Analytical methods for characterization of the precursors

NMR spectra were measured in $D_2O$ at 27 °C. $^{1}H$ and $^{183}W$ NMR spectra were recorded on a Bruker Avance 500 spectrometer at 500.1 and 20.84 MHz respectively. According to conventions for standards, chemical shifts are referenced with respect to TMS and 1 M $Na_2WO_4$ aqueous solution for $^{1}H$ and $^{183}W$ respectively.

Fourier Transform Infrared (FT-IR) spectra were recorded on a 6700 FT-IR Nicolet spectrophotometer, using diamond ATR technique. The spectra were recorded on non-diluted compounds in the range 400-4000 $cm^{-1}$. ATR correction was applied.

UV-Vis spectra of powdered compounds have been collected by using a Perkin-Elmer Lambda 750 spectrophotometer equipped with a powder sample holder set. The UV-Vis spectra of solutions were recorded on a Perkin-Elmer Lambda-750 using calibrated 0.1 cm quartz cell.

Energy-dispersive X-ray spectra were performed using a SEM-FEG (Scanning Electron Microscope enhanced by a Field Emission Gun) equipment (JSM 7001-F, Jeol). The measurements were acquired with a SDD XMax 50 $mm^2$ detector and the Aztec (Oxford) system working at 15 kV and 10 mm distance. The quantification is realized with the standard library provided by the constructor using Lα lines.

The number of water molecules and tetra-*n*-hexylammonium cations was determined by thermal gravimetric (TGA) analysis with a Mettler Toledo TGA/DSC 1, STAR$^{e}$ System apparatus or with a NETZSCH TG 209 F1 device under air flow (50 mL $min^{-1}$) at a heating rate of 5°C $min^{-1}$ up to 800°C.

### 2.3.4 Single crystal X-Ray diffraction study

Intensity data collections were carried out at $T$ = 200(2) K with a Bruker X8 APEX2 CCD, using the MoKα wavelength (λ = 0.71073 Å). Crystals were glued in paratone to prevent any loss of solvent. An empirical absorption correction was applied using the SADABS program [70] based on the method of Blessing.[71] The structures were solved by direct methods and refined by full-matrix least squares using the SHELX-TL package.[72] Heavier atoms (Mo) were initially located by direct methods. The remaining non-hydrogen atoms were located from Fourier differences and were refined with anisotropic thermal

parameters. Positions of the hydrogen atoms belonging to the organic ligand Acac-Bu were calculated and refined isotropically using the gliding mode. Data collection, structure refinement details and crystallographic data for single-crystal X-ray diffraction study of $[Mo_3S_4(acac\text{-}Bu)_3(H_2O)_3]Cl \bullet H_2O$ can be found in **Table 2-1**, including the CIF file. CCDC 1854697 also contains the supplementary crystallographic data, which can be obtained free of charge via www.ccdc.cam.ac.uk/data_request/cif.

### 2.3.5 Preparation of the modified Si surfaces

A piece of *p*-type (1-5 Ω cm resistivity, boron doped, 250 $\mu$m thickness, Siltronix) or $n^+$-type (0.001 Ω cm resistivity, phosphorus doped, 250 $\mu$m thickness, Siltronix) Si(100) was sonicated for 10 minutes successively in acetone, ethanol and ultra-pure 18.2 MΩ cm water (Veolia Water STI) to degrease it. It was then cleaned with piranha solution (3:1 v/v concentrated $H_2SO_4$/30% $H_2O_2$) for 30 min at 100 °C, followed by copious rinsing with ultra-pure water to eliminate heavy metals and organic residues.

*Caution: The concentrated aqueous $H_2SO_4/H_2O_2$ (piranha) solution is highly dangerous, particularly in contact with organic materials, and should be handled extremely carefully.*

For electrochemical measurements, the decontaminated surface was further processed to fabricate the photocathode. An ohmic contact was established on the backside Si surface with a metal wire by first scrubbing the surface with sand paper and a diamond glass cutter and then applying a droplet of InGa eutectic (99.99%, Alfa Aesar). A layer of silver paste (Electron Microscopy Sciences) was then deposited on the contact. After drying of the silver paste, the metal wire was inserted in a glass capillary, and the electrode area (0.20 to 0.45 $cm^2$) was defined with an epoxy-based resin (Loctite 9460, Henkel) that covered all the back of the Si surface as well as the silver paste. The assembled electrode was then placed into an oven at 90 °C overnight to cure the resin.

The Si surface sealed in epoxy was freshly hydrogenated by immersing the electrode into HF 10% wt (~5.7 M) for 2 min, followed by copious rinsing with ultrapure water and drying under an argon stream.

*Caution: Proper precautions must be used when handling hydrogen fluoride. Hydrogen fluoride is extremely corrosive for human tissue, contact resulting in painful, slow-healing burns. Laboratory work with HF should be conducted only in an efficient hood, with the operator wearing a full-face shield and protective clothing.*

The cluster solution was prepared at 1 mM in methanol (CHROMASOLV®, for HPLC, ≥ 99.9%) by dissolving $[Mo_3S_4(acac\text{-}Bu)_3(H_2O)_3]Cl{\bullet}H_2O$ or $[(n\text{-}C_6H_{13})_4N]_5AsW_{12}Mo_3S_4(H_2O)_3O_{42}$ followed by sonication for ca. 15 min. The solution was then diluted with methanol to reach the final concentration of 0.5 or 0.1 mM. The freshly hydrogenated Si(100) surface was modified with the $Mo_3S_4(acac\text{-}Bu)$ or $Mo_3S_4(AsW_{12})$ cluster by drop-casting of the $[Mo_3S_4(acac\text{-}Bu)_3(H_2O)_3]Cl{\bullet}H_2O$ or $[(n\text{-}C_6H_{13})_4N]_5AsW_{12}Mo_3S_4(H_2O)_3O_{42}$ solution at 0.1, 0.5 or 1 mM in methanol, yielding a cluster loading of $7.2 \times 10^{-6}$, $3.6 \times 10^{-5}$ or $7.2 \times 10^{-5}$ mmol $cm^{-2}$, respectively. The modified photocathodes were further used for electrochemical measurements after evaporation of the solvent at room temperature for 5-10 min.

### 2.3.6 Electrochemical Measurements

The linear sweep voltammograms (LSVs) were performed in a homemade three-neck cell comprising a quartz window in which were inserted a KCl saturated calomel reference electrode (SCE) and a Pt counter electrode (the counter electrode was separated from the rest of the cell by a glass frit). The cell was filled with the electrolytic solution containing either 1.0 mol $L^{-1}$ $H_2SO_4$ (pH 0.3) or 0.1 mol $L^{-1}$ KCl + 0.5 mol $L^{-1}$ $KHCO_3$ (pH 7.3) and was deaerated by bubbling Ar for at least 30 min prior to experiments. The photocathode (hydrogen-terminated *p*-type Si(100) or freshly covered by the metallic cluster using the protocol described above) was disposed in front of the quartz window and used as a working electrode. The light was provided by a solar simulator with a fluence of 100 mW $cm^{-2}$ (LS0106, LOT Quantum Design) equipped with a AM 1.5G filter. Electrochemical measurements were performed with a potentiostat/galvanostat Autolab PGSTAT 302N (Eco Chemie BV) equipped with the GPES and FRA softwares. LSVs were recorded at 20 mV/s. Unless specified, all the LSVs and the reported potentials were intentionally not corrected by the Ohmic drop. The Ohmic drop was determined before each experiment by measuring the impedance of the system at 100 kHz and it was found to be around 20-100 Ω depending on the type of the tested photoelectrode and the used electrolytic medium. The geometrical areas of the electrodes used for LSVs were in the range 0.20-0.45 $cm^2$ and their exact value was measured using the ImageJ software in order to calculate the current densities. Potentials *vs* SCE were converted into potential *vs* reversible hydrogen electrode (RHE) using the equation: $E_{RHE} = E_{SCE} + 0.24 + 0.059 \times pH$ (that was experimentally verified in our operating conditions with a bare platinum electrode). The preparative-scale electrolysis was performed in a Hoffman cell comprising a quartz window and two closed graduated cylinders above the working electrode and the counter electrode. The volumes of $H_2$ and $O_2$ gases were measured in-situ during the electrolysis, more details can be found in ref 60. For the determination of the Faradaic

yield, the theoretical volume of produced $H_2$ ($V_{H_2}^T$) was calculated using the electrical charge used during the electrolysis using the following equation:

$$V_{H_2}^T = \left(\frac{Q}{2F}\right) \times \left(\frac{RT}{P}\right)$$

with *Q* being the charge passed during the electrolysis, *F* being the Faraday constant, *R* being the gas constant, *T* being the ambient temperature and *P* being the atmospheric pressure.

### 2.3.7 Additional Instrumentation

XPS measurements were performed with a Mg K$\alpha$ 1254 eV X-ray source, using a VSW HA100 photoelectron spectrometer with a hemispherical photoelectron analyzer, working at an energy pass of 20 eV for survey and resolved spectra. The experimental resolution was then 1.0 eV. The binding energy for the main C–C peak has been taken at 285.0 eV as an internal reference level for all measurements. Spectral analysis included a Shirley background subtraction and peak separation using mixed Gaussian-Lorentzian functions.

AFM images were acquired on a NT-MDT NTEGRA microscope in semicontact mode with FM tips (resonance frequency around 60 kHz). The images were treated and analyzed with the open-source Gwyddion software.

### 2.3.8 Calculation methods of the cluster surface coverage and the turnover frequency (TOF)

2.3.8.1 Calculation of the cluster surface coverage by XPS

The surface coverages of $Mo_3S_4$(acac-Bu) and $Mo_3S_4(AsW_{12})$ remaining after electrolysis, $\theta_{Mo3S4(acac\text{-}Bu)}$ and $\theta_{Mo3S4(AsW12)}$ respectively, were obtained by comparing the Mo 3d or W 4f XPS intensities ($I_{Mo3d}$ or $I_{W4f}$) to the one-plane Si intensity $I_{Si,plane}$, calculated using the signal of the clean uncovered Si (i.e. Si(100)-H) $I_{Si,clean}$ through:

$$I_{\mathrm{Si,plane}} = I_{\mathrm{Si,clean}} \frac{a_{Si}}{\lambda_{Si}^{Si}} = KN_s \quad (1)$$

where $N_s$ is the number of Si atoms per unit surface ($N_s = 6.8 \times 10^{14}$ cm$^{-2}$), [73] $\lambda_{Si}^{Si} = 1.3$ nm is the electron mean free path in Si [74] and $a_{Si}$ is the interplane distance perpendicular to the surface. *K*, which includes

X-ray excitation flux, the transmission and detection efficiencies of the analyzer, remains unchanged under identical experimental conditions.

$I_{Mo3d}$ and $I_{W4f}$ were estimated using the total area under the Mo 3d ($\int$ Mo) or W 4f ($\int$ W) signal, respectively (eq 2 and 3).

$$I_{\mathrm{Mo3d}} = \frac{\int \mathrm{Mo}}{\sigma_{\mathrm{Mo}} x_{\mathrm{Mo}}} \quad (2)$$

$$I_{\mathrm{W4f}} = \frac{\int \mathrm{W}}{\sigma_{\mathrm{W}} x_{\mathrm{W}}} \quad (3)$$

where $\sigma_{Mo}$ and $\sigma_W$ are the atomic sensitivity factors for Mo 3d ($\sigma_{Mo}$ = 9.74) and W 4f ($\sigma_W$ = 5.75), respectively; $x_{Mo}$ and $x_W$ are the number of Mo and W atoms in the $Mo_3S_4$(acac-Bu) ($x_{Mo}$ = 3) and $Mo_3S_4(AsW_{12})$ ($x_W$ = 12) clusters, respectively.

$\theta_{Mo3S4(acac\text{-}Bu)}$ and $\theta_{Mo3S4(AsW12)}$ can then be calculated using the following equations:

$$\theta_{Mo_3S_4(\mathrm{acac-Bu})} = \frac{I_{\mathrm{Mo3d}}}{I_{\mathrm{Si,plane}}} N_{\mathrm{s}} \quad (4)$$

$$\theta_{Mo_3S_4(\mathrm{AsW_{12}})} = \frac{I_{\mathrm{W4f}}}{I_{\mathrm{Si,plane}}} N_{\mathrm{s}} \quad (5)$$

Following this procedure, $\theta_{Mo3S4(acac\text{-}Bu)}$ = (8.0 ± 0.5) × $10^{13}$ $cm^{-2}$ and $\theta_{Mo3S4(AsW12)}$ = (2.0 ± 0.6) × $10^{13}$ $cm^{-2}$ were determined.

2.3.8.2 Determination of the turnover frequency (TOF)

The turnover frequency (in $s^{-1}$) was calculated using the following equation:

$$\mathrm{TOF} = \frac{n_{\mathrm{H_2}}}{n_{\mathrm{c}} t A} \quad (6)$$

where $n_{H2}$, $n_c$, $t$ and $A$ are the number of evolved $H_2$ moles, the number of active cluster sites (in mol $cm^{-2}$), the electrolysis time and the surface area (in $cm^2$), respectively. [75, 76]

The HER photocurrent densities $j$ (in A $cm^{-2}$) were determined from *iR*-corrected LSV curves and can be expressed as a function of $n_{H2}$ according to

$$j = \frac{Q_{\mathrm{H_2}}}{tA} = \frac{2\rho n_{\mathrm{H_2}} F}{tA} \quad (7)$$

where $Q_{H2}$, $\rho$ and $F$ are the consumed charge during the production of $H_2$ moles, $\rho$ is the Faradaic efficiency and $F$ is the Faraday constant (96485 C $mol^{-1}$), respectively, considering that two moles of electrons are required to form one mole of $H_2$.

From eq 6 and 7, it can be easily deduced:

$$TOF = \frac{j}{2\rho F n_c} \quad (8)$$

In eq 8, $n_c$ was taken as the average of the cluster densities estimated from XPS and AFM data, namely (1.05 ± 0.38) × $10^{-10}$ mol $cm^{-2}$ and (2.5 ± 1.5) × $10^{-11}$ mol $cm^{-2}$ for the optimized $Mo_3S_4$(acac-Bu)- and $Mo_3S_4$($AsW_{12}$)-modified photocathodes, respectively; $\rho$ was assumed to be 100%, as experimentally verified from potentiostatic electrolysis tests in a Hoffman cell.

## 2.4 Conclusions

In this work, we have demonstrated that a *p*-type Si photocathode coated with a polyoxothiometalate electrocatalyst was catalytically more efficient than a photocathode coated with the parent thiomolybdate incorporating an organic ligand for the simulated sunlight-driven HER under acid pH conditions. These findings were supported by a higher onset potential and a lower overvoltage at 10 mA $cm^{-2}$, in spite of a ca 4-7 times smaller catalyst coverage. Under such conditions, the polyoxothiometalate-modified photocathode produced $H_2$ quantitatively with a promising stability of 40 h in controlled-potential electrolysis tests. In contrast, the photocurrents measured at a thiomolybdate-modified surface gradually decreased (ca. 20%) under the same conditions. At neutral pH, the situation was inversed and the beneficial effect of the POM for the HER was not observed. These results show that, due to their high metal nuclearity, POMs represent relevant molecular systems for multi-electron transfer engineering and then ideal candidates to tackle challenging electrocatalytic process of great societal interest, namely the $CO_2$ reduction.

**References**

[1] Cook, T. R.; Dogutan, D. K.; Reece, S. Y.; Surendranath, Y.; Teets, T. S.; Nocera, D. C. Solar Energy Supply and Storage for the Legacy and Nonlegacy Worlds. *Chemical. Reviews*. **2010**, *110*, 6474-6502.

[2] Lewis, N. S.; Nocera, D. G. Powering the Planet: Chemical Challenges in Solar Energy Utilization. *Proceedings of the National Academy of Sciences. USA.* **2006**, *103*, 15729-15735.

[3] Walter, M. G.; Warren, E. L.; McKone, J. R.; Boettcher, S. W.; Mi, Q.; Santori, E. A.; Lewis, N. S. Solar Water Splitting Cells. *Chemical. Reviews.* **2010**, *110*, 6446-6473.

[4] Zhang, X. G. In *Electrochemistry of Silicon and its Oxide*. Kluwer Academic Publishers: New York, **2004**.

[5] Sivula, K.; van de Krol, R. Semiconducting Materials for Photoelectrochemical Energy Conversion. *Nature Reviews Materials.* **2016**, *1*, 1-16.

[6] Sun, K.; Shen, S.; Liang, Y.; Burrows, P. E.; Mao, S. S.; Wang, D. Enabling Silicon for Solar-Fuel Production. *Chemical. Reviews.* **2014**, *114*, 8662-8719.

[7] Wrighton, M. S. Thermodynamics and Kinetics Associated with Semiconductor Based Photoelectrochemical Cells for the Conversion of Light to Chemical Energy. *Pure and Applied Chemistry.* **1985**, *57*, 57-68.

[8] Boettcher, S. W.; Warren, E. L.; Putnam, M. C.; Santori, E. A.; Turner-Evans, D.; Kelzenberg, M. D.; Walter, M. G.; McKone, J. R.; Brunschwig, B. S.; Atwater, H. A.; Lewis, N. S. Photoelectrochemical Hydrogen Evolution Using Si Microwire Arrays. *Journal of the American Chemical Society.* **2011**, *133*, 1216−1219.

[9] Dai, P.; Xie, J.; Mayer, M. T.; Yang, X.; Zhan, J.; Wang, D. Solar Hydrogen Generation by Silicon Nanowires Modified with Platinum Nanoparticle Catalysts by Atomic Layer Deposition. *Angewandte Chemie International Edition.* **2013**, *52*, 11119−11123.

[10] Fabre, B.; Li, G.; Gouttefangeas, F.; Joanny, L.; Loget, G. Tuning the Photoelectrocatalytic Hydrogen Evolution of Pt-Decorated Silicon Photocathodes by the Temperature and Time of Electroless Pt Deposition. *Langmuir*. **2016**, *32*, 11728-11735.

[11] Truong, T.-G.; Meriadec, C.; Fabre, B.; Bergamini, J.-F.; de Sagazan, O.; Ababou-Girard, S.; Loget, G. Spontaneous Decoration of Silicon Surfaces with $MoO_x$ Nanoparticles for the Sunlight-Assisted Hydrogen Evolution Reaction. *Nanoscale*. **2017**, *9*, 1799-1804.

[12] Bao, X.-Q.; Petrovykh, D. Y.; Alpuim, P.; Stroppa, D. G.; Guldris, N.; Fonseca, H.; Costa, M.; Gaspar, J.; Jin, C.; Liu, L. Amorphous Oxygen-Rich Molybdenum Oxysulfide Decorated p-Type Silicon Microwire Arrays for Efficient Photoelectrochemical Water Reduction. *Nano Energy*. **2015**, *16*, 130-142.

[13] Hou, Y.; Abrams, B. L.; Vesborg, P. C. K.; Björketun, M. E.; Herbst, K.; Bech, L.; Setti, A. M.; Damsgaard, C. D.; Pedersen, T.; Hansen, O.; Rossmeisl, J.; Dahl, S.; Norskov, J. K.; Chorkendorff, I. Bioinspired Molecular Co-Catalysts Bonded to a Silicon Photocathode for Solar Hydrogen Evolution. *Nature materials.* **2011**, *10*, 434-438.

[14] Seger, B.; Herbst, K.; Pedersen, T.; Abrams, B.; Vesborg, P. C. K.; Hansen, O.; Chorkendorff, I. $Mo_3S_4$ Clusters as an Effective $H_2$ Evolution Catalyst on Protected Si Photocathodes. *Journal of the Electrochemical Society.* **2014**, *161*, H722-H724.

[15] Seger, B.; Laursen, A. B.; Vesborg, P. C. K.; Pedersen, T.; Hansen, O.; Dahl, S.; Chorkendorff, I. Hydrogen Production Using a Molybdenum Sulfide Catalyst on a Titanium-Protected $n^+p$-Silicon Photocathode. *Angewandte Chemie International Edition.* **2012**, *51*, 9128-9131.

[16] Laursen, A. B.; Pedersen, T.; Malacrida, P.; Seger, B.; Hansen, O.; Vesborg, P. C.; Chorkendorff, I. $MoS_2$: An Integrated Protective and Active Layer on n(+)p-Si for Solar $H_2$ Evolution. *Physical Chemistry Chemical Physics*. **2013**, *15*, 20000-20004.

[17] Morales-Guio, C. G.; Hu, X. Amorphous Molybdenum Sulfides as Hydrogen Evolution Catalysts. *Accounts of chemical research.* **2014**, *47*, 2671-2681.

[18] Tran, P. D.; Pramana, S. S.; Kale, V. S.; Nguyen, M.; Chiam, S. Y.; Batabyal, S. K.; Wong, L. H.; Barber, J.; Loo, J. Novel Assembly of an $MoS_2$ Electrocatalyst onto a Silicon Nanowire Array Electrode to Construct a Photocathode Composed of Elements Abundant on the Earth for Hydrogen Generation. *Chemistry–A European Journal.* **2012**, *18*, 13994-13999.

[19] Ding, Q.; Meng, F.; English, C. R.; Caban-Acevedo, M.; Shearer, M. J.; Liang, D.; Daniel, A. S.; Hamer, R. J.; Jin, S. Efficient Photoelectrochemical Hydrogen Generation Using Heterostructures of Si and Chemically Exfoliated Metallic $MoS_2$. *Journal of the American Chemical Society.* **2014**, *136*, 8504-8507.

[20] Ding, Q.; Zhai, J.; Caban-Acevedo, M.; Shearer, M. J.; Li, L.; Chang, H.-C.; Tsai, M.-L.; Ma, D.; Zhang, X.; Hamers, R. J.; He, J.-H.; Jin, S. Designing Efficient Solar-Driven Hydrogen Evolution Photocathodes Using Semitransparent $MoQ_xCl_y$ (Q = S, Se) Catalysts on Si Micropyramids. *Advanced Materials.* **2015**, *27*, 6511-6518.

[21] Benck, J. D.; Lee, S. C.; Fong, K. D.; Kibsgaard, J.; Sinclair, R.; Jaramillo, T. F. Designing Active and Stable Silicon Photocathodes for Solar Hydrogen Production Using Molybdenum Sulfide Nanomaterials. *Advanced Energy Materials.* **2014**, *4*, 1400739.

[22] King, L. A.; Hellstern, T. R.; Park, J.; Sinclair, R.; Jaramillo, T. F. Highly Stable Molybdenum Disulfide Protected Silicon Photocathodes for Photoelectrochemical Water Splitting. *ACS applied materials & interfaces.* **2017**, *9*, 36792-36798.

[23] McCrory, C. C. L.; Jung, S.; Ferrer, I. M.; Chatman, S. M.; Peters, J. C.; Jaramillo, T. F. Benchmarking Hydrogen Evolving Reaction and Oxygen Evolving Reaction Electrocatalysts for Solar Water Splitting Devices. *Journal of the American Chemical Society.* **2015**, *137*, 4347-4357.

[24] Llusar, R.; Uriel, S. Heterodimetallic Chalcogen-Bridged Cubane-Type Clusters of Molybdenum and Tungsten Containing First-Row Transition Metals. *European Journal of Inorganic Chemistry*. **2003**, *7*, 1271–1290.

[25] Pino-Chamorro, J. Á.; Gushchin, A. L.; Fernández-Trujillo, M. J.; Hernández-Molina, R.; Vicent, C.; Algarra, A. G.; Basallote, M. G. Mechanism of [3+2] Cycloaddition of Alkynes to the $[Mo_3S_4(acac)_3(py)_3][PF_6]$ Cluster. *Chemistry–A European Journal.* **2015**, *21*, 2835 – 2844.

[26] Duval, S.; Dumur, F.; Guénée, L.; Marrot, J.; Simonnet-Jégat, C.; Cadot, E. Synthesis and Characterization of $[Mo_3S_4(NDABu)\ (HNDABu)_2]^{3-}$ and $[Mo_3S_4(HNDAPr)_3]^{2-}$ Anions as Building Blocks for Organic–Inorganic Hybrid Solids. *European Journal of Inorganic Chemistry.* **2013**, 1149–1156.

[27] Duval, S.; Floquet, S.; Simonnet-Jégat, C.; Marrot, J.; Ngo Biboum, R.; Keita, B.; Nadjo, L.; Haouas, M.; Taulelle, F.; Cadot, E. Capture of the $[Mo_3S_4]^{4+}$ Cluster within a $\{Mo_{18}\}$ Macrocycle Yielding a Supramolecular Assembly Stabilized by a Dynamic H-Bond Network. *Journal of the American Chemical Society.* **2010**, *132*, 2069–2077.

[28] Müller, A.; Fedin, V. P.; Kuhlmann, C.; Fensker, H. D.; Baum, G.; Bögge, H.; Hauptfleisch, B. 'Adding' Stable Functional Complementary, Nucleophilic and Electrophilic Clusters: a Synthetic Route to $[\{(SiW_{11}O_{39})Mo_3S_4(H_2O)_3(\mu\text{-}OH)\}_2]^{10-}$ and $[\{(P_2W_{17}O_{61})Mo_3S_4(H_2O)_3(\mu\text{-}OH)\}_2]^{14-}$ as Examples. *Chemical Communications.* **1999**, 1189–1190.

[29] Duval, S.; Pilette, M. A.; Marrot, J; Simonnet-Jégat, C.; Sokolov, M.; Cadot, E. Selective Inclusion of $Cu^+$ and $Ag^+$ Electron-Rich Metallic Cations within Supramolecular Polyoxometalates Based on $\{AsW_9O_{33}\}$-$\{Mo_3S_4\}$ Combinations. *Chemistry–A European Journal.* **2008**, *14*, 3457 -3466.

[30] Sadakane, M.; Steckhan, E. Electrochemical Properties of Polyoxometalates as Electrocatalysts. *Chemical reviews.* **1998**, *98*, 219-237.

[31] Ueda, T.; Electrochemistry of Polyoxometalates: From Fundamental Aspects to Applications. *ChemElectroChem*. **2018**, *5*, 823-838.

[32] Hernandez-Molina, R.; Sokolov, M.; Clegg, W.; Esparza, P.; Mederos, A. Preparation and Characterization of Triangular Clusters $[M_3Q_4(acac)_3(py)_3]^+$ (M = Mo, W; Q = S, Se). *Inorganica chimica acta*. **2002**, *331*, 52-58.

[33] Thouvenot, R.; Fournier, M.; Franck, R.; Rocchiccioli-Deltcheff, C. Vibrational Investigations of Polyoxometalates. 3. Isomerism in Molybdenum (VI) and Tungsten (VI) Compounds related to the Keggin Structure. *Inorganic Chemistry*. **1984**, *23*, 598-605.

[34] Thouvenot, R.; Rocchiccioli-Deltcheff, C. Vibrational Studies of Heteropolyanions related to $\alpha$-$P_2W_{18}O_{62}^{6-}$ -I- Infrared Evidence of the Structure of $\alpha$-1 and $\alpha$2-$P_2W_{17}O_{61}^{10-}$. *Spectroscopy letters*. **1979**, *12*, 127-138.

[35] Chen, Y. G.; Gong, J.; Qu, L. Y. Tungsten-183 Nuclear Magnetic Resonance Spectroscopy in the Study of Polyoxometalates. *Coord. Chemical reviews*. **2004**, *248*, 245-260.

[36] Jaramillo, T. F.; Bonde, J.; Zhang, J.; Ooi, B.-L.; Andersson, K.; Ulstrup, J.; Chorkendorff, I. Hydrogen Evolution on Supported Incomplete Cubane-type $[Mo_3S_4]^{4+}$ Electrocatalysts. *The Journal of Physical Chemistry C*. **2008**, *112*, 17492-17498.

[37] Tran, P. D.; Tran, T. V.; Orio, M.; Torelli, S.; Truong, Q. D.; Nayuki, K.; Sasaki, Y.; Chiam, S. Y.; Yi, R.; Honma, I.; Barber, J.; Artero, V. Coordination Polymer Structure and Revisited Hydrogen Evolution Catalytic Mechanism for Amorphous Molybdenum Sulfide. *Nature materials.* **2016**, *15*, 640-646.

[38] Kristensen, J.; Zhang, J. D.; Chorkendorff, I.; Ulstrup, J.; Ooi, B. L. Assembled Monolayers of $Mo_3S_4^{4+}$ Clusters on Well-Defined Surfaces. *Dalton Transactions.* **2006**, 3985-3990.

[39] Duval, S.; Floquet, S.; Simonnet-Jégat, C.; Marrot, J.; Ngo Biboum, R.; Keita, B.; Nadjo, L.; Haouas, M.; Taulelle, F.; Cadot, E. Capture of the $[Mo_3S_4]^{4+}$ Cluster Within a $\{Mo_{18}\}$ Macrocycle Yielding a Supramolecular Assembly Stabilized by a Dynamic H-Bond Network. *Journal of the American Chemical Society.* **2010**, *132*, 2069-2077.

[40] Benck, J. D.; Hellstern, T. R.; Kibsgaard, J.; Chakthranont, P.; Jaramillo, T. F. Catalyzing the Hydrogen Evolution Reaction (HER) with Molybdenum Sulfide Nanomaterials, *Acs Catalysis.* **2014**, *4*, 3957-3971.

[41] Kibsgaard, J.; Jaramillo, T. F.; Besenbacher, F. Building an Appropriate Active-Site Motif into a Hydrogen-Evolution Catalyst with Thiomolybdate $[Mo_3S_{13}]^{2-}$ Clusters. *Nature chemistry.* **2014**, *6*, 248-253.

[42] Du, K.; Zheng, L.; Wang, T.; Zhuo, J.; Zhu, Z.; Shao, Y.; Li, M. Electrodeposited $Mo_3S_3$ Films from $(NH_4)_2Mo_3S_{13}\bullet 2H_2O$ for Electrocatalysis of Hydrogen Evolution Reaction. *ACS applied materials & interfaces*. **2017**, *9*, 18675-18681.

[43] Wang, H.; Lu, Z.; Kong, D.; Sun, J.; Hymel, T. M.; Cui, Y. Electrochemical Tuning of $MoS_2$ Nanoparticles on Three-Dimensional Substrate for Efficient Hydrogen Evolution. *ACS Nano*. **2014**, *8*, 4940-4947.

[44] Li, D. J.; Maiti, U. N.; Lim, J.; Choi, D. S.; Lee, W. J.; Oh, Y.; Lee, G. Y.; Kim, S. O. Molybdenum Sulfide/N-Doped CNT Forest Hybrid Catalysts for High-Performance Hydrogen Evolution Reaction. *Nano letters*. **2014**, 14, 1228-1233.

[45] Li, Y.; Wang, H.; Xie, L.; Liang, Y.; Hong, G.; Dai, H. $MoS_2$ Nanoparticles Grown on Graphene: An Advanced Catalyst for the Hydrogen Evolution Reaction. *Journal of the American Chemical Society*. **2011**, 133, 7296-7299.

[46] Laursen, A. B.; Vesborg, P. C. K.; Chorkendorff, I. A High-Porosity Carbon Molybdenum Sulphide Composite with Enhanced Electrochemical Hydrogen Evolution and Stability. *Chemical Communications*. **2013**, 49, 4965-4967.

[47] Dominey, R. N.; Lewis, N. S.; Bruce, J. A.; Bookbinder, D. C.; Wrighton, M. S. Improvement of Photoelectrochemical Hydrogen Generation by Surface Modification of *p*-Type Silicon Semiconductor Photocathodes. *Journal of the American Chemical Society.* **1982**, *104*, 467-482.

[48] Baltrusaitis, J.; Mendoza-Sanchez, B.; Fernandez, V.; Veenstra, R.; Dukstiene, N.; Roberts, A.; Fairley, N. Generalized Molybdenum Oxide Surface Chemical State XPS Determination via Informed Amorphous Sample Model. *Applied Surface Science*. **2015**, *326*, 151-161.

[49] Merki, D.; Fierro, S.; Vrubel, H.; Hu, X. Amorphous Molybdenum Sulfide Films as Catalysts for Electrochemical Hydrogen Production in Water. *Chemical Science*. **2011**, *2*, 1262-1267.

[50] Weber, T.; Muijsers, J. C.; Niemantsverdriet, J. W. Structure of Amorphous $MoS_3$. *The Journal of Physical Chemistry*. **1995**, *99*, 9194-9200.

[51] Souza, A. L.; Tremiliosi Filho, G.; Kubota, L. T.; Mendes, R. K.; Botelho do Rego, A. M.; Oliveira, Jr, O. N.; Henry de Villeneuve, C.; Chazalviel, J. N.; Allongue, P.; Ozanam, F.; Rodrigues Filho, U. P. Poly(Dimethylsiloxane) as a Pre-Coating in Layer-by-Layer Films Containing Phosphotungstate Nanoclusters Electrochemically Sensitive Toward *s*-Triazines. *RSC Advances.* **2014**, *4*, 29612-29621.

[52] Yi, Z.-H.; Cui, X.-B.; Zhang, X.; Chen, Y.; Xu, J.-Q.; Yang, G.-D.; Liu, Y.-B.; Yu, X.-Y.; Yu, H.-H.; Duan, W.-J. A Novel 2D Layer Structural Compound Constructed from Tetra-Capped Pseudo-Keggin Heteropolytungstates interacting with Copper Coordination Fragments: $[Cu(en)_2(H_2O)]_2[Cu(en)_2]_2[AsW_2^{VI}W_7^{V}V_7^{IV}O_{44}]\bullet 2H_2O$. *Inorganic Chemistry Communications.* **2007**, *10*, 1448-1452.

[53] Chen, W.-C.; Li, H.-L.; Wang, X.-L.; Shao, K.-Z.; Su, Z.-M.; Wang, E.-B. Assembly of Cerium (III)-Stabilized Polyoxotungstate Nanoclusters with $SeO_3^{2-}$ / $TeO_3^{2-}$ Templates: From Single Polyoxoanions to Inorganic Hollow Spheres in Dilute Solution. *Chemistry–A European Journal*. **2013**, *19*, 11007-11015.

[54] Shibahara, T.; Tsuru, H.; Kuroya, H. XPS Spectra of Incomplete Cubane-Type Cluster with $Mo_3O_{4-n}S_n^{4+}$ Core ($n$ = 0-4). *Inorganica chimica acta*. **1988**, *150*, 167-168.

[55] Chatt, J.; Elson, C. M.; Leigh, G. J.; Connor, J. A. X-Ray Photoelectron Emission Studies of Some Complexes of Molybdenum in Formal Oxidation States of III, IV, V, and VI. *Journal of the Chemical Society, Dalton Transactions.* **1976**, 1351-1354.

[56] Halada, G. P.; Clayton, C. R. Comparison of Mo-N and W-N Synergism during Passivation of Stainless Steel through X-Ray Photoelectron Spectroscopy and Electrochemical Analysis. *Journal of Vacuum Science & Technology A*. **1993**, *11*, 2342-2347.

[57] Cicero, R. L.; Linford, M. R.; Chidsey, C. E. D. Photoreactivity of Unsaturated Compounds with Hydrogen-Terminated Silicon (111). *Langmuir*. **2000**, *16*, 5688-5695.

[58] Zhang, X. G. *Electrochemistry of silicon and its oxide*; Kluwer Academic: New York, **2001**, p 47.

[59] Yzambart, G.; Fabre, B.; Lorcy, D. Multiredox Tetrathiafulvalene-Modified Oxide-Free Hydrogen-Terminated Si (100) Surfaces. *Langmuir.* **2012**, *28*, 3453-3459.

[60] Loget, G.; Padilha, J. C.; Martini, E. A.; de Souza, M. O.; de Souza, R. F. Efficiency and Stability of Transition Metal Electrocatalysts for the Hydrogen Evolution Reaction using Ionic Liquids as Electrolytes. *International Journal of Hydrogen Energy*. **2009**, *34*, 84–90.

[61] Boudart, M. Turnover Rates in Heterogeneous Catalysis. *Chemical reviews.* **1995**, *95*, 661-666.

[62] Costentin, C.; Drouet, S.; Robert, M.; Savéant, J.-M. Turnover Numbers, Turnover Frequencies, and Overpotential in Molecular Catalysis of Electrochemical Reactions. Cyclic Voltammetry and Preparative-Scale Electrolysis. *Journal of the American Chemical Society.* **2012**, *134*, 11235-11242.

[63] Hellstern, T. R.; Kibsgaard, J.; Tsai, C.; Palm, D. W.; King, L. A.; Abild-Pedersen, F.; Jaramillo, T. F. Investigating Catalyst-Support Interactions to Improve the Hydrogen Evolution Reaction Activity of Thiomolybdate $[Mo_3S_{13}]^{2-}$ Nanoclusters. *ACS Catalysis.* **2017**, *7*, 7126-7130.

[64] Jaramillo, T. F.; Jorgensen, K. P.; Bonde, J.; Nielsen, J. H.; Horch, S.; Chorkendorff, I. Identification of Active Edge Sites for Electrochemical $H_2$ Evolution from $MoS_2$ Nanocatalysts. *Science*. **2007**, *317*, 100-102.

[65] Khusnutdinova, D.; Beiler, A. M.; Wadsworth, B. L.; Jacob, S. I.; Moore, G. F. Metalloporphyrin-Modified Semiconductors for Solar Fuel Production. *Chemical science.* **2017**, *8*, 253-259.

[66] Gu, J.; Yan, Y.; Young, J. L.; Steirer, K. X.; Neale, N. R.; Turner, J. A. Water Reduction by a p-$GaInP_2$ Photoelectrode Stabilized by an Amorphous $TiO_2$ Coating and a Molecular Cobalt Catalyst. *Nature materials.* **2016**, *15*, 456-462.

[67] Jürgensen, A.; Moffat, J. B. The Stability of 12-Molybdosilicic, 12-Tungstosilicic, 12-Molybdophosphoric and 12-Tungstophosphoric Acids in Aqueous Solution at Various pH. *Catalysis letters.* **1995**, *34*, 237-244.

[68] Madou, M. J.; Loo, B. H.; Frese, K. W.; Morrison, S. R. Bulk and Surface Characterization of the Silicon Electrode. *Surface Science.* **1981**, *108*, 135-152.

[69] Shibahara, T.; Yamasaki, M.; Sakane, G.; Minami, K.; Yabuki, T.; Ichimura, A. Syntheses and Electrochemistry of Incomplete Cubane-Type Clusters with $M_3S_4$ Cores (M = Mo, W). X-Ray Structures of $[W_3S_4(H_2O)_9](CH_3C_6H_4SO_3)_4 \bullet 9H_2O$, $Na_2[W_3S_4(Hnta)_3] \bullet 5H_2O$, and $(bpyH)_5[W_3S_4(NCS)_9] \bullet 3H_2O$. *Inorganic Chemistry.* **1992**, *31*, 640-647.

[70] Sheldrick G.M. SADABS. Program for scaling, correction of area detector data. University of Göttingen, Germany, **1997**.

[71] Blessing R.H. An Empirical Correction for Absorption Anisotropy. *Acta Crystallographica*. **1995**, *A51*, 33-38.

[72] Sheldrick G.M. SHELX-TL version 5.03, Software Package for the Crystal Structure Determination, Siemens Analytical X-ray Instrument Division. Madison, WI USA, **1994**.

[73] Zhang, X. G. *Electrochemistry of silicon and its oxide*; Kluwer Academic: New York, **2001**, p 47.

[74] Powell, C. J.; Jablonski, A. *NIST Electron Effective Attenuation Length Database*; National Institute of Standards and Technology: Gaithersburg, MD, **2001**.

[75] Boudart, M. Turnover Rates in Heterogeneous Catalysis. *Chemical. Reviews.* **1995**, *95*, 661-666.

[76] Benck, J. D.; Hellstern, T. R.; Kibsgaard, J.; Chakthranont, P.; Jaramillo, T. F. Catalyzing the Hydrogen Evolution Reaction (HER) with Molybdenum Sulfide Nanomaterials. *ACS Catalysis.* **2014**, *4*, 3957-3971.

# Chapter 3. X-ray Absorption Spectroscopy Study of $Mo_3S_4$ based Polyoxothiometalate Electrocatalysts during HER

## 3.1 Introduction:

In **Chapter 2**, we have demonstrated that a *p*-type silicon photocathode coated with a Mo-based polyoxothiometalate electrocatalyst was catalytically more efficient than a photocathode coated with the parent thiomolybdate incorporating an organic ligand for the simulated sunlight-driven HER under acid pH conditions. However, the HER mechanism is still unclear which provides an interesting opportunity to explore the active properties of these deposited films. By using X-ray absorption spectroscopy (XAS), which is considered as a preferential tool for providing element-specific insights into materials, it is possible to explore the contribution and the electronic properties of each element within a material.[1] In this chapter, we report on the use of XAS for an in-depth understanding of HER catalytic mechanisms. Actually, XAS refers to how X-rays are absorbed by an atom at energies near and above the core-level binding energies of that particular atom. The absorption of X-rays on the high energy side of absorption is not monotonously altered in the condensed matter, but has a complicated behavior which extends beyond the edge up to about 1 keV. This non-monotonic variation has received the name of X-ray absorption fine structure (XAFS). XAFS is typically divided into two regimes: X-ray absorption near edge structure (XANES) and extended X-ray absorption fine structure (EXAFS). [2] Here, both of these two energetic domains have been explored to clarify the environmental structure around Mo and W atoms in $Mo_3S_4$-POM electrocatalysts on the silicon photocathode surface during *in operando* HER measurements. The structure of this chapter is as follows: Section 3.2 gives the general background of the technique and the theory of XAS. Section 3.3 presents a brief introduction to the synchrotron, as well as a description of the experimental methods and the host station where our XAS experiments were carried out. Section 3.4 discusses XAS spectra that describe the oxidation states of transition metal elements (Mo and W) in our samples and reference compounds, as well as their chemical environment changes during the HER electrolysis in acidic experimental conditions. Finally, the results are summarized and conclusions, in view of prediction for the catalytic reaction mechanism as well as possible improvements, are drawn in the section 3.5. Overall, in this study, comprehensive electronic structure studies, using XAS and photoelectrocatalytic investigations, suggest to advance on the determination of a HER mechanism.

## 3.2 Theory of X-ray Absorption Spectroscopy

Nowadays, a wide range of X-ray spectroscopic techniques such as X-ray photoelectron spectroscopy (XPS), X-ray diffraction (XRD), energy-dispersive X-ray spectroscopy (EDX) and X-ray absorption spectroscopy (XAS) are available for the characterization of electrocatalyst materials deposited at the photocathode surface for device applications. The focus of this chapter will be onto the combination

of XAS and photoelectrocatalytic investigations in order to investigate the local atomic structure, coordination number, valence state and hybridization of the probe atoms. To perform valuable X-ray spectroscopic experiments, an intense and tunable X-ray source is indispensable, which leads to the need for synchrotron radiation sources that are now available all over the world. The electrons inside the synchrotron ring are forced to move at a constant velocity with a circular trajectory for emitting X-rays. These X-rays are depending on the synchrotron ring, within the energy range from 0.1 to 100 keV, i.e. wavelength from 100 down to 0.1 Å, which almost covering the whole range of the atomic core energy level of binding energies and interatomic distances, respectively.

### 3.2.1 X-rays and Synchrotron as X-ray Source

X-rays are electromagnetic waves which were first discovered by a German physicist William Roentgen in 1895. Their wavelengths are much shorter than visible light, but longer than high energy gamma rays, as shown in **Figure 3-1**.

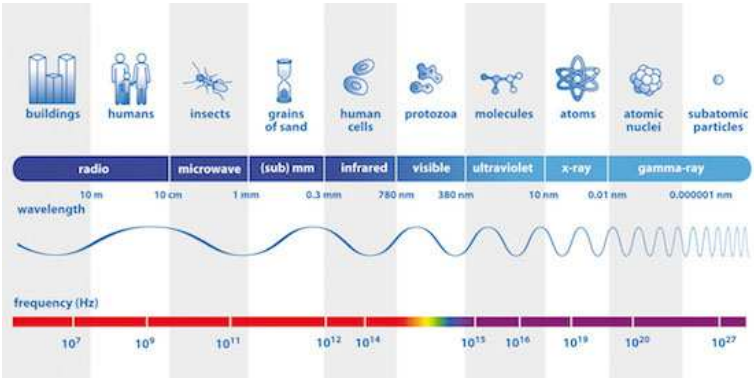


**Figure 3-1**: The electromagnetic spectrum, from radio waves to gamma-rays. [Image credits: Website of European Space Agency (ESA)]

For X-ray absorption spectroscopy analysis, the modern and most intense source of X-rays is a synchrotron. Comparing to an X-ray tube, the flux of X-radiation obtained from synchrotron sources is up to $10^{10}$ times more intense. In a synchrotron, the electrons are accelerated, then are directed into a storage ring with auxiliary components such as bending magnets and ondulators. The conversion from high-energy electron into light or some other forms of electromagnetic radiation can be supplied by this strong magnetic field perpendicular to the electron beam (**Figure 3-2**). In a synchrotron storage ring, the electrons with more than 1 GeV energies can be maintained for many hours. The most

important property of synchrotron radiation is its brightness, and because of its high vacuum environment, high polarization and stability, synchrotron radiation is considered as a unique and rather extraordinary source for a wide variety of science and technological experiments.[3]

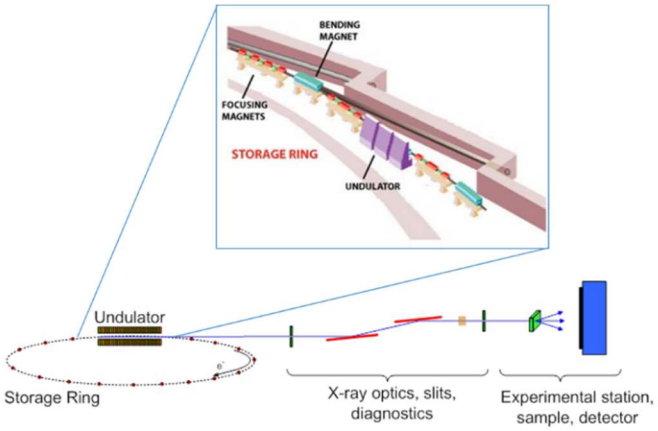


**Figure 3-2**: A synchrotron radiation beamline. [Image credits: Pablo. Fajardo, *Instrumentation Services and Development Division*, European Synchrotron Radiation Facility (ESRF), Grenoble.]

### 3.2.2 X-rays Absorption and Absorption Edges

When a beam of X-rays of the energy *E*, passes through a homogeneous sample of the thickness *x*, it looses intensity due to its interaction with the matter of the sample (**Figure 3-3**).

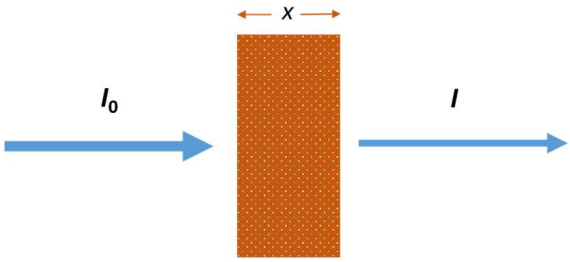


**Figure 3-3**: Simple scheme of an X-ray absorption measurement in transmission mode. Here *x* is the material thickness and $I_0$ and *I* are the initial and transmitted intensities, respectively.

In analogy to the Lambert-Beer law, this attenuation can be generally described by:

$$I\ (E) = I_0(E)e^{-\mu(E).x}$$

or

$$\ln\left(\frac{I}{I_0}\right) = -\mu(E).x$$

where $I_0(E)$ and $I(E)$ are the incident and transmitted X-ray intensities, and $\mu(E)$ is the linear absorption coefficient, which is related to the properties of the material and describes how strongly X-rays are absorbed as a function of X-ray energy $E$.[4,5] Absorption edge can be observed by an absorption increasing drastically at certain energies, when the energy of the incident photons is just sufficient to cause excitation of a core electron of the absorbing atom to a continuum state, and producing a photoelectron. Furthermore, absorbed radiation energies at these edges correspond to the binding energies of electrons in the K, $L_I$, $L_{II}$, $L_{III}$, etc, shells ($1s_{1/2}$, $2s_{1/2}$, $2p_{1/2}$ and $2p_{3/2}$ orbitals or states) of the absorbing elements (**Figure 3-4**), e.g., the K absorption edge arises from the electronic transition from innermost 1s state (K level) to unoccupied state above the Fermi energy ($E_F$) level. Apart from this, the absorption coefficient decreases monotonically with increasing energy, until the next absorption edge is reached,[2] e.g., two major transitions (K, and L edges) for Mo by X-ray absorption spectrum are described in **Figure 3-5**.

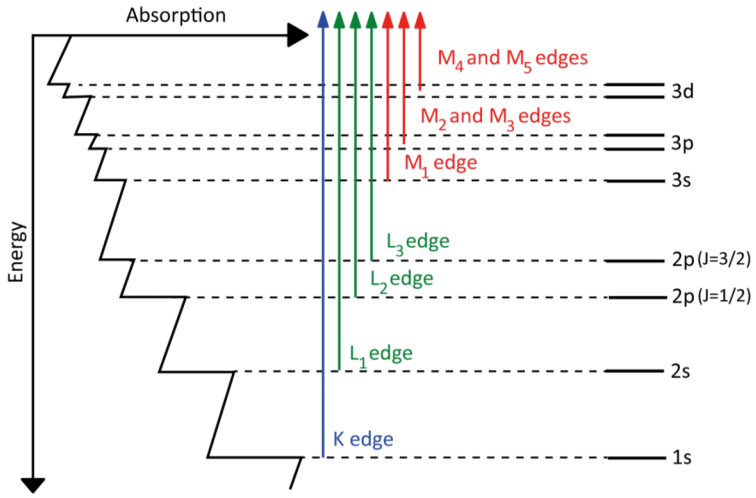


**Figure 3-4**: Transitions of the K, L, and M edges that contribute to XAS edges. (Figure downloaded from *Wikimedia Commons*: https://en.wikipedia.org/wiki/X-ray_absorption_spectroscopy)

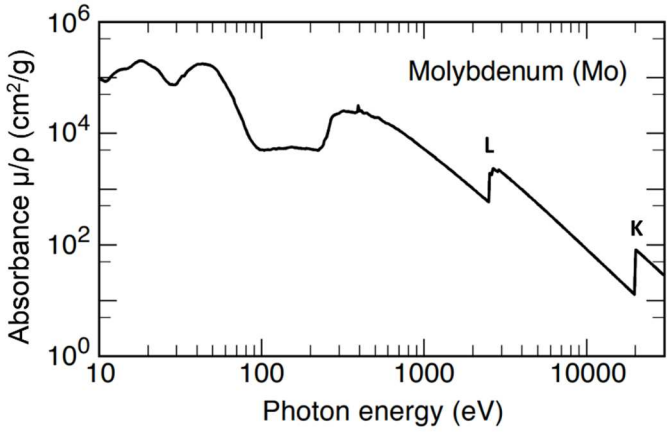


**Figure 3-5**: X-ray absorption spectrum for Mo. L edge in the 2000 - 3000 eV range and K edge appeared at about 20,000 eV, corresponding to excitation of an electron from *n*=1 and 2 shells, respectively. (*n*: principle quantum number of the electron.) [Image credits: Website of European Synchrotron Radiation Facility (ESRF), Grenoble.]

### 3.2.3 X-ray Absorption Spectroscopy

In a XAS experiment, X-rays emerging from a synchrotron, are tuned according to an 'absorption edge' of element, the absorption is detected in dependence on the X-ray energy. These absorption edges are characteristic for each element due to the emission of a deep-bound electron. These characteristics make XAS element-specific and are important when dealing with. Most of the absorption spectrum is quite smooth and their oscillatory features are able to be found directly above an edge, which called fine structure.[2]

Traditionally, this fine structure is divided into two energy regions. The first termed as X-ray absorption near edge structure (XANES), occurs in the region from before the edge to approximately 40 eV above the edge, which provides mainly information about the electronic and geometric structures of the chosen element. The second termed as the extended X-ray absorption fine-structure spectroscopy (EXAFS), by which the local atomic environment from about 0 to 10 Å around the chosen atoms is accessible, extends from about 40 eV to 1000 eV above the edge. Actually, both XANES and EXAFS provide element-specific insights into materials. In the EXAFS regime, which is far above an absorption edge and arises from the interaction of the absorbing atom with photoelectron waves backscattered by neighboring atoms, single scattering paths (in which the photoelectron scatters from the only atom before returning to the central atom) usually apply and near-neighbor distances and coordination numbers can readily be obtained. For the XANES, it is often complicated by multiple-scattering effects (in which the photoelectron scatters from more than one atom before returning to the central atom)

and may in consequence produce a spectrum rich in structure. However, multiple-scattering is harder to interpret and simulate than single-scattering.[6, 7] In **Figure 3-6**, a typical K-edge X-ray absorption spectrum for a transition metal is shown along with the standard division into two regions, i.e., XANES and EXAFS.

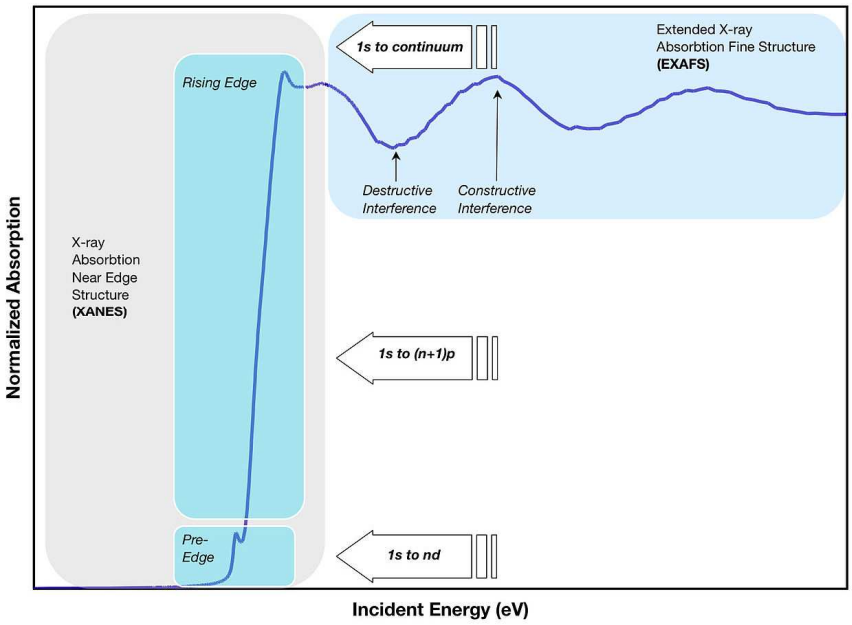


**Figure 3-6**: K-edge X-ray absorption spectrum of a transition metal compound and its division into two regions (XANES and EXAFS). Dominant electron transitions (1s to *n* = 3, 4, or 5) are assigned to each region. [8]

There are several XAFS (Total energy range XAFS = XANES + EXAFS) detection modes, e.g., transmission,[9] electron yield XAFS,[10] fluorescence,[11] and partial fluorescence yield.[12] Among them, the most common detection modes during a XAS experiment are transmission and fluorescence detections (**Figure 3.7**).

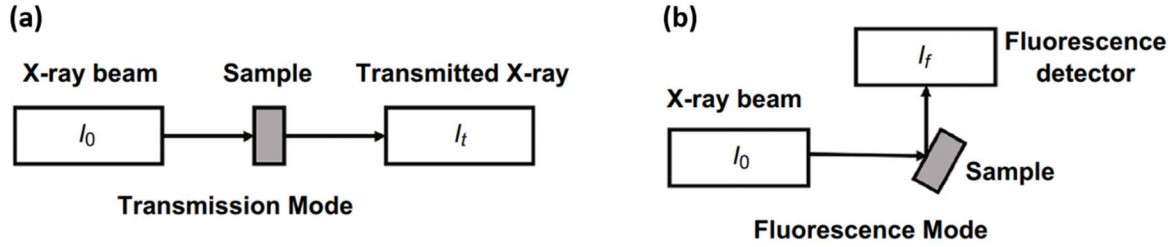


**Figure 3-7**: Experimental setup for transmission and fluorescence XAFS detection modes.[13]

- *Transmission detection of XAFS*

As shown in **Figure 3-7 (a)**, a XAFS spectrum originates from the fact that the probability of an electron to be ejected from a core level is dependent on the energy of the incoming beam ($I_0$). The X-ray interacts with the sample of interest and the intensity of the transmitted beam after the sample ($I_t$) is measured, while the energy of the X-rays ($I_0$) is scanned during an experiment. For the transmission detection, a homogeneous sample is required and is an important factor because variations in the thickness or pinholes in the pellet can significantly affect the spectral shape by introducing a non-linear response.[14] Moreover, transmission mode experiments are standard and suitable for hard X-rays, which have higher frequencies and higher energies compare to soft X-rays. In contrast, soft X-rays with lower frequency and lower energy are usually not measured in transmission mode.[16]

- *Fluorescence detection of XAFS*

Fluorescence mode measures the emitted X-rays from the elements [**Figure 3-7 (b)**]. The intensity of this fluorescence is proportional to the absorption caused by the investigated element, which introduces a change of spectral shape. The self-absorption or saturation effects can also affect the fluorescence intensity. Thus, this mode is well-adapted for diluted and non-homogeneous samples.[15]

#### 3.2.3.1 XANES

XANES spectroscopy using synchrotron radiation is a well-established technique where a photon is absorbed and an electron is excited from a core state to an empty state. The photon energy has to be equal or higher than the binding energy of this core-level to excite an electron in a given core-level. When the photon energy is scanned, this excitation gives rise to the opening of a new absorption channel, and the energy of an absorption edge therefore corresponds to the core-level energy, which is characteristic for each element, making XANES an element-selective technique.[16] For a XANES analysis of metal K-edges, the 1s edge of the 3d transition metals, which shows fine structure and edge shifts, can be used without the explicit calculation of the density of states. For example, the $Mo^{4+}$ edges are shifted to higher energy with respect to the $Mo^{3+}$ edges. The shift to higher energies with higher oxidation state is a general phenomenon that can be used to determine the oxidation state of 3d transition metals in unknown systems.

As a result, XANES spectrum can be described qualitatively (and nearly quantitatively) in terms of coordination chemistry, molecular orbitals, band-structure and multiple-scattering. Actually, a lot of

chemical information are obtainable from the XANES region, such as formal valence state, ligand type, and coordination environment, which can be determined by the edge position and shape of XANES spectrum. Hence, edge features reflect oxidation states and coordination environments in the vicinity of the absorber element. As a fingerprinting technique based on edge features, XANES is easier to interpret than the extraction and the fit of the EXAFS spectrum. Decomposition of the spectral components can differentiate between different site symmetries and assist in quantifying oxidation states.[2, 17]

3.2.3.2 EXAFS

The EXAFS spectrum results from an oscillatory modulation in the X-ray absorption coefficient on the high-energy side of the absorption edge.[18] The ability of EXAFS to provide information about an atom's local environment has widespread application. Analysis of the EXAFS spectrum yields the number and type of atoms and accurate absorber-neighbor distances. Actually, the EXAFS region is sensitive to the radial distribution of electron density around the absorbing atoms and is used for quantitative determination of bond length and coordination number.

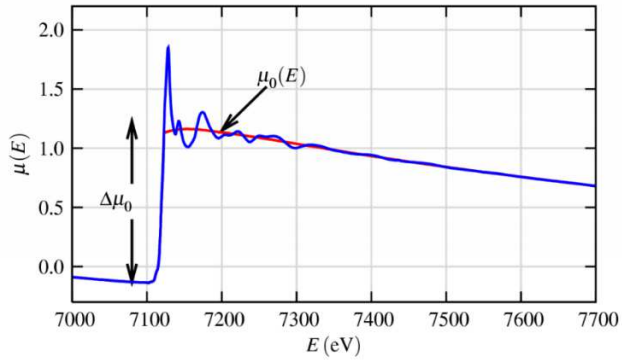


**Figure 3-8**: An example of X-ray absorption spectrum, Fe K-edge X (FeO), $\mu$ is shown with smooth background function $\mu_0$ and the edge-step $\Delta\mu_0$.[19]

From the absorption spectrum shown in **Figure 3-8**, the EXAFS function *χ(k)* can be obtained:

$$\chi(k) = \frac{\mu - \mu_0}{\Delta\mu_0}$$

where $\mu_0$ is the hypothetical smooth background absorption coefficient due to the transition of interest, and $\mu$ is the measured absorption coefficient, and $\Delta\mu_0$ is the measured jump in the absorption $\mu$ at the threshold energy $E_0$.

The appearance of EXAFS is considered as the origin of the EXAFS oscillations (**Figure 3-9**). If the binding energy of the core electron is $E_0$, absorption of an X-ray photon of energy $E > E_0$ generates a photoelectron of energy $E - E_0$. Because EXAFS is better understood in terms of the wave behavior of the photo-electron created in the absorption process, it is common to convert the X-ray energy to $k$, the wavenumber of the photo-electron, which has dimension of 1/distance and could be defined as:

$$k = \sqrt{\frac{2m(E - E_0)}{h^2}}$$

where $m$ is the electron mass. From **Figure 3-8**, the EXAFS is oscillatory and decays quickly with $k$. Furthermore, EXAFS curves are often presented with $\chi(k)$ multiplied by a power of $k$ typically $k^2$ or $k^3$ in order to emphasize the oscillations at high $k$ values.[19]

The different beatings observed in the oscillations correspond to different near-neighbor coordination shells, which can be described and modeled according to the following EXAFS equation:

$$\chi(k) = \sum_j \frac{N_j f_j(k) e^{-2k^2\sigma_j^2}}{kR_j^2} sin\left[2kR_j + \delta_j(k)\right]$$

where $f(k)$ and $\delta(k)$ are scattering properties, amplitude and phase, respectively, of the neighboring atoms related to the excited atom, $N$ is the number of neighboring atoms, $R$ is the distance from the absorbing atom to the neighboring atoms, and $\sigma^2$ is the disorder in the neighbor distance (Debye-Waller). From this EXAFS equation, $N$, $R$, and $\sigma^2$ can be determined by knowing the scattering amplitude $f(k)$ and phase-shift $\delta(k)$ obtained using reference compounds or *ab-initio* calculations.

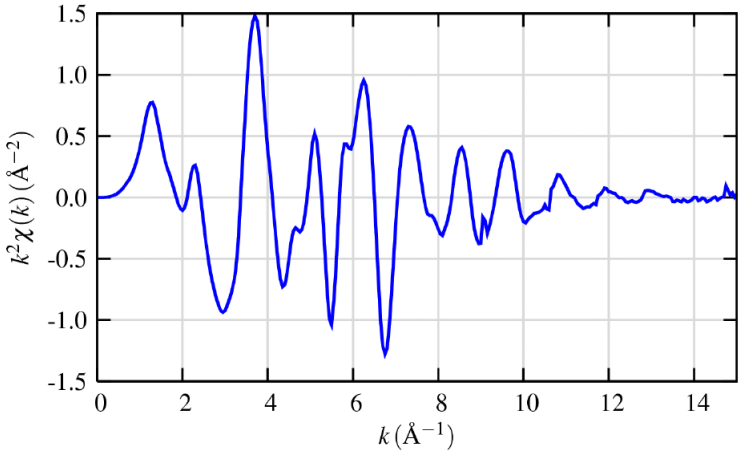


**Figure 3-9**: EXAFS spectrum of FeO at Fe K-edge.[19]

## 3.3 Experimental Section

### 3.3.1 ROCK Beamline at SOLEIL

3.3.1.1 Quick-EXAFS beamline

The SOLEIL's ROCK (Rocking Optics for Chemical Kinetics) beamline, funded by the French *Agence Nationale de la Recherche* in the framework of the national program, is one of the dedicated infrastructures for the *operando* characterization of materials by time-resolved Quick-EXAFS. Quick-EXAFS can supply a sub-second time resolution in the monitoring of kinetics by the advent of 3rd generation synchrotron radiation, and allows an access to a deeper and more accurate temporal description of the chemical species involved during operative use of these materials. The research of catalytic or (photo-) electrochemical properties of materials used for energy applications and their local order evolution can be simultaneously achieved onto this X-ray Absorption beamline.[20]

3.3.1.2 ROCK Beamline Design and Experimental Conditions

The ROCK beamline is devoted to the study of fast kinetic process in nanomaterials used in catalysis and batteries. Quick-EXAFS monochromators installed at ROCK can oscillate over an angular amplitude (Δθ) of central Bragg angle up to 4°. The Si (111) and Si (220) crystals equipping those monochromators allow to work at energies between 4 and 43 keV. These monochromators are surrounded by optics designed to obtain the highest flux possible delivered by a SOLEIL's bending magnet source. The reactions of several distinct elements under *in operando* conditions can be carried out on this designed optical setup. The optical layout of ROCK is shown schematically in **Figure 3-10**.

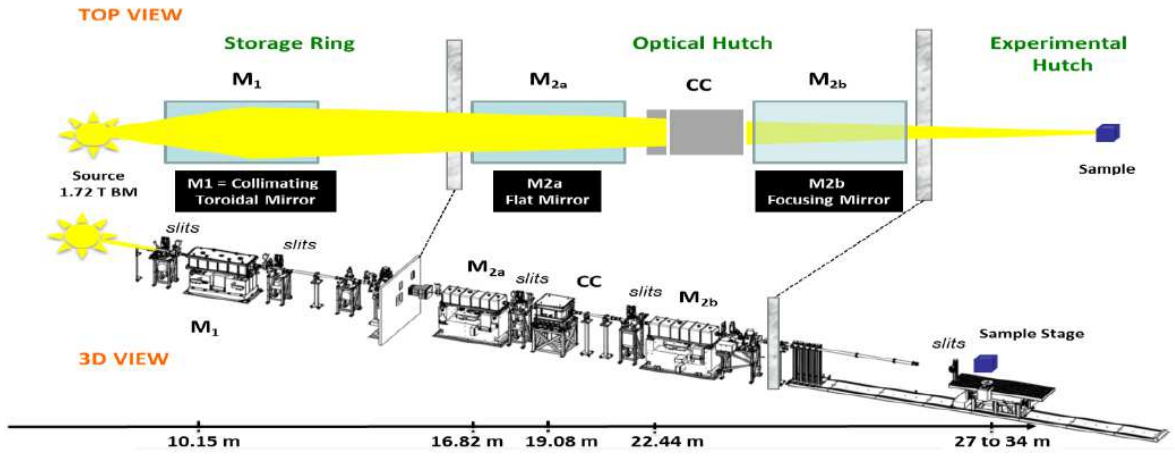


**Figure 3-10**: Optical layout of the ROCK beamline.[20]

Monochromatic beam current of 500 mA is applied at ROCK beamline in this experiment, and top-up operation mode is introduced in light sources. In top-up operation, the beam losses can be compensated by frequent injections into the storage ring. The aim of a top-up operation is to overcome lifetime limitations and to keep a constant photon flux at the beamline by providing practically constant beam current in the storage ring.[21]

### 3.3.2 Catalyst-Modified Photocathodes Preparation

A piece of *p*-type (15-20 Ω cm resistivity, boron-doped, 300 µm thickness, Siltronix) Si (511) wafer was sonicated for 10 min successively in acetone, ethanol, and ultrapure 18.2 MΩ cm water (Veolia Water STI) to degrease it. It was then cleaned with piranha solution at 100 °C for 30 min followed by copious rinsing with ultrapure water to eliminate heavy metals and organic residues. The wafer was cut in the size of ca. 1.5 cm × 1.5 cm which is suitable for our electrochemical flow cell. The electrochemical XAS experimental cell, made of acid and alkali resistant materials, will be presented in section 3.3.3. After preparation, each prepared silicon surface was freshly hydrogenated by completely immersing into HF 10% wt (~ 5.7 M) for 2 min. The surface was then copiously rinsed with ultrapure water and quickly dried under an argon stream.

The $[Mo_3S_4(acac\text{-}Bu)_3(H_2O)_3]Cl.H_2O$ and $(TBA)_6[PW_{11}O_{39}Mo_3S_4]_2(H_2O)_3(\mu\text{-}OH)_2.15H_2O$ solutions were prepared at 1 mM in acetonitrile (anhydrous, 99.8%, from Sigma) by dissolving these two clusters followed by a sonication for ca. 15 min. The $(TBA)_6[PW_{11}O_{39}Mo_3S_4(H_2O)_3(\mu\text{-}OH)_2].15H_2O$ solution was then diluted with acetonitrile to the final concentration of 0.1 mM. The respective concentrations of these two cluster solutions correspond to the optimal concentrations leading to maximum catalytic activity (see section **2.2.2**). The freshly hydrogenated *p*-type Si (511) surface was modified by the drop-casting method with each cluster using the $[Mo_3S_4(acac\text{-}Bu)_3(H_2O)_3]Cl.H_2O$ or $(TBA)_6[PW_{11}O_{39}Mo_3S_4]_2(H_2O)_3(\mu\text{-}OH)_2.15H_2O$ solution at 1 mM or 0.1 mM in acetonitrile, respectively. After evaporation of the solvent at room temperature for 5-10 min, the modified silicon surface was further positioned into the experimental cell and used for electrochemical and XAS measurements.

NB: in a preliminary study, we have used *p*-type Si(100) samples on the ROCK beamline, but intense diffraction peaks of silicon were visible on the EXAFS spectra. For that reason, we have then switched to less diffracting Si(511).

### 3.3.3 *In Operando* Electrochemical XAS Measurements

A three-dimensional (3D) printed electrochemical flow cell was fabricated as shown in **Figure 3-11**. The working electrode compartment has an incoming X-ray window of 0.6 cm × 0.4 cm in front of the modified silicon surface. This window was covered by a Mylar film by means of an O-ring seal rubber from the inside part of the cell in order to ensure X-ray transmission and to achieve sealing condition during the XAS electrochemical experiments. A Pt wire as reference electrode and a carbon counter electrode were used to connect the working compartment through two holes of 0.1 cm in diameter at the corner of the cell.

For electrochemical measurements, an Ohmic contact was established between the backside of Si surface and an steel base plate (for fluorescence mode) or a steel base plate with a ca. 7 mm-diameter hole in its center (for transmission mode). This Ohmic contact was achieved by first scrubbing the backside of surface with sand paper and a diamond glass cutter and then applying a droplet of InGa eutectic (99.99%, Alfa Aesar). Then the cluster modified silicon surface was fixed in the middle of the working compartment. The inlet and outlet of the device were designed in order to realize the electrolyte flow from the base to the top of the cell during the XAS electrochemical experiments.

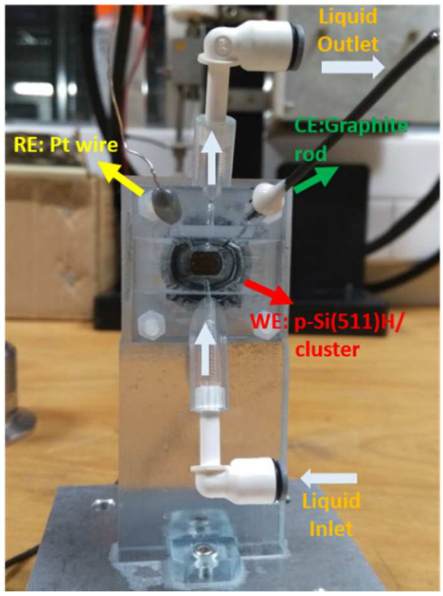


**Figure 3-11**: Photograph of the electrochemical cell used for *in operando* experimental setup.

For Mo K-edge and W K-edge XAS measurements, the X-ray absorption spectra were recorded at different positions on the prepared silicon electrode to check the homogeneity of the studied material and its stability under the beam. For each element, the spectra were first recorded on the dry

deposited cluster film in air and then recorded in pH 0.3 sulfuric acid solution under static- or steady-state flow conditions.

For *in operando* X-ray spectroscopy combined with electrochemistry, our electrochemical cell was set on ROCK beamline in fluorescence mode for Mo and W K-edge measurements (as shown in **Figure 3-12**) or in transmission mode only for W K-edge measurements. For comparison, the X-ray absorption spectra were recorded under precatalytic (before electrolysis at open circuit potential) and catalytic conditions (after 1h, 2h and 4h electrolysis at -0.52 V vs RHE) in pH 0.3 sulfuric acid solution, respectively. A chronoamperometry curve was also recorded during the XAS measurement.

Measurements of reference compounds $Mo^{(+IV)}S_2$, $Mo^{(+IV)}O_2$, $Mo^{(+VI)}O_3$ and $(NH_4)_2Mo^{(+VI)}S_4$ as well as our catalyst powders $[Mo_3S_4(acac\text{-}Bu)_3(H_2O)_3]Cl.H_2O$ and $(TBA)_6[PW_{11}O_{39}Mo_3S_4]_2(H_2O)_3(\mu\text{-}OH)_2.15H_2O$ were also carried out. A pellet (5 mm diameter) of each compound was prepared and introduced onto the sample stage, then measured in the transmission mode at the Mo K-edge at room temperature. All our XAS spectra were recorded with 100 ms step time. Spectra of the XANES region (19960.0 eV to 20072.0 eV) with a step width of 0.5 eV were recorded. Spectra of the EXAFS region (20072.0 eV to 21220.0 eV) were recorded with a step width of 1 eV.

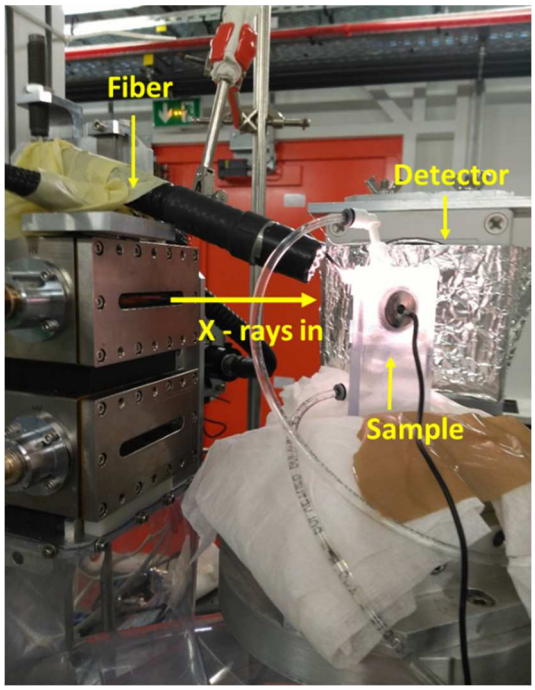


**Figure 3-12**: Experimental setup for *in operando* XAS electrochemical tests (in fluorescence mode) at ROCK beamline.

## 3.4 Results and Discussion

### 3.4.1 Mo K-edge XANES

All the Mo K-edge XANES spectra have been normalized and are presented from 19960 eV to 20090 eV for both reference compounds and catalysts. In the XANES energy range, the catalyst-modified single crystal silicon (511) did not show any X-ray diffraction (XRD) signal. We therefore used XANES to study the evolution of Mo valence and structural information for our electrocatalysts using the fingerprint method.

3.4.1.1 Mo K-edge XANES spectra of reference compounds

Reference compounds with different Mo oxidation states from $Mo^{(+III)}$ to $Mo^{(+VI)}$, as well as different sulfur or oxide ligands were selected in our study, aiming at understanding the trend of Mo pre-edge and edge energy. The Mo-K edge XAS measurements of the reference compounds $Mo^{(+III)}Cl_3$, $Mo^{(+IV)}S_2$, $Mo^{(+IV)}O_2$, $Mo^{(+VI)}O_3$ and $(NH_4)_2Mo^{(+VI)}S_4$ were carried out and their XANES spectra are shown in **Figure 3-13 (a)** and **Figure 3-13 (b)**.

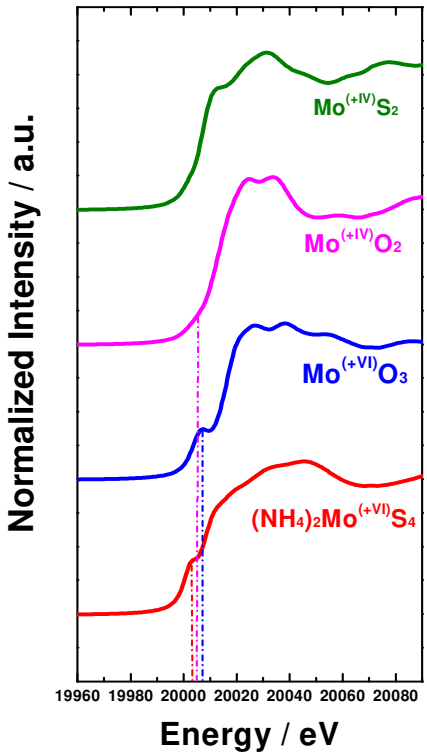


**Figure 3-13 (a)**: Comparison of Mo K-edge XANES spectra for reference compounds in the pre-edge region (energy positions indicated by dashed lines).

The discussion of Mo K-edge XANES spectra can be divided into two sections, the pre-edge peak and the edge position:

- *Pre-edge peak of XANES spectra*

Much of the interest in the XANES spectra of Mo-containing reference compounds was focused on the pre-edge peak found at the left side of the Mo K-edge, especially $MoO_2$, $MoO_3$, and $(NH_4)_2MoS_4$ in **Figure 3-13 (a)**.

First, the intensity of pre-edge peak is sensitive to the symmetry of the absorbing atom and can provide structural information about the first coordination shell. For Mo, the pre-edge peak is attributed to a 1s → 4d transition which is dipole-forbidden for structures having an inversion center. Therefore, compounds in which the absorbing atom is tetrahedrally coordinated show more intense pre-edge peaks than those observed in case of octahedrally coordinated compounds, which are usually weak.[22] This is illustrated in **Figure 3-13 (a)** where the pre-edge peak of tetrahedrally coordinated $(NH_4)_2MoS_4$ has the highest intensity. The first coordination shells of $MoS_2$ and $MoO_2$ are distorted octahedra, which present a weak pre-edge.

Second, when the oxidation state of Mo in the reference compounds increases, the pre-edge intensity increases because of a higher transition probability. For example, higher oxidation state of Mo in $Mo^{(+VI)}O_3$ and $(NH_4)_2Mo^{(+VI)}S_4$ presents a higher pre-edge intensity compared with $Mo^{(+IV)}S_2$ and $Mo^{(+IV)}O_2$ (**Figure 3-13 (a)**). Furthermore, the number of O atoms coordinated with the absorbing Mo atom can also influence the pre-edge peak position. If we compare $MoO_3$ and $(NH_4)_2MoS_4$, having the same (+VI) oxidation state, one can observed a shift toward higher energy of the pre-edge peak for $MoO_3$. This is due to the more favorable π to π* transition for the O atom (in $MoO_3$) with respect to the S atom (in $(NH_4)_2MoS_4$) leading to a higher 1s → 4d transition energy.

We can therefore conclude that the pre-edge energy is determined not only by the oxidation state of Mo, but also by the number of coordinating O atoms.

- *Edge of XANES spectra*

The edge of Mo K-edge XANES spectra is due to core transitions from 1s to 5p ($5p_x$, $5p_y$, and $5p_z$ orbitals) final states. Like the pre-edge, the oxidation state and coordinated atoms influence both Mo K-edge shape and energy. In **Figure 3-13 (b)**, Mo-K edge XANES spectra of different reference compounds are presented and compared. A comparison of the position in energy at the half height of the edge of each XANES spectrum was done [dashed lines in **Figure 3-13 (b)**]. Indeed, the edges of XANES presented by

large energy intervals are difficult to be compared directly. As shown in **Figure 3-13 (b)**, XANES spectrum of $MoO_3$, corresponding to a (+VI) oxidation state of Mo, shows a value equal to 20016.6 eV. This value is higher ($\Delta E$ = 3.1 eV) than the one of $MoO_2$, corresponding to a (+IV) oxidation state of Mo. The same comparison can be done between $MoS_2$ and $MoO_2$ [both at the same (+IV) oxidation state]. The edge energy of the $MoO_2$ spectrum is higher than the one of the $MoS_2$ compound ($\Delta E$ = 6.8 eV). This is in accordance with a previous publication,[23] where the XANES spectrum of $MoO_2$ displays a higher edge energy due to its coordinated O atoms compared to the S atoms, despite the identical oxidation state of $Mo^{(+IV)}$. This feature has also been confirmed with the reference compounds $(NH_4)_2MoS_4$ ($\Delta E$ = 8.1 eV), which contains Mo $^{(+VI)}$ and S coordinating atoms, and $MoO_3$ ($Mo^{(+VI)}$ and O atoms).

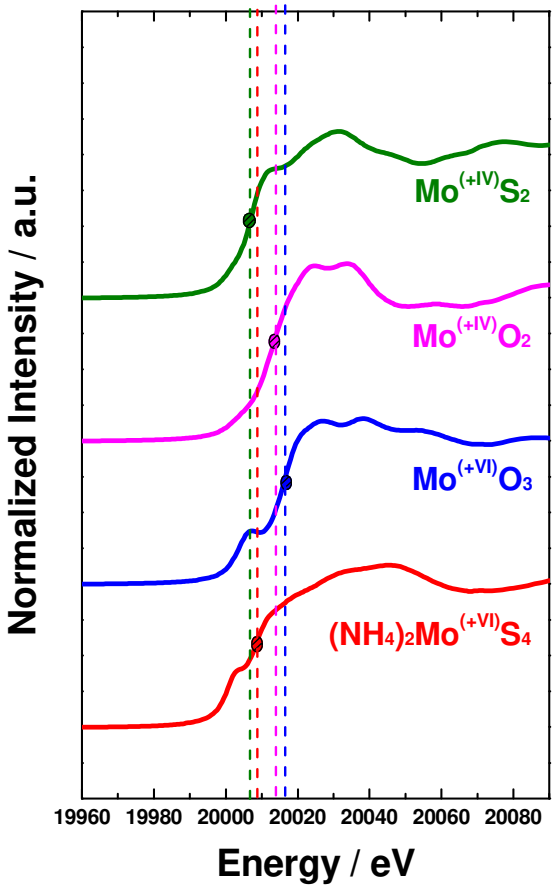


**Figure 3-13 (b)**: Comparison of Mo K-edge XANES spectra for reference compounds in the edge part (energy positions indicated by dashed lines).

3.4.1.2 Mo K-edge XANES spectra of catalysts

XANES spectra (Mo K-edge) of $[Mo_3S_4(acac\text{-}Bu)_3(H_2O)_3]Cl.H_2O$ and $(TBA)_6[PW_{11}O_{39}Mo_3S_4]_2(H_2O)_3(\mu\text{-}OH)_2.15H_2O$ (abbreviated as $Mo_3S_4$-POM) catalysts were recorded in powder form (pellets) and compared to those of the reference compounds (**Figure 3-14**). Both catalysts contain $Mo^{(+IV)}$ and S coordinating atoms. As expected, their Mo K-edge XANES spectra are similar and present a good match with the $Mo_3S_4$ reference compound reported in literature.[23] Moreover, its edge energy (20008.1 eV and 20007.4 eV) are close to the one of $MoS_2$ reference compound (20006.7 eV), which has the same oxidation state. In addition, their edge energies are slightly lower than the one of $(NH_4)_2MoS_4$ (20008.5 eV), which has an identical number of coordinated S atoms, but a higher oxidation state (+VI).

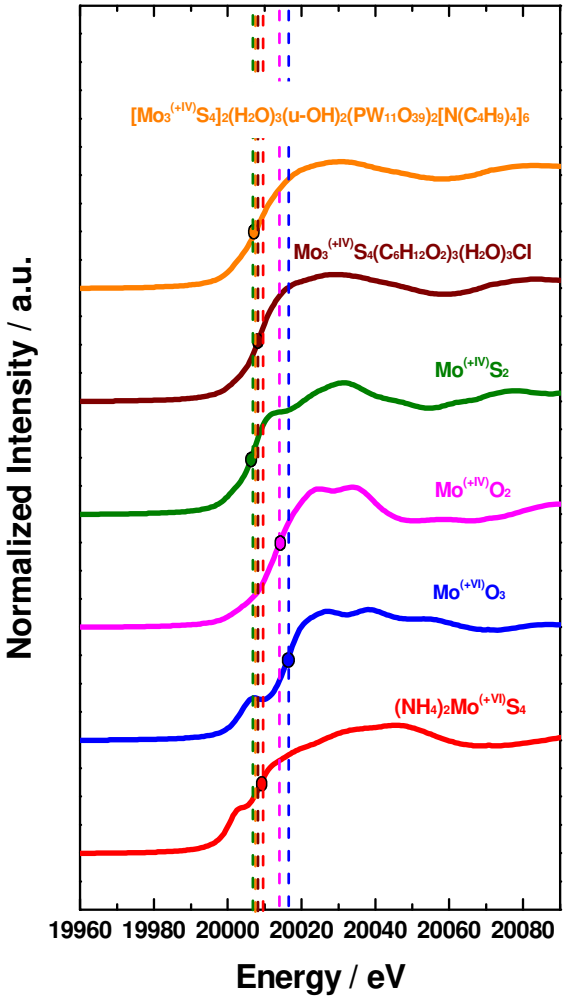


**Figure 3-14**: Comparison of rising edge energy (dashed lines) in Mo K-edge XANES spectra for $[Mo_3S_4(acac\text{-}Bu)_3(H_2O)_3]Cl.H_2O$, $Mo_3S_4$-POM catalysts (in the form of pellets) and reference compounds.

3.4.1.3 Mo K-edge XANES of $Mo_3S_4$-POM catalyst under precatalytic and catalytic conditions

The Mo K-edge XANES spectra were recorded *in operando* under precatalytic (at the OCP under illumination) and catalytic conditions (at -0.52 V vs RHE under illumination) (**Figure 3-15**) using a custom-made spectroelectrochemical flow cell described in Section **3.3.3**. We have recorded the Mo K-edge XANES spectra of $Mo_3S_4$-POM film deposited on a *p*-type Si (511) photocathode surface before (0 h) and after 2 h, 3 h, and 4 h electrolysis at -0.52 V vs. RHE (conversion of potentials vs. Pt reference electrode to reversible hydrogen electrode following $E_{RHE} = E_{Pt} + 0.48$ V in this work) under illumination using an optical fiber. A shift of the pre-edge peak to higher energies was observed during the first 4 hours electrolysis. Interestingly, for an electrochemical reduction process, it is expected that the oxidation state of Mo should be decreased, which could be theoretically indicated by a decreasing pre-edge energy. However, we found that the pre-edge energy of Mo increased during the electrolytic process in **Figure 3-15**. In this case, this opposite trend would be rather consistent with changes in the Mo environment resulting from the substitution of S coordinating atoms by O atoms. Such a result indicates that the electrochemically reduced $Mo_3S_4$-POM electrocatalyst is a mixture of coordinating species, which is in agreement with our previous work,[24] and can be described as $[Mo_3O_{4-n}S_n]^{4+}$-POM. Moreover, the intensity of the pre-edge peak decreased gradually during the electrolysis process, until 3 hours after electrolysis. The decrease of the pre-edge peak suggests that the newly formed species were most likely structurally octahedral coordinated Mo species (Mo-O). Furthermore, the same trend is observed for the edge energy under precatalytic and catalytic conditions. Indeed, a shift to higher energies is evidenced in **Figure 3-16** during 4 h electrolysis process. The superimposition of the Mo K-edge XANES spectra shown in **Figure 3-17** underlines that the edge peak intensity increases together with the decreasing pre-edge peak intensity. This also indicates a symmetry change of the first Mo coordination shell from tetrahedral to octahedral coordination during electrolysis process.[25,26]

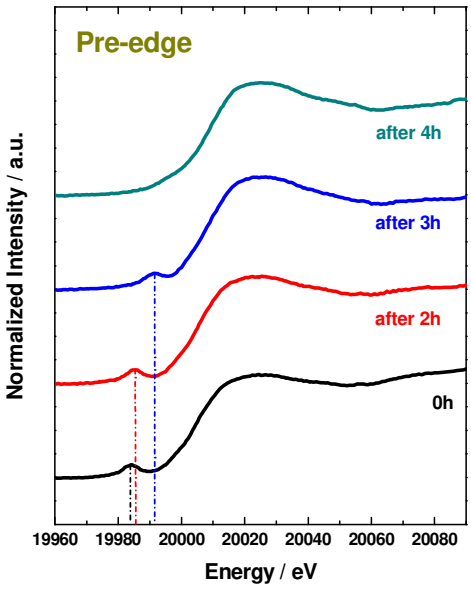


**Figure 3-15**: Comparison of the pre-edge peak position (dashed lines) in Mo K-edge XANES spectra of the $Mo_3S_4$-POM catalyst under precatalytic and catalytic conditions in 1.0 mol $L^{-1}$ $H_2SO_4$ (pH = 0.3) solution at -0.52 V vs RHE under illumination.

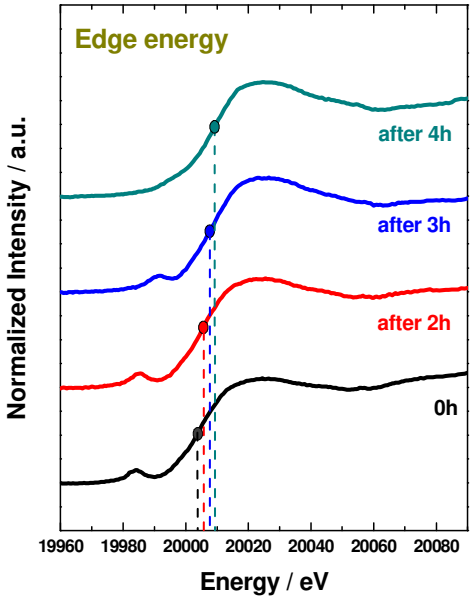


**Figure 3-16**: Comparison of the edge energy (dashed lines) in Mo K-edge XANES spectra of the $Mo_3S_4$-POM catalyst under precatalytic and catalytic conditions in 1.0 mol $L^{-1}$ $H_2SO_4$ (pH = 0.3) solution at -0.52 V vs RHE under illumination.

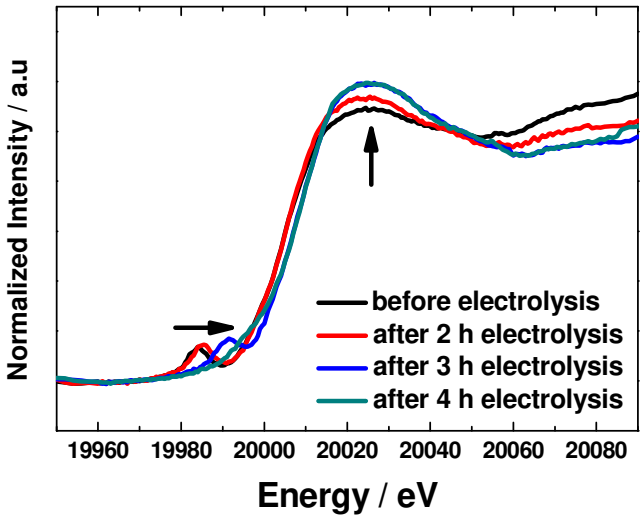


**Figure 3-17**: Comparison of the edge peak intensity in Mo K-edge XANES spectra of the $Mo_3S_4$-POM catalyst under precatalytic and catalytic conditions in 1.0 mol $L^{-1}$ $H_2SO_4$ (pH = 0.3) solution at -0.52 V vs RHE under illumination.

3.4.1.4 Electrochemical results during XANES measurements

The electrochemical response of the $Mo_3S_4$-POM modified *p*-type Si(511) photocathode at pH 0.3 during XANES measurements is depicted in **Figure 3-18** (NB: all potentials are referred to the RHE). Before electrolysis (precatalytic state), linear sweep voltammetry (LSV) curves of the $Mo_3S_4$-POM catalyst modified photocathode were recorded in the dark then under illumination. As expected for a *p*-type semiconductor photocathode, no significant photocurrent was measured in the dark, while the LSV curve under illumination was similar to that reported in our previous Chapter 2, and yielded a light-limited catalytic current density of ca. -19 mA $cm^{-2}$ at -1.02 V vs. RHE (blue line in **Figure 3-18**). After 7.5 h electrolysis, a significant photocurrent was also found under illumination when compared with the situation in the dark. Importantly, the LSV curve has shifted to more positive potentials, indicating that the $Mo_3S_4$-POM modified photocathode after electrolysis was considerably catalytically superior to that before electrolysis. Moreover, the light-limited catalytic photocurrent density increased to ca. -22 mA $cm^{-2}$ (red line in **Figure 3-18**). Overall, such observations reveal that the $Mo_3S_4$-POM modified *p*-type Si(511) photocathode maintains its HER activity after electrolysis.

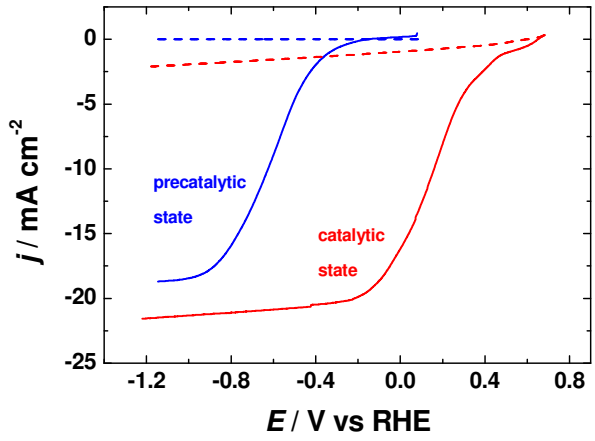


**Figure 3-18**: LSV curves of the $Mo_3S_4$-POM catalyst modified *p*-type Si(511) photocathode before (blue lines) and after 7.5 h cathodic electrolysis (red lines) under illumination (solid lines) and in the dark (dashed lines). Electrolyte: 1.0 mol $L^{-1}$ $H_2SO_4$ (pH = 0.3) solution.

The controlled-potential electrolysis test of $Mo_3S_4$-POM modified *p*-type Si(511) photocathode was carried out for more than 7.5 h in the electrolytic medium during an *in operando* XAS experiment. Interestingly, as shown in **Figure 3-19**, the shape of the chronoamperometric curve in the first 2.8 h is similar to that of the *I* – *t* curve monitored for the $Mo_3S_4(AsW_{12})$ modified photocathode during the long-term stability test (see section **2.2.5**). Cathodic photocurrent densities increased slightly (from -8 to -11 mA $cm^{-2}$) at the beginning of the electrolysis process, which is attributed to the catalyst desorption at the Si/catalyst interface yielding an increase in the light absorption by silicon, until reaching a stable state. In addition, an abrupt increase of ca. -8 mA $cm^{-2}$ (from -11 to -19 mA $cm^{-2}$) of the photocurrent density was noticed after 3 h electrolysis. We believe that this unexpected event was caused by a brutal change of the operating conditions that happened during the test (in spite of us). Indeed such a drastic photocurrent change could have been caused by, for instance, a drift of the illumination spot or the breaking of the sample. Note that this measurement was performed overnight and unfortunately could not be repeated because of the limited beamtime.

We consider that our XAS results obtained at 3 h and 4 h, i.e. after the abrupt photocurrent change, are also worth to compare with those recorded previously (at 0 h and 2 h). Consequently, any conclusions can not be drawn from such XAS spectra even though the significant changes observed during this period would support changes in both the oxidation state and the coordination of Mo. Similarly, we speculate that the post-electrolysis changes observed in the LSV response are probably affected in the same manner by this unexpected event (**Figure 3-18**).

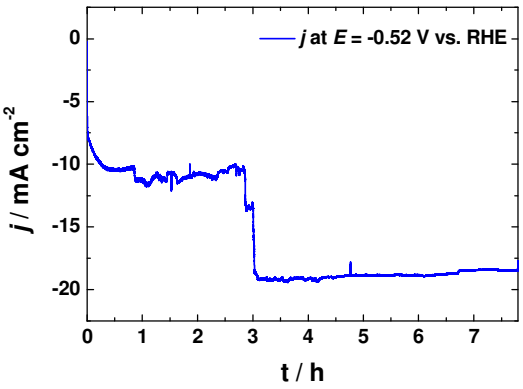


**Figure 3-19**: Photocurrent density-time curve under continuous illumination obtained during the controlled potential electrolysis at -0.52 V vs RHE in a circulating pH 0.3 solution using the $Mo_3S_4$-POM catalyst modified *p*-type Si(511) photocathode.

### 3.4.2 Mo K-edge EXAFS and other XAS results

The Mo K-edge EXAFS spectra of $Mo_3S_4$-POM catalyst and reference compounds were also recorded. Unfortunately, both the *p*-type Si(100) (preliminary experiments on the ROCK beamline) and Si(511) surfaces showed some unexpected intense diffraction peaks in EXAFS region (**Figure 3-20**) preventing any analyses to obtain structural information.

Moreover, W K-edge XAS spectra of $Mo_3S_4$-POM catalyst were recorded. Unfortunately, due to too intense diffraction peaks, no results can be derived from the XANES and EXAFS spectra.

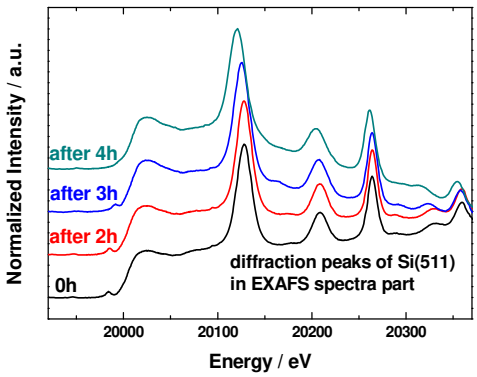


**Figure 3-20**: Presence of unexpected *p*-type Si(511) diffraction peaks on the Mo K-edge EXAFS spectra of $Mo_3S_4$-POM catalyst under precatalytic and catalytic conditions (after 2 h, 3 h and 4 h electrolysis in a circulating pH 0.3 solution).

## 3.5 Conclusions

We have investigated both the oxidation state and coordination structural changes of Mo that occur in a $Mo_3S_4$-POM-based hydrogen-evolving electrocatalyst in acidic (pH = 0.3) solution under controlled-potential electrolysis conditions. These investigations were carried out by combining *in operando* X-ray absorption spectroscopy with electrochemistry. Following the analysis of Mo K-edge XAS data of reference compounds, the relationships between the absorbing Mo-atom properties and XANES features are well understood. Further XANES analysis of $Mo_3S_4$-POM catalyst in acidic conditions reveals a change of coordination of Mo centers during the electrocatalytic process. From our data, we suggest the formation of an octahedral first coordination shell (Mo-O) instead of a tetrahedral species (Mo-S) for Mo atom due to partial substitution of $S^{2-}$ sulfide ligands by $O^{2-}$ oxo groups, which is consistent with our previous observation and provides a deeper knowledge in the HER mechanism for $Mo_3S_4$-POM electrocatalyst. We note that an unexpected event also happened during our experiments, leading to an abrupt change in the photocurrent density after 3 h electrolysis. As a consequence, some data has not been interpreted. We have thus experienced some difficulties in performing this XAS study essentially due to particular experimental conditions required for such measurements (namely miniaturized photoelectrochemical cell and electrodes, use of a confined liquid medium and possible leakage of electrolyte). Unfortunately, our measurements could not be repeated because of the limited beamline time.

**References**

[1] Stöhr, J. NEXAFS spectroscopy (Vol. 25). *Springer Science & Business Media*, **2013**.

[2] Gaur, A., Shrivastava, B. D., Nigam, H. L. X-Ray Absorption Fine Structure (XAFS) Spectroscopy–A Review. *Proceedings of the Indian National Science Academy*. **2013**, *79*(Part B), 921-966.

[3] Winick, H., Doniach, S. Synchrotron radiation research. *Springer Science & Business Media*, **2012**.

[4] Agarwal, B. K. X-ray spectroscopy: an introduction (Vol. 15). *Springer*, **2013**.

[5] Rehr, J. J., Albers, R. C. Theoretical approaches to x-ray absorption fine structure. *Reviews of Modern Physics*. **2000**, *72*(3), 621.

[6] Newville, M. Fundamentals of XAFS. Consortium for advanced radiation sources. *University of Chicago, Chicago, IL*, **2004**.

[7] Norman, D. X-ray absorption spectroscopy (EXAFS and XANES) at surfaces. *Journal of Physics C: Solid State Physics.* **1986**, *19*(18), 3273.

[8] Wikipedia, X-ray absorption.

[9] Saraev, A. A., Zaikina, O. O., Sosnin, G. A., Yeletsky, P. M., Tsapina, A. M., Zubavichus, Y. V., Yakovlev, V. A., Kaichev, V. V. XAS study of Mo-based dispersed catalysts for upgrading of heavy oil. *Radiation Physics and Chemistry*, **2019**.

[10] Lei, W., Mi, Y., Feng, R., Liu, P., Hu, S., Yu, J., Liu, X., Rodriguez, J. A., Wang, J., Zheng, L., Tang, K. Hybrid 0D–2D black phosphorus quantum dots–graphitic carbon nitride nanosheets for efficient hydrogen evolution. *Nano Energy*. **2018**, *50*, 552-561.

[11] Yamamoto, T., Yukumoto, A. Discrepancy in the quantitative oxidation-state analysis of Eu species in sulfide phosphors by K-, L1- and L3-edge XANES spectrometry: choice of absorption edge and measurement mode. *Journal of Analytical Atomic Spectrometry*. **2018**, *33*(4), 585-592.

[12] Feng, R., Lei, W., Sui, X., Liu, X., Qi, X., Tang, K., Liu, G., Liu, M. Anchoring black phosphorus quantum dots on molybdenum disulfide nanosheets: A 0D/2D nanohybrid with enhanced visible− and NIR− light photoactivity. *Applied Catalysis B: Environmental*. **2018**, *238*, 444-453.

[13] Wang, M., Árnadóttir, L., Xu, Z. J., Feng, Z. In situ X-ray absorption spectroscopy studies of nanoscale electrocatalysts. *Nano-Micro Letters*. **2019**, *11*(1), 47.

[14] Schroeder, S. L., Moggridge, G. D., Chabala, E., Ormerod, R. M., Rayment, T., Lambert, R. M. In situ studies of catalysts under reaction conditions by total electron-yield XAS. Possibilities and limitations of a new experimental technique. *Faraday Discussions*. **1996**, *105*, 317-336.

[15] Bunker, G. Introduction to XAFS: a practical guide to X-ray absorption fine structure spectroscopy. *Cambridge University Press*, **2010**.

[16] Henderson, G. S., De Groot, F. M., Moulton, B. J. X-ray absorption near-edge structure (XANES) spectroscopy. *Reviews in Mineralogy and Geochemistry*. **2014**, *78*(1), 75-138.

[17] Berry, A. J., Hack, A. C., Mavrogenes, J. A., Newville, M., Sutton, S. R. A XANES study of Cu speciation in high-temperature brines using synthetic fluid inclusions. *American Mineralogist*. **2006**, *91*(11-12), 1773-1782.

[18] Lee, P. A., Citrin, P. H., Eisenberger, P. T., Kincaid, B. M. Extended X-ray absorption fine structure—its strengths and limitations as a structural tool. *Reviews of Modern Physics*. **1981**, *53*(4), 769.

[19] Newville, M. Fundamentals of XAFS. *Reviews in Mineralogy and Geochemistry*. **2014**, *78*(1), 33-74.

[20] Briois, V., La Fontaine, C., Belin, S., Barthe, L., Moreno, T., Pinty, V., Carcy, A., Girardot, R., Fonda, E. ROCK: the new Quick-EXAFS beamline at SOLEIL. *In Journal of Physics: Conference Series*. **2016**, *712*(1), 012149. IOP Publishing.

[21] Ohkuma, H. Top-up operation in light sources. *Proceedings. European Particle Accelerator Conference*. **2008**, *8*, 36.

[22] Fay, M. J., Proctor, A., Hoffmann, D. P., Houalla, M., Hercules, D. M. Determination of the Mo surface environment of $Mo/TiO_2$ catalysts by EXAFS, XANES and PCA. *Microchimica Acta*. **1992**, *109*(5-6), 281-293.

[23] Lassalle-Kaiser, B., Merki, D., Vrubel, H., Gul, S., Yachandra, V. K., Hu, X., Yano, J. Evidence from in situ X-ray absorption spectroscopy for the involvement of terminal disulfide in the reduction of protons by an amorphous molybdenum sulfide electrocatalyst. *Journal of the American Chemical Society*. **2014**, *137*(1), 314-321.

[24] Fu, D., Fabre, B., Loget, G., Mériadec, C., Ababou-Girard, S., Cadot, E., Leclerc-Laronze, N., Marrot, J., de Ponfilly, Q. Polyoxothiometalate-Derivatized silicon photocathodes for sunlight-driven hydrogen evolution reaction. *ACS Omega*. **2018**, *3*(10), 13837-13849.

[25] Briois, V., Cartier, C., Momenteau, M., Maillard, P., Zarembowitch, J., Dartyge, E., Fontaine, A., Tourillon, G., Thuéry, P., Verdaguer, M. Spectroscopie d'absorption des rayons X au seuil K: complexes moléculaires du cobalt. *Journal de Chimie Physique*. **1989**, *86*, 1623-1634.

[26] Briois, V., Moulin, C. C. D., Verdaguer, M. Seuils d'absorption des rayons X: un outil de caractérisation indispensable en chimie de coordination. *Actualité Chimique*. **2000**, *3*, 31-40.

# Chapter 4. Efficient Reduction of $CO_2$ to Formate at Bi-Modified *p*-Si Photocathodes

## 4.1 Background

The electrochemical reduction of $CO_2$ to useful fuels and chemicals has attracted great attention. The conversion of $CO_2$ to added value products using electrical or solar energy at ambient temperatures and pressures provides a significant contribution to our future energy supply.[1] Formic acid (HCOOH) is an important and commonly found product in $CO_2$ reduction reaction (CDRR), since it needs only two protons and two electrons to be produced, but requires slightly higher reduction potential than that for CO formation. Formate has a high product value per electron ($ 16.1 × $10^{-3}$/electron).[2] Moreover, it is widely employed in industrial areas such as pharmaceutical synthesis and can be converted for syngas.[3] Compared to gaseous products such as CO and hydrocarbons, formate has the advantage of easy storage and transportation.[4] Several metal catalysts (e.g. Pb, Cd, Hg, In, Sn, and Tl, as first described by Hori [5]) can promote the conversion of $CO_2$ to formate. Beside of these traditional metal electrocatalysts, Bismuth (Bi), which is nontoxic and inexpensive, has been first introduced through the pioneering research by Komatsu *et al.* in 1995[6] and is expected to have a great potential for reduction of $CO_2$ to formic acid. However, this material remains relatively underexplored and most of the previous studies were realized in ionic liquids or aprotic electrolytes, promoting its CDRR activity and leading to CO as the main product.[7,8,9,10] Meanwhile, several other studies were carried out in aqueous solutions in order to produce formate with high Faradaic efficiency (FE).[11,12,13] Unfortunately, the reduction activity is quite low, with reported current densities generally below 10 mA $cm^{-2}$ [14,15,16] which makes unpractical HCOOH production on Bi.[2] In addition, its low stability still remains a challenging issue for the $CO_2$ conversion applications. Thus, the development of robust Bi-based electrocatalysts with high selectivity, and improved catalytic activity at low overpotential is significantly required.

## 4.2 Motivation and Aims of This Work

In recent years, several studies employing different forms of Bi-based electrocatalysts (e.g. nanoparticles,[9] nanodendrites,[16] nanowires,[17] nanosheets,[1] and microstructures[18]) synthesized by electrodeposition, (considered as a convenient technique for the growth of immobilized catalyst without the requirement of high vacuum or high temperature)[19] have shown that their catalytic performance is highly structure-dependent.[20] However, synthesis of Bi-based catalysts for photoelectrocatalysis has been only scarcely reported. With these considerations in mind, if the catalytic activity of Bi could be transposed to *p*-type silicon photocathodes, the performance of these photocathodes is expected to be further enhanced for CDRR. We anticipate that such systems could realize the heterogeneous chemical reduction of $CO_2$ to HCOOH at the interface of the light-absorbing

semiconducting material and the liquid electrolyte and that the deposited Bi should be stable due to the relatively positive $E^0$ of the $Bi^{3+}/Bi^0$ couple (0.293V vs SHE), which is important for an electrode operating in aqueous solution. In this work, the Bi-modified photocathodes were prepared by a simple electrodeposition method using monocrystalline Si. To the best of our knowledge, Bi-based catalyst modified *p*-Si photocathodes have never been reported for $CO_2$ conversion applications.

## 4.3. Results and Discussion

### 4.3.1 Electrodeposition for Preparing Bi-modified Photocathodes

We have performed a preliminary study where the electrodeposition time was varied in order to determine the time leading to the maximum catalytic activity. The electrodeposition was performed under illumination of the *p*-Si working electrode in an aqueous 1 M $HNO_3$ solution containing 20 mmol $L^{-1}$ $Bi(NO_3)_3 \bullet 5H_2O$ at -0.3 V vs SCE. **Figure 4-1 (a)** shows that the chronoamperometry (CA) curves followed the same trend for the three tested times (5 s, 30 s, and 60 s). We can observe in these curves that the absolute value of the current density constantly decreases, which could suggest that the active electrode surface does not increase over time and/or that the Bi electrodeposit reduces the light absorption of the SC substrate (causing a decrease of the concentration of photogenerated electrons). As shown in **Figure 4-1 (b),** the visual appearance of the deposit was in good agreement with the increasing values of charge over time, because a greater amount of Bi-based coating was observed for longer deposition times.

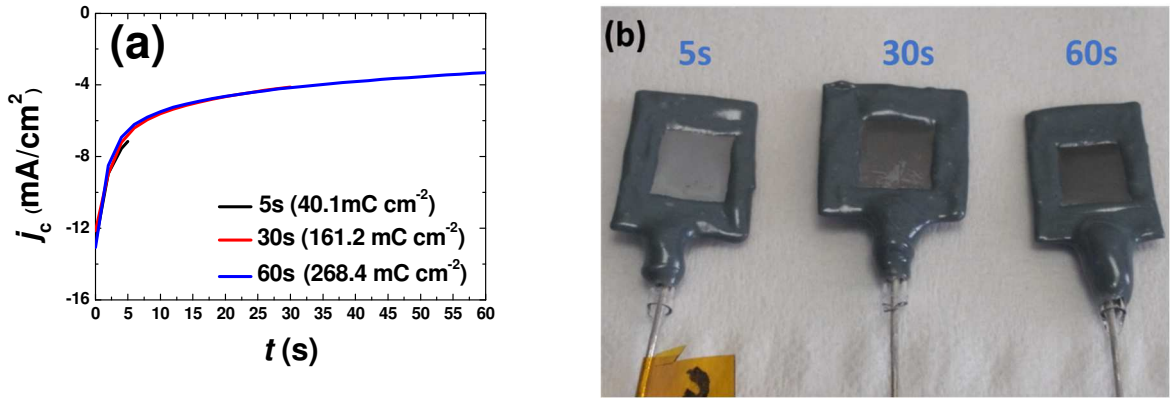


**Figure 4-1**: (a) Chronoamperometry (CA) curves recorded on freshly-prepared *p*-SiH photocathodes for illuminated electrodeposition process at *E* = -0.3 V *vs* SCE; (b) Digital photographs of Bi-modified *p*-Si photocathodes prepared through electrochemical reduction of $Bi^{3+}$ in acidic aqueous solution during 5 s, 30 s and 60 s.

Interestingly, $Bi^{3+}$ ions have sufficient oxidizing power to etch Si. Li *et al.* have illustrated the possible etching mechanism of planar Si wafers in $Bi(CH_3COO)_3$ and hydrofluoric acid (HF) mixed aqueous solution : after oxidizing Si to $SiO_2$, $Bi^{3+}$ ions themselves are reduced to metallic Bi on surface, which leads to the creation of the Si-Bi interface. Once the interface is formed, more $Bi^{3+}$ ions are preferentially reduced at the metallic Bi surface, and holes are injected through the metal to underneath Si. Therefore, the continuous oxidation of Si could contribute to the growth of metallic Bi deposits.[21] In this work, the treatment of our *p*-Si photocathodes in 10 % HF solution could also provide an assisted chemically etching before Bi electrodeposition process, which could lead to an improved Bi adhesion but could also oxidize Si before and/or during the electrodeposition process. Note that our conditions are very different from these used in that reference and that the existence and the extent of this phenomenon were not studied in our work as our process was found to be suitable for modifying *p*-Si with Bi.

### 4.3.2 Electrochemical Tests of Bi-modified Photocathodes for CDRR

#### 4.3.2.1 Optimization of Bi-modified Photocathodes

For Bi-modified Si photocathodes, the amount and morphology of the Bi deposits should be affected by the electrodeposition time, which could influence the CDRR performance in aqueous solution. In our work, the photoelectrochemical response of the freshly prepared Bi-modified surfaces through the various electrodeposition times was then first examined for HER. **Figure 4-2** shows the polarization curves under cathodic bias for Bi-modified Si photocathodes electrodeposited for 5 s, 30 s, and 60 s [namely *p*-Si/Bi (5s), *p*-Si/Bi (30s), and *p*-Si/Bi (60s)] which were recorded in Ar-saturated 0.5 mol $L^{-1}$ $KHCO_3$ solution (pH = 8.3). As expected, negligible reduction current densities were measured in the dark for all electrodes with various electrodeposition times and cathodic current densities were significantly increased under simulated sunlight (AM 1.5G, 100 mW $cm^{-2}$) conditions. Subtle differences can be observed among these modified electrodes, in particular, *p*-Si/Bi (5s) is found to have a less negative onset potential with -0.87 V vs SCE (at $j_c$ = -0.5 mA $cm^{-2}$) combined with a higher photocurrent density of -10.1 mA $cm^{-2}$ (at $E$ = -1.5 V vs. SCE) compared to *p*-Si/Bi (30s) and *p*-Si/Bi (60s) photocathodes. The latter two photocathodes yielded lower photocurrent densities probably owing to an excessive amount of the deposited Bi-based catalyst, which suggests that higher loaded deposits may limit the light absorption and reduce the photoelectric conversion efficiency.

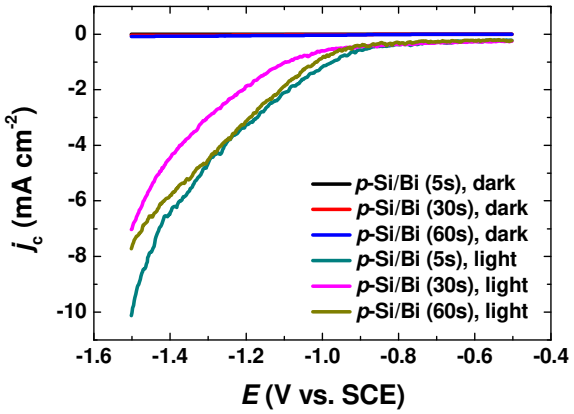


**Figure 4-2**: Linear sweep voltammogram (LSV) curves of *p*-Si/Bi (5s), *p*-Si/Bi (30s), and *p*-Si/Bi (60s) in Ar-saturated 0.5 mol $L^{-1}$ $KHCO_3$ solution in dark and under illumination (100 mW $cm^{-2}$). Scan rate: 20 mV $s^{-1}$.

*NB:* For all the electrochemical measurements, potential versus SCE was not converted into potential versus RHE, which is different from Chapter 2, because of the different pH in Ar-saturated 0.5 M $KHCO_3$ solution (pH = 8.3) and in $CO_2$-saturated 0.5 M $KHCO_3$ solution (pH = 7.2). Furthermore, numerous reports on the $CO_2$ electrocatalytic reduction showed electrochemical data with potentials referenced against SCE.[8,20]

For $CO_2$ reduction, **Figure 4-3** shows the polarization curves under cathodic bias for *p*-Si/Bi (5s), *p*-Si/Bi (30s), and *p*-Si/Bi (60s), which were recorded in $CO_2$-saturated 0.5 mol $L^{-1}$ $KHCO_3$ solution under illumination. No significant difference was found between these three Bi-modified photocathodes at higher potential in the potential range of -0.3 V to -0.9 V / SCE, however, at potentials more negative than -0.9 V, light-limited cathodic currents were found for all these Bi-modified photocathodes, *p*-Si/Bi (5s) shows ca. 4 and 3 times higher light-limited cathodic current than those measured for *p*-Si/Bi (30s) and *p*-Si/Bi (60s), respectively. From the aforementioned measurements, we conclude that *p*-Si/Bi (5s) is the best photocathode with optimal catalytic activity.

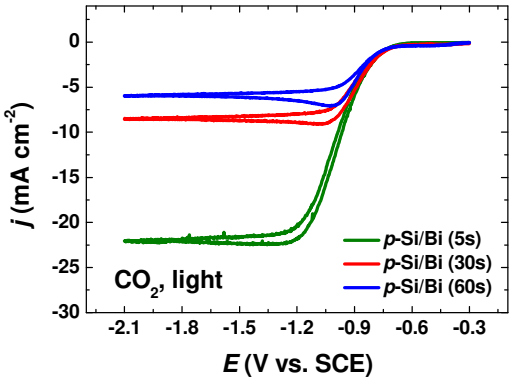


**Figure 4-3:** CV curves obtained on *p*-Si/Bi (5s), *p*-Si/Bi (30s), and *p*-Si/Bi (60s) photocathodes in $CO_2$-saturated 0.5 mol $L^{-1}$ $KHCO_3$ solution under illumination (100 mW $cm^{-2}$). Scan rate: 20 mV $s^{-1}$.

4.3.2.2 Electrochemical $CO_2$ Reduction at *p*-Si/Bi (5s) Photocathode

From preliminary electrochemical data obtained for Bi-modified photocathodes, it can be concluded that the *p*-Si/Bi (5s) photocathode displays both an improved HER onset potential and higher photocurrent densities compared to the other electrodes. To evaluate the catalytic activity of this system towards CDRR, CV experiments with a sweep rate of 20 mV $s^{-1}$ were carried out in Ar or $CO_2$ saturated 0.5 mol $L^{-1}$ $KHCO_3$ aqueous solutions under illumination. As shown in **Figure 4-4 (a)**, on *p*-Si/Bi (5s) photocathode, no significant current was measured under Ar or under $CO_2$ in dark conditions. In contrast, under illumination, much larger photocurrent response was observed under $CO_2$ compared to that under an Ar atmosphere within the potential window -0.6 V to -1.7 V / SCE, which demonstrates its catalytic activity for $CO_2$ reduction. Focusing on the potential required to reach a photocurrent density of 10 mA $cm^{-2}$ as a photoelectrode activity metric, the reduction photocurrent of 10 mA $cm^{-2}$ under a $CO_2$ atmosphere was obtained at about -0.88 V vs SCE on the *p*-Si/Bi (5s) photocathode. Moreover, the stability of the Bi-modified photocathodes was evaluated by performing sequential cyclic voltammetry (CV) experiments in the same electrolyte as mentioned above, applying a sweep rate of 20 mV $s^{-1}$. Such experiments demonstrate that the photoelectrochemical activity of the modified photocathode is not significantly changed during a repeated cycling in $CO_2$-saturated electrolyte [**Figure 4-4 (b)**].

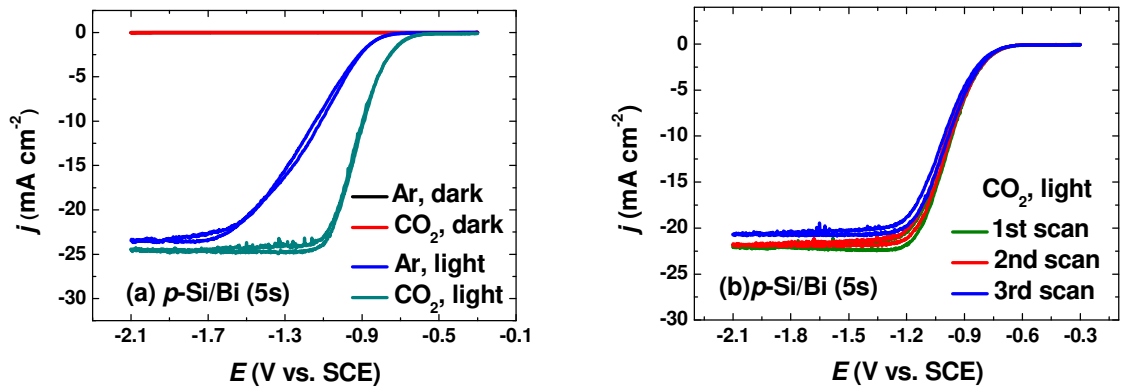


**Figure 4-4**: (a) CV curves of *p*-Si/Bi (5s) photocathode in Ar-saturated or $CO_2$-saturated 0.5 mol $L^{-1}$ $KHCO_3$ aqueous solutions, in dark or under simulated sunlight illumination (100 mW $cm^{-2}$) and (b) three successive CV cycles of *p*-Si/Bi (5s) photocathode in $CO_2$-saturated electrolyte. All curves were recorded at a scan rate of 20 mV $s^{-1}$.

### 4.3.3 Characterizations of the Electrodeposited Bi-Modified Si Surfaces

The morphology and composition of the electrodeposited Bi-based catalyst on the photocathode surface were probed by a combination of analytical methods such as scanning electron microscopy (SEM), energy-dispersive X-ray (EDX) analysis, and X-ray photoelectron spectroscopy (XPS). We have not only analyzed the different freshly prepared Bi-modified photocathode surfaces but also the optimized Bi-modified photocathode [i.e. *p*-Si/Bi (5s)] after electrolysis for 30 min in a $CO_2$-saturated 0.5 mol $L^{-1}$ $KHCO_3$ aqueous solution. All these microscopic and spectroscopic techniques provide a greater understanding of our photoelectrochemical system.

#### 4.3.3.1 SEM Morphological Characterizations

The structural composition of different Bi-modified surfaces, i.e. *p*-Si/Bi (5s), *p*-Si/Bi (30s), and *p*-Si/Bi (60s) has been examined by SEM. **Figure 4-5 (a - c)** shows SEM images for all the surfaces before electrolysis. For *p*-Si/Bi (60s), a dense "dendrite-like" electrodeposit is observed on the Si surface. *p*-Si/Bi (30s) exhibits less compact dendrites which coexist with smaller particles that are in close contact with the Si. When the electrodeposition reaction time is decreased to 5 s, only a few dendrites are found on the surface [**Figure 4-5 (c')**], however, many small particles with sizes comparable to those of particles observed for longer times were visible on the Si. This is indicating that the nucleation occurred within these 5 s, and suggests that the growth of dendrites initiates at these nuclei [**Figure 4-**

**5 (c')**]. A similar Bi deposition has been reported by Ding *et al.* in the frame of their study of $Bi^{3+}$-assisted chemical etching mechanism of planar Si wafers.[21] **Figure 4-5 (d)** shows the SEM image of *p*-Si/Bi (5s) photocathode after 30 min of CDRR, at -0.9 V *vs* SCE in $CO_2$-saturated 0.5 mol $L^{-1}$ $KHCO_3$ aqueous solution. A drastic change of the initial structure is noticed, with microsheets that are formed on the surface. Moreover, the *p*-Si/Bi (5s) photocathode surface appears less homogenous after 30 min of CDRR than that before electrolysis, which is consistent with a loss of Bi catalyst during the CDRR. We suppose that the film remaining after electrolysis is responsible for the catalytic activity under our experimental conditions.

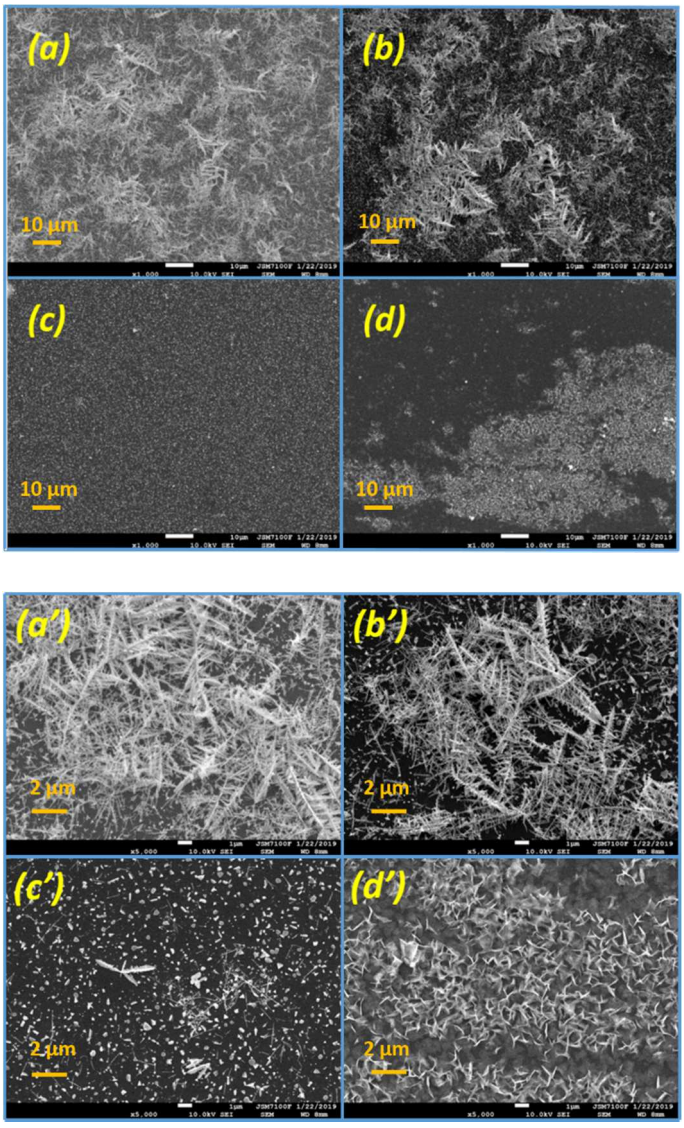


**Figure 4-5**: SEM images of *p*-Si/Bi (60s) **(a, a')**, *p*-Si/Bi (30s) **(b, b')** and *p*-Si/Bi (5s) photocathodes **(c, c')** electrodeposited from 1 M $HNO_3$ solution containing 20 mmol $L^{-1}$ $Bi(NO_3)_3 \bullet 5H_2O$. *p*-Si/Bi (5s) photocathode after 30 min electrolysis at -0.9 V vs. SCE in $CO_2$-saturated 0.5 mol $L^{-1}$ $KHCO_3$ aqueous solution **(d, d')**.

4.3.3.2 EDX Elemental Analysis

The presence of Bi on Si was confirmed by EDX analyses that were performed in several regions of several independently prepared samples [**Figure 4-6 (insets)**]. Bi and Si were identified as the principal elemental components for all the freshly modified photocathode surfaces [i.e. *p*-Si/Bi (60s), *p*-Si/Bi (30s), and *p*-Si/Bi (5s)], [**Figure 4-6 (a-c)**], with a smaller Bi ratio for *p*-Si/Bi (5s) photocathode, well in line with the electrochemical, SEM and optical observations. Interestingly, after 30 min of CDRR, a significant amount of C and O elements was detected at the surface of *p*-Si/Bi (5s) photocathode [**Figure 4-6 (d)**].

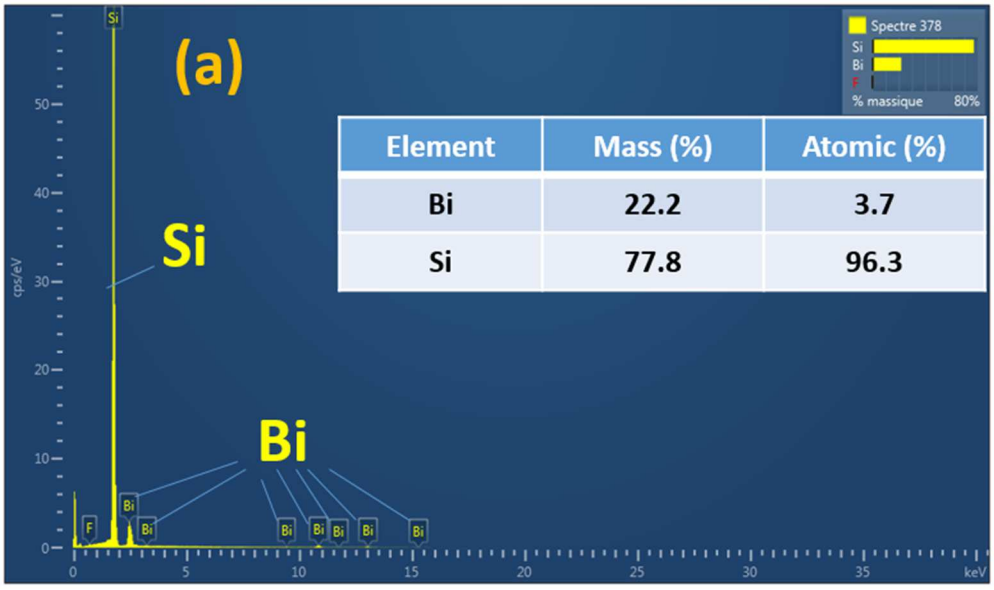


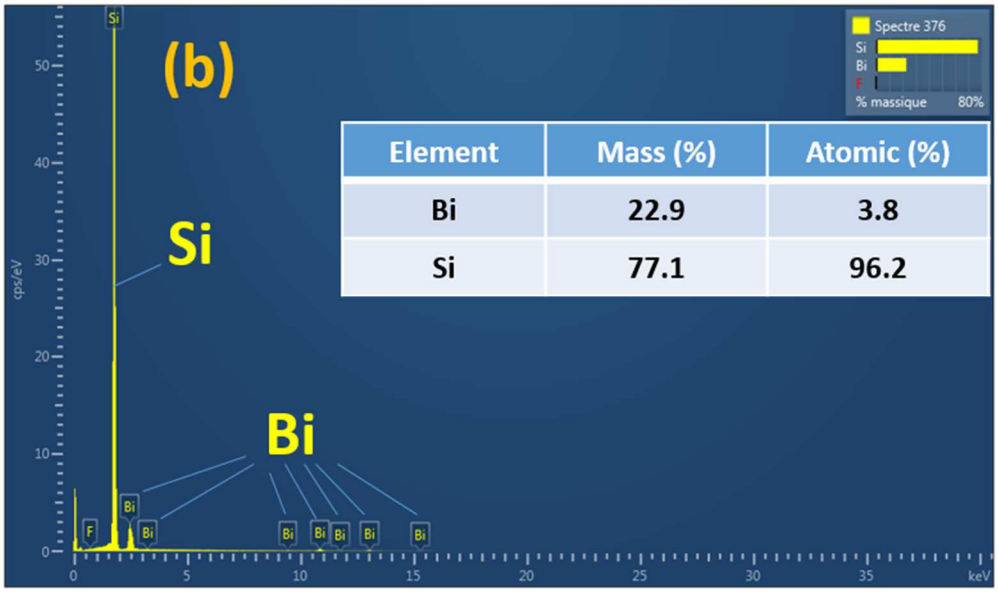

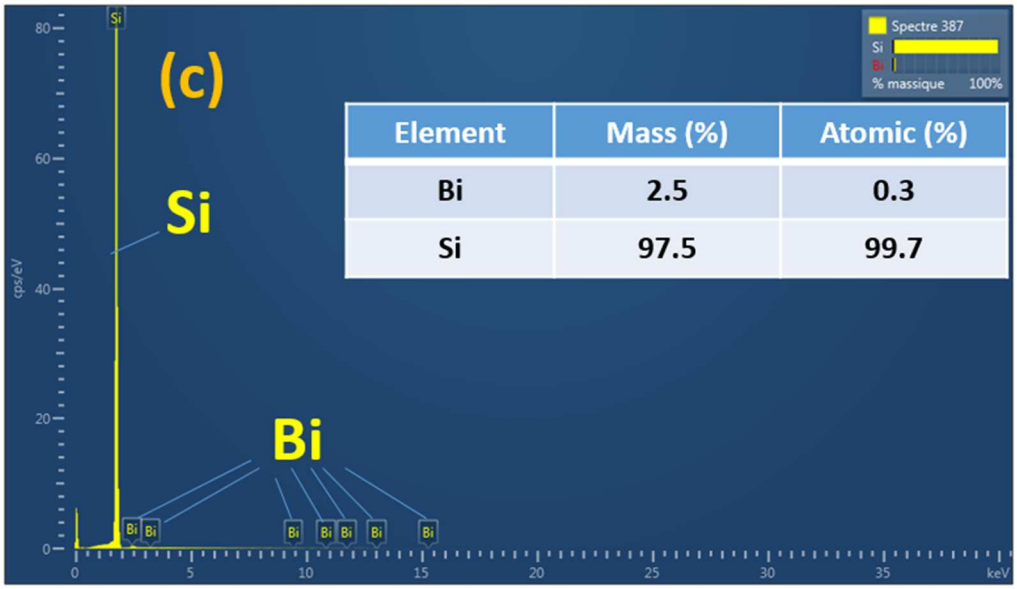


| Element | Mass (%) | Atomic (%) |
|---|---|---|
| Bi | 2.5 | 0.3 |
| Si | 97.5 | 99.7 |

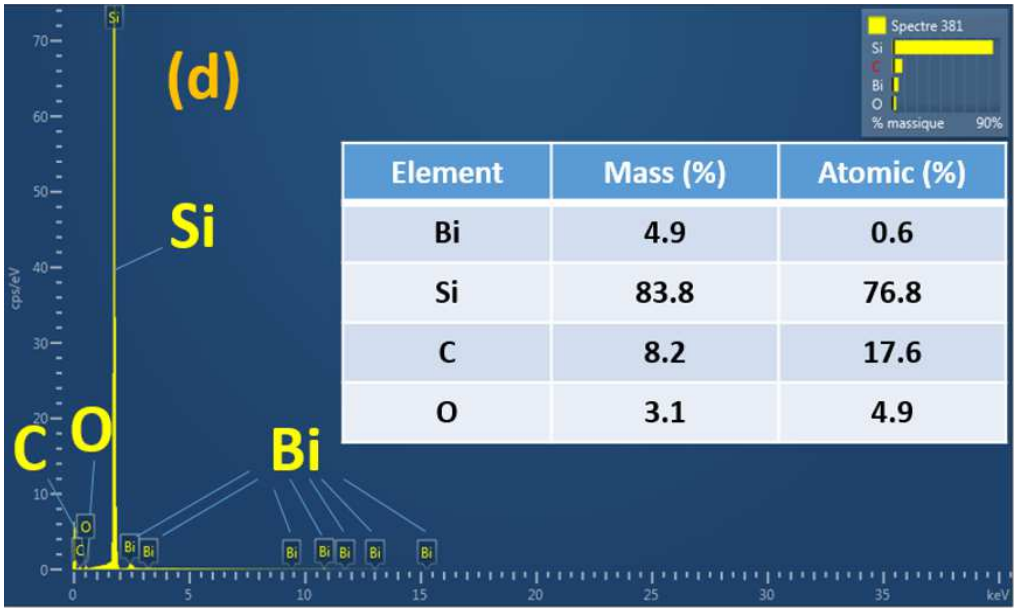


| Element | Mass (%) | Atomic (%) |
|---|---|---|
| Bi | 4.9 | 0.6 |
| Si | 83.8 | 76.8 |
| C | 8.2 | 17.6 |
| O | 3.1 | 4.9 |

**Figure 4-6**: EDX spectra recorded before electrolysis for *p*-Si/Bi (60s) (a), *p*-Si/Bi (30s) (b), *p*-Si/Bi (5s) (c), and *p*-Si/Bi (5s) after 30 min electrolysis at -0.9 V vs SCE in $CO_2$-saturated 0.5 mol $L^{-1}$ $KHCO_3$ aqueous solution (d).

4.3.3.3 XPS Surface Analysis

The surface of the *p*-Si/Bi (5s) photocathode was also analyzed by XPS. All elements revealed by EDX were also detected by XPS (**Figure 4-7**), which identified Bi, C, O, and Si as the principal elemental components for the as-prepared Bi-modified photocathode before and after 30 min electrolysis (at -0.9 V vs SCE in $CO_2$-saturated 0.5 mol $L^{-1}$ $KHCO_3$ aqueous solution [**Figure 4-8 (a-d)**]. Any shift due to sample charging was corrected by using the C 1s (285.0 eV) as an internal reference.

After electrolysis, the presence of a peak in the C 1s spectrum at 286.7 eV [**Figure 4-8 (b)**], which is attributed to C–O bonds, indicates that small amount of intermediate species is incorporated onto the electrodeposited material during the CDRR electrolysis. These intermediate species are probably attributed to carbonates ($Bi_2O_2CO_3$)[22] from the reaction with $CO_2$, and this is consistent with EDX analysis. For the O 1s spectrum, the lower-binding-energy (530.1 eV) is due to metal oxide oxygen, while the higher-binding-energy (531.8 eV) is probably due to the existence of hydroxyl groups, which was also introduced from CDRR electrolysis process [**Figure 4-8 (c)**].[23] Moreover, the bismuth 4f spectrum shows two distinct doublets attributed to the Bi $4f_{7/2}$ peaks, the lower binding energy (BE) contribution at 157.1 eV is assigned to $Bi^0$, whereas a significantly more intense contribution at higher BE (159.5 eV) is assigned to $Bi^{3+}$ species, [**Figure 4-8 (a)**]. [24] We note that both $Bi^0$ and $Bi^{3+}$ ions have previously been detected for Bi material electrodeposited from a concentrated acidic solution.[25] The Bi $4f_{7/2}$ and Bi $4f_{5/2}$ peak positions of 159.5 eV and 164.8 eV are consistent with bismuth oxide ($Bi_2O_3$). Furthermore, the component separation of Bi ($4f_{7/2}$ - $4f_{5/2}$) = 5.30 eV and the intensity ratio of $Bi^{3+}$ $4f_{7/2}$ to $Bi^{3+}$ $4f_{5/2}$ (~1.3) are both in good agreement with the theoretical ratio of 1.33 for $Bi_2O_3$ .[23] All these XPS results indicate that the surface Bi atoms are mainly in the form of $Bi_2O_3$, which is likely to generate spontaneously over electrodeposited $Bi^0$.

After cathodic $CO_2$ reduction electrolysis for 30 min with the electrodeposited material, the position of the characteristic XPS Bi 4f signals was not changed. However, a certain amount of the electrodeposited material has been released into the electrolyte solution during the electrochemical test (about 34 %), as confirmed by the decrease in the intensity of Bi 4f XPS signals.

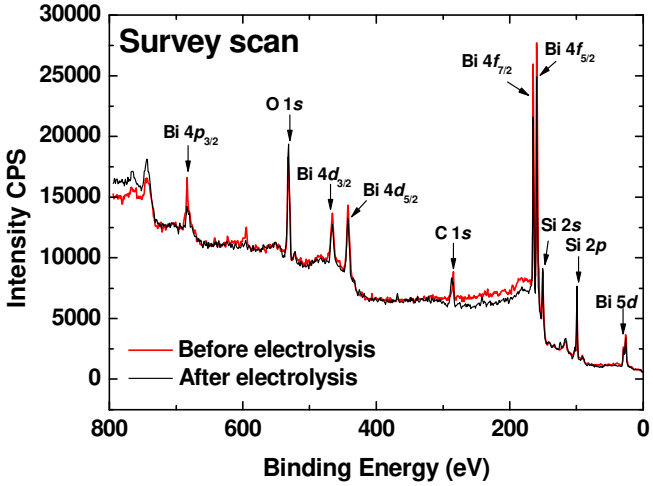


**Figure 4-7**: XPS survey spectra of the freshly prepared *p*-Si/Bi (5s) photocathode before (red solid line) and after cathodic electrolysis at -0.9 V vs SCE for 30 min under simulated sunlight (black solid line).

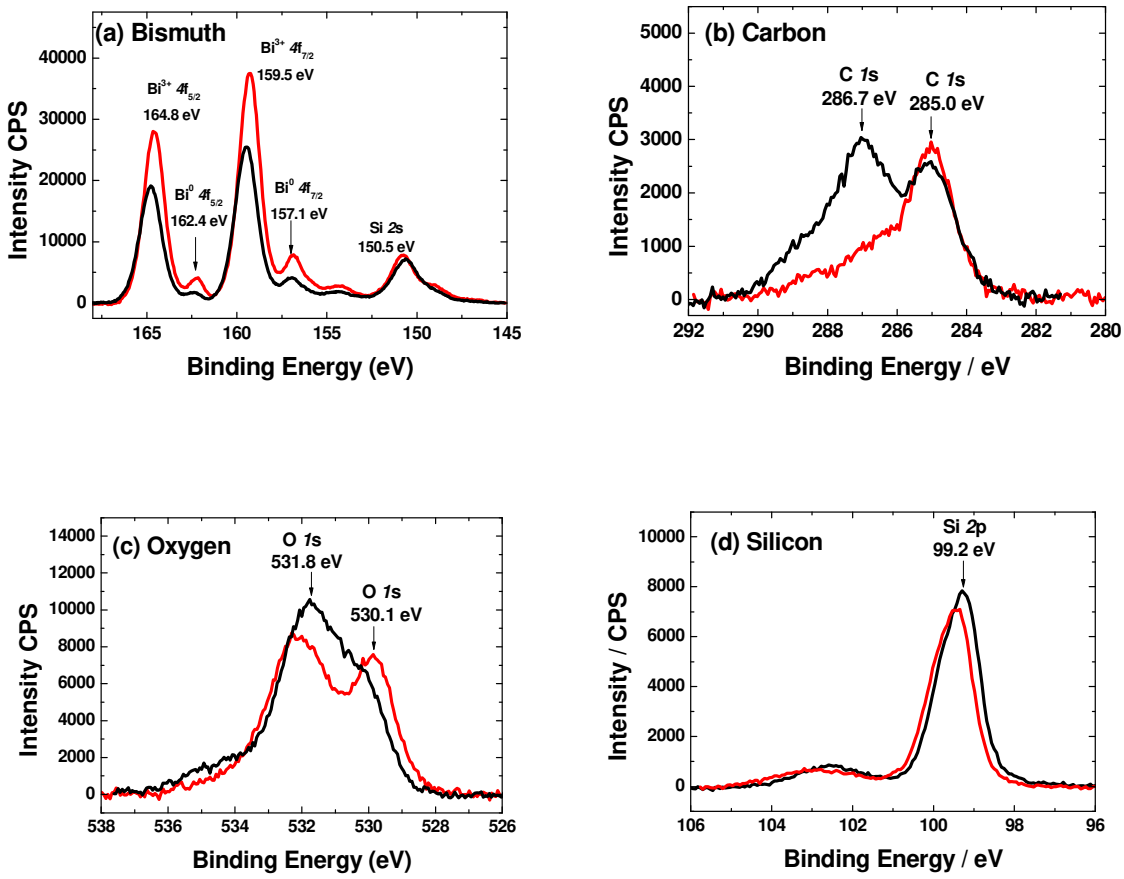


**Figure 4-8**: High-resolution XPS spectra of Bi 4f (a), C 1s (b), O 1s (c), and Si 2p (d) recorded for the freshly prepared *p*-Si/Bi (5s) photocathode before (red solid line) and after cathodic electrolysis at -0.9 V vs SCE for 30 min under simulated sunlight (black solid line).

### 4.3.4 Catalytic Activity and Stability of *p*-Si/Bi (5s) Photocathode for CDRR

Controlled potential electrolysis tests under continuous illumination were carried out at various potentials to evaluate the catalytic activity and the stability of *p*-Si/Bi (5s) for CDRR. CA curves (**Figure 4-9**) of *p*-Si/Bi (5s) photocathode in Ar-saturated and $CO_2$-saturated 0.5 M $KHCO_3$ solutions were recorded by applying the following potentials: -0.9 V, -1.3 V, -1.7 V, and -2.1 V vs SCE, respectively. Under $CO_2$ atmosphere, the cathodic photocurrent density was significantly higher compared to that under Ar atmosphere at all applied potentials, which is a good indicator of the catalytic activity for CDRR. In terms of stability, at applied potentials of -0.9 V and -1.3 V vs SCE, a 10% decrease in the cathodic photocurrent density was measured after 30 min electrolysis in $CO_2$-saturated solution. Conversely, at more negative potentials, less decrease in the photocurrent density was observed, and the *p*-Si/Bi (5s) photocathode yielded appreciable cathodic photocurrent (>24 mA $cm^{-2}$) in $CO_2$-

saturated electrolyte (**Figure 4-10**). Such a cathodic photocurrent is higher than that measured for the recently reported $Bi^{3+}$-assisted chemical etching Si photocathode.[21] After electrolysis at -1.7 V vs SCE under illumination in $CO_2$-saturated electrolyte during 30 min, the CV curve **(Figure 4-11)** showed no significant change relative to the curve recorded before electrolysis, and the light-limited cathodic current within the range -1.1 V to -2.1 V vs SCE was found to decrease slightly from -24 mA $cm^{-2}$ to -23 mA $cm^{-2}$, which is consistent with CA measurements.

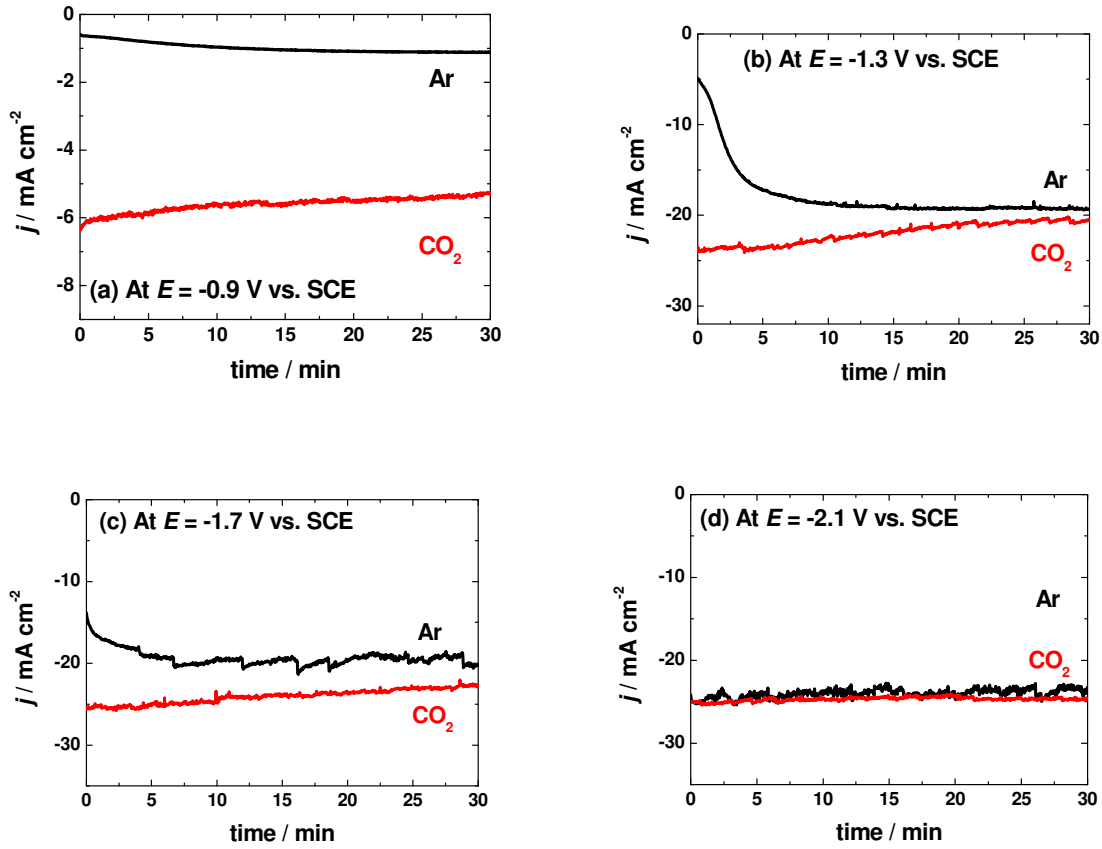


**Figure 4-9**: CA curves recorded under continuous illumination during the various controlled potential electrolysis tests at -0.9 V (a), -1.3 V (b), -1.7 V (c), and -2.1V (d) vs SCE in Ar-saturated (black solid line) or $CO_2$-saturated (red solid line) 0.5 M $KHCO_3$ solution using *p*-Si/Bi (5s) photocathodes.

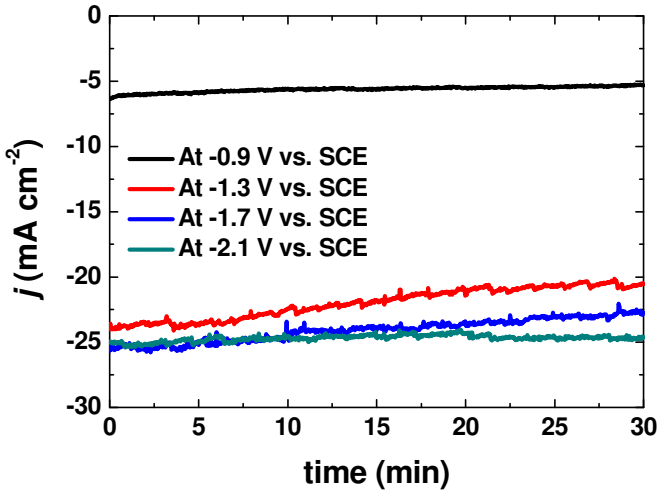


**Figure 4-10**: CA curves of *p*-Si/Bi (5s) photocathodes at different applied potentials in $CO_2$-saturated 0.5 M $KHCO_3$ solution.

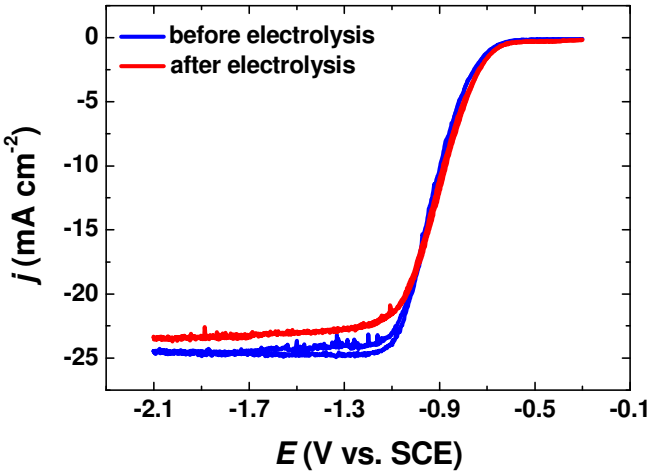


**Figure 4-11**: CV curves of *p*-Si/Bi (5s) photocathode recorded in $CO_2$-saturated 0.5 mol $L^{-1}$ $KHCO_3$ aqueous solutions (pH = 7.2), under simulated sunlight illumination (100 mW $cm^{-2}$) before and after 30 min electrolysis at applied potential of -1.7 V / SCE. All curves were recorded with a scan rate of 20 mV $s^{-1}$.

### 4.3.5 Detection of the CDRR Products Generated on *p*-Si/Bi (5s)

To further investigate the CDRR products generated on the *p*-Si/Bi (5s) photocathode, we analyzed the gaseous and liquid phases after 30 min of electrolysis, which was performed at potentials mentioned previously in 0.5 M $KHCO_3$ solutions under illumination. Resulting gaseous products (CO or $H_2$) were measured by gas chromatography (GC) and the dissolved products (formate) were detected by ion chromatography (IC) with an aliquot of the electrolyte collected at the end of the electrolysis. These analyses were achieved using both Ar- and $CO_2$-saturated electrolytes.

On the one hand, the liquid product analysis suggests that formate is the major product from CDRR during that period of time. It is generated by $2e^-/2H^+$ conversion of $CO_2$ at potentials more negative than -0.9 V *vs* SCE. The Faradaic efficiency (FE) for that reaction reaches 72.1% at -1.7 V vs SCE with an average partial photocurrent density of formate, i.e. $j_{formate}$ = -17.4 mA $cm^{-2}$. This formate selectivity is maintained at -2.1 V vs SCE with FE = 73.0% and $j_{formate}$ = -18.0 mA $cm^{-2}$. It is actually very interesting to note that these two parameters are statistically identical, which is consistent with previous researches, and is probably caused by the mass transport limitation of $CO_2$.[19,26] Moreover, the rates of formate production by *p*-Si/Bi (5s) photocathode have been evaluated. The $j_{formate}$ values obtained at -1.7 V vs SCE correspond to an average sustained activity for formate production of 14.9 mg $h^{-1}$ $cm^{-2}$, which is almost the same as that for -2.1 V vs SCE (15.5 mg $h^{-1}$ $cm^{-2}$). In contrast, at less negative applied potential, we found that FE for formate decreased drastically to 20.0% at -0.9 V vs SCE and 12.1% at -1.3 V vs SCE. Comparing to the $j_{formate}$ at -1.7 V vs SCE, partial cathodic current densities for formate decreased by a factor of ca. 16 and 6 at -0.9 V and -1.3 V vs. SCE, respectively (**Figure 4-12** and **Table 4-1**).

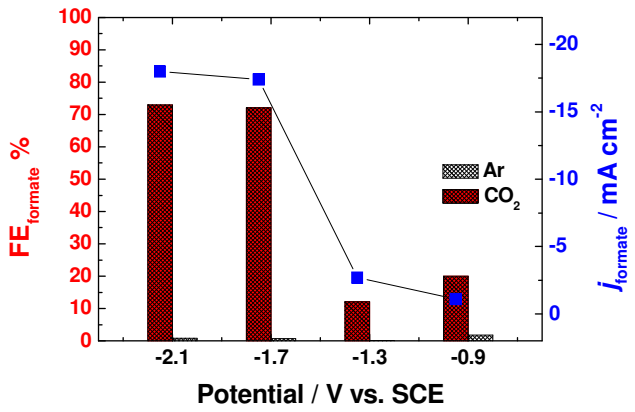


**Figure 4-12**: Potential-dependent formate Faradaic efficiency at illuminated *p*-Si/Bi (5s) in 0.5 M $KHCO_3$ solution after 30 min electrolysis and cathodic photocurrent density for formate at corresponding potentials.

| *E* (V vs. SCE) | -0.9 | -1.3 | -1.7 | -2.1 |
|---|---|---|---|---|
| *j* (mA $cm^{-2}$) | -5.6 | -22.0 | -24.1 | -24.7 |
| $j_{formate}$ (mA $cm^{-2}$) | -1.1 | -2.7 | -17.4 | -18.0 |
| $FE_{formate}$ (%) | 20.0% | 12.1% | 72.1% | 73.0% |
| $r_{formate}$ (µmol $h^{-1}$ $cm^{-2}$) | 19.1 | 50.6 | 324.8 | 336.5 |
| $r_{formate}$ (mg $h^{-1}$ $cm^{-2}$) | 0.9 | 2.3 | 14.9 | 15.5 |

**Table 4-1** Performance of *p*-Si/Bi (5s) for formate production (total photocurrent density *j*, partial formate photocurrent density $j_{formate}$, formate Faradaic efficiency $FE_{formate}$, and formate production rate $r_{formate}$) at various applied potentials in $CO_2$-saturated 0.5 M $KHCO_3$ solution.

On the other hand, the gaseous product analysis indicates that *p*-Si/Bi (5s) photocathode suffers from parasitic HER in the presence of $CO_2$, and its electrocatalytic activity is partially attributed to $H_2$ production with FE of $H_2$ ranging from 9.2% to 23.3% in the selected potential range [**Figure 4-13** and **Table 4-2 (a)**]. In addition, GC analysis also reveals that little CO was produced with very low FE comprised between 0.9% and 2.2%. Other gaseous products (e.g. $CH_4$) were not detected, probably because of their absence or concentration below the apparatus detection limit.

In order to demonstrate that formate originates from the reduction of $CO_2$, we have additionally carried out control experiments in Ar-saturated 0.5 M $KHCO_3$ electrolyte. Under these conditions, a negligible amount of formate was detected and CO was not produced [**Table 4-2 (b)**]. Interestingly, a constant $H_2$ FE around 23% was found at all applied potentials in the absence of any $CO_2$ feed gas, suggesting that HER is a potential-independent process for the *p*-Si/Bi (5s) photocathode in our experimental conditions.

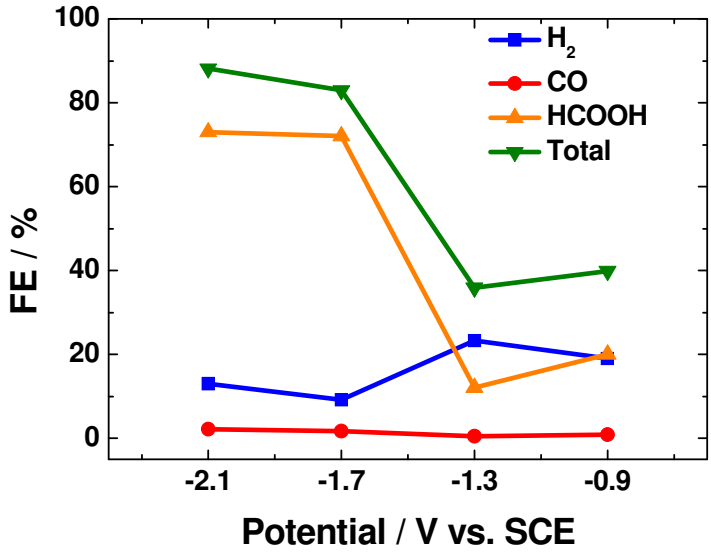


**Figure 4-13**: Potential-dependent Faradaic efficiencies for formate, $H_2$, CO, and sum for the detected products on illuminated *p*-Si/Bi (5s) photocathode in $CO_2$-saturated 0.5 M $KHCO_3$ after 30 min electrolysis.

Several aspects in this selectivity issue are worth to be explored and discussed. First, in the presence of $CO_2$, the total FE for the least cathodic potentials (i.e. -0.9 V and -1.3 V vs SCE) is close to 40% [**Table 4-2 (a)**], and the control experiment in the absence of $CO_2$ yields coincidentally almost the same total FE around 24% [**Table 4-2 (b)**], which are far from the expected value of 100%. In our understanding, this is probably due to some undetected products (e.g. ethylene, ethanol, and methanol[27,28]) either in the gaseous phase or in the liquid phase, which could not be detected by our analytical techniques. Another possibility is the presence of parasitic electrochemical reaction(s) occurring at the surface of *p*-Si/Bi (5s) photocathode, which would consume electrons during the controlled potential electrolysis. Second, in order to increase the FE for formate, Ding *et* al.[21] demonstrated recently that decreasing the light intensity to 50 mW $cm^{-2}$ caused the photocurrent density reducing by half, but slightly promoted the formate selectivity (by 10 ~ 20%) presumably because under illumination at 100 mW $cm^{-2}$ (1 sun), the photogenerated electron flux was too high to be rapidly consumed via $CO_2$ reduction on Bi. Finally, if we compare the chronoamperometric curves under Ar and under $CO_2$ conditions in **Figure 4-9 (b-d)**, the cathodic photocurrents are almost the same at the end of electrolysis analyzing time within the potential range -1.3 V to -2.1 V vs SCE. However, the formate Faradaic efficiencies for these applied potentials under Ar condition are much lower than we measured under $CO_2$ condition,

this could also be explained by the occurring parasitic electrochemical reactions under Ar condition in our experiments.

| **(a)** *E* (V vs. SCE) | -0.9 | -1.3 | -1.7 | -2.1 |
|---|---|---|---|---|
| $FE_{H_2}$ (%) | 19.0 | 23.3 | 9.2 | 13.0 |
| $FE_{CO}$ (%) | 0.9 | 0.5 | 1.7 | 2.2 |
| $FE_{HCOOH}$ (%) | 20.0 | 12.1 | 72.1 | 73.0 |
| $FE_{Total}$ (%) | 39.9 | 35.9 | 83.0 | 88.2 |

| **(b)** *E* (V vs. SCE) | -0.9 | -1.3 | -1.7 | -2.1 |
|---|---|---|---|---|
| $FE_{H_2}$ (%) | 22.9 | 24.2 | 23.8 | 22.8 |
| $FE_{CO}$ (%) | - | - | - | - |
| $FE_{HCOOH}$ (%) | 1.8 | 0.2 | 0.7 | 0.9 |
| $FE_{Total}$ (%) | 24.7 | 24.4 | 24.5 | 23.7 |

**Table 4-2**: Faradaic efficiencies for formate, $H_2$, CO, and total FE at various applied potentials in $CO_2$-saturated 0.5 M $KHCO_3$ solution (a) and in Ar-saturated 0.5 M $KHCO_3$ solution (b) as control experiments.

## 4.4 Experimental Section

### 4.4.1 Chemicals

Bismuth nitrate pentahydrate ($Bi(NO_3)_3 \bullet 5H_2O$, 98%) was purchased from Acros Organics, nitric acid ($HNO_3$, 65%) from Sigma-Aldrich, potassium bicarbonate ($KHCO_3$, 99.7~100.5%) from Alfa Aesar, Ar and $CO_2$ (Alphagaz, Air Liquid) were used as supplied. The chemicals used for the cleaning and etching of silicon wafer pieces (30% hydrogen peroxide, 96~97% concentrated sulfuric acid and 50% hydrofluoric acid solutions) were of VLSI (hydrogen peroxide, from Sigma-Aldrich) and MOS (sulfuric acid from O-BASF and HF from Sigma-Aldrich) semiconductor grade. Acetone (MOS electronic grade,

Erbatron from Carlo Erba) and anhydrous ethanol (96%, RSE electronic grade, Erbatron from Carlo Erba) were used without further purification. Ultrapure water from a Purelab Classic UV purification system from Veolia Water STI (resistivity of 18.2 MΩ $cm^{-1}$) was used to prepare all aqueous solutions.

### 4.4.2 Silicon Electrode Preparation

All Teflon vials and tweezers used for cleaning of silicon were previously decontaminated in piranha solution (3:1 v/v concentrated $H_2SO_4$/30% $H_2O_2$) at 100°C for 30min, followed by copious rising with ultrapure water.

***Caution**: the concentrated aqueous $H_2SO_4/H_2O_2$ (piranha) solution is very dangerous, particularly in contact with organic materials, and should be handled extremely carefully.*

The *p*-type (1-5 Ω cm resistivity, boron-doped, double side polished, 250 µm thickness) Si (100) wafer was purchased from Siltronix. The wafer was cut in ca. 1 cm × 1 cm pieces and degreased by sonication for 10 min successively in acetone, ethanol, and ultrapure 18.2 MΩ cm water. They were then cleaned with piranha solution at 100 °C for 30 min followed by copious rising with ultrapure water to eliminate heavy metals and organic residues.

For electrochemical experiments, the decontaminated surface was further processed to fabricate the photocathode. An Ohmic contact was established on the backside Si surface with a metal wire by first scrubbing the surface with sand paper and a diamond glass cutter and applying a droplet of InGa eutectic (99.99%, Alfa Aesar). A layer of silver paste (Electron Microscopy Sciences) was then deposited on the contact. After drying of the silver paste, the metal wire was inserted in a glass capillary, and the electrode area (0.16-0.45 $cm^2$) was defined with an epoxy-based resin (Loctite 9460, Henkel) that covered all the backside of the Si surface as well as the silver paste. The assembled electrode was then placed into an oven at 90°C overnight to cure the resin.

After preparation, the silicon surface sealed in epoxy was freshly hydrogenated by immersing the electrode into HF 10% (~ 5.7 M) for 2 min. The surface was then copiously rinsed with ultrapure water and quickly dried under an argon stream.

***Caution:** Proper precautions must be performed when handling hydrogen fluoride. Hydrogen fluoride is extremely corrosive for human tissue, contact resulting in painful, slow-healing burns and even death. Before being trained to use HF, the operator must complete HF awareness training. Laboratory work*

*with HF should be conducted only in an efficient hood, with the operator wearing a full-face shield and protective clothing.*

### 4.4.3 Bi Electrodeposition

The electrodeposition of Bi on the freshly hydrogenated *p*-type silicon (*p*-SiH) photocathode was carried out in an aqueous 1 M $HNO_3$ solution (40 mL) containing 20 mmol $L^{-1}$ $Bi(NO_3)_3 \bullet 5H_2O$ by electroreduction of $Bi^{3+}$ to $Bi^0$. Prior to electrodeposition, the sonicated $Bi(NO_3)_3 \bullet 5H_2O$ solution was purged with argon for at least 15 min and then sealed properly. For electrodeposition, a three-electrode electrochemical cell with a *p*-SiH working electrode, a Pt wire counter electrode, and a saturated calomel electrode (SCE) as reference electrode, was used. The silicon electrode was immersed into the deposition solution and illuminated with a halogen optical fiber (Fiber-Lite DC-950 Illuminator). The illumination power has not been measured but we can estimate it between 30 and 100 mW $cm^{-2}$. Bi was deposited at -0.3 V vs SCE. After electrodeposition, the modified photocathodes were immediately rinsed thoroughly with ultrapure water and dried under an argon stream.

### 4.4.4 Electrochemical Measurements

All electrochemical experiments were carried out using an Auto-Lab PGSTAT 302N electrochemical workstation equipped with the GPES and FRA softwares. LSV and CV curves were both recorded at 20 mV $s^{-1}$ and intentionally not corrected by the Ohmic drop. The cell resistance was determined before each experiment by measuring the impedance of the system at 100 kHz, and it was found to be between 15 and 30 Ω. The geometrical area of the photocathodes (between 0.16 and 0.45 $cm^2$) was measured using the ImageJ software.

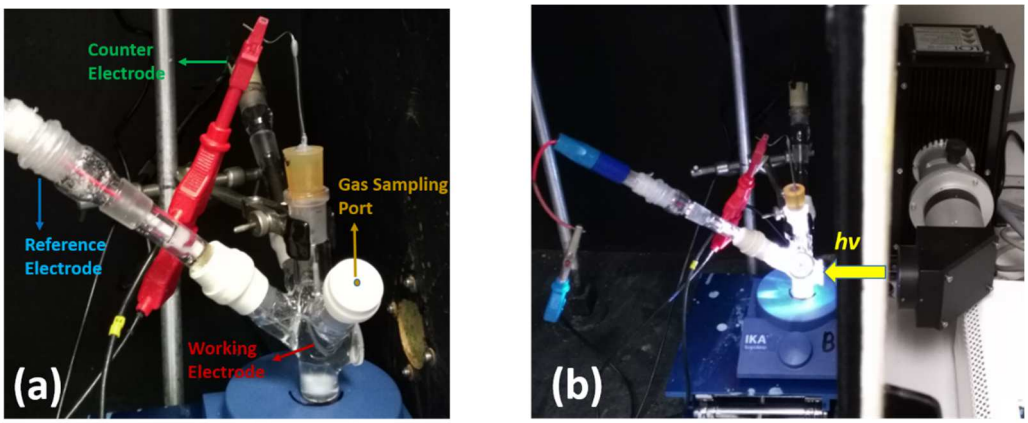


**Figure 4-14**: Photographs showing the photoelectrochemical cell (a) and its arrangement in front of the solar simulator (b).

For electrochemical $CO_2$ reduction studies, the electrolytic solution (aqueous 0.5 M $KHCO_3$) was purged with argon or carbon dioxide for at least 20 min before measurements in the electrochemical cell (see **Figure 4-14**). The $CO_2$ reduction measurements were performed in this cell comprising a quartz window in which were inserted a KCl saturated calomel reference electrode (SCE) and a graphite rod counter electrode (the counter electrode was separated from the rest by a glass frit). The *p*-Si/Bi photocathode was disposed in front of the quartz window and used as the working electrode. The light source was provided by a solar simulator with a fluence of 100 mW $cm^{-2}$ (LS0106, LOT Quantum Design) equipped with an AM 1.5G filter.

### 4.4.5 Gas Chromatography

Gas chromatography (GC) measurements for the detection and quantification of the gas produced from electrolysis (e.g. CO and $H_2$) were performed by PerkinElmer® Clarus® 580 gas chromatograph equipped with two detectors: a Thermal Conductivity Detector (TCD) and a Flame Ionization Detector (FID), and two columns: a Restek® Haysep Q (1 mm × 2 m) micropacked column and a Restek® ShinCarbon ST (1 mm × 2 m) micropacked column. The detection of gaseous products was carried out at TCD temperature of 50 °C and FID temperature of 380 °C. For the determination of the Faradaic efficiency, at first, different volumes (i.e. 5 µL, 10 µL, 15 µL, and 20 µL) of mixed calibrated gases containing $H_2$ (10%, v/v), CO (10%, v/v), $CH_4$ (5%, v/v), $CO_2$ (20%, v/v), and He (55%, v/v) (from Air Products) were analyzed by experimental GC system in order to depict a relationship between the molar amount of related gas and the corresponding chromatogram peak area (**Figure 4-15**). Then, Faradaic efficiency of each detected gas during the electrolysis was calculated by using the following equation:

$$FE\% = \frac{\alpha n F}{Q}$$

where $\alpha$ is the number of electrons transferred (e.g. $\alpha$ = 2 for CO and $H_2$), $n$ is the number of moles of the target product, $F$ is the Faraday constant and $Q$ is the consumed electrical charge. For CO and $H_2$ detection, according to the calibrated curves in **Figure 4-15**,

$$n_{\mathrm{CO}} = \frac{A_{\mathrm{CO}}}{2.94 \times 10^{14}} \times \frac{V_{\mathrm{Headspace}}}{V_{\mathrm{Sample}}}$$

$$n_{\mathrm{H2}} = \frac{A_{\mathrm{H2}}}{2.56 \times 10^{14}} \times \frac{V_{\mathrm{Headspace}}}{V_{\mathrm{Sample}}}$$

where *A* is the chromatogram peak area of target product CO or $H_2$, $V_{Headspace}$ is the volume of space above the electrolyte in the electrochemical cell, which was measured after each electrolysis reaction, and $V_{Sample}$ is the sample injection volume.

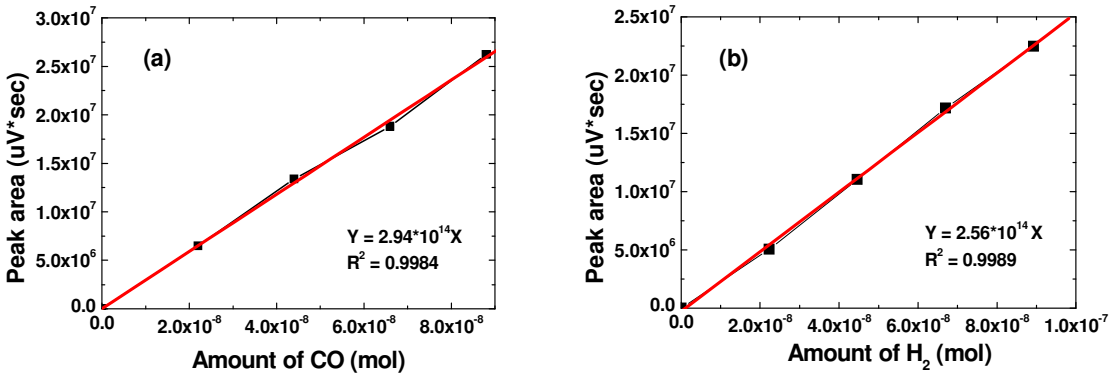


**Figure 4-15**: Calibration curves for CO (a) and $H_2$ (b) obtained with different volumes of calibrated gases.

### 4.4.6 Additional Instrumentation

For Ionic Chromatography (IC) analysis, the concentration of formate ions (diluted four times) before and after electrolysis was determined using Dionex DX120 IC equipped with a conductivity detector and a Dionex AS19 (4 mm × 250 mm) ion-exclusion column. The sample was eluted with potassium hydroxide at a flow rate of 1 mL $min^{-1}$. The detection was carried out by conductivity with a Self-Regenerating Suppressor (SRS).

The surface morphology of electrode materials was analyzed by scanning electronic microscopy (SEM), using a Jeol JSM 7100F (10kV) instrument, equipped with a field emission gun, operating in high vacuum conditions, at an accelerating voltage variable from 2 to 20 keV, depending on the observation needs.

Energy-dispersive X-ray spectroscopy (EDX) was performed using a Silicon Drift Detector (SDD) - X-Max (Oxford Instruments) and the AZtecEnergy software.

XPS measurements were performed with an Mg Kalpha (hv) 1254 eV X-ray source, using a VSW HA100 photoelectron spectrometer with a hemispherical photoelectron analyzer, working at an energy pass of 20 eV for survey and resolved spectra. The experimental resolution was 1.0 eV.

## 4.5 Conclusions

In this work, we have deposited Bi on *p*-type Si under acidic aqueous conditions *via* an easy electrodeposition pathway. We have shown that the electrodeposited Bi promotes the electrocatalytic reduction of $CO_2$ to formate. Furthermore, our photoelectrochemical system takes advantage from the use of photoactive *p*-Si as the immobilization substrate for significantly decreasing the CDRR onset potential with respect to what has been published before. Both composition and morphology of the deposited Bi cocatalyst could be tuned by controlling the electrodeposition time and the optimal *p*-Si/Bi (5s) photocathode exhibited the highest photocurrent density (-24.1 mA $cm^{-2}$) with partial formate photocurrent density $j_{formate}$ = -17.4 mA $cm^{-2}$ at -1.7 V vs. SCE (corresponding to a 0.84 V overpotential for $CO_2$ to formate conversion). Such values highlight the excellent catalytic activity for CDRR of our photocathodes, outperforming that of recently reported Bi-based catalysts (see **Table 1-2** in chapter 1). Moreover, under our conditions, the formate production rate reached 14.9 mg $h^{-1}$ $cm^{-2}$ with a Faradaic efficiency of 72%. We anticipate that the conversion efficiency of $CO_2$ could be further improved by using structured silicon surfaces,[29] and/or Bi nanostructures,[1,20] or by modulating the illumination level. Overall, this study unveils a new prospect of Bi-modified photocathodes for the solar conversion of $CO_2$ to formate.

**References**

[1] Yang, H., Han, N., Deng, J., Wu, J., Wang, Y., Hu, Y., Ding, P., Li, Y., Lu, J. Selective $CO_2$ reduction on 2D mesoporous Bi nanosheets. *Advanced Energy Materials*. **2018**, *8*(35), 1801536.

[2] Jouny, M., Luc, W., Jiao, F. General techno-economic analysis of $CO_2$ electrolysis systems. *Industrial & Engineering Chemistry Research*. **2018**, *57*(6), 2165-2177.

[3] Sponholz, P., Mellmann, D., Junge, H., Beller, M. Towards a practical setup for hydrogen production from formic acid. *ChemSusChem*. **2013**, *6*(7), 1172-1176.

[4] Agarwal, A. S., Zhai, Y., Hill, D., Sridhar, N. The electrochemical reduction of carbon dioxide to formate/formic acid: engineering and economic feasibility. *ChemSusChem*. **2011**, *4*(9), 1301-1310.

[5] Hori, Y., Kikuchi, K., Suzuki, S. Production of CO and $CH_4$ in electrochemical reduction of $CO_2$ at metal electrodes in aqueous hydrogen carbonate solution. *Chemistry Letters*. **1985**, *14*(11), 1695-1698.

[6] Komatsu, S., Yanagihara, T., Hiraga, Y., Tanaka, M., Kunugi, A. Electrochemical reduction of $CO_2$ at Sb and Bi electrodes in $KHCO_3$ solution (E). *Denki Kagaku*. **1995**, *63*, 217-217.

[7] DiMeglio, J. L., Rosenthal, J. Selective conversion of $CO_2$ to CO with high efficiency using an inexpensive bismuth-based electrocatalyst. *Journal of the American Chemical Society*. **2013**, *135*(24), 8798-8801.

[8] Medina-Ramos, J., Pupillo, R. C., Keane, T. P., DiMeglio, J. L., Rosenthal, J. Efficient conversion of $CO_2$ to CO using tin and other inexpensive and easily prepared post-transition metal catalysts. *Journal of the American Chemical Society*. **2015**, *137*(15), 5021-5027.

[9] Zhang, Z., Chi, M., Veith, G. M., Zhang, P., Lutterman, D. A., Rosenthal, J., Overbury, S. H., Dai, S., Zhu, H. Rational design of Bi nanoparticles for efficient electrochemical $CO_2$ reduction: the elucidation of size and surface condition effects. *ACS Catalysis*. **2016**, *6*(9), 6255-6264.

[10] Medina-Ramos, J., DiMeglio, J. L., Rosenthal, J. Efficient reduction of $CO_2$ to CO with high current density using in situ or ex situ prepared Bi-based materials. *Journal of the American Chemical Society*. **2014**, *136*(23), 8361-8367.

[11] Kim, S., Dong, W. J., Gim, S., Sohn, W., Park, J. Y., Yoo, C. J., Jang, H. W., Lee, J. L. Shape-controlled bismuth nanoflakes as highly selective catalysts for electrochemical carbon dioxide reduction to formate. *Nano Energy*. **2017**, *39*, 44-52.

[12] Koh, J. H., Won, D. H., Eom, T., Kim, N. K., Jung, K. D., Kim, H., Hwang, Y. J., Min, B. K. Facile $CO_2$ electro-reduction to formate via oxygen bidentate intermediate stabilized by high-index planes of Bi dendrite catalyst. *ACS Catalysis*. **2017**, *7*(8), 5071-5077.

[13] Han, N., Wang, Y., Yang, H., Deng, J., Wu, J., Li, Y., Li, Y. Ultrathin bismuth nanosheets from in situ topotactic transformation for selective electrocatalytic $CO_2$ reduction to formate. *Nature Communications*. **2018**, *9*(1), 1320.

[14] Zhang, S., Kang, P., Meyer, T. J. Nanostructured tin catalysts for selective electrochemical reduction of carbon dioxide to formate. *Journal of the American Chemical Society*. **2014**, *136*(5), 1734-1737.

[15] Lv, W., Zhou, J., Bei, J., Zhang, R., Wang, L., Xu, Q., Wang, W. Electrodeposition of nano-sized bismuth on copper foil as electrocatalyst for reduction of $CO_2$ to formate. *Applied Surface Science*. **2017**, *393*, 191-196.

[16] Zhong, H., Qiu, Y., Zhang, T., Li, X., Zhang, H., Chen, X. Bismuth nanodendrites as a high performance electrocatalyst for selective conversion of $CO_2$ to formate. *Journal of Materials Chemistry A*. **2016**, *4*(36), 13746-13753.

[17] Ananthi, A., Kumar, S. S., Phani, K. L. Facile one-step direct electrodeposition of bismuth nanowires on glassy carbon electrode for selective determination of folic acid. *Electrochimica Acta*. **2015**, *151*, 584-590.

[18] Zhang, X., Lei, T., Liu, Y., Qiao, J. Enhancing $CO_2$ electrolysis to formate on facilely synthesized Bi catalysts at low overpotential. *Applied Catalysis B: Environmental*. **2017**, *218*, 46-50.

[19] Guo, S. X., Zhang, Y., Zhang, X., Easton, C. D., MacFarlane, D. R., Zhang, J. Phosphomolybdic acid-assisted growth of ultrathin bismuth nanosheets for enhanced electrocatalytic reduction of $CO_2$ to formate. *ChemSusChem*. **2019**, *12*(5), 1091-1100.

[20] Zhang, H., Ma, Y., Quan, F., Huang, J., Jia, F., Zhang, L. Selective electro-reduction of $CO_2$ to formate on nanostructured Bi from reduction of BiOCl nanosheets. *Electrochemistry Communications*. **2014**, *46*, 63-66.

[21] Ding, P., Hu, Y., Deng, J., Chen, J., Zha, C., Yang, H., Han, N., Gong, Q., Li, L., Wang, T., Zhao, X. Controlled chemical etching leads to efficient silicon–bismuth interface for photoelectrochemical $CO_2$ reduction to formate. *Materials Today Chemistry*. **2019**, *11*, 80-85.

[22] Huang, H., Xiao, K., Yu, S., Dong, F., Zhang, T., Zhang, Y. Iodide surface decoration: a facile and efficacious approach to modulating the band energy level of semiconductors for high-performance visible-light photocatalysis. *Chemical Communications*, **2016**, *52*(2), 354-357.

[23] Dharmadhikari, V. S., Sainkar, S. R., Badrinarayan, S., Goswami, A. Characterisation of thin films of bismuth oxide by X-ray photoelectron spectroscopy. *Journal of Electron Spectroscopy and Related Phenomena*. **1982**, *25*(2), 181-189.

[24] Medina-Ramos, J., DiMeglio, J. L., Rosenthal, J. Efficient reduction of $CO_2$ to CO with high current density using in situ or ex situ prepared Bi-based materials. *Journal of the American Chemical Society*. **2014**, *136*(23), 8361-8367.

[25] DiMeglio, J. L., Rosenthal, J. Selective conversion of $CO_2$ to CO with high efficiency using an inexpensive bismuth-based electrocatalyst. *Journal of the American Chemical Society*. **2013**, *135*(24), 8798-8801.

[26] Li, F., Chen, L., Knowles, G. P., MacFarlane, D. R., Zhang, J. Hierarchical mesoporous $SnO_2$ nanosheets on carbon cloth: a robust and flexible electrocatalyst for $CO_2$ reduction with high efficiency and selectivity. *Angewandte Chemie International Edition*. **2017**, *56*(2), 505-509.

[27] Han, Z., Kortlever, R., Chen, H. Y., Peters, J. C., Agapie, T. $CO_2$ reduction selective for C≥2 products on polycrystalline copper with N-substituted pyridinium additives. *ACS Central Science*. **2017**, *3*(8), 853-859.

[28] Kuhl, K. P., Cave, E. R., Abram, D. N., Jaramillo, T. F. New insights into the electrochemical reduction of carbon dioxide on metallic copper surfaces. *Energy & Environmental Science*. **2012**, *5*(5), 7050-7059.

[29] Beeman, J. W., Bullock, J., Wang, H., Eichhorn, J., Towle, C., Javey, A., Toma, F. M., Mathews, N., Ager, J. W. Si photocathode with Ag-supported dendritic Cu catalyst for $CO_2$ reduction. *Energy & Environmental Science*. **2019**, *12*(3), 1068-1077.

# Conclusions and Perspectives

## Conclusions:

Silicon is an attractive semiconductor material for a wide range of energy-related applications. In particular, functionalized silicon surfaces can be used as photocathodes and can be employed to promote photoelectrochemical conversion of protons to hydrogen as well as $CO_2$ reduction to yield solar fuels. In this thesis, we first summarized different types of electrocatalytic systems and discussed optical and thermodynamic properties of *p*-type silicon surfaces for photoelectrocatalysis.

We reported in chapter 2 the photoelectrocatalytic properties of $\{Mo_3S_4\}$-based cluster assemblies incorporating a polyoxotungstate $\{AsW_{12}O_{42}\}$ matrix on *p*-type silicon surfaces. As expected, such photocathodes showed a superior catalytic activity and a better robustness compared with photocathodes modified with $\{Mo_3S_4\}$ clusters bearing a simple organic ligand. We have demonstrated that our optimized photoelectrodes exhibit efficient catalytic performance with a promising stability for the simulated sunlight-driven HER under acid pH conditions. In order to understand the electrocatalytic mechanism of the $Mo_3S_4$-POM cocatalyst immobilized on silicon surface, chapter 3 has described XAS investigations of functionalized silicon photocathodes for sunlight-driven HER through a *in operando* solid state study. XANES analysis revealed a progressive oxidation state change of absorption Mo atom, and a coordination structural change caused by the partial substitution of $S^{2-}$ sulfide ligands by $O^{2-}$ oxo groups during electrolysis process in acidic solution.

Chapter 4 presented the electrocatalytic performance of photocathodes modified with Bi-based catalysts for the conversion of $CO_2$ to formic acid. The optimal catalyst coverage was determined and such functionalized and optimized photocathodes exhibited an excellent catalytic activity with improved photocurrent densities and high product conversion selectivity. Our research confirmed that silicon photocathodes comprising Bi can promote $CO_2$ conversion efficiencies and can achieve good production yields.

In summary, the results described in this thesis demonstrate the versatility of functionalized silicon photocathodes. The immobilization of cocatalysts on H-terminated silicon surfaces by various deposition methods were attempted and studied. Such functionalized silicon photocathodes present significant photoelectrocatalytic activities towards the targeted applications.

## Future Perspectives:

1. From our research, it is clear that $\{Mo_3S_4\}$-based polyoxothiometalates can be considered as a new class of electrocatalysts, which can considerably improve the catalytic activity and the stability of the silicon photocathodes when used for the photoelectrochemical HER. Unfortunately, after a lot of

works focused on $CO_2$ reduction, their electrocatalytic activity for suitable $CO_2$ conversion applications has not been demonstrated yet. However, because of the high metal nuclearity of polyoxothiometalates, they might represent relevant molecular systems for multielectron transfer engineering. In this context, future research and development focusing on $CO_2$ reduction is still worth to be attempted.

2. As we mentioned in chapter 3, the electrocatalytic mechanism of $\{Mo_3S_4\}$-POM catalyst for HER is partially determined through *in operando* XAS analysis. Few information was obtained from EXAFS spectrum essentially due to the overlapping of diffraction peaks of underlying monocrystalline silicon substrate. Further investigations could underway to understand in more details the structure of these catalysts under experimental conditions and their reaction mechanism.

3. The silicon photocathode modified by Bi could be applied and developed on structured silicon surfaces, such as micropyramid arrays or micro/nanowires. We anticipate that further work on these designed structural silicon surfaces will help in improving both photocurrent response and conversion efficiency of $CO_2$ reduction. Furthermore, electrodeposition is one promising deposition technology for producing metallic or alloy coatings in (photo-) electrochemistry. Using electrodeposition offers many advantages: relatively low cost, control of grain size (micro- or nano- structured electrodeposits), low processing temperature, as well as ease of scale-up. In our opinion, this practical deposition method could be explored with other abundant main-group metals, such as Sn and Pb, which have been demonstrated to be good catalysts to produce formate with greater FE in $CO_2$-saturated aqueous solution. We anticipate that this strategy can be applied onto functionalized hydrogenated silicon photoelectrodes for $CO_2$ reduction. Finally, in order to improve $CO_2$ reduction selectivity, the mechanism of formation (i.e. nucleation and growth steps) of micro- (or nano-) structured metallic electrodeposits on our photoelectrodes might also be studied and possibly elucidated in a future research.

UNIVERSITE MATIERE BRETAGNE MOLECULES LOIRE ET MATERIAUX

UNIVERSITÉ DE RENNES 1

**Titre :** Conversion photoélectrochimique des protons et $CO_2$ à partir de photocathodes en silicium fonctionnalisées

**Mots clés :** surface de silicium, photocathode, polyoxothiométallate, bismuth, production d'hydrogène, réduction du $CO_2$.

**Résumé :** La fonctionnalisation de surfaces de silicium hydrogéné par des catalyseurs électrochimiques suscite un fort intérêt pour la production solaire de dihydrogène et pour la conversion du $CO_2$ en combustibles. Dans le cadre de cette thèse, nous avons déposé des clusters ou des polyoxothiométallates contenant l'entité $\{Mo_3S_4\}$ sur cette surface par drop-casting pour la production d'hydrogène. Par la suite, nous avons étudié la modification de ces surfaces avec du bismuth électrodéposé, puis nous avons utilisé ces surfaces fonctionnalisées pour la réduction du $CO_2$.

**Title :** Photoelectrochemical conversion of protons and $CO_2$ from functionalized silicon photocathodes

**Keywords :** silicon surface, photocathode, polyoxothiometalate, bismuth, hydrogen production, electro-reduction of $CO_2$.

**Abstract :** The functionalization of hydrogenated silicon surfaces by electrochemical catalysts is of high interest for the photoassisted production of dihydrogen and for $CO_2$ valorization into solar fuels. In this thesis, we have shown that the $\{Mo_3S_4\}$-based clusters or polyoxothiometalates deposited onto hydrogen-terminated surfaces by drop-casting method can be employed for hydrogen production. Moreover, we have studied silicon modified by electroplated Bi and used the corresponding photocathodes for $CO_2$ conversion.

# Résumé

Ces travaux de thèse ont porté sur l'élaboration et la caractérisation de photocathodes à base de Si de type-*p* modifiées avec des électrocatalyseurs du type POM (Polyoxometalates) ou métalliques à base de bismuth (Bi) pour les réactions HER (Hydrogen Evolution Reaction) et CDRR ($CO_2$ reduction reaction) respectivement.

La production d'énergie basée sur la combustion de combustibles fossiles a provoqué une grave pollution de l'environnement et le réchauffement de la planète. Par conséquent, l'utilisation de sources d'énergie à haute densité massique telles que l'hydrogène, ainsi que la conversion des émissions de $CO_2$ en produits à haute valeur ajoutée sont deux domaines qui ont fait l'objet d'une attention considérable de la part des chercheurs désireux d'évoluer vers un environnement durable. Dans ce cadre, la conversion photoélectrochimique utilisant l'énergie solaire apparaît comme une méthode prometteuse . Pour cela, le silicium représente un candidat idéal pour la conversion de l'énergie solaire en raison de son abondance terrestre et de ses propriétés semi-conductrices particulières. Avec une petite bande interdite d'environ 1.1 eV et un bord de bande de conduction approprié, le silicium de type *p* est considéré comme un matériau prometteur pour la photocathode. Cependant, ses performances sont fortement affectées par sa faible stabilité et son activité catalytique.Des recherches sont donc en cours pour trouver des stratégies efficaces afin d'améliorer ses performances. Dans ce cadre, le contrôle de la morphologie de surface, la stratégie de modification de la surface ainsi que les jonctions à l'interface sont des paramètres essentiels qui font actuellement l'objet de recherches approfondies.

Dans la première application, les matériaux électrocatalytiques d'intérêt étudiés sont dérivés de clusters $\{Mo_3S_4\}$ comme complexes de coordination incorporés dans le réseau des polyoxométallates (POM). Les polyoxométallates (POMs) sont des entités polynucléaires résultant de la connexion de polyèdres $[MO_y]^{n-}$ où M est un centre métallique. Les POMs représentent des espèces intermédiaires entre l'ion métallate basique mononucléaire $[MO_4]^{n-}$ libre en solution et l'oxyde métallique $MO_x$ solide. L'entité $\{Mo_3S_4\}$ est utilisée dans la formation de complexes de coordination du fait de sa réactivité avec un grand nombre de métaux de transition. Ce composé dit pseudo-cuboïdal possède trois atomes de molybdène susceptibles de réagir avec des ligands aux propriétés très diverses (aquo, amino, hydrure, halogénure,…). Les

systèmes comportant des métaux de transition et des entités soufrées sont très étudiés car ils possèdent d'excellentes propriétés catalytiques. Les assemblages POM-entité thiomolybdique comportant des métaux de transition et des entités soufrées sont très étudiés car ils possèdent d'excellentes propriétés catalytiques. Ils sont engagés dans des processus de transfert d'électrons et de protons et sont souvent impliqués dans les sites actifs de molécules biologiques.

La seconde application liée à l'énergie des semi-conducteurs en silicium de type *p* est la réaction d'électro-réduction du $CO_2$ (CDRR). Des photocathodes en silicium de type *p* modifiées avec différents co-catalyseurs ont été développées pour réduire le $CO_2$ en carburants organiques. L'incorporation de cocatalyseurs pourrait améliorer considérablement les performances des électrodes semi-conductrices pour la réduction de $CO_2$. Parmi les cocatalyseurs, le bismuth (Bi), un cocatalyseur de métal non toxique et peu coûteux, est capable de réduire le $CO_2$ en acide formique. Par conséquent, le développement de silicium de type *p* comportant des électrocatalyseurs à base de bismuth est prévu pour obtenir une sélectivité de réduction élevée, et réaliser une activité catalytique favorable pour la réduction photoélectrochimique du $CO_2$.

La thèse est divisée en quatre chapitres principaux, précédés d'une introduction générale et suivis d'une conclusion générale. L'un des objectifs de cette thèse est également axé sur une approche fondamentale consistant à proposer des corrélations structure-activité.

Dans le chapitre 1, la partie bibliographique est consacrée à l'état de l'art sur la production électrocatalytique d'hydrogène par réduction de $H^+$ et à la réduction du $CO_2$. Dans une première partie, la réaction HER est abordée d'un point de vue mécanistique avec une présentation des différentes catégories d'électrocatalyseurs efficaces pour surmonter certaines limitations relatives au surpotentiel et à la barrière cinétique apparaissant dans ces réactions. Un éclairage particulier est fait notamment sur l'utilisation de complexes moléculaires immobilisés sur des électrodes et sur l'importance de la modification des ligands possédant des fonctions d'accroche appropriées. Les POMs sont ensuite décrits et leurs utilisations comme électrocatalyseurs discutées. Dans une seconde partie, nous nous sommes intéressés aux concepts de base de la réaction de CDRR et aux co-catalyseurs spécifiques relatifs à cette réaction d'intérêt : des métaux, notamment le Bi, des oxydes métalliques, des chalcogénures, des complexes organo-métalliques et certaines catégories de POMs. Ce chapitre bibliographique se termine par unediscussion des phénomènes photoélectrocatalytiques se produisant à l'interface semi-

conducteur/électrolyte, des divers semi-conducteurs d'intérêt pour la photo-dissociation de l'eau et pour la réduction photo-assistée du $CO_2$, et de l'utilisation de photocathodes à base de Si modifiées par des co-catalyseurs.

Le chapitre 2 (intitulé « Polyoxothiometalate-Derivatized Silicon Photocathodes for Sunlight-Driven Hydrogen Evolution Reaction ») est centré sur l'élaboration de photocathodes à base de Si, décorées avec des structures polyoxotungstates ($AsW_{12}O_{42}$) intégrant des entités à base de $\{Mo_3S_4\}$. Ces photocathodes modifiées sont ensuite évaluées vis-à-vis de la réaction HER en conditions acides, et les activités sont corrélées aux propriétés structurales et aux modifications chimiques. Cette approche vise à surmonter les limitations intrinsèques du silicium en termes de cinétique de transfert de charge et tire profit de la capacité de fonctionnalisation des POMs. Dans ce cadre, nous avons tout à bord caractérisé les précurseurs moléculaires utilisés, puis le matériau $Mo_3S_4$-POM résultant, avant d'optimiser la teneur sur les électrodes de Si. Les structures $Mo_3S_4$-POM sont déposées par drop-casting sur les surfaces Si(100)-H. Cette étape est ensuite validée par suivi du photocourant cathodique pour la réaction HER sous irradiation solaire artificielle (AM 1.5G, 100 mW $cm^{-2}$), par voltampérométrie cyclique et par des caractérisations détaillées (XPS, AFM) avant et après réaction d'électrolyse. Les photocathodes modifiées présentant les meilleures activités [celles recouvertes de 7.2 x $10^{-5}$ mmol $cm^{-2}$ pour $Mo_3S_4$(acac-Bu) ou 7.2 x $10^{-6}$ mmol $cm^{-2}$ pour $Mo_3S_4$-POM] ont été étudiées sousirradiation. Nous avons ensuite enregistré les courbes chronoampérométriques correspondantes durant l'électrolyse pour les 2 types de photocathodes modifiées. Les réponses photoélectrochimiques ont mise en avant la stabilisation des électrodes modifiées en milieu acide après une courte période d'activation d'environ 5 minutes, qui pourrait être liée à un relargage du dépôt de l'électrode. Nous avons ensuite déterminé les « turnover frequencies » (TOFs) en fonction du potentiel appliqué. Des valeurs élevées (en considérant le nombre de sites actifs estimé par des mesures XPS et AFM) ont été calculées. De telles photocathodes modifiées présentaient des densités de photocourant cathodique supérieures à -26 mA $cm^{-2}$ ainsi qu'une excellente stabilité pour la réduction des protons en $H_2$ dans le milieu acide pendant plus de 45 h.

Le chapitre 3 (intitulé « X-ray absorption spectroscopy study of $Mo_3S_4$ based polyoxothiometalate electrocatalysts during HER ») est consacré à des mesures de spectroscopie d'absorption des rayons X (X-ray Absorption Spectroscopy XAS) sous conditions *operando* (réalisées au synchrotron SOLEIL sur la ligne ROCK) afin de suivre l'évolution de

l'environnement des atomes de Mo des électocatalyseurs $Mo_3S_4$-POM déposés sur la photocathode de Si. Après avoir rappelé quelques principes de base et conditions expérimentales de la technique, nous avons décrit la préparation des échantillons reposant sur le dépôt des co-catalyseurs sur l'électrode de type *p*-Si hydrogénée. Des résultats préliminaires obtenus à partir de composés de référence à l'état solide ont permis d'établir les liens entre l'évolution du pré-seuil et du seuil de Mo dans le spectre XAS avec les changements de degré d'oxydation du Mo ou de la structure de coordination du Mo. Ensuite, nous avons enregistré les spectres XAS de la surface modifiée par l'électrocatalyseur $Mo_3S_4$-POM en milieu acide avant et au cours d'une réaction d'électrolyse. Les données obtenues sont en accord avec un changement de coordination des centres de Mo durant la réaction, suggérant la formation d'une première sphère de coordination (M-O) de géométrie octaédrique plutôt que d'espèces (Mo-S) de géométrie tétraédrique. Ces changements peuvent être expliqués par la substitution partielle, autour des centres Mo, des ligands sulfure $S^{2-}$ par des groupements oxo $O^{2-}$, ce qui corrobore certains résultats déjà mis en évidence dans le chapitre 2.

Le chapitre 4 (intitulé « Efficient reduction of $CO_2$ to formate at Bi-modified *p*-Si photocathode ») porte sur la modification de photocathodes de Si avec des cocatalyseurs à base de Bi et sur leurs performances catalytiques vis-à-vis de la réduction photo-assistée du $CO_2$.Au démarrage de cette étude, aucune étude n'avait été publiée sur l'intégration de catalyseurs à base de Bi sur Si pour la réduction photoélectrocatalytique du $CO_2$. L'objectif visé était la conversion du $CO_2$ préférentiellement en formate. Les photocathodes modifiées Bi ont été préparées par photoélectrodéposition du précurseur $Bi(NO_3)_3.5H_2O$ en milieu 1M $HNO_3$ sous illumination. Nous avons tout à bord optimisé la méthode de photoélectrodéposition en termes de durée, pour en conclure qu'une augmentation de la durée d'illumination n'était pas bénéfique au regard de l'activité des électrodes ainsi préparées. Les photocathodes obtenues ont, dans un premier temps, été évaluées vis-à-vis de la réaction d'HER ainsi que CDRR. Nous avons mis en évidence que la durée de déposition la plus courte (5s) conduit à la fois à un potentiel de seuil moins négatif et à des densités de photocourant cathodique plus élevées. Les caractérisations de ces photocathodes modifiées Bi ont ensuite été réalisées par MEB, EDX et XPS. Les caractérisations morphologiques montrent des structures dendritiques de plus en plus denses avec la durée de déposition. Ces surfaces apparaissent moins homogènes après réaction de CDRR d'une durée de 30 min, en adéquation avec l'hypothèse préalable de perte de Bi due à la réaction. Les analyses XPS confirment la présence de Bi sous forme $Bi^0$ et $Bi^{3+}$, ces dernières espèces étant attribuées à

la présence de $Bi_2O_3$. Après électrolyse, nous avons constaté la modification de certains pics caractéristiques observés sur les spectres XPS de $C_{1s}$ et $O_{1s}$. Enfin, les produits de réaction ont été identifiés et quantifiés en phase gazeuse (CO, $H_2$) et liquide (formate dissout) après 30 minutes de réaction, en termes d'efficacité faradique, de sélectivité, de densité de photocourant et de vitesse de formation. Il a ainsi été observé que la formation de formate est la réaction majoritaire. Néanmoins, des réactions parasites telles que HER se produisent et des traces de CO ont été détectées. En résumé, de telles photocathodes modifiées à partir de Bi présentent des densités de photocourant cathodique d'environ -24 mA $cm^{-2}$ et un rendement faradique pour formate supérieur à 72%.

La conclusion générale résume les principaux points marquants de ce travail de thèse et quelques perspectives dans le domaine de l'activation photoélectrochimique de petites molécules ont été ensuite proposées.